Universidade de Aveiro
2022

LUÍS CARLOS MARQUES RUIVO

OTIMIZAÇÃO CATALÍTICA DO GÁS BRUTO RESULTANTE DA GASIFICAÇÃO DE BIOMASSA EM LEITO FLUIDIZADO

CATALYTIC UPGRADING OF BIOMASS-DERIVED RAW GAS IN FLUIDIZED BED GASIFIERS

Universidade de Aveiro
2022

LUÍS CARLOS MARQUES RUIVO

OTIMIZAÇÃO CATALÍTICA DO GÁS BRUTO RESULTANTE DA GASIFICAÇÃO DE BIOMASSA EM LEITO FLUIDIZADO

CATALYTIC UPGRADING OF BIOMASS-DERIVED RAW GAS IN FLUIDIZED BED GASIFIERS

Tese apresentada à Universidade de Aveiro para cumprimento dos requisitos necessários à obtenção do grau de Doutor em Ciência e Engenharia de Materiais, realizada sob a orientação científica do Doutor Jorge Ribeiro Frade, Professor Catedrático do Departamento de Engenharia de Materiais e Cerâmica da Universidade de Aveiro e co-orientação do Doutor Luís António da Cruz Tarelho, Professor Associado do Departamento de Ambiente e Ordenamento da Universidade de Aveiro.

Este trabalho teve apoio financeiro da FCT, Portugal, através da bolsa de doutoramento SFRH/BD/129901/2017 e dos projetos de investigação POCI-01-0145-FEDER-030661 e CENTRO-01-0145-FEDER-000005.

This work was funded by FCT, Portugal, through the PhD grant ref. SFRH/BD/129901/2017 and research projects POCI-01-0145-FEDER-030661 and CENTRO-01-0145-FEDER-000005.

PD + F

PROGRAMAS DE DOUTORAMENTO FCT

o júri

Presidente

Prof. Doutor João Manuel da Costa e Araújo Pereira Coutinho
professor catedrático da Universidade de Aveiro

Vogais

Prof. Doutor Carlos Peréz Bergmann
professor catedrático da Universidade Federal do Rio Grande do Sul

Prof. Doutor Adélio Miguel Magalhães Mendes
professor catedrático da Faculdade de Engenharia da Universidade do Porto

Prof. Doutora Maria Amélia Nortadas Duarte de Almeida Lemos
professora associada da Universidade de Lisboa

Prof. Doutor Luís António da Cruz Tarelho
professor associado da Universidade de Aveiro

Prof. Doutora Maria Paula da Silva Seabra
professora auxiliar da Universidade de Aveiro

Agradecimentos

Embora seja um título individual, não poderia deixar de expressar o mais profundo agradecimento a todos os que de alguma forma contribuíram para a concretização deste trabalho.

Ao Professor Doutor Jorge Frade, o meu sincero agradecimento pela amizade, orientação e motivação permanente ao longo do doutoramento. A sua sabedoria e ética de trabalho marcarão para sempre o meu percurso pessoal e profissional. Igualmente, manifesto o meu reconhecimento e apreço ao Professor Doutor Luis Tarelho pelo apoio ilimitado que concedeu durante o doutoramento.

A minha gratidão é também extensível aos colegas e técnicos do Departamento de Engenharia de Materiais e Cerâmica (DEMAC) e do Departamento de Ambiente e Ordenamento (DAO) da Universidade de Aveiro pelo contributo valioso que tiveram para a execução das tarefas.

Por fim, não podia deixar de agradecer à minha incrível família pelo apoio incondicional, sem o qual não teria alcançado esta meta. Aos meus pais, sogros e Fabiana, obrigado por tudo o que fazem por mim!

Keywords Biomass, Gasification, Tar, Hydrogen, Iron Catalysts.

Abstract

Gasification of lignocellulosic biomass is a thermochemical conversion route with high potential to reduce the dependence on fossil fuels. Still, current gasification technologies present technical limitations that turn their large-scale exploitation unfeasible, mostly due to the presence of tar in the producer gas that incites several operational constrains. Amongst the existing techniques for tar removal, catalytic hot gas cleaning has been proposed as an attractive approach, highlighting the need to explore alternative catalysts with potential applicability in gasification processes with limited economic feasibility. The present thesis aimed to explore the catalytic potential of low-cost iron-based materials to improve the quality of biomass-derived gas. In order to obtain insights about the dependence of catalyst performance on the thermochemical conditions of the gasification process, a graphical approach based on experimental data and thermodynamic modelling were developed. Attention was given to potential deactivation mechanisms resulting from gas-solid interactions, as well as to the stability of relevant iron catalytic systems when exposed to biomass gas atmospheres. Thermodynamic predictions suggest that minimal changes in the redox atmosphere of the gasifier can have a significant impact on the catalytic nature of iron. Moreover, controlled operating parameters contributes to enhance the tolerance of iron-based catalysts to deactivation by coke, H_2S poisoning and/or carbonation. One should also consider suitable composition changes to enhance their redox properties and their thermochemical stability, possibly combined with microstructural or nanostructural development during materials processing. A novel $Fe_{2-x}Ni_xTiO_5$ catalyst with low Ni load was developed and tested for downstream upgrading of biomass-derived gas. The material was prepared by combining mechanical activation and microwave firing. The catalytic performance towards steam reforming reactions was studied in a fixed bed tubular reactor, using a mixture of C_7H_8 and $C_{10}H_8$ as model tar compounds, as well as downstream a fluidized bed gasifier. The reforming studies revealed a high conversion of model tar compounds for reaction temperatures above 700 ºC. The addition of Ni promoted both steam reforming and water-gas-shift reactions, increasing H_2 content in the producer gas. The $Fe_{2-x}Ni_xTiO_5$ catalyst also exhibited 78 % decrease in total tar concentration at 800 ºC when applied in a fixed bed reactor, located downstream of a bench-scale fluidized bed gasifier. A gradual decline in the catalytic activity was observed with increased time on stream, possibly because of structural changes in iron active sites and sulphur chemisorption on Ni surface. The in-situ performance of a highly gas permeable $Fe_{2-x}Mn_xO_3$ catalyst during biomass gasification was also studied, seeking to promote tar conversion by oxidation reactions. The catalysts were obtained through the functionalization of porous ceramic structures by incipient wetness impregnation, with subsequent microwave-assisted thermal treatment.

Particular attention was given to the influence of the operating conditions on the tar conversion ability. The $Fe_{2-x}Mn_xO_3$ catalyst showed high activity in converting tar compounds with increasing reaction temperature and equivalence ratio, while decreasing the residence time showed a negative impact on catalyst performance. Catalytic conversion of tar compounds followed a redox-type mechanism, facilitated by the variable oxygen stoichiometry of mixed Fe/Mn oxides. Further analysis of the spent catalysts revealed sulphur interactions, which increased with temperature and did not correlate with the catalytic performance. This can be explained by the wide redox stability range of divalent manganese oxide and its enhanced tolerance to H_2S. Under optimal operating conditions, the catalyst promoted 83 % decrease in tar concentration, as well as a relevant increase in gasification parameters, such as the gas yield (0.81 to 0.93 $\mathrm{Nm^3_{dry,gas}} \cdot \mathrm{kg^{-1}_{dry,fuel}}$), carbon conversion efficiency (53.1 to 65.1 %) and cold gas efficiency (50.7 to 61.6 %). One also sought to explore the in-situ operation of composite catalysts based on siderite and concrete precursor mixtures for H_2-enriched gas production. A cost-effective granulation method has been developed for the preparation of catalysts, followed by thermal treatment in N_2 atmosphere. Catalytic performance towards water-gas-shift reaction was studied in a fixed bed reactor and Taguchi experimental design was applied to clarify the influence of experimental parameters on H_2 promotion. The influence of the experimental parameters on H_2 promotion had the following order: reaction temperature (43.1 %), concrete mass ratio (30.2 %), and steam to carbon molar ratio (26.7 %). These contributions were associated with the redox behaviour of iron oxides with mixed valence, derived from the siderite precursor, with corresponding O_2 storage ability, and extended conditions for carbonation/decarbonation of the concrete precursor, which may provide CO_2 storage ability. When integrated into the freeboard zone of a bubbling fluidized bed gasifier, one observed a significant increase in the H_2:CO molar ratio (1.9 to 3.3), H_2 yield (33.8 to 48.6 $\mathrm{g_{H_2}} \cdot \mathrm{kg^{-1}_{dry,fuel}}$), carbon conversion efficiency (54.1 to 58.6 %) and cold gas efficiency (55.0 to 60.9 %). Though the catalyst exhibited resistance to sintering, post-mortem analysis suggests loss of active species after repeated cycles of regeneration due to thermal-induced stresses, which caused a slight decrease in activity. In conclusion, the results of this thesis demonstrate that the application of iron-based catalysts in biomass gasification is feasible when dealing with low-cost precursors, showing similar performance to other catalysts found in literature. However, additional improvements should be considered before those materials might be applicable in future gasification concepts.

Palavras-chave Biomassa, Gasificação, Alcatrão, Hidrogénio, Catalisadores

Resumo

A gasificação de biomassa lignocelulósica é um processo de conversão termoquímica com elevado potencial para reduzir a dependência dos combustíveis fósseis. No entanto, as tecnologias existentes apresentam limitações técnicas que inviabilizam a sua exploração em grande escala, principalmente devido à presença de alcatrão no gás produzido que incita diversos problemas operacionais. Entre os métodos existentes para a remoção de alcatrão, a conversão térmica por via catalítica assume particular interesse, destacando-se a necessidade de explorar catalisadores alternativos com aplicabilidade em processos de gasificação de biomassa com alta sensibilidade económica. A presente tese procurou explorar o potencial de materiais de baixo custo à base de ferro para melhorar a qualidade do gás de gasificação. Por forma a obter orientações sobre o desempenho dos catalisadores em condições de gasificação, foi desenvolvida uma abordagem gráfica com base em dados experimentais e modelação termodinâmica. Especial atenção foi dada a potenciais mecanismos de desativação resultantes de interações gás-sólido, assim como à estabilidade de sistemas catalíticos de ferro relevantes quando expostos à atmosfera gasosa. Os cálculos termodinâmicos sugerem que pequenas variações na atmosfera redox do gasificador podem ter um impacto significativo no comportamento catalítico do ferro. Adicionalmente, o controlo eficaz dos parâmetros de operação permite melhorar a tolerância de catalisadores à base de ferro à desativação por depósitos de carbono, envenenamento por H_2S e/ou carbonatação. Deve-se também considerar alterações de composição química durante o processamento dos materiais como um pré-requisito para melhorar as propriedades redox e garantir estabilidade termoquímica. Um catalisador $Fe_{2-x}Ni_xTiO_5$ com carga de Ni reduzida foi desenvolvido e testado para a otimização do gás a jusante do gasificador. O material foi preparado através de métodos de ativação mecânica e calcinação por micro-ondas. O desempenho catalítico em reações de reformação com vapor foi estudado em reator de leito fixo, utilizando uma mistura de C_7H_8 e $C_{10}H_8$ como compostos modelo de alcatrão, assim como a jusante de um gasificador de leito fluidizado. Os estudos em reações de reformação revelaram uma elevada conversão para temperaturas de reação acima de 700 ºC. A adição de Ni promoveu simultaneamente as reações de reformação com vapor e water-gas-shift, aumentando o conteúdo de H_2 no gás. O catalisador $Fe_{2-x}Ni_xTiO_5$ também exibiu uma redução de 78 % na concentração total de alcatrão a 800 ºC, quando aplicado em reator de leito fixo localizado a jusante de um gasificador de biomassa laboratorial. Um declínio gradual da atividade catalítica ao longo do tempo foi observado, possivelmente como resultado de alterações estruturais no ferro e adsorção química de enxofre na superfície de Ni.

A performance in-situ de um catalisador $Fe_{2-x}Mn_xO_3$ com elevada permeabilidade a gás foi também avaliada em gasificação de biomassa, procurando-se promover a conversão de alcatrão através de reações de oxidação. O catalisador resultou da funcionalização de estruturas cerâmicas porosas através de impregnação por via húmida, com subsequente tratamento térmico por micro-ondas. Foi dada particular atenção ao impacto das condições de operação na capacidade de conversão de alcatrão. O catalisador $Fe_{2-x}Mn_xO_3$ mostrou elevada atividade na conversão de alcatrão com o aumento da temperatura de reação e da razão de equivalência, enquanto a diminuição do tempo de residência teve um efeito negativo. A conversão catalítica de alcatrão seguiu um mecanismo do tipo redox, facilitado pela estequiometria de oxigénio variável dos óxidos de Fe/Mn. A análise pós-teste dos catalisadores revelou interações com enxofre, sendo que estas aumentaram com a temperatura mas não apresentaram uma correlação com o desempenho catalítico. Isto pode ser explicado pela maior estabilidade redox do óxido de manganês divalente e a sua maior tolerância ao H_2S. Em condições ótimas de operação, o catalisador promoveu uma redução de alcatrão de 83 %, assim como um aumento significativo dos parâmetros de gasificação, tais como a produção específica de gás (0.81 a 0.93 $\mathrm{Nm^3_{dry,gas}\cdot kg^{-1}_{dry,fuel}}$), eficiência de conversão de carbono (53.1 a 65.1 %) e eficiência do gás arrefecido (50.7 a 61.6 %). Por outro lado, procurou-se também explorar a operação in-situ de compósitos baseados em misturas de siderite e cimento, com o propósito de aumentar o conteúdo de H_2 no gás de gasificação. Foi desenvolvido um método de granulação rentável para a preparação dos catalisadores, seguido de tratamento térmico em atmosfera inerte. O desempenho catalítico na reação de water-gas-shift foi estudado em reator de leito fixo, tendo sido aplicado um planeamento de Taguchi para avaliar o impacto dos parâmetros experimentais na promoção de H_2. A influência dos parâmetros experimentais na promoção de H_2 apresentou a seguinte ordem: temperatura de reação (43.1 %), conteúdo de cimento (30.2 %) e rácio molar vapor/carbono (26.7 %). Estas contribuições foram associadas ao comportamento redox dos óxidos de ferro com estado de valência misto, derivados do precursor de siderite e com correspondente capacidade de armazenamento de O_2, e a condições alargadas de carbonatação/descarbonatação do precursor de cimento que pode oferecer capacidade de armazenamento de CO_2. Quando integrado no freeboard de um gasificador de leito fluidizado borbulhante, observou-se um aumento significativo do rácio molar H_2:CO (1.9 a 3.3), produção específica de hidrogénio (33.8 a 48.6 $\mathrm{g_{H_2}\cdot kg^{-1}_{dry,fuel}}$), eficiência de conversão de carbono (54.1 a 58.6 %) e na eficiência do gás arrefecido (55.0 to 60.9 %). Apesar do catalisador ter apresentado resistência à degradação térmica, a análise post-mortem sugeriu perda de espécies catalíticas depois de ciclos de regeneração consecutivos, em resultado de stresses térmicos que causaram uma quebra na atividade catalítica. Em conclusão, os resultados obtidos nesta tese demonstram que a aplicação de catalisadores à base de ferro, processados a partir de precursores de baixo custo, é viável em gasificação de biomassa, mostrando desempenhos similares a outros catalisadores reportados na literatura. Contudo, estratégias de otimização adicionais devem ser avaliadas por forma a aumentar as perspetivas de aplicação destes materiais em tecnologias de gasificação.

TABLE OF CONTENTS

LIST OF PUBLICATIONS

This thesis is a summary of the following publications which are cited in the text by their roman numerals. All articles are reproduced with permission from copyright holders.

Paper I

▪ **Luís Ruivo**, Tiago Silva, Daniel Neves, Luís A.C. Tarelho, Jorge Frade. "*Thermodynamic Guidelines for Improved Operation of Iron-based Catalysts in Gasification of Biomass"*. The Article is currently submitted in the Energy Journal.

Paper II

▪ **L. C. M. Ruivo**, D. T. Pio, A. A. Yaremchenko, L. A. C. Tarelho, J. R. Frade, E. Kantarelis, K. Engvall. "*Iron-based catalyst ($Fe_{2-x}Ni_xTiO_5$) for tar decomposition in biomass gasification"*. Fuel 300 (2021) 120859. https://doi.org/10.1016/j.fuel.2021.120859.

Paper III

▪ **Luís Ruivo**, Hortência Oliveira, Helena Gomes, Nuno Cruz, Aleksey Yaremchenko, Luís A.C. Tarelho, Jorge Frade. "*Siderite/Concrete catalysts for H_2-enriched gas production from biomass steam gasification"*. Energy Conversion and Management 255 (2022) 115280. https://doi.org/10.1016/j.enconman.2022.115280.

Paper IV

▪ **Luís Ruivo**, Helena Gomes, Daniela V. Lopes, Aleksey A. Yaremchenko, Catarina Vilas-Boas, Luís A.C. Tarelho, Jorge R. Frade. "*Catalytic O_2-Steam Gasification of Biomass over $Fe_{2-x}Mn_xO_3$ Oxides Supported on Ceramic Foam Filters"*. Fuel 324 (2022) 124566. (https://doi.org/10.1016/j.fuel.2022.124566).

Other related articles were published during the course of the work and contributed to the results presented here, namely:

Paper V

▪ I. Antunes, **L.C.M. Ruivo**, L.A.C. Tarelho, A.A. Yaremchenko, J.R. Frade. "*Solid state synthesis of $Ca_2Fe_2O_5$ by reactive firing of calcite and siderite"*. The Article is currently submitted in Ceramics International Journal.

Paper VI

▪ D.T. Pio, H. G. M. F. Gomes, **L. C. M. Ruivo**, M. A. A. Matos, J. F. Monteiro, J. R. Frade, L. A. C. Tarelho. *"Concrete as low-cost catalyst to improve gas quality during biomass gasification in a pilot-scale gasifier".* Energy 233 (2021) 120931. https://doi.org/10.1016/j.energy.2021.120931.

Paper VII

▪ D. T. Pio, **L. C. M. Ruivo**, L. A. C. Tarelho, J. R. Frade, E. Kantarelis, K. Engvall. *"Tar formation during eucalyptus gasification in a bubbling fluidized bed reactor: Effect of feedstock and reactor bed composition"*. Energy Conversion and Management 229 (2021) 113749. https://doi.org/10.1016/j.enconman.2020.113749.

Paper VIII

▪ D. T. Pio, H. G. M. F. Gomes, L. A. C. Tarelho, **L. C. M. Ruivo**, R. G. Pinto, J. R. Frade, F. M. S. Lemos. *"Ilmenite as low-cost catalyst for producer gas quality improvement from a biomass pilot-scale gasifier"*. Energy Reports 6 (2020) 325–330. https://doi.org/10.1016/j.egyr.2019.08.063.

Although the content is not included in this document, other papers out of the scope of the thesis but published during the PhD are:

Paper IX

▪ Daniela V. Lopes, Aleksey D. Lisenkov, **Luís C.M. Ruivo**, Aleksey A. Yaremchenko, Jorge R. Frade, Andrei V. Kovalevsky. *"Prospects of Using Pseudobrookite as an Iron-Bearing Mineral for the Alkaline Electrolytic Production of Iron"*. Materials 15 (2022) 1440. https://doi.org/10.3390/ma15041440.

Paper X

▪ Felix Charvet, Felipe Silva, **Luís Ruivo**, Luís Tarelho, Arlindo Matos, José Figueiredo da Silva, Daniel Neves. *"Pyrolysis Characteristics of Undervalued Wood Varieties in the Portuguese Charcoal Sector"*. Energies 14 (2021) 2537. https://doi.org/10.3390/en14092537.

Paper XI

▪ **Luís Ruivo**, Michael Russo, Rúben Lourenço, Daniel Pio. Energy management in the Portuguese ceramic industry: Analysis of real-world factories. Energy 237 (2021) 121628. https://doi.org/10.1016/j.energy.2021.121628.

Paper XII

▪ M.A. Russo, **L. Ruivo**, D. Carvalho, N. Martins, A. Monteiro. Decarbonizing the energy supply one pandemic at a time. Energy Policy 159 (2021) 112644. https://doi.org/10.1016/j.enpol.2021.112644.

Paper XII

▪ N. Cruz, A. Avellan, **L. Ruivo**, F.C. Silva, P.F.A.M. Römkens, L.A.C. Tarelho, S. Rodrigues. Preparation of soil improvers using biomass ash and organic recovered wastes: impact of variable formulations and stabilization conditions on materials' properties. The Article is currently submitted and under review in Journal of Cleaner Production.

PRESENTATIONS AT CONFERENCES

L. Ruivo, R. Pinto, L. Tarelho, A. Yaremchenko, J. Frade. *Synthesis of $FeTiO_3$ and Fe_2SiO_4-based catalysts by reactions of SiC-Fe_2O_3 under controlled redox conditions*. Presented at "12ª Reunión del Grupo Especializado de Química de Estado Sólido" (QIES), Tenerife – Spain, 17-20 June 2018.

L. Ruivo, Yaremchenko, K. Engvall, E. Kantarelis, J. Frade, L. Tarelho. *Catalytic Upgrading of Biomass-Derived Raw Gas in Fluidized Bed Gasifiers*. Presented at 27th European Biomass Conference & Exhibition" (EUBCE), Lisbon – Portugal, 27-30 May 2019.

F. Charvet, **L. Ruivo**, D.T. Pio, H.G.M.F. Gomes, L.A.C. Tarelho, A. Matos, J. Figueiredo da Silva, D. Neves. *Characterization of Charcoal Production in a Brick Kiln: a Case Study in Portugal*. Presented at 29th European Biomass Conference & Exhibition" (EUBCE), Online Conference, 26-29 April 2021.

D. Neves, F. Charvet, **L. Ruivo**, A. Matos, L.A.C. Tarelho, J. Figueiredo da Silva. *Current Practices of Charcoal Production in Southern Portugal: A Case-Study in a Large Production Site*. 29th European Biomass Conference & Exhibition" (EUBCE), Online Conference, 26-29 April 2021.

1. INTRODUCTION

The need for replacing fossil fuels with alternative energy sources more beneficial to the environment is one of the main challenges associated with the increasing global energy demand. Oil, coal and natural gas have been the main sources of primary energy, representing around 70 % of consumption at a global scale [1]. This strong dependence on fossil fuels is the main source of greenhouse gas emissions, for which the environmental impact is well established. In order to mitigate the impact of climate change, the European Union (EU) intends to ensure the decarbonization of the energy system by 2050, through the transition to a circular bioeconomy, supported by renewable energy sources [2].

However, the current scenario is still far from the defined objectives, given that renewable resources only represent 16 % of primary energy world consumption [3]. The evolution of primary energy supply for Portugal and Europe (Figure 1.1) was taken from IEA statistics and shows a more optimistic scenario for Portugal, where around 30 % of the final energy consumption is provided by renewable sources [4]. The evolution of Portuguese energy mix shows major dependence on oil, which accounted for more than 60 % of the primary energy supply until the end of 20th century; this share decreased gradually over the last 2 decades, converging to about 40 % before the actual crises. This evolution corresponds to simultaneous growth of the natural gas supply, which started by 1997 and has reached close to 26 % of the Portuguese energy mix in 2020. Coal has been largely intended for electricity generation until 2018 and then dropped sharply due to a political decision to close these thermoelectric power infrastructures. Biomass, biofuels and waste account for the greatest contribution of renewable energy (Figure 1.2), and increased over the last decades to about 16.5 % of the Portuguese energy mix in 2020. It comprises mainly biomass from forestry management or its by-products, wastes from agriculture, and solid urban wastes. Biomass is used mainly for heating, whereas its contribution to electricity generation is much smaller. Biofuels represent only about 4.7 % of the renewable energies and is intended for transports. Still, the contribution of renewable energies to transports is expected to increase steadily in the coming years with steady growth of electric mobility. The hydroelectric sector shows great variability, whereas wind generation increased rapidly during the first decade of this century and almost levelled afterwards. Solar energy includes a thermal contribution and photovoltaic generation, which showed the fastest relative growth in the most recent years. However, its contribution to total electricity supply is still small.

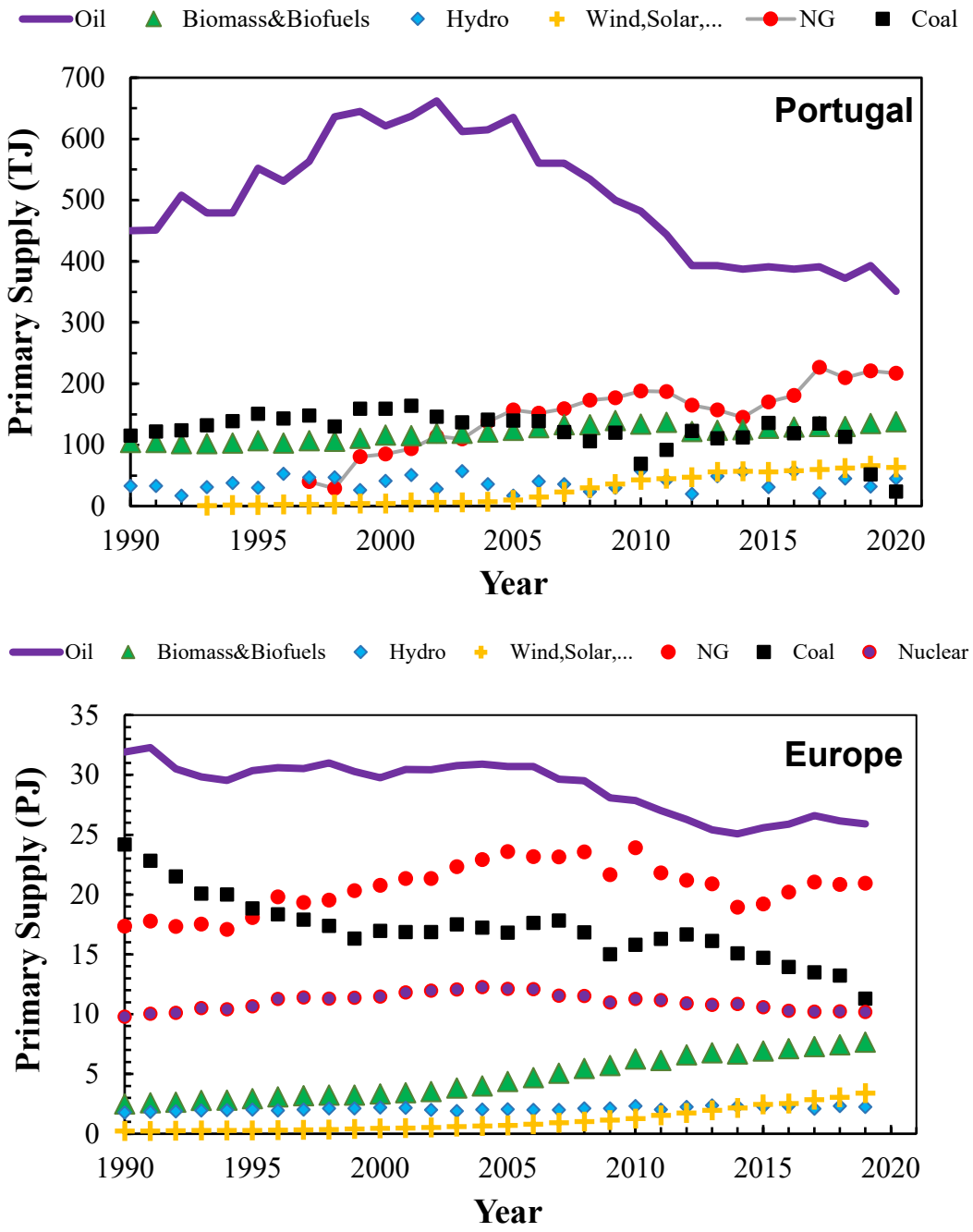

Figure 1.1 – Evolution of primary energy supply in Portugal (top) and in Europe (bottom), de-convoluted with contributions of oil, natural gas, coal, nuclear, biofuels and waste, hydroelectric, and other renewables (wind, solar and tides), based on IEA statistics available online (https://www.iea.org).

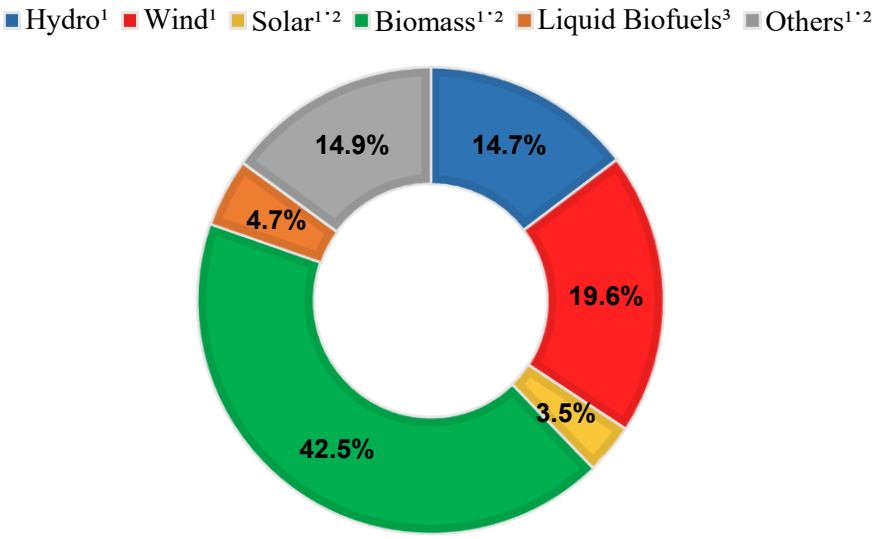

Figure 1.2 – Distribution of final energy consumption from renewable energy sources in Portugal [4]. The numbers indicate the application of each type of source (1 – Electricity Generation 2 - Thermal Energy Generation 3 – Synthesis of Transports Fuels).

The evolution of the energy mix for Europe (Figure 1.1) is slightly different, with higher share of natural gas and coal in the European mix, combined with a significant contribution of nuclear generation of electricity. The contribution of biomass and biofuels is the highest of renewable energies, showing systematic growth mainly in the last 2 decades, from about 3.9 % in 2000 to 9.4 in 2019. The contribution of solar, wind and tides also shows sustainable growth from about 0.5 % in 2000 to 4.1% in 2019, whereas the contribution of hydroelectric generation (≈ 3 %) did not changed significantly.

This summary of the Portuguese and European energy mix shows clearly that biomass and biofuels represent, by far, the highest contribution to renewable energies, and is highly underestimated by the public opinion; this may be related to the fact that biomass is mostly a very low grade energy and much of the available information on renewable energy refers mainly to electricity. Thus, the potential of biomass depends on prospects to develop efficient processes for upgrading, from pre-processing as solid fuels (e.g. pellets for domestic heating), to gasification and pyrolysis methods. Gasification has the greatest potential to produce the key syngas components (CO + H_2) for subsequent production of synthetic fuels from renewable sources.

1.1. Biomass as a Renewable Energy Source

Biomass is considered carbon neutral, at least in the short time scale, since the amount of CO_2 released during the combustion of the raw material is equivalent to the amount absorbed during its growth process. According to Directive (EU) 2018/2001 that establishes a common framework for the promotion of energy from renewable sources [5], biomass is defined as "the biodegradable fraction of products, waste and residues with biological origin, from agriculture, including vegetal and animal substances, forestry and related industries, fisheries and aquaculture, as well as the biodegradable fraction of waste, including industrial and municipal waste of biological origin". The classification of biomass as an energy resource encompasses different categories, each with specific properties and applications, namely [6]:

• Forest Biomass – includes woody biomass of forest origin resulting from forestry, silviculture and wood processing industry (e.g. logs, branches, bark, chips, among others);

• Agricultural Waste – encompasses a set of agricultural and animal by-products with potential for energy recovery (e.g. straw, cereal husks, olive pits, among others);

• Solid Urban Waste – consists of the organic and biodegradable fraction of waste from urban solid waste and wastewater treatment plants (e.g. food waste, sludge, among others).

Biomass is mainly composed by polymers (cellulose, hemicellulose and lignin), along with residual amounts of extractives such as resins [7]. The contents of additional components such as moisture (3 to 63 wt.%, wet basis) and ash (0.1 to 46 wt.%, dry basis) depend largely on the type of biomass and origin [8]. These raw materials generally have a high volatility (48 to 86 wt.%, dry basis), which contrasts with the lower fixed carbon content (1 to 38 wt.%, dry basis) [8]. The calorific value of biomass is determined by its chemical composition (CHONS), with a value which in theory can vary between that of cellulose (≈ 17 $\mathrm{MJ} \cdot \mathrm{kg}_{\mathrm{F,db}}^{-1}$) and lignin (≈ 25 $\mathrm{MJ} \cdot \mathrm{kg}_{\mathrm{F,db}}^{-1}$) [9,10]. The higher the moisture content in the biomass, the lower its calorific value, due to the energy required to evaporate the water. Additionally, the biomass has a wide range of apparent density (150 – 900 $\mathrm{kg}_{\mathrm{F}} \cdot \mathrm{Nm}^{-3}$) [11,12], which means that its handling, transport and storage have variable added costs that must be considered in an economic feasibility analysis.

1.2. Thermochemical Conversion of Biomass – Gasification

Lignocellulosic biomass can be converted to added-value energy products via mechanical (e.g. densification), biochemical (e.g. hydrolysis) and thermochemical methods (e.g. combustion, pyrolysis and gasification) [13,14]. Among all these processes, gasification is considered an attractive route to promote the integration of bio-based fuels, produced from low-value or residual biomass sources by a circular economy perspective [15,16]. It can also be used in other applications, such as electricity generation in combustion engines or gas turbines, and as feedstock for the synthesis of valuable chemicals (e.g. ammonia and methanol) [17]. The process occurs at relatively high temperature (800 – 950 ºC) and involves the partial conversion of a solid carbonaceous material such as biomass into a gas fuel through interaction with steam, air or pure oxygen.

The producer gas mainly includes CO, H_2, CO_2, CH_4, C_xH_y and N_2 (dry basis), if air is used as a gasification agent [18], and thermodynamic calculations may be used to predict the expected impact of oxygen additions on gas composition. Gasification of cellulose ($C_6H_{10}O_5$) may be used as a model system and simulations of impact of oxygen:cellulose on producer gas composition provide guidelines for operating conditions (Figure 1.3). The oxygen:biomass ratio for an ideal biomass with cellulose composition should be close to $O_2 : C_6H_{10}O_5 \approx 0.5$, on assuming preferential conversion to the syngas components:

$$0.5O_2 + C_6H_{10}O_5 \rightarrow 6CO + 5H_2 \quad (1.1)$$

This ideal feed of gasification agent $O_2 : C_6H_{10}O_5 \approx 0.5$ is within thermodynamic predictions for conditions when the yields of CO and H_2 reach their maxima, at temperatures close to 900 ºC. Note that O_2-lean conditions may induce onset of hydrocarbons (mainly CH_4) and carbon residues, and oxygen-rich conditions yield increasing contents of fully oxidised species (CO_2 and H_2O). Still, thermodynamic predictions for gasification at temperatures below 800 ºC indicate a gap between the maxima of CO yield and H_2 yield, as shown in Figure 1.3. Higher oxygen:cellulose ratio may prevent carbon deposition and decreasing contents of hydrocarbons require, but yield higher fractions of fully oxidised gases CO_2 and H_2O.

In addition, the elemental composition of different biomass varies, depending on their contents of cellulose, hemicellulose and lignin. In the case of lignin, the stoichiometric oxygen feed required for preferential conversion to syngas components should increase as:

$$26.5O_2 + C_{81}H_{92}O_{28} \rightarrow 81CO + 46H_2 \quad (1.2)$$

Thus, the stoichiometric feed of gasification agent depends on the difference between the contents of carbon and oxygen, which tends to be higher for lignin-rich feedstock, whereas the H:C ratio determines the composition of syngas components. In addition, differences in C:H ratio between cellulose, hemicellulose and lignin may determine differences in key gasification parameters, namely carbon conversion efficiency, cold gas efficiency and lower heating value [19].

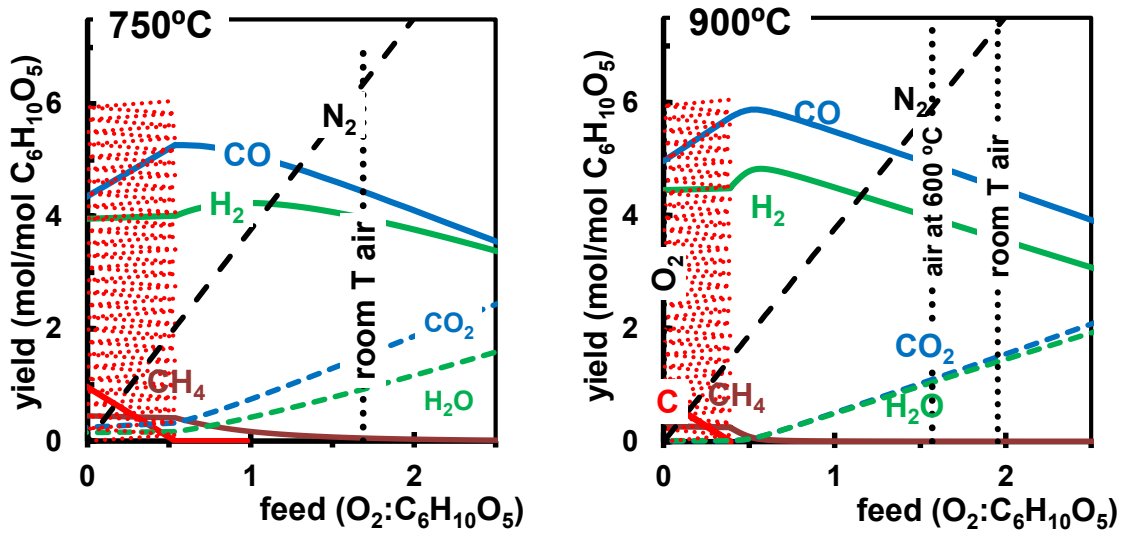

Figure 1.3 – Thermodynamic predictions of gas yields for gasification of cellulose vs oxygen:cellulose ratio at 750 ºC and 900 ºC. The shaded area shows conditions for co-existence of carbon with gaseous species and dotted vertical lines shows conditions for adiabatic operation, using room air at room temperature or pre-heated at 600 ºC.

The biomass gasification process includes endothermic reactions (Table 1.1), which require thermal energy; this may rely on gradual onset of exothermic oxidation reactions, in autothermal conditions (direct gasification), or an external heat source, in alothermal (indirect) gasification [20]. Autothermal gasification requires increasing additions of gasification agent, well above the stoichiometric ratio, to promote the internal heat source provided by partial oxidation to CO_2 and H_2O. Thus, the producer gas is downgraded by increased fractions of CO_2 and H_2O, and also by increased dilution with N_2 since air is commonly used as gasification agent. Figure 1.3 also indicates that CO yield decreases faster than H_2 yield with increasing feed of gasification agent, at least at relatively low temperatures; this agrees with experimental evidence of dependence on equivalence ratio [21]. Still, the feed of gasification agent must also exceed the stoichiometric ratio even with an external heating source, to enhance the carbon conversion efficiency and to minimize formation of tars, even when catalysts are used to overcome kinetic limitations.

The lower limit of gasification agent required for operation in adiabatic conditions is also shown in Figure 1.3 (vertical dotted lines) and can be taken as guidelines for autothermal operation. Differences between conditions for autothermal operation at 750 ºC and 900 ºC are related to the dependence of sensible heat of the producer gas on temperature; this indicates that the expected advantages of higher operating temperatures are downgraded by requirements of higher additions of gasification agent (air) and corresponding dilution of the producer gas with N_2, combined with higher conversion of CO and H_2 to fully oxidised species, reducing the LHV of the raw gas [22].

Figure 1.3 also shows prospects to counter the negative impact of autothermal operation by pre-heating the gasification agent (air); this may be achieved by heat exchangers to recover part of the sensible heat of the producer gas to pre-heat the gasification agent (air). These predictions indicate that autothermal conditions may be reached with lower feed of pre-heated air, allowing higher yields of CO and H_2, and also lowering the content of N_2 in the producer gas.

Figure 1.4 simulates gasification with pure oxygen, to avoid dilution with N_2 and to minimize the contents of fully oxidised species in the producer gas. As illustrated, N_2-free condition lowers the sensible heat of the raw producer gas and minimizes the requirements of exothermic reactions based on complete oxidation to CO_2 and H_2O. Prospects for this alternative process depend on availability of oxygen at affordable prices and also evolution of other emerging oxygen-based technologies, such as oxygen storage materials for oxy-fuel combustion. Oxygen storage materials have also been proposed for chemical looping gasification, relying on metal/oxide pairs (e.g. Ni/NiO) and/or mixed valence oxides (e.g. $Fe/FeO/Fe_3O_4/Fe_2O_3$) used as oxygen storage materials to sustain the oxygen balance [23]. Note that the notation of “chemical looping gasification” is vague since this has also been used for technologies based on CO_2 storage materials, to seek optimized yield of H_2 [24]. Steam gasification or gasification of biomass with controlled residual humidity may offer additional opportunities to promote indirect gasification without requiring supply of air as gasification agent, as described on assuming preferential conversion of cellulose (1.3) or lignin (1.4) to CO and H_2:

$$H_2O + C_6H_{10}O_5 \rightarrow 6CO + 6H_2 \quad (1.3)$$

$$53H_2O + C_{81}H_{92}O_{28} \rightarrow 81CO + 99H_2 \quad (1.4)$$

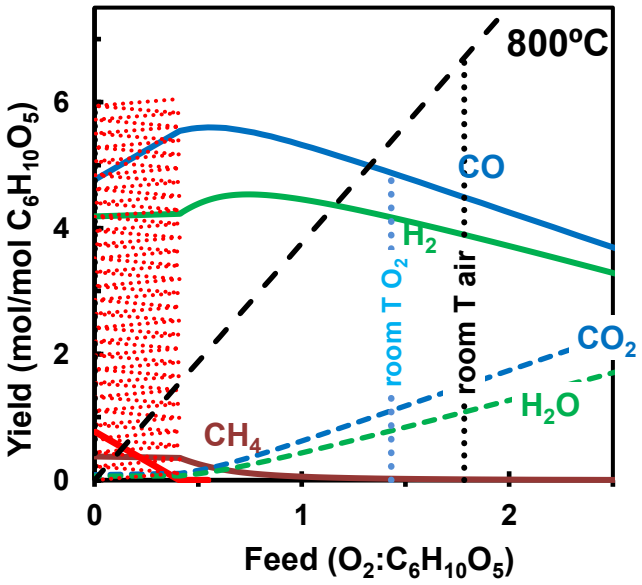

Figure 1.4 – Thermodynamic predictions of gas yields for gasification of cellulose vs oxygen:cellulose ratio, at 800 ºC, using either air or pure O_2 as gasification agent.

Thus, steam gasification may induce changes in composition of resulting producer gas, with emphasis on increased yield of H_2 and corresponding H_2:CO ratio, to meet different requirements as fuel or as a commodity for subsequent chemical processes. Indirect gasification with steam improves the quality of the gas mixture, despite having a lower biomass conversion rate, due to the lower reactivity between steam and the carbonized fraction. Otherwise, one may consider utilization of CO_2 as gasification agent [25] to increase the CO:H_2 ratio, as indicated by ideal conversion to syngas components (1.5). Gasification agents may also be combined with chemical looping gasification, relying on mixed valence oxides as oxygen storage materials [26]. However, utilization of these alternative gasification agents entails additional costs for external heating that must be taken into account in the energy and economic feasibility analysis [27].

$$CO_2 + C_6H_{10}O_5 \rightarrow 7CO + 5H_2 \qquad (1.5)$$

One may also consider autothermal steam gasification, as illustrated by thermodynamic predictions in Figure 1.5. In this case, steam gasification (or gasification of biomass with humidity) would require higher supply of air to reach conditions for autothermal operation, with corresponding increase in fully oxidised species in the producer gas, and even higher dilution with N_2, as shown on comparing results in Figure 1.4 and Figure 1.5. Excessive humidity will cause further downgrading.

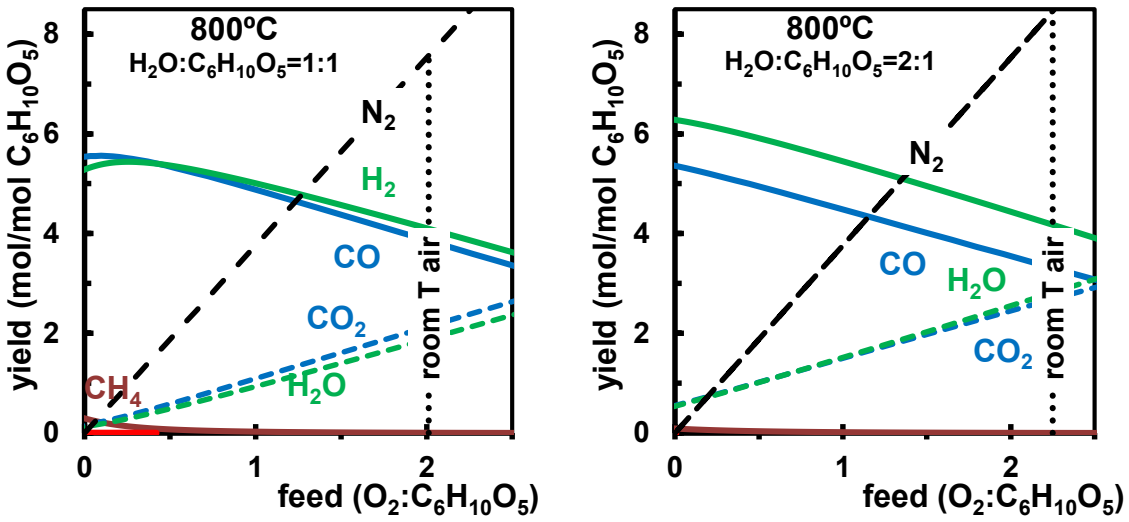

Figure 1.5 – Thermodynamic simulation of oxy-steam gasification of cellulose at 800 ºC, with ideal stoichiometric ratio $H_2O: C_6H_{10}O_5 = 1:1$ (left) or $H_2O: C_6H_{10}O_5 = 2:1$ (right).

Table 1.1 – Main chemical reactions involved in biomass gasification[18,20,28,29].

Gasification Reactions			
	Stoichiometry	Reaction Enthalpy ΔHº at 298 K (kJ·mol^{-1})	Reaction type
(1)	C (s) + CO_2 (g) ↔ 2CO (g)	+ 205	Boudouard
(2)	C (s) + H_2O (g) ↔ CO (g) + H_2 (g)	+ 130	Water Gas
(3)	C (g) + 2H_2 (g) ↔ CH_4 (g)	+ 124	Hydrogenation
(4)	CO (g) + H_2O (g) ↔ CO_2 (g) + H_2 (g)	- 41	Water-Gas-Shift
(5)	CO_2 (g) + 4H_2 (g) ↔ CH_4 (g) + 2H_2O (g)	-164	Methanation
(6)	CO (g) + 3H_2 (g) ↔ CH_4 (g) + H_2O (g)	- 173	
Oxidation Reactions			
	Stoichiometry	Reaction Enthalpy ΔHº at 298 K (kJ·mol^{-1})	Reaction type
(7)	C (s) + O_2 (g) → CO_2 (g)	- 394	Oxidation
(8)	C (s) + 0.5O_2 (g) → CO (g)	- 111	
(9)	CO (g) + 0.5O_2 (g) → CO_2 (g)	- 283	
(10)	H_2 (g) + 0.5O_2 (g) → H_2O (g)	- 242	

The real biomass compositions also contain impurities such as alkalis and sulphur, the solid inorganic fraction of the biomass feedstock, and unwanted condensable compounds (tars) formed during the thermochemical process, which depend on gasification conditions (Table 1.2). Table 1.2 also summarizes operational problems resulting from these impurities or contaminants, and main cleaning technologies. Requirements for representative applications are also listed in (Table 1.3).

Table 1.2 – Producer gas impurities, operational constraints and cleaning methods [30].

Impurities	Examples	Problems	Cleaning Technologies
Particles	Ash, Char, Soot, Dust, Bed Material	Erosion	Cyclones, Filters, Electrostatic Precipitators
Alkalis	Potassium, Sodium, Chlorine Compounds	Erosion, Corrosion	Condenser, Ceramic Filter, Adsorber
Nitrogen	NH_3, HCN	NO_x Formation	Scrubbing, Catalysts
Sulfur	H_2S, COS	Corrosion, Air Pollutants Emissions	Scrubber, Adsorber, Catalysts
Tar	Aromatic Hydrocarbons	Deposition, Plugging, Corrosion, Blocking	Physical Separation, Thermal Cracking, Catalysts

Table 1.3 – Producer gas quality requirements for different end-use applications [31,32].

Application	Tar $mg \cdot Nm^{-3}$	Particles $mg \cdot Nm^{-3}$	Alkalis $mg \cdot Nm^{-3}$	Nitrogen $mg \cdot Nm^{-3}$	Chlorine $mg \cdot Nm^{-3}$	Sulfur $mg \cdot Nm^{-3}$
Combustion Engines	< 50	< 50	< 1.0	< 50	< 10	< 100
Gas Turbines	0.1-120	< 30	< 0.25	-	-	< 20 ppm_v
Fuel Cells	< 1.0	< 0.2		< 1.0 ppm_v		
Synthetic Fuels	< 0.1	-		< 1.0 ppm_v		

The presence of undesired aromatic compounds (tar) in the producer gas is one of the main sources of operational problems. Tar is a complex mixture of organic compounds with molecular weight greater than benzene, which comprises single to multiple ring aromatic compounds along with oxygenated hydrocarbons [33]. Tar concerns are related to its condensation at temperatures < 400 ºC, causing blocking and fouling of engines, filter and pipe plugging and catalysts deactivation in downstream processing [34,35]. Based on this, gas conditioning for tar abatement is needed to ensure the required gas quality for subsequent applications.

Tar formation is the result of a series of complex thermochemical reactions, such as chemolysis, depolymerisation, oxidation, polymerisation and cycloaddition [36]. As illustrated in Figure 1.6, the composition of tars is highly dependent on the process temperature and can be divided into primary (e.g. phenol), secondary (e.g. toluene and xylene) and tertiary (e.g. pyrene, indene and naphthalene) products, roughly placed at 200 to 400 ºC, 500 to 700 ºC and 800 to 900 ºC, respectively [37]. According to Milne et al. [38] primary and tertiary tars are mutually exclusive, since primary products are destroyed before tertiary products appear. In the case of bubbling fluidized bed (BFB) gasifiers, as the operation takes place between 700 and 850 ºC [39], a mixture of secondary and tertiary tar products can be expected in the biomass-derived gas.

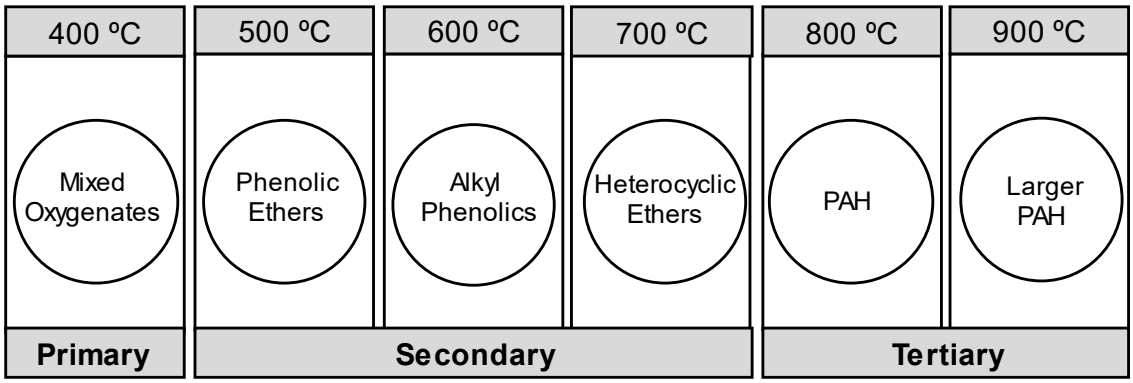

Figure 1.6 – Biomass-derived tar evolution as a function of temperature.

1.3. Catalytic Hot Gas Cleaning and Upgrading

1.3.1 Tar Conversion Mechanisms

The elimination of tar in syngas is divided into primary or secondary treatment strategies. The primary measures aim to limit the formation of tars and other unwanted compounds inside the gasifier, by optimizing the operating conditions, changes in the reactor design and the use of additives/catalysts [40]. However, the impact of these measures is limited, which makes the application of complementary methods downstream of the gasifier necessary. The application of secondary treatment techniques can be done at low or high temperature (Cold or Hot Gas Cleanup), with emphasis on physical separation processes such as water or oil washers, thermal decomposition (Thermal Cracking) and catalytic conversion. [41,42]. Physical separation strategies are based on cooling the gas below the dew point temperature of the tar, in order to guarantee its condensation. Thermal decomposition, on the other hand, aims to increase the tar conversion rate by significantly increasing the gas temperature (> 1100 ºC). Although effective in tar removal, the associated cost and energy consumption affect the overall performance of the process, making the application of these techniques economically unfeasible [43,44].

A more interesting option is based on thermocatalytic tar decomposition, wherein the catalyst converts tar to syngas components (CO and H_2), and also may promote the reforming reactions of light hydrocarbons, increasing the carbon conversion efficiency without severe heat penalties [45]. Additionally, this technique allows for high tar conversion rates in a temperature range compatible with gasification processes (700 – 900 ºC), which makes the method more efficient and attractive from an economic point of view [46,47]. The method involves a set of parallel reactions (Table 1.4) depending on operating conditions and the type of catalyst applied [48]. The H_2O content of the biomass-derived raw gas will promote steam reforming reactions (11 in Table 1.4), while CO_2 content will induce dry reforming reactions (12 in Table 1.4). Thermal cracking of tar compounds (13) is also expected at higher temperatures. Furthermore, oxidation reactions (14) and (15) can also have a significant preponderance on tar decomposition during gasifier operation if the type of catalyst employed shows O_2 storage ability. Thus, the application of catalysts aims to thermodynamically favour the main tar conversion mechanisms at lower temperatures, compatible with the biomass gasification process. Additional reactions such as carbon gasification (1-2 in Table 1.1), water-gas-shift (4) and methanation (5)-(6) can also be promoted, contributing to increase the overall gasification efficiency. These reactions are mostly endothermic, which makes them extremely temperature dependent.

Table 1.4 – Main mechanisms of tar conversion during biomass gasification [31,32].

	Stoichiometry	ΔH^o at 298 K (kJ/mol)	Reaction
(11)	$C_nH_m + n \cdot H_2O \rightarrow n \cdot CO + (0.5 \cdot m + n) \cdot H_2$		Reforming
(12)	$C_nH_m + n \cdot CO_2 \rightarrow 2n \cdot CO + 0.5 \cdot m \cdot H_2$	+ 250-350	Dry Reforming
(13)	$C_nH_m \rightarrow C_{n-x}H_{m-y} + x \cdot C + y \cdot H_2$		Cracking
(14)	$C_nH_m + (n/2) \cdot O_2 \rightarrow n \cdot CO + (m/2) \cdot H_2$	Exothermic	Partial Oxidation
(15)	$C_nH_m + (n + m/4) \cdot O_2 \rightarrow n \cdot CO_2 + (m/2) \cdot H_2O$		Oxidation

Catalytic tar cleaning has been the subject of intense research in recent decades, seeking to develop more economical and efficient methods. Depending on the location of its application, catalysts can be classified as a primary or secondary cleaning method, and must meet the following requirements [49,50]:

i) high catalytic activity in the conversion of tar and other light hydrocarbons;

ii) selectivity in the conversion of tar into H_2 and CO;

iii) resistance to deactivation caused by carbon deposition, sulfur poisoning or sintering;

iv) low production cost;

v) ability to regenerate.

The application of catalysts inside the gasifier (primary method) implies that the material must have additional characteristics, namely high friction resistance and the minimal toxic elements in its composition. On the other hand, the severe conditions inside the gasifier increase the risk of deactivation of the catalysts by carbon deposition, contamination (e.g. sulfur, chlorine and alkalis), microstructural changes due to high temperatures or fragmentation of the catalyst particles due to erosion. As such, research has mainly focused on the secondary post-gasification treatment, through the catalytic steam reforming of tar [51–53].

1.3.2. Natural Mineral Catalysts

The main types of catalysts for tar conversion include mineral or synthetic catalysts [54]. Mineral catalysts are characterized by their low cost, and are usually activated by a pre-heat treatment before their use in fluidized bed reactors as a primary cleaning method. Table 1.5 shows the main results obtained for different mineral catalysts, tested under real gasification conditions or using synthetic mixtures.

Representative examples of natural mineral used as catalysts are dolomite $Ca_{1-x}Mg_xCO_3$ or limestone $CaCO_3$, and olivine $(Mg,Fe)_2SiO_4$, which showed considerable catalytic activity [55–64]. The performance of dolomite is poorly understood and may be related to the carbonation/decarbonation capacity of alkaline earth carbonates ($CaCO_3$ and $MgCO_3$) under the thermochemical conditions of gasification, namely the temperature range and the presence of CO_2 in the generated producer gas [62,63]; this suggests that the CO_2 storage capacity of alkaline earth components contributes to tar reforming reactions (by dry reforming), as can be exemplified with thermodynamic calculations of the Gibbs free energy variation for dry reforming of naphthalene (ΔG = -18 kJ·mol^{-1} for $C_{10}H_8 + 10MgCO_3 \rightarrow 20CO + 4H_2 + 10MgO$ at 1073 K). However, dolomite-based catalyst granules have low friction resistance, leading to rapid degradation of the material particles inside the gasifier [57,63], possibly due to excessive volume changes associated with decarbonation, reaching ≈ - 61 % for $MgCO_3 \rightarrow MgO + CO_2$ and ≈ - 55 % for $CaCO_3 \rightarrow CaO + CO_2$.

Olivine shows higher friction resistance which makes it an interesting choice as a primary catalyst. The catalytic activity of olivine is associated with the presence of iron species with different valence states (Fe^0, Fe^{2+} or Fe^{3+}) on the surface of the material, after its calcination in reducing atmosphere at high temperature [55,56]. Several authors reported that zero valent iron (Fe^0) is more active than the oxidized species (Fe^{2+} or Fe^{3+}) in breaking C-C and C-H bonds in hydrocarbons [58–60], contributing to a higher tar conversion rate by cracking and/or reforming reactions. This allows one to predict that the reducing atmosphere of the synthesis gas plays a decisive role in the catalytic activity of iron-based materials. The end composition of olivine is a less common mineral fayalite (Fe_2SiO_4), which was also proposed to upgrade the gas obtained by direct gasification of biomass with air [65]. Its stability in conditions of biomass gasification is limited, as found by thermodynamic assessment (Figure 1.7). Nevertheless, this may be taken as a limiting model for olivine and shows prospects for operation under relatively wide ranges of gasifying agent.

Table 1.5 – Performance of different natural mineral catalysts in the conversion of tar.

Catalyst	Pre-Treatment	Conditions	Gasifier Agent	Cleaning Method	Tar Conversion	Catalyst Testing Conditions	Ref.
Olivine	-	Real	Vapor	Primary	31-99 %	Tar (11-49 g/Nm^3); 770-900 ºC	[66–69]
Olivine	-	Real	Ar	Primary	24-45 %	Tar (5-130 g/Nm^3); 800-870 ºC	[70–72]
Olivine	-	Real	Ar+Vapor	Primary	31-54 %	Tar (4-19 g/Nm^3); 800-850 ºC	[73,74]
Olivine	-	Synthetic	-	-	90 %	(H_2+CO+CO_2+CH_4) + $C_{10}H_8$ (2 g/Nm^3); 800 ºC	[75]
Olivine	-	Synthetic	-	-	22 %	H_2O+C_7H_8 (29 g/Nm^3); 850 ºC	[76]
Olivine	Calcination, 850 ºC; 2h	Synthetic	-	-	25 %	H_2O+ C_6H_5OH (42 g/Nm^3); 750 ºC	[77]
Olivine	Calcination, 900 ºC; 4-10h	Real	Vapor	Primary	65-79 %	Tar (33-142 g/Nm^3); 800-900 ºC	[78,79]
Olivine	Calcination, 900 ºC; 4h	Synthetic	-	-	31 %	H_2O+ C_7H_8 (20 g/Nm^3); 850 ºC	[80]
Olivine	Calcination, 900 ºC;10-20h	Synthetic	-	-	80-81 %	H_2O+ $C_{10}H_8$ (5 g/Nm^3) ;900 ºC	[56]
Olivine	Calcination, 1100 ºC; 4h	Real	Ar	Secondary	74 %	Tar (8 g/Nm^3); 850 ºC	[81]
Olivine	Calcination, 1200 ºC; 6h	Real	Ar	Primary	60 %	Tar (8 g/Nm^3); 800 ºC	[50]
Olivine	Calcination, 1600 ºC; 4h	Synthetic	-	-	4 %	H_2O+ $C_{11}H_{10}$ (3 g/Nm^3) ; 900 ºC	[82]
Dolomite	-	Real	O_2+Vapor	Primary	58 %	Tar (10 g/Nm^3); 800 ºC	[83]
Dolomite	Calcination, 850 ºC; 2h	Real	Ar+Vapor	Primary	87 %	Tar (4 g/Nm^3); 850 ºC	[73]
Dolomite	Calcination, 850 ºC; 2h	Synthetic	-	-	31 %	H_2O+ C_6H_5OH (42 g/Nm^3); 750 ºC	[77]
Dolomite	Calcination, 900 ºC; 1h	Real	Ar	Secondary	63 %	Tar (4 g/Nm^3); 900 ºC	[84]
Dolomite	Calcination, 900 ºC; 4h	Real	O_2+Vapor	Primary	89 %	Tar (6 g/Nm^3); 850 ºC	[85]
Dolomite	Calcination, 900 ºC; 4h	Real	Ar+Vapor	Secondary	89 %	Tar (9 g/Nm^3); 850 ºC	[86]
Dolomite	Calcination, 900 ºC; 3h	Real	Vapor	Secondary	84 %	Tar (5 g/Nm^3); 800 ºC	[87]
Calcite	-	Real	Vapor	Primary	86 %	Tar (5 g/Nm^3); 720 ºC	[88]
Ilmenite	-	Real	Vapor	Primary	45 %	Tar (50 g/$kg_{daf,fuel}$); 828 ºC	[69]
Ilmenite	-	Real	Vapor	Primary	60-68 %	Tar (25-39 g/$kg_{daf,fuel}$); 850 ºC	[89–91]
Ilmenite	-	Real	Vapor	Primary	35 %	Tar (28 g/Nm^3); 800 ºC	[92]
Magnesite	-	Real	Ar+Vapor	Primary	22 %	Tar (7 g/Nm^3); 835 ºC	[93]
Bauxite	-	Real	Vapor	Primary	71 %	Tar (50 g/kg_{daf}); 815 ºC	[69]
Limonite	Calcination, 900 ºC; 0.5h	Synthetic	-	-	55 %	C_7H_8 (1000 ppm);800 ºC	[94]

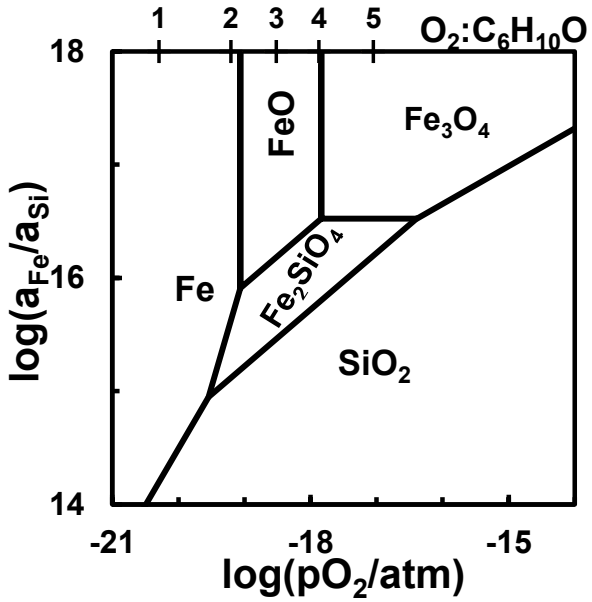

Figure 1.7 – Thermodynamic predictions vs the activity ratio a_{Fe}: a_{Si} and redox conditions, at 800 ºC [65]. The corresponding ratio of oxygen:cellulose ratio is shown in secondary axis, as a guidelines for conditions of biomass gasification.

Hematite-rich ores have also been tested as gasification catalysts [26], with emphasis on applicability in chemical looping gasification of biomass, based on the variable valence of iron oxides on redox cycling between trivalent and divalent states, and their oxygen storage ability. Similar applicability was reported for manganese ore [26]. These transition metal oxides show a versatile range of mixed valence, which depends on redox conditions and may enable N_2-free gasification by promoting steam gasification and/or chemical looping [95]. Iron species readily oxidise to Fe_2O_3 in air and reduce to FeO or even to metallic Fe under conditions of gasification, depending on the CO:CO_2 ratio.

Other natural minerals such as goethite $FeO_x(OH)_y$ or limonite and siderite $FeCO_3$ [96] undergo ready thermochemical decomposition to hematite in oxidising conditions, or magnetite in reducing conditions. The oxide products of these thermal decomposition show higher surface area, which may explain the enhanced performance in gas yields and conversion of tars [96]. Gas yield and efficiency (gasification and carbon conversion) may also be promoted by adjusting the ratio between hematite and carbon contents in the biomass feed [97]. This ratio may promote cracking and reforming reactions of light aromatics (benzene, toluene) depending on temperature [98].

Hematite-rich ores also contain significant fractions of gangue components such as silica and alumina, alkaline earths (Mg, Ca) and other transition elements (Ti, Cr, V…). These may be combined as binary oxide compounds (e.g. $FeTiO_3$) and small fractions may be dissolved in solid solutions of iron oxides [99]. Ilmenite $FeTiO_3$ was found to improve tar conversion by steam reforming, mainly at temperatures T ≥ 800 ºC, and showed better performance than iron oxides (Fe_2O_3 or Fe_3O_4) [89], possibly because ilmenite improves the redox stability of Fe species with enhanced activity (Fe^0, Fe^{II}). The spent catalysts shows co-existence of $FeTiO_3$ (as major phase) with TiO_2 and metallic Fe (minor phase).

1.3.3. Synthetic Catalysts

1.3.3.1. Ni-based Catalysts

Synthetic catalysts have been mainly focused on the development of metal-metal oxide catalysts, supported on ceramic substrates. The most representative examples are Ni-based catalysts, with a wide variety of supports and processed by different methods [100]. NiO oxide readily reduces to metallic Ni under the thermochemical conditions of gasification, even with CO-lean conditions (e.g. for $CO:CO_2 = 0.01$), as shown in Figure 1.8, assisting air gasification [21], as well as steam gasification or oxy-steam gasification [101,102]. Ni catalysts also promote cracking reactions and possibly also tar reforming by analogy with the demonstrated performance of Ni commercial catalysts which were developed for reforming of heavy hydrocarbons [103]. However, Ni-based catalysts tend to be readily de-activated by carbon in primary treatment, even when the gasification agent is steam [101], indicating that the activity of Ni-based catalysts is a compromise between promotion of reforming and cracking reactions, and ready nucleation of carbon. Sulphur contamination and corresponding onset of the low melting phase NiS, with melting temperature $T_m \approx 797$ ºC, and a Ni-S eutectic with eutectic temperature < 650 ºC [104] also spoil the catalytic activity and induce microstructural degradation. Thus, the applicability of Ni-based catalysts may be critically dependent on carbon and sulphur tolerance, microstructural stability without grain growth, and ability to retain stable activity [105].

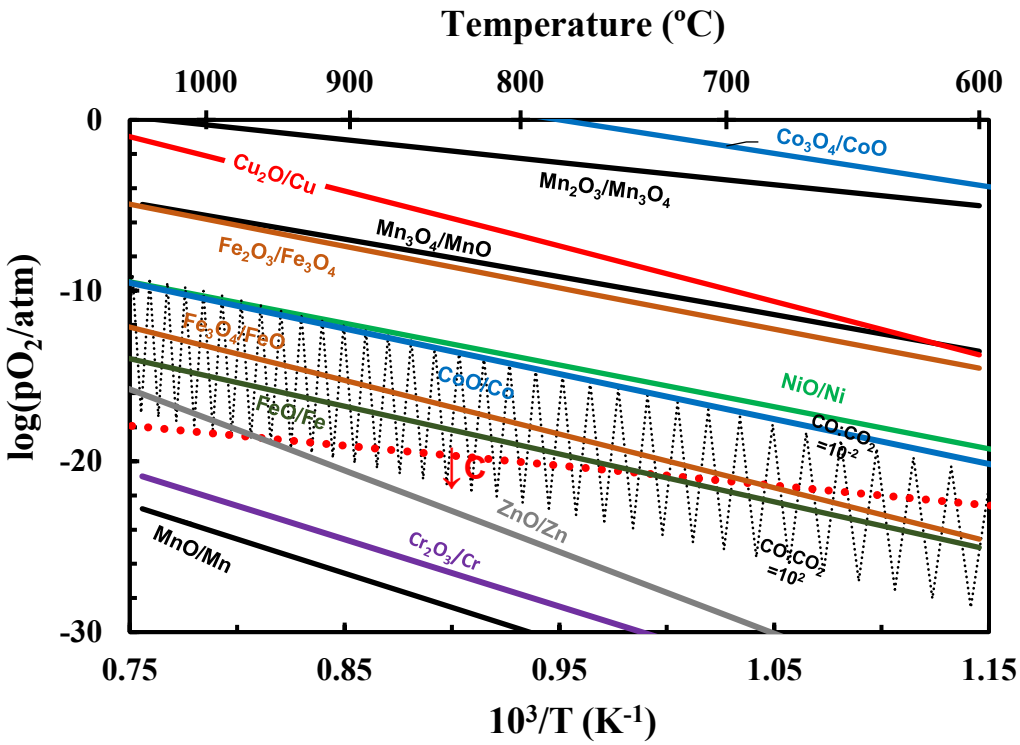

Figure 1.8 – Thermodynamic predictions of thermochemical stability ranges of common transition metals and their oxides. The shaded area shows the expected conditions of gasification, from CO-lean ($\mathrm{CO}:\mathrm{CO_2} = 10^{-2}$) to CO-rich ($\mathrm{CO}:\mathrm{CO_2} = 10^{2}$) conditions, and a dotted line shows conditions for onset of carbon deposition ($2\mathrm{CO} \rightarrow \mathrm{C} + \mathrm{CO_2}$).

Increasing gasification temperature tends to improve carbon tolerance of Ni-based catalysts but worsens sulphur poisoning and microstructural ageing. These limitations of Ni-based catalysts stimulated research on alternative cracking catalysts which combine Ni as the main active component with a suitable support (e.g. Al_2O_3) and/or an additional component acting as promoter (e.g. MgO), or corresponding multicomponent compounds such as (Ni,Mg)O, $NiAl_2O_4$, or $NiMgAl_2O_5$ [106]. These compounds were assessed as catalysts for steam reforming of tars and water gas shift at relatively low temperatures (≤ 700 ºC). In this temperature range these compounds may extend the redox tolerance relative to Ni/NiO equilibrium, as found for $NiAl_2O_4$ [107], and shown in Figure 1.9. The thermochemical conditions of biomass gasification at higher temperatures are likely to induce gradual segregation of metallic Ni from $NiAl_2O_4$, with corresponding formation of a Ni-lean secondary phase ($NiAl_{32}O_{49}$).

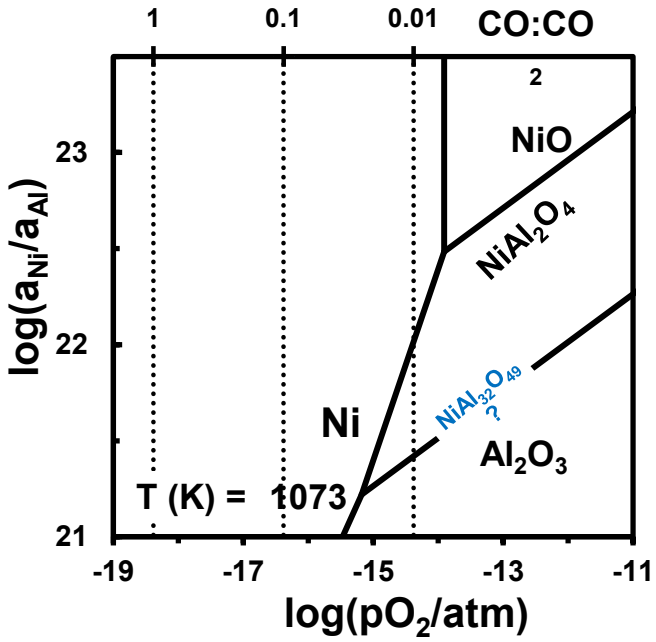

Figure 1.9 – Stability of the Ni-Al-O system vs the activity ratio and oxygen partial pressure, at 800 ºC [107]. The corresponding CO:CO_2 range is shown as secondary axis.

Highly basic alkaline oxides (K_2O, Na_2O…) and alkaline earth oxides (BaO, SrO, CaO, MgO) interact with acidic gases (CO_2, HCl…), as indicated by free energy of carbonation reactions (Table 1.6), and are likely to promote the catalytic activity of water gas shift and reforming reactions, and oppose methanation [108]. There is also convincing evidence that the fractions of alkaline and alkaline earth oxides in the solid fraction (ashes) of gasification may assist this catalytic activity, even without the catalytic contribution of Ni [109]. However, the volatility and low melting temperatures of alkaline oxides (e.g. ≈ 740 ºC for K_2O), or low eutectic temperatures in relevant systems (e.g. $K_2O - SiO_2$ and $Na_2O - SiO_2$ [110]) raise major difficulties, unless one considers alternative concepts based on alkaline-containing compounds, as reported for sodium titanates [111], which were proposed to upgrade the H_2:CO ratio and to remove tars.

Table 1.6 – Gibbs free energy of formation of carbonates of alkali or earth alkali oxides, and divalent transition metal oxides by reaction with carbon dioxide, at 298 K.

Carbonate	ΔG^o (kJ·mol^{-1})
Li_2CO_3	-634
Na_2CO_3	-734
K_2CO_3	-808
$MgCO_3$	-506
$CaCO_3$	-589
$SrCO_3$	-641
$BaCO_3$	-677
$MnCO_3$	-517
$FeCO_3$	-478
$CoCO_3$	-486
$ZnCO_3$	-474

1.3.3.2. Fe-based Catalysts

The cost, risks of de-activation and potential toxicity of Ni-based catalysts stimulated research on synthetic catalysts based on the most abundant transition metal (Fe), deposited on different substrates and seeking mainly secondary tar conversion; this included infiltration of char with $FeCl_3 \cdot 6H_2O$ [112], or processing Ni-Fe alloys or intermetallic compounds Ni_3Fe or Fe_3Ni_2 supported on char by hydrothermal carbonization [113]. Catalysts in the system $Fe_2O_3 - Al_2O_3$ were also prepared by co-precipitation, and tested in 2-stage biomass gasification [114]. The catalyst played a key role on yield of H_2 which increased by a factor of about 5 in steam gasification and 3 without steam. The catalyst also promoted increasing yield of CO without steam, whereas increased CO_2:CO ratio was reported by steam gasification. Direct evidence of conversion of naphthalene was also demonstrate with $Fe - FeAl_2O_4$ composites [115], and conversion of toluene was demonstrated by Fe-biochar catalysts [116].

Fe-based spinels $(Fe, Ce, M)_3O_4$, with different additives (M = Co, Cr, Mo, Zr, Hf) [117,118] and $(Fe, Nb, M)_3O_4$ with M = Cu, Ni, Co, Mn [119] were also proposed as catalysts for water gas shift reaction at intermediate temperatures (< 600 ºC). The catalytic activity of these spinels may be related to changes in the relative fractions of Fe^{3+} and Fe^{2+}, induced mainly by charge compensation of higher valence species (Ce^{4+} and Nb^{5+}) combined with changes in octahedral and tetrahedral sites of the spinel structure, and possibly even onset of metallic species of readily reduced metals.

Iron oxides have also been proposed for chemical looping gasification, by analogy with natural iron ores [23,26]; this relies on phase changes in the Fe-O system (Fe, $Fe_{1-x}O$, $Fe_3O_{4+\delta}$, Fe_2O_3) upon redox cycling (Figure 1.8), and the variable oxygen stoichiometry of some of these phases [120,121]. However, most of these phase transformations cause excessive volume changes, as listed in Table 1.7, and corresponding risks of ready collapse of catalyst particles, mainly if the redox cycle involves complete reduction to metallic Fe (i.e. $\approx -53\ \%$ for $Fe_2O_3 \rightarrow 2Fe + 1.5O_2$).

Table 1.7 – Volume changes in relevant transformations of the Co-O, Cu-O, Fe-O, Mn-O and Ni-O systems upon redox cycling.

Transformation	Volume Change
$Co_3O_4 \rightarrow 3{\cdot}CoO + 0.5{\cdot}O_2$	-11 %
$Co_3O_4 \rightarrow 3{\cdot}Co + 2{\cdot}O_2$	-50 %
$CoO \rightarrow Co + 0.5{\cdot}O_2$	-43 %
$2{\cdot}CuO \rightarrow Cu_2O + 0.5{\cdot}O_2$	-5.0 %
$Cu_2O \rightarrow 2Cu + 0.5{\cdot}O_2$	-41 %
$CuO \rightarrow Cu + 0.5{\cdot}O_2$	-44 %
$3{\cdot}Fe_2O_3 \rightarrow 2{\cdot}Fe_3O_4 + 0.5{\cdot}O_2$	-2.0 %
$Fe_2O_3 \rightarrow 2{\cdot}FeO + 0.5{\cdot}O_2$	-18 %
$Fe_2O_3 \rightarrow 2{\cdot}Fe + 1.5{\cdot}O_2$	-53 %
$Fe_3O_4 \rightarrow 3{\cdot}FeO + 0.5{\cdot}O_2$	-16 %
$Fe_3O_4 \rightarrow 3{\cdot}Fe + 2{\cdot}O_2$	-52 %
$FeO \rightarrow Fe + 0.5{\cdot}O_2$	-43 %
$3{\cdot}Mn_2O_3 \rightarrow 2{\cdot}Mn_3O_4 + 0.5{\cdot}O_2$	-11 %
$Mn_2O_3 \rightarrow 2{\cdot}MnO + 0.5{\cdot}O_2$	-23 %
$Mn_2O_3 \rightarrow 2{\cdot}Mn + 1.5{\cdot}O_2$	-57 %
$Mn_3O_4 \rightarrow 3{\cdot}MnO + 0.5{\cdot}O_2$	-14 %
$Mn_3O_4 \rightarrow 3{\cdot}Mn + 2{\cdot}O_2$	-52 %
$MnO \rightarrow Mn + 0.5{\cdot}O_2$	-44 %
$NiO \rightarrow Ni + 0.5{\cdot}O_2$	-41 %

Other Fe-based catalysts rely on mixed compounds with other transition metal oxides, such as synthetic iron titanates (e.g. Fe_2TiO_5, [122]). In this case, Fe_2TiO_5 reduces to $FeTiO_3$ and Fe_3O_4, or even onset of metallic Fe, under the thermochemical conditions of biomass gasification. Titanomagnetite catalysts also evolve to $FeTiO_3$+Fe_3O_4+Fe composites under gasification and were proposed to suppress the H_2S contents of producer gas obtained by biomass gasification [123].

The brownmillerite $Ca_2Fe_2O_5$ or $CaO/Ca_2Fe_2O_5$ composites were also tested, seeking catalysts with double functionalities [124]. These catalysts were prepared by impregnation of CaO with iron nitrate solution, with subsequent calcination. The proposed catalytic mechanism comprises the role of the alkaline earth component to catalyse gasification of char and the contribution of $Ca_2Fe_2O_5$ to decompose polyaromatic tars. Optimum overall performance relied on partial coverage of the CaO nucleus by a discontinuous $Ca_2Fe_2O_5$ shell. Other $CaO/Ca_2Fe_2O_5/Fe_2O_3$ composites with higher iron contents were proposed to optimize the yield of H_2 by chemical looping steam gasification [125].

1.3.3.3. Catalysts Based on Other Transition Metals

A variety of other elements also induce changes in activity of Ni-based catalysts towards relevant gasification reactions (Table 1.1), with emphasis on readily reduced metals, such as Co and Cu (Figure 1.8). The performance of Co-based catalysts in steam reforming of naphthalene was better than for Ni-based catalysts, with higher carbon conversion [126]. Other approaches relied on alloying, namely Ni-Cu [127] or Ni-Co [128]. Double metal Ni-Co catalysts may promote higher conversion of tars by steam reforming, and higher contents of H_2, CO and CH_4 [129]. Still, cobalt and nickel raise similar concerns about cost and environmental impact or toxicity [130].

Synthetic Co-based catalysts have also been proposed, seeking either primary tar conversion in steam gasification [131] or secondary steam reforming of tars [132], and Co-MgO catalysts were found to perform better than the corresponding Ni-MgO catalysts [126]. These catalysts were processed by infiltration of magnesia supports, with cobalt nitrate solution. Co-precipitation and subsequent calcination was used to process alternative composite catalysts in the ternary system $CoO_x - MgO - Al_2O_3$, with incorporation of cobalt in $Mg_{1-x}Co_xO$ solid solution or $(Mg,Co)Al_2O_4$ spinels, and onset of metallic Co after a reduction pre-treatment [128]. Ternary compositions showed higher catalytic activity and better tolerance to carbon deposition than binary compositions.

Oxides of other transition metals have also been proposed for chemical looping gasification [133], relying on reduction of metallic oxides to metal (Cu or Co) in gasification conditions, and ready re-oxidation in air (Figure 1.8). Still, manganese oxides offer the best prospects for commercial utilization based on the diversity of redox changes, lower cost, and non-toxicity. Applicability of readily reduced metals is also problematic, due to risks of massive shrinkage upon complete reduction (Table 1.7). Potential applicability of manganese oxides in chemical looping gasification may rely on phase transformations from oxidising to reducing atmospheres (Figure 1.8), combined with deviations from nominal

stoichiometry (e.g. $Mn_{1-\delta}O$ [134]) with important deviations from the nominal oxygen stoichiometry. Note that he redox conditions of gasification are unable to induce reduction to metallic Mn (Figure 1.8), and this redox tolerance of manganese oxides may be extended to the mixed oxide system Mn-Fe-O, which has also been proposed for chemical looping [135]. Though mixed oxide catalysts with oxygen storage ability may be extended to other combinations of different transition metal oxides [136], best prospects are expected mainly for combinations with redox stable oxides such as MnO_x-MgO [137]. Mn-based catalysts have also been proposed for tar conversion [138], and to clean high contents of H_2S in biomass derived gas [139].

Attempts to upgrade Ni-based catalysts may also include additions of other transition oxides such as CrO_x, TiO_x or VO_x [108]. These oxides cannot be reduced to metallic state even in CO-rich conditions. Still manganese oxides (Figure 1.8) whereas Cr_2O_3 cannot be reduced even in CO-rich conditions. On the contrary, vanadium oxides show a rich diversity of Magneli phases V_nO_{2n-1} on changing from reducing gas mixtures to oxidising atmospheres, starting with the V_2O_3/V_3O_5 equilibrium close to CO-lean conditions and also close to the NiO/Ni equilibrium (Figure 1.10). Still, it is far from clear if this proximity contributes to the enhanced catalytic activity of Ni-based catalysts in relevant reactions such as promoting methanation of CO_2 and reverting the water gas shift reaction, enhancing the yield of CO [108]. Vanadium-based catalysts were also prepared from multicomponent hydrotalcite precursors and proposed for steam reforming of toluene [108]. Their contents of V can be adjusted to optimize the yield of H_2. In addition, vanadium oxides are likely to promote sulphur tolerance, by promoting oxidation of H_2S [140]. However, the applicability of vanadium-based catalysts may be limited to relatively low temperatures, due to the low melting temperature of V_2O_5 ($T_m \approx 670$ ºC) [141], and also low eutectic temperatures in relevant binary systems such as $V_2O_5 - Al_2O_3$ ($T_{eut} \approx 640$ ºC) [142], $V_2O_5 - SiO_2$ ($T_{eut} \leq 675$ ºC) [143], $V_2O_5 - CaO$ ($T_{eut} \leq 618$ ºC), etc.

Onset of titanium oxide Magneli phases Ti_nO_{2n-1} only occurs for highly reducing conditions, i.e., outside the redox conditions of gasification (Figure 1.10). Thus, the catalytic role of these reduced phases is debatable, except possibly by enhancing the microstructural stability of the active components with intermediate compounds, (e.g. $Ni/NiTiO_3/TiO_2$ catalysts [108], or $Fe/Fe_3O_4/FeTiO_2$ [122]).

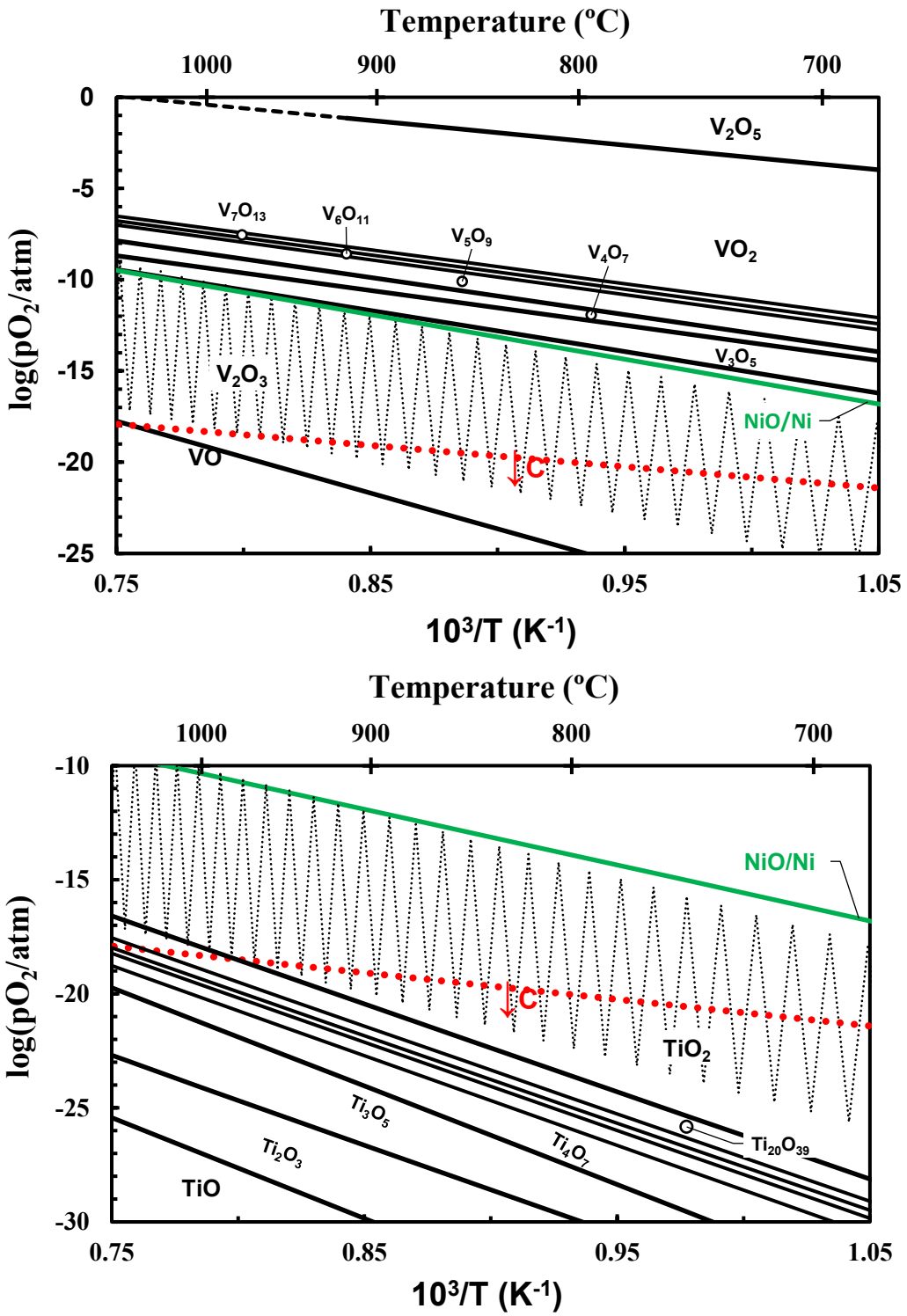

Figure 1.10 – Thermodynamic predictions of the thermochemical stability ranges of vanadium and titanium oxides. The shaded area shows the expected conditions of gasification, from CO-lean conditions ($CO:CO_2 = 10^{-2}$) to CO-rich ($CO:CO_2 = 10^{2}$) gas mixtures, and the dotted line shows conditions for onset of carbon deposition ($2CO \rightarrow C + CO_2$).

1.3.3.4. Catalysts Based on Rare Earth Oxides

Ceria-based catalysts have also been proposed for tar reforming, without significant risks of de-activation by carbon deposition and tolerance to sulphur [144]. These catalysts allow significant oxygen deficiency $CeO_{2-\delta}$, with prospects for chemical looping, combined with partial reduction of tetravalent Ce^{4+} to trivalent Ce^{3+}, eventually evolving to Magneli phases under CO-rich conditions (Figure 1.11). The fluorite structure of ceria also allows high flexibility to form highly stable and durable solid solutions $(Ce,Zr)O_{2-\delta}$, which find widespread applicability as catalysts for soot combustion or NO_x abatement based on solid solutions with zirconia [145] and $(Ce,Zr,Mn)O_{2-\delta}$ catalysts were proposed for naphthalene steam reforming [146]. Other tar conversion catalysts may combine ceria with other redox stable rare earth oxides with trivalent state (Gd_2O_3, La_2O_3…) and transition metal oxides (e.g. MnO_x or FeO_x) [147]. One may also consider other rare earths with co-existence of trivalent and tetravalent states (e.g. PrO_x [148]) contributing to a versatile combination of different valence states for the rare earths and transition metal oxides, with impact on catalytic activity and chemical looping ability. Still, the effective applicability in biomass conversion may be prevented by high cost and scarcity of rare earths, taking into account their widespread use in catalytic processes and other energy technologies.

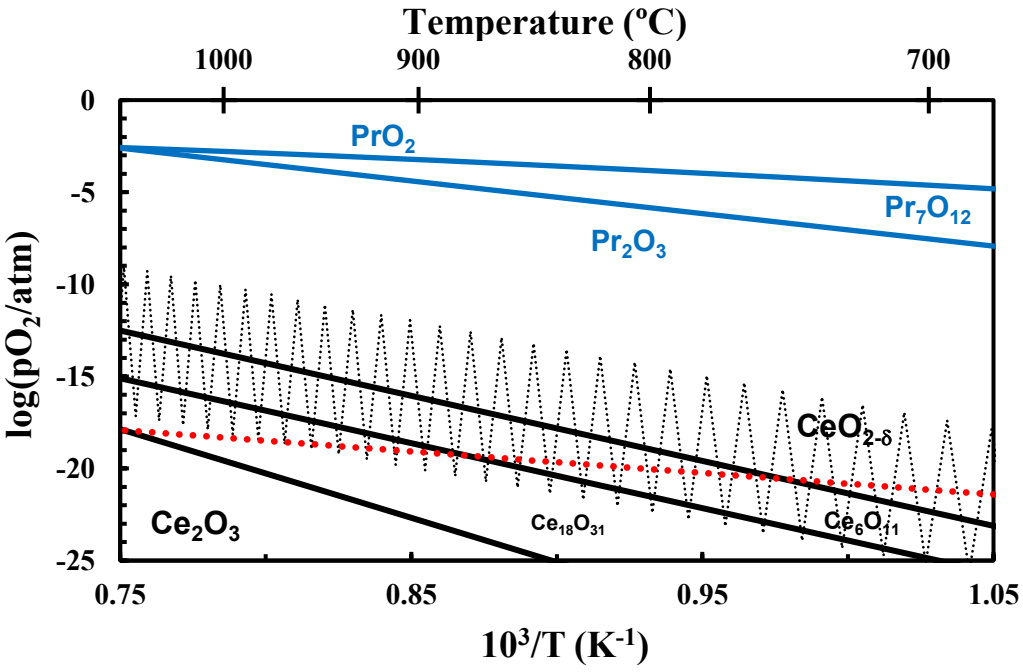

Figure 1.11 – Thermodynamic predictions of the thermochemical stability ranges of CeO_x and PrO_x oxides. The shaded area shows the expected conditions of gasification, from CO-lean conditions ($CO:CO_2 = 10^{-2}$) to CO-rich ($CO:CO_2 = 10^{2}$) gas mixtures, and the dotted line shows conditions for onset of carbon deposition ($2CO \rightarrow C + CO_2$).

1.3.3.5. Waste-Based Catalysts

Metallurgic wastes from steel industry are, probably, the most representative case of industrial wastes proposed as catalysts for biomass gasification. These wastes are Fe-rich, combined with high fractions of silica and significant fractions of alkaline earth oxides, mainly when blast furnace slags or dust are used [149]. Their performance as primary tar reforming can be upgraded by incorporation of Ni, with higher yields mainly of H_2, significant decrease of tars and higher carbon conversion, indicated by higher yields of both CO, CO_2 and CH_4 [150]. Steam gasification enhances the yields of CO and H_2, mainly for Ni-free catalysts. Fe/Cr-rich wastes were proposed as catalysts for WGS reactions with tolerance to high concentrations of tars and H_2S [151]. Electroplating sludges also contains significant fractions of several transition elements (Ni, Co, Fe…) with potential catalytic [152].

Red mud from the aluminium industries was also assessed as catalysts for tar elimination, and improved performance was observed mainly after functionalization in reducing atmospheres [153]. Red mud catalysts also promote pyrolysis at lower temperatures, with higher yields of the liquids and lowers the viscosity of these bio-oils [154]. Red mud-based catalysts may undergo significant oxygen storage ability and the contents of silica and alumina enhance their tolerance to thermal and redox cycles, without undue microstructural degradation [155]; this also raises prospects for chemical looping gasification. Though these waste derived catalysts were prone to degradation by onset of carbon deposition, previous acid treatment minimized this drawback. Steam additions affected the catalytic performance by promoting oxidation of the fraction of metallic Fe.

Cement or concrete wastes have also been tested as gasification catalysts or promoters [156–158] taking into account their high contents of alkaline earth components (calcia), combined with silica, alumina and often also a significant fraction of iron oxide; this raises prospects for higher H_2 yield by promoting the water gas shift reaction. In fact, cement showed better performance than inert beds (e.g. silica). However, the catalytic performance of concrete was lower than observed for dolomite or limestone [156]. In addition, some authors tested the use of calcite or aragonite-based shells from food wastes as gasification promoters [159], taking into account their natural microstructural or nanostructural features.

Chromium-treated leather residues are relevant Cr-rich wastes, and their catalytic activity was demonstrated by steam gasification of corresponding biochar with high gas yield, high H_2:CO and high catalytic index [160]. Though one does not expect toxicity issues related to Cr^{VI} is prospective thermochemical conditions of gasification, this still requires convincing evidence.

References

[1] International Energy Agency. Key World Energy Statistics 2021 - Statistics Report. 2021.
[2] European Commission. A Clean Planet for all. A European long-term strategic vision for a prosperous, modern, competitive and climate neutral economy 2018:1–25.
[3] European Commission D-G for E. EU Energy in Figures: Statistical Pocketbook 2021. 2021.
[4] Direção Geral de Energia e Geologia (DGEG). Balanços Energéticos Sintéticos. 2020.
[5] European Union. Directive (EU) 2018/2001 of the European Parliament and of the Council on the promotion of the use of energy from renewable sources. Off J Eur Union 2018;2018:1–128.
[6] Demirbas A. Potential applications of renewable energy sources, biomass combustion problems in boiler power systems and combustion related environmental issues. Prog Energy Combust Sci 2005;31:171–92.
[7] McKendry P. Energy production from biomass (part 1): Overview of biomass. Bioresour Technol 2002;83:37–46.
[8] Vassilev S V., Baxter D, Andersen LK, Vassileva CG. An overview of the chemical composition of biomass. Fuel 2010;89:913–33.
[9] Blokhin A V., Voitkevich O V., Kabo GJ, Paulechka YU, Shishonok M V., Kabo AG, et al. Thermodynamic properties of plant biomass components. Heat capacity, combustion energy, and gasification equilibria of cellulose. J Chem Eng Data 2011;56:3523–31. https://doi.org/10.1021/je200270t.
[10] Voitkevich O V., Kabo GJ, Blokhin A V., Paulechka YU, Shishonok M V. Thermodynamic properties of plant biomass components. Heat capacity, combustion energy, and gasification equilibria of lignin. J Chem Eng Data 2012;57:1903–9. https://doi.org/10.1021/je2012814.
[11] Charvet F, Silva F, Ruivo L, Tarelho L, Matos A, da Silva JF, et al. Pyrolysis characteristics of undervalued wood varieties in the portuguese charcoal sector. Energies 2021;14:1–16. https://doi.org/10.3390/en14092537.
[12] Dhar SA, Sakib TU, Hilary LN. Effects of pyrolysis temperature on production and physicochemical characterization of biochar derived from coconut fiber biomass through slow pyrolysis process. Biomass Convers Biorefinery 2020. https://doi.org/10.1007/s13399-020-01116-y.
[13] Sikarwar VS, Zhao M, Fennell PS, Shah N, Anthony EJ. Progress in biofuel production from gasification. Prog Energy Combust Sci 2017. https://doi.org/10.1016/j.pecs.2017.04.001.
[14] McKendry P. Energy production from biomass (part 2): conversion technologies. Bioresour Technol 2002;83:47–54. https://doi.org/10.1016/S0960-8524(01)00119-5.
[15] Huber GW, Iborra S, Corma A. Synthesis of transportation fuels from biomass: Chemistry, catalysts, and engineering. Chem Rev 2006;106:4044–98. https://doi.org/10.1021/cr068360d.
[16] Fremaux S, Beheshti SM, Ghassemi H, Shahsavan-Markadeh R. An experimental study on hydrogen-rich gas production via steam gasification of biomass in a research-scale fluidized bed. Energy Convers Manag 2015;91:427–32. https://doi.org/10.1016/j.enconman.2014.12.048.
[17] Peng WX, Wang LS, Mirzaee M, Ahmadi H, Esfahani MJ, Fremaux S. Hydrogen and syngas production by catalytic biomass gasification. Energy Convers Manag 2017;135:270–3. https://doi.org/10.1016/j.enconman.2016.12.056.
[18] Sikarwar VS, Zhao M, Clough P, Yao J, Zhong X, Memon MZ, et al. An overview of advances in biomass gasification. Energy Environ Sci 2016;9:2939–77. https://doi.org/10.1039/c6ee00935b.
[19] Yu H, Wu Z, Chen G. Catalytic gasification characteristics of cellulose, hemicellulose and lignin. Renew Energy 2018;121:559–67. https://doi.org/10.1016/j.renene.2018.01.047.
[20] Jenkins RG. Thermal Gasification of Biomass – A Primer. Bioenergy, 2015. https://doi.org/10.1016/b978-0-12-407909-0.00016-x.
[21] Caballero MA, Corella J, Aznar MP, Gil J. Biomass gasification with air in fluidized bed. Hot gas cleanup with selected commercial and full-size nickel-based catalysts. Ind Eng Chem Res 2000;39:1143–54. https://doi.org/10.1021/ie990738t.
[22] Ruan R, Zhang Y, Chen P, Liu S, Fan L, Zhou N, et al. Biofuels: Introduction. Biomass, Biofuels, Biochem. Biofuels Altern. Feed. Convers. Process. Prod. Liq. Gaseous Biofuels,

2019. https://doi.org/10.1016/B978-0-12-816856-1.00001-4.
[23] Huang Z, He F, Feng Y, Zhao K, Zheng A, Chang S, et al. Synthesis gas production through biomass direct chemical looping conversion with natural hematite as an oxygen carrier. Bioresour Technol 2013;140:138–45. https://doi.org/10.1016/j.biortech.2013.04.055.
[24] Acharya B, Dutta A, Basu P. Chemical-looping gasification of biomass for hydrogen-enriched gas. Energy and Fuels 2009;23:5077–83. https://doi.org/10.1021/ef9003889.
[25] Reyes L, Abdelouahed L, Campusano B, Buvat JC, Taouk B. Exergetic study of beech wood gasification in fluidized bed reactor using CO2 or steam as gasification agents. Fuel Process Technol 2021;213:106664. https://doi.org/10.1016/j.fuproc.2020.106664.
[26] Adánez J, Condori O, de Diego LF, Garcia-Labiano F, Izquierdo MT, Abad A. Syngas production in a 1.5 kWth biomass chemical looping gasification unit using Fe and Mn ores as the oxygen carrier. Energy and Fuels 2021;35:17182–96. https://doi.org/10.1021/acs.energyfuels.1c01878.
[27] Pfeifer C, Koppatz S, Hofbauer H. Steam gasification of various feedstocks at a dual fluidised bed gasifier: Impacts of operation conditions and bed materials. Biomass Convers Biorefinery 2011. https://doi.org/10.1007/s13399-011-0007-1.
[28] Shen Y, Yoshikawa K. Recent progresses in catalytic tar elimination during biomass gasification or pyrolysis - A review. Renew Sustain Energy Rev 2013;21:371–92. https://doi.org/10.1016/j.rser.2012.12.062.
[29] Heidenreich S, Foscolo PU. New concepts in biomass gasification. Prog Energy Combust Sci 2015;46:72–95. https://doi.org/10.1016/j.pecs.2014.06.002.
[30] Bridgwater A V. The technical and economic feasibility of biomass gasification for power generation. Fuel 1995;74:631–53. https://doi.org/10.1016/0016-2361(95)00001-L.
[31] Van Loo S, Koppejan J. The Handbook of Biomass Combustion & Co-firing. Routledge; 2010.
[32] Basu P. Pyrolysis and Torrefaction. Biomass Gasif. Des. Handb., 2010. https://doi.org/10.1016/b978-0-12-374988-8.00003-9.
[33] Maniatis K, Beenackers AACM. Tar Protocols. IEA Bioenergy Gasification Task: Introduction. Biomass and Bioenergy 2000;18:1–4. https://doi.org/10.1016/S0961-9534(99)00072-0.
[34] Artetxe M, Alvarez J, Nahil MA, Olazar M, Williams PT. Steam reforming of different biomass tar model compounds over Ni/Al2O3 catalysts. Energy Convers Manag 2017;136:119–26. https://doi.org/10.1016/j.enconman.2016.12.092.
[35] Dayton D. A review of the literature on catalytic biomass tar destruction. 2002. https://doi.org/10.2172/15002876.
[36] Yu H, Zhang Z, Li Z, Chen D. Characteristics of tar formation during cellulose, hemicellulose and lignin gasification. Fuel 2014. https://doi.org/10.1016/j.fuel.2013.10.080.
[37] Elliott DC. Relation of reaction time and temperature to chemical composition of pyrolysis oils. ACS Symp Ser 1988:55–65. https://doi.org/10.1021/bk-1988-0376.ch006.
[38] Milne T a, Evans RJ. Biomass Gasifier " Tars ": Their Nature , Formation , and Conversion. Constraints 1998. https://doi.org/10.2172/3726.
[39] Pio DT, Tarelho LAC, Matos MAA. Characteristics of the gas produced during biomass direct gasification in an autothermal pilot-scale bubbling fluidized bed reactor. Energy 2017;120:915–28. https://doi.org/10.1016/j.energy.2016.11.145.
[40] Devi L, Ptasinski KJ, Janssen FJJG. A review of the primary measures for tar elimination in biomass gasification processes. Biomass and Bioenergy 2003;24:125–40. https://doi.org/10.1016/S0961-9534(02)00102-2.
[41] Torres W, Pansare SS, Goodwin JG. Hot gas removal of tars, ammonia, and hydrogen sulfide from biomass gasification gas. Catal Rev - Sci Eng 2007. https://doi.org/10.1080/01614940701375134.
[42] Li D, Tamura M, Nakagawa Y, Tomishige K. Metal catalysts for steam reforming of tar derived from the gasification of lignocellulosic biomass. Bioresour Technol 2015;178:53–64. https://doi.org/10.1016/j.biortech.2014.10.010.
[43] Saroğlan A. Tar removal on dolomite and steam reforming catalyst: Benzene, toluene and xylene reforming. Int J Hydrogen Energy 2012. https://doi.org/10.1016/j.ijhydene.2012.02.045.
[44] Wang L, Hisada Y, Koike M, Li D, Watanabe H, Nakagawa Y, et al. Catalyst property of Co-Fe alloy particles in the steam reforming of biomass tar and toluene. Appl Catal B Environ 2012. https://doi.org/10.1016/j.apcatb.2012.03.025.
[45] Abdoulmoumine N, Adhikari S, Kulkarni A, Chattanathan S. A review on biomass gasification

syngas cleanup. Appl Energy 2015;155:294–307. https://doi.org/10.1016/j.apenergy.2015.05.095.
[46] Guan G, Kaewpanha M, Hao X, Abudula A. Catalytic steam reforming of biomass tar: Prospects and challenges. Renew Sustain Energy Rev 2016;58:450–61. https://doi.org/10.1016/j.rser.2015.12.316.
[47] Woolcock PJ, Brown RC. A review of cleaning technologies for biomass-derived syngas. Biomass and Bioenergy 2013. https://doi.org/10.1016/j.biombioe.2013.02.036.
[48] De Lasa H, Salaices E, Mazumder J, Lucky R. Catalytic steam gasification of biomass: Catalysts, thermodynamics and kinetics. Chem Rev 2011;111:5404–33. https://doi.org/10.1021/cr200024w.
[49] Claude V, Courson C, Köhler M, Lambert SD. Overview and Essentials of Biomass Gasification Technologies and Their Catalytic Cleaning Methods. Energy and Fuels 2016;30:8791–814. https://doi.org/10.1021/acs.energyfuels.6b01642.
[50] Sutton D, Kelleher B, Ross JRH. Review of literature on catalysts for biomass gasification. Fuel Process Technol 2001;73:155–73. https://doi.org/10.1016/S0378-3820(01)00208-9.
[51] Han J, Kim H. The reduction and control technology of tar during biomass gasification/pyrolysis: An overview. Renew Sustain Energy Rev 2008;12:397–416. https://doi.org/10.1016/j.rser.2006.07.015.
[52] Shahbaz M, yusup S, Inayat A, Patrick DO, Ammar M. The influence of catalysts in biomass steam gasification and catalytic potential of coal bottom ash in biomass steam gasification: A review. Renew Sustain Energy Rev 2017. https://doi.org/10.1016/j.rser.2017.01.153.
[53] Sikarwar VS, Zhao M, Fennell PS, Shah N, Anthony EJ. Progress in biofuel production from gasification. Prog Energy Combust Sci 2017;61:189–248. https://doi.org/10.1016/j.pecs.2017.04.001.
[54] Abu El-Rub Z, Bramer EA, Brem G. Review of catalysts for tar elimination in biomass gasification processes. Ind Eng Chem Res 2004;43:6911–9. https://doi.org/10.1021/ie0498403.
[55] Świerczyński D, Courson C, Bedel L, Kiennemann A, Vilminot S. Oxidation reduction behavior of iron-bearing olivines (Fe xMg1-x)2SiO4 used as catalysts for biomass gasification. Chem Mater 2006;18:897–905. https://doi.org/10.1021/cm051433+.
[56] Devi L, Craje M, Thüne P, Ptasinski KJ, Janssen FJJG. Olivine as tar removal catalyst for biomass gasifiers: Catalyst characterization. Appl Catal A Gen 2005;294:68–79. https://doi.org/10.1016/j.apcata.2005.07.044.
[57] Makwana JP, Joshi AK, Athawale G, Singh D, Mohanty P. Air gasification of rice husk in bubbling fluidized bed reactor with bed heating by conventional charcoal. Bioresour Technol 2015;178:45–52. https://doi.org/10.1016/j.biortech.2014.09.111.
[58] Virginie M, Courson C, Niznansky D, Chaoui N, Kiennemann A. Characterization and reactivity in toluene reforming of a Fe/olivine catalyst designed for gas cleanup in biomass gasification. Appl Catal B Environ 2010;101:90–100. https://doi.org/10.1016/j.apcatb.2010.09.011.
[59] Polychronopoulou K, Bakandritsos A, Tzitzios V, Fierro JLG, Efstathiou AM. Absorption-enhanced reforming of phenol by steam over supported Fe catalysts. J Catal 2006;241:132–48. https://doi.org/10.1016/j.jcat.2006.04.015.
[60] Nordgreen T, Liliedahl T, Sjöström K. Metallic iron as a tar breakdown catalyst related to atmospheric, fluidised bed gasification of biomass. Fuel 2006;85:689–94. https://doi.org/10.1016/j.fuel.2005.08.026.
[61] Simell PA, Hirvensalo EK, Smolander VT, Krause AOI. Steam reforming of gasification gas tar over dolomite with benzene as a model compound. Ind Eng Chem Res 1999;38:1250–7. https://doi.org/10.1021/ie980646o.
[62] Valverde JM, Perejon A, Medina S, Perez-Maqueda LA. Thermal decomposition of dolomite under CO2: Insights from TGA and in situ XRD analysis. Phys Chem Chem Phys 2015;17:30162–76. https://doi.org/10.1039/c5cp05596b.
[63] Rapagnà S, Gallucci K, Foscolo PU. Olivine, dolomite and ceramic filters in one vessel to produce clean gas from biomass. Waste Manag 2018;71:792–800. https://doi.org/10.1016/j.wasman.2017.07.038.
[64] Zhang Z, Liu L, Shen B, Wu C. Preparation, modification and development of Ni-based catalysts for catalytic reforming of tar produced from biomass gasification. Renew Sustain Energy Rev 2018;94:1086–109. https://doi.org/10.1016/j.rser.2018.07.010.

[65] Pio DT, Tarelho LAC, Pinto RG, Matos MAA, Frade JR, Yaremchenko A, et al. Low-cost catalysts for in-situ improvement of producer gas quality during direct gasification of biomass. Energy 2018;165:442–54. https://doi.org/10.1016/j.energy.2018.09.119.
[66] Cortazar M, Alvarez J, Lopez G, Amutio M, Santamaria L, Bilbao J, et al. Role of temperature on gasification performance and tar composition in a fountain enhanced conical spouted bed reactor. Energy Convers Manag 2018;171:1589–97. https://doi.org/10.1016/j.enconman.2018.06.071.
[67] Marinkovic J, Thunman H, Knutsson P, Seemann M. Characteristics of olivine as a bed material in an indirect biomass gasifier. Chem Eng J 2015;279:555–66. https://doi.org/10.1016/j.cej.2015.05.061.
[68] Koppatz S, Pfeifer C, Hofbauer H. Comparison of the performance behaviour of silica sand and olivine in a dual fluidised bed reactor system for steam gasification of biomass at pilot plant scale. Chem Eng J 2011;175:468–83. https://doi.org/10.1016/j.cej.2011.09.071.
[69] Berdugo Vilches T, Marinkovic J, Seemann M, Thunman H. Comparing Active Bed Materials in a Dual Fluidized Bed Biomass Gasifier: Olivine, Bauxite, Quartz-Sand, and Ilmenite. Energy and Fuels 2016;30:4848–57. https://doi.org/10.1021/acs.energyfuels.6b00327.
[70] Christodoulou C, Grimekis D, Panopoulos KD, Pachatouridou EP, Iliopoulou EF, Kakaras E. Comparing calcined and un-treated olivine as bed materials for tar reduction in fluidized bed gasification. Fuel Process Technol 2014;124:275–85. https://doi.org/10.1016/j.fuproc.2014.03.012.
[71] Meng J, Wang X, Zhao Z, Zheng A, Huang Z, Wei G, et al. Highly abrasion resistant thermally fused olivine as in-situ catalysts for tar reduction in a circulating fluidized bed biomass gasifier. Bioresour Technol 2018;268:212–20. https://doi.org/10.1016/j.biortech.2018.07.135.
[72] Arena U, Zaccariello L, Mastellone ML. Fluidized bed gasification of waste-derived fuels. Waste Manag 2010;30:1212–9. https://doi.org/10.1016/j.wasman.2010.01.038.
[73] Tuomi S, Kaisalo N, Simell P, Kurkela E. Effect of pressure on tar decomposition activity of different bed materials in biomass gasification conditions. Fuel 2015;158:293–305. https://doi.org/10.1016/j.fuel.2015.05.051.
[74] Miccio F, Piriou B, Ruoppolo G, Chirone R. Biomass gasification in a catalytic fluidized reactor with beds of different materials. Chem Eng J 2009;154:369–74. https://doi.org/10.1016/j.cej.2009.04.002.
[75] Kuhn JN, Zhao Z, Felix LG, Slimane RB, Choi CW, Ozkan US. Olivine catalysts for methane- and tar-steam reforming. Appl Catal B Environ 2008;81:14–26. https://doi.org/10.1016/j.apcatb.2007.11.040.
[76] Kuba M, Havlik F, Kirnbauer F, Hofbauer H. Influence of bed material coatings on the water-gas-shift reaction and steam reforming of toluene as tar model compound of biomass gasification. Biomass and Bioenergy 2016;89:40–9. https://doi.org/10.1016/j.biombioe.2015.11.029.
[77] Constantinou DA, Fierro JLG, Efstathiou AM. A comparative study of the steam reforming of phenol towards H 2 production over natural calcite, dolomite and olivine materials. Appl Catal B Environ 2010;95:255–69. https://doi.org/10.1016/j.apcatb.2010.01.003.
[78] Erkiaga A, Lopez G, Amutio M, Bilbao J, Olazar M. Steam gasification of biomass in a conical spouted bed reactor with olivine and γ-alumina as primary catalysts. Fuel Process Technol 2013;116:292–9. https://doi.org/10.1016/j.fuproc.2013.07.008.
[79] Tursun Y, Xu S, Abulikemu A, Dilinuer T. Biomass gasification for hydrogen rich gas in a decoupled triple bed gasifier with olivine and NiO/olivine. Bioresour Technol 2019;272:241–8. https://doi.org/10.1016/j.biortech.2018.10.008.
[80] Morin M, Nitsch X, Pécate S, Hémati M. Tar conversion over olivine and sand in a fluidized bed reactor using toluene as model compound. Fuel 2017;209:25–34. https://doi.org/10.1016/j.fuel.2017.07.084.
[81] Devi L, Ptasinski KJ, Janssen FJJG. Pretreated olivine as tar removal catalyst for biomass gasifiers: Investigation using naphthalene as model biomass tar. Fuel Process Technol 2005;86:707–30. https://doi.org/10.1016/j.fuproc.2004.07.001.
[82] Michel R, Łamacz A, Krzton A, Djéga-Mariadassou G, Burg P, Courson C, et al. Steam reforming of α-methylnaphthalene as a model tar compound over olivine and olivine supported nickel. Fuel 2013;109:653–60. https://doi.org/10.1016/j.fuel.2013.03.017.
[83] Tian Y, Zhou X, Lin S, Ji X, Bai J, Xu M. Syngas production from air-steam gasification of biomass with natural catalysts. Sci Total Environ 2018;645:518–23.

https://doi.org/10.1016/j.scitotenv.2018.07.071.
[84] Devi L, Ptasinski KJ, Janssen FJJG, Van Paasen SVB, Bergman PCA, Kiel JHA. Catalytic decomposition of biomass tars: Use of dolomite and untreated olivine. Renew Energy 2005;30:565–87. https://doi.org/10.1016/j.renene.2004.07.014.
[85] Berrueco C, Montané D, Matas Güell B, del Alamo G. Effect of temperature and dolomite on tar formation during gasification of torrefied biomass in a pressurized fluidized bed. Energy 2014;66:849–59. https://doi.org/10.1016/j.energy.2013.12.035.
[86] Lv P, Yuan Z, Wu C, Ma L, Chen Y, Tsubaki N. Bio-syngas production from biomass catalytic gasification. Energy Convers Manag 2007. https://doi.org/10.1016/j.enconman.2006.10.014.
[87] Wang T, Chang J, Lv P, Zhu J. Novel catalyst for cracking of biomass tar. Energy and Fuels 2005. https://doi.org/10.1021/ef030116r.
[88] Saw WL, Pang S. The influence of calcite loading on producer gas composition and tar concentration of radiata pine pellets in a dual fluidised bed steam gasifier. Fuel 2012. https://doi.org/10.1016/j.fuel.2012.07.013.
[89] Min Z, Asadullah M, Yimsiri P, Zhang S, Wu H, Li CZ. Catalytic reforming of tar during gasification. Part I. Steam reforming of biomass tar using ilmenite as a catalyst. Fuel 2011;90:1847–54. https://doi.org/10.1016/j.fuel.2010.12.039.
[90] Min Z, Yimsiri P, Zhang S, Wang Y, Asadullah M, Li CZ. Catalytic reforming of tar during gasification. Part III. Effects of feedstock on tar reforming using ilmenite as a catalyst. Fuel, 2013. https://doi.org/10.1016/j.fuel.2012.09.019.
[91] Lind F, Berguerand N, Seemann M, Thunman H. Ilmenite and nickel as catalysts for upgrading of raw gas derived from biomass gasification. Energy and Fuels 2013;27:997–1007. https://doi.org/10.1021/ef302091w.
[92] Lind F, Seemann M, Thunman H. Continuous catalytic tar reforming of biomass derived raw gas with simultaneous catalyst regeneration. Ind Eng Chem Res 2011;50:11553–62. https://doi.org/10.1021/ie200645s.
[93] Siedlecki M, Nieuwstraten R, Simeone E, Jong W De, Verkooijen AHM. Effect of magnesite as bed material in a 100 kWth steam-oxygen blown circulating fluidized-bed biomass gasifier on gas composition and tar formation. Energy and Fuels 2009. https://doi.org/10.1021/ef900420c.
[94] Zou X, Ma Z, Liu H, Chen D, Wang C, Zhang P, et al. Green synthesis of Ni supported hematite catalysts for syngas production from catalytic cracking of toluene as a model compound of biomass tar. Fuel 2018. https://doi.org/10.1016/j.fuel.2017.12.063.
[95] Ge H, Guo W, Shen L, Song T, Xiao J. Biomass gasification using chemical looping in a 25kWth reactor with natural hematite as oxygen carrier. Chem Eng J 2016;286:174–83. https://doi.org/10.1016/j.cej.2015.10.092.
[96] He L, Hui H, Li S, Lin W. Production of light aromatic hydrocarbons by catalytic cracking of coal pyrolysis vapors over natural iron ores. Fuel 2018;216:227–32. https://doi.org/10.1016/j.fuel.2017.12.005.
[97] Huang Z, He F, Feng Y, Liu R, Zhao K, Zheng A, et al. Characteristics of biomass gasification using chemical looping with iron ore as an oxygen carrier. Int J Hydrogen Energy 2013;38:14568–75. https://doi.org/10.1016/j.ijhydene.2013.09.022.
[98] Tsubouchi N, Mochizuki Y, Byambajav E, Takahashi S, Hanaoka Y, Ohtsuka Y. Catalytic Performance of Limonite Ores in the Decomposition of Model Compounds of Biomass-Derived Tar. Energy and Fuels 2017;31:3898–904. https://doi.org/10.1021/acs.energyfuels.7b00192.
[99] PAN F, ZHU Q shan, DU Z, SUN H yan. Oxidation Kinetics, Structural Changes and Element Migration during Oxidation Process of Vanadium-titanium Magnetite Ore. J Iron Steel Res Int 2016;23:1160–7. https://doi.org/10.1016/S1006-706X(16)30171-6.
[100] Chan FL, Tanksale A. Review of recent developments in Ni-based catalysts for biomass gasification. Renew Sustain Energy Rev 2014;38:428–38. https://doi.org/10.1016/j.rser.2014.06.011.
[101] Baker EG, Mudge LK, Brown MD. Steam Gasification of Biomass with Nickel Secondary Catalysts. Ind Eng Chem Res 1987;26:1335–9. https://doi.org/10.1021/ie00067a012.
[102] Caballero MA, Aznar MP, Gil J, Martín JA, Francés E, Corella J. Commercial Steam Reforming Catalysts to Improve Biomass Gasification with Steam-Oxygen Mixtures. 1. Hot Gas Upgrading by the Catalytic Reactor. Ind Eng Chem Res 1997;36:5227–39. https://doi.org/10.1021/ie970149s.

[103] Aznar MP, Caballero MA, Gil J, Martín JA, Corella J. Commercial steam reforming catalysts to improve biomass gasification with steam-oxygen mixtures. 2. Catalytic tar removal. Ind Eng Chem Res 1998;37:2668–80. https://doi.org/10.1021/ie9706727.
[104] Waldner P, Pelton AD. Thermodynamic modeling of the Ni-S system. Z Met 2004;95:672–81. https://doi.org/10.3139/146.018005.
[105] Sehested J. Four challenges for nickel steam-reforming catalysts. Catal Today 2006;111:103–10. https://doi.org/10.1016/j.cattod.2005.10.002.
[106] Garcia L, Benedicto A, Romeo E, Salvador ML, Arauzo J, Bilbao R. Hydrogen production by steam gasification of biomass using Ni-Al coprecipitated catalysts promoted with magnesium. Energy and Fuels 2002;16:1222–30. https://doi.org/10.1021/ef020035f.
[107] Vitorino NMD, Kovalevsky A V., Ferro MC, Abrantes JCC, Frade JR. Design of NiAl2O4 cellular monoliths for catalytic applications. Mater Des 2017;117:332–7. https://doi.org/10.1016/j.matdes.2017.01.003.
[108] Liang C, Ye Z, Dong D, Zhang S, Liu Q, Chen G, et al. Methanation of CO2: Impacts of modifying nickel catalysts with variable-valence additives on reaction mechanism. Fuel 2019;254:115654. https://doi.org/10.1016/j.fuel.2019.115654.
[109] Yu J, Guo Q, Gong Y, Ding L, Wang J, Yu G. A review of the effects of alkali and alkaline earth metal species on biomass gasification. Fuel Process Technol 2021;214:106723. https://doi.org/10.1016/j.fuproc.2021.106723.
[110] Zhang L, Schmetterer C, Masset PJ. Thermodynamic description of the M2O-SiO2 (M = K, Na) systems. Comput Mater Sci 2013;66:20–7. https://doi.org/10.1016/j.commatsci.2012.04.040.
[111] Yuan H, Wu S, Yin X, Huang Y, Guo D, Wu C. Adjustment of biomass product gas to raise H2/CO ratio and remove tar over sodium titanate catalysts. Renew Energy 2018;115:288–98. https://doi.org/10.1016/j.renene.2017.08.025.
[112] Guo F, Li X, Liu Y, Peng K, Guo C, Rao Z. Catalytic cracking of biomass pyrolysis tar over char-supported catalysts. Energy Convers Manag 2018. https://doi.org/10.1016/j.enconman.2018.04.094.
[113] Lin Q, Zhang S, Wang J, Yin H. Synthesis of modified char-supported Ni–Fe catalyst with hierarchical structure for catalytic cracking of biomass tar. Renew Energy 2021;174:188–98. https://doi.org/10.1016/j.renene.2021.04.084.
[114] Azhar Uddin M, Tsuda H, Wu S, Sasaoka E. Catalytic decomposition of biomass tars with iron oxide catalysts. Fuel 2008;87:451–9. https://doi.org/10.1016/j.fuel.2007.06.021.
[115] Noichi H, Uddin A, Sasaoka E. Steam reforming of naphthalene as model biomass tar over iron-aluminum and iron-zirconium oxide catalyst catalysts. Fuel Process Technol 2010;91:1609–16. https://doi.org/10.1016/j.fuproc.2010.06.009.
[116] Kastner JR, Mani S, Juneja A. Catalytic decomposition of tar using iron supported biochar. Fuel Process Technol 2015. https://doi.org/10.1016/j.fuproc.2014.09.038.
[117] Reddy GK, Boolchand P, Smirniotis PG. Sulfur tolerant metal doped Fe/Ce catalysts for high temperature WGS reaction at low steam to CO ratios - XPS and Mossbauer spectroscopic study. J Catal 2011;282:258–69. https://doi.org/10.1016/j.jcat.2011.06.016.
[118] Damma D, Smirniotis PG. Recent advances in iron-based high-temperature water-gas shift catalysis for hydrogen production. Curr Opin Chem Eng 2018;21:103–10. https://doi.org/10.1016/j.coche.2018.09.003.
[119] Damma D, Jampaiah D, Welton A, Boolchand P, Arvanitis A, Dong J, et al. Effect of Nb modification on the structural and catalytic property of Fe/Nb/M (M = Mn, Co, Ni, and Cu) catalyst for high temperature water-gas shift reaction. Catal Today 2020;355:921–31. https://doi.org/10.1016/j.cattod.2019.02.029.
[120] Kang YB, Jung IH. Thermodynamic modeling of oxide phases in the Fe–Mn–O system. J Phys Chem Solids 2016;98:237–46. https://doi.org/10.1016/j.jpcs.2016.07.017.
[121] Stir M, Ishizaki K, Vaucher S, Nicula R. Mechanism and kinetics of the reduction of magnetite to iron during heating in a microwave E-field maximum. J Appl Phys 2009;105:124901. https://doi.org/10.1063/1.3148264.
[122] Ruivo LCM, Pio DT, Yaremchenko AA, Tarelho LAC, Frade JR, Kantarelis E, et al. Iron-based catalyst (Fe2-xNixTiO5) for tar decomposition in biomass gasification. Fuel 2021;300:120859. https://doi.org/10.1016/j.fuel.2021.120859.
[123] Wang Y, Pang S. Investigation of hydrogen sulphide removal from simulated producer gas of biomass gasification by titanomagnetite. Biomass and Bioenergy 2018;109:61–70.

https://doi.org/10.1016/j.biombioe.2017.12.021.
[124] Huang BS, Chen HY, Chuang KH, Yang RX, Wey MY. Hydrogen production by biomass gasification in a fluidized-bed reactor promoted by an Fe/CaO catalyst. Int J Hydrogen Energy 2012;37:6511–8. https://doi.org/10.1016/j.ijhydene.2012.01.071.
[125] Hu Q, Shen Y, Chew JW, Ge T, Wang CH. Chemical looping gasification of biomass with Fe2O3/CaO as the oxygen carrier for hydrogen-enriched syngas production. Chem Eng J 2020;379:122346. https://doi.org/10.1016/j.cej.2019.122346.
[126] Furusawa T, Tsutsumi A. Comparison of Co/MgO and Ni/MgO catalysts for the steam reforming of naphthalene as a model compound of tar derived from biomass gasification. Appl Catal A Gen 2005;278:207–12. https://doi.org/10.1016/j.apcata.2004.09.035.
[127] Huang S, Xu H, Li H, Guo Y, Sun Z, Du Y, et al. Preparation and characterization of char supported Ni–Cu nanoalloy catalyst for biomass tar cracking together with syngas-rich gas production. Fuel Process Technol 2021;218:106858. https://doi.org/10.1016/j.fuproc.2021.106858.
[128] Wang L, Li D, Watanabe H, Tamura M, Nakagawa Y, Tomishige K. Catalytic performance and characterization of Co/Mg/Al catalysts prepared from hydrotalcite-like precursors for the steam gasification of biomass. Appl Catal B Environ 2014;150–151:82–92. https://doi.org/10.1016/j.apcatb.2013.12.002.
[129] Wang L, Li D, Koike M, Watanabe H, Xu Y, Nakagawa Y, et al. Catalytic performance and characterization of Ni-Co catalysts for the steam reforming of biomass tar to synthesis gas. Fuel 2013;112:654–61. https://doi.org/10.1016/j.fuel.2012.01.073.
[130] Sule K, Umbsaar J, Prenner EJ. Mechanisms of Co, Ni, and Mn toxicity: From exposure and homeostasis to their interactions with and impact on lipids and biomembranes. Biochim Biophys Acta - Biomembr 2020;1862:183250. https://doi.org/10.1016/j.bbamem.2020.183250.
[131] Tasaka K, Furusawa T, Tsutsumi A. Biomass gasification in fluidized bed reactor with Co catalyst. Chem Eng Sci 2007;62:5558–63. https://doi.org/10.1016/j.ces.2007.01.040.
[132] Furusawa T, Tsutsumi A. Development of cobalt catalysts for the steam reforming of naphthalene as a model compound of tar derived from biomass gasification. Appl Catal A Gen 2005;278:195–205. https://doi.org/10.1016/j.apcata.2004.09.034.
[133] Aghabararnejad M, Patience GS, Chaouki J. TGA and kinetic modelling of Co, Mn and Cu oxides for Chemical Looping Gasification (CLG). Can J Chem Eng 2014;92:1903–10. https://doi.org/10.1002/cjce.22046.
[134] Stokłosa A. Point defects diagrams for pure and doped manganese oxide Mn 1-δO in the temperature range of 1173-1830 K. Mater Chem Phys 2012;134:1136–45. https://doi.org/10.1016/j.matchemphys.2012.04.006.
[135] Preisner NC, Block T, Linder M, Leion H. Stabilizing Particles of Manganese-Iron Oxide with Additives for Thermochemical Energy Storage. Energy Technol 2018;6:1–13. https://doi.org/10.1002/ente.201800211.
[136] Zhao X, Zhou H, Sikarwar VS, Zhao M, Park AHA, Fennell PS, et al. Biomass-based chemical looping technologies: The good, the bad and the future. Energy Environ Sci 2017;10:1885–910. https://doi.org/10.1039/c6ee03718f.
[137] Shulman A, Cleverstam E, Mattisson T, Lyngfelt A. Chemical - Looping with oxygen uncoupling using Mn/Mg-based oxygen carriers - Oxygen release and reactivity with methane. Fuel 2011;90:941–50. https://doi.org/10.1016/j.fuel.2010.11.044.
[138] Bendoni R, Miccio F, Medri V, Benito P, Vaccari A, Landi E. Geopolymer composites for the catalytic cleaning of tar in biomass-derived gas. Renew Energy 2019;131:1107–16. https://doi.org/10.1016/j.renene.2018.08.067.
[139] Cheah S, Olstad JL, Jablonski WS, Magrini-Bair KA. Regenerable manganese-based sorbent for cleanup of simulated biomass-derived syngas. Energy and Fuels 2011;25:379–87. https://doi.org/10.1021/ef101337v.
[140] Cecilia JA, Soriano DM, Natoli A, Rodríguez-Castellón E, López Nieto JM. Selective oxidation of hydrogen sulfide to sulfur using vanadium oxide supported on porous clay heterostructures (PCHs) formed by pillars silica, silica-zirconia or silica-titania. Materials (Basel) 2018;11:1562. https://doi.org/10.3390/ma11091562.
[141] You Z, Jung IH. Critical Evaluation and Thermodynamic Optimization of the Fe-P System. Metall Mater Trans B Process Metall Mater Process Sci 2020;51:3108–29. https://doi.org/10.1007/s11663-020-01939-0.

[142] Yamaguchi O, Uegaki T, Miyata Y, Shimizu K. Formation of AlVO4 Solid Solution from Alkoxides. J Am Ceram Soc 1987;70:C-198-C-200. https://doi.org/10.1111/j.1151-2916.1987.tb05725.x.
[143] Feng D, Zhang J, Li M, Chen M, Zhao B. Phase Equilibria of the SiO2–V2O5 system. Ceram Int 2020;46:24053–9. https://doi.org/10.1016/j.ceramint.2020.06.183.
[144] Li R, Roy A, Bridges J, Dooley KM. Tar Reforming in Model Gasi fi er E ffl uents : Transition Metal / Rare Earth Oxide Catalysts 2014.
[145] Bueno-López A. Diesel soot combustion ceria catalysts. Appl Catal B Environ 2014;146:1–11. https://doi.org/10.1016/j.apcatb.2013.02.033.
[146] Bampenrat A, Meeyoo V, Kitiyanan B, Rangsunvigit P, Rirksomboon T. Naphthalene steam reforming over Mn-doped CeO2-ZrO2 supported nickel catalysts. Appl Catal A Gen 2010;373:154–9. https://doi.org/10.1016/j.apcata.2009.11.008.
[147] Lee J, Li R, Janik MJ, Dooley KM. Rare Earth/Transition Metal Oxides for Syngas Tar Reforming: A Model Compound Study. Ind Eng Chem Res 2018;57:6131–40. https://doi.org/10.1021/acs.iecr.8b00682.
[148] Fagg DP, Marozau IP, Shaula AL, Kharton V V., Frade JR. Oxygen permeability, thermal expansion and mixed conductivity of GdxCe0.8-xPr0.2O2-δ, x=0, 0.15, 0.2. J Solid State Chem 2006;179:3347–56. https://doi.org/10.1016/j.jssc.2006.06.028.
[149] Niu X, Shen L. Ca- and Mg-rich waste as high active carrier for chemical looping gasification of biomass. Chinese J Chem Eng 2021;38:145–54. https://doi.org/10.1016/j.cjche.2020.09.024.
[150] Guo F, Zhao X, Peng K, Liang S, Jia X, Qian L. Catalytic reforming of biomass primary tar from pyrolysis over waste steel slag based catalysts. Int J Hydrogen Energy 2019;44:16224–33. https://doi.org/10.1016/j.ijhydene.2019.04.190.
[151] Chianese S, Loipersböck J, Malits M, Rauch R, Hofbauer H, Molino A, et al. Hydrogen from the high temperature water gas shift reaction with an industrial Fe/Cr catalyst using biomass gasification tar rich synthesis gas. Fuel Process Technol 2015;132:39–48. https://doi.org/10.1016/j.fuproc.2014.12.034.
[152] Han J, Shan R, Gu J, Yuan H, Chen Y. Chemical looping gasification using Nickel-containing electroplating sludge and dyeing sludge as oxygen carrier. Waste Manag 2022;141:194–201. https://doi.org/10.1016/j.wasman.2022.01.016.
[153] Cheng L, Wu Z, Zhang Z, Guo C, Ellis N, Bi X, et al. Tar elimination from biomass gasification syngas with bauxite residue derived catalysts and gasification char. Appl Energy 2020;258:114088. https://doi.org/10.1016/j.apenergy.2019.114088.
[154] Veses A, Aznar M, López JM, Callén MS, Murillo R, García T. Production of upgraded bio-oils by biomass catalytic pyrolysis in an auger reactor using low cost materials. Fuel 2015;141:17–22. https://doi.org/10.1016/j.fuel.2014.10.044.
[155] Shen X, Yan F, Zhang Z, Li C, Zhao S, Zhang Z. Enhanced and environment-friendly chemical looping gasification of crop straw using red mud as a sinter-resistant oxygen carrier. Waste Manag 2021;121:354–64. https://doi.org/10.1016/j.wasman.2020.12.028.
[156] Weerachanchai P, Horio M, Tangsathitkulchai C. Effects of gasifying conditions and bed materials on fluidized bed steam gasification of wood biomass. Bioresour Technol 2009;100:1419–27. https://doi.org/10.1016/j.biortech.2008.08.002.
[157] Sui M, Li G ying, Guan Y lin, Li C ming, Zhou R qing, Zarnegar AM. Hydrogen and syngas production from steam gasification of biomass using cement as catalyst. Biomass Convers Biorefinery 2020;10:119–24. https://doi.org/10.1007/s13399-019-00404-6.
[158] Inayat M, Sulaiman SA, Bhayo BA, Shahbaz M. Application of response surface methodology in catalytic co-gasification of palm wastes for bioenergy conversion using mineral catalysts. Biomass and Bioenergy 2020;132:105418. https://doi.org/10.1016/j.biombioe.2019.105418.
[159] Guan G, Chen G, Kasai Y, Lim EWC, Hao X, Kaewpanha M, et al. Catalytic steam reforming of biomass tar over iron- or nickel-based catalyst supported on calcined scallop shell. Appl Catal B Environ 2012. https://doi.org/10.1016/j.apcatb.2011.12.009.
[160] Ferreira SD, Junges J, Scopel B, Manera C, Osório E, Lazzarotto IP, et al. Steam Gasification of Biochar Derived from the Pyrolysis of Chrome-Tanned Leather Shavings. Chem Eng Technol 2019;42:2530–8. https://doi.org/10.1002/ceat.201800660.

2. SCOPE OF THE THESIS

2.1. Objectives

The successful conversion of biomass into chemicals and advanced transportation fuels through gasification can only be unlocked via the development of cost-effective catalysts. Current catalytic solutions including noble metals, rare earth elements and nickel-based materials exhibit high performance in tar conversion reactions, but their high costs, toxicity and ready deactivation under operating conditions have motivated research into sustainable alternatives that offer appealing properties to address such drawbacks. Amongst different options, iron-based catalysts combined high availability with minimal environmental risks. Though their catalytic activity for tar conversion is usually poorer than other types of catalysts (e.g. noble metals), such materials are more likely to become economically feasible by avoiding highly expensive noble metals or other critical elements.

The present thesis focuses on the catalytic upgrading of raw gas resulting from the gasification of lignocellulosic biomass. The main challenge is to explore the potential of low-cost materials to improve producer gas quality by promoting water-gas-shift and tar conversion reactions. This is mainly supported by the design of iron-containing systems inspired by natural minerals and large-scale materials that are otherwise viewed as waste, and using sustainable processing routes, to allow upscaling from laboratory-scale research to an industrial context. Preliminary studies with low-cost materials are conducted to identify low-cost precursors of interest for catalyst processing. The composition and processing methods of catalysts are designed for subsequent catalytic tests, also seeking enhanced catalytic activity by structural and redox design.

Iron titanate catalysts with adjusted Ni loads are proposed for steam reforming of biomass-derived tar in downstream applications. The expected flexibility of this system for compositional, structural and redox configurations are used to design prospective catalysts with additional functionalities such as self-heating ability to assist endothermic reactions. Catalysts are processed by combining mechanical activation and highly energy efficient microwave firing. Thermodynamic modelling is also applied as guidelines to design materials inspired by natural minerals such as ilmenite, and to assess their compatibility with biomass gasification conditions. Suitable thermochemical treatments under reducing conditions are used to induce controlled precipitation of bi-metallic precipitates (Ni-Fe alloys or intermetallics), providing active sites for tar conversion.

Dedicated tar conversion catalysts for in-situ applications in biomass gasifiers are also exploited through the integration of highly gas permeable ceramics structures in the

freeboard zone of fluidized bed gasifiers. Interconnecting cells is expected to ensure facile impregnation of nitrate solutions for uniform functionalization and in-situ formation of nanostructured active sites, after thermal treatment under controlled conditions. The Fe-O-Mn system is selected for catalytic studies since it offers prospects to design non-toxic catalysts with suitable magnetic properties for magnetic separation, as well as for microwave assisted operation. The emphasis is on catalysts with spinel structure $(Fe,Mn)_3O_4$ because of the flexibility to adjust their composition, distribution of mixed valence cations and degree of inversion by redistribution in octahedral and tetrahedral positions. Furthermore, the role of redox changes on such structures is expected to yield guidelines for selective catalytic oxidation of tar compounds under biomass gasification conditions, which may involve partial or/and complete oxidation reactions.

One also seeks developments based on catalysts for in-situ H_2-enriched gas production during biomass steam gasification. Starting from the idea of combining the ability to uptake/release both O_2 and CO_2, the Ca-Fe-O system is proposed as potential candidate. The research is focuses on granulated composite materials based on siderite and concrete precursor mixtures, allowing to improve the economic viability by decreasing system and production costs. Note that concrete wastes contain significant fractions of Ca-rich silicates with potential CO_2 adsorption ability. Siderite $FeCO_3$ also undergoes ready thermal decomposition before reaching gasification temperatures, and the resulting Fe oxides are likely to evolve from the unstable divalent state (FeO) to higher oxidation (Fe_3O_4), while retaining fine microstructures, with expected impact on water-gas-shift reaction. A cost-effective and scalable procedure based on mechanical granulation was developed for the preparation of composite catalysts. Brownmillerite catalysts processed by the reactive firing of calcite and a siderite mineral are also explored for prospective catalytic applications.

On the other hand, the main mechanisms of catalytic tar conversion indicate a strong dependence on the redox behaviour of the metal active sites. Tolerance of catalysts to different contaminants in biomass-derived gas might affect their lifetime, which ultimately influences the feasibility of the biomass gasification process. This highlights that the design of suitable operating conditions is essential for further improvement of catalyst performance. Prospective guidelines are derived from thermodynamic modelling, which also provides insights about the operation of iron-based catalysts under biomass gasification conditions. This is intended to provide comprehensive guidelines for the selection of proper operating conditions for iron-based catalysts, rather than relying mainly on empiricism, and to minimize the impact of some underestimated deactivation mechanisms resulting from gas-solid interactions.

2.2. Thesis Outline

This thesis is mainly based on the papers contained in Chapter 3 to 6, which have been organized to achieve the objectives of the present work. Chapter 3 (Paper I) presents a graphical approach to support the operation of iron-based catalysts under biomass gasification conditions. Chapters 4 and 5 focus on the study of catalytic tar conversion through reforming (Paper II) and oxidation (Paper III) reactions, respectively, presenting the most important results and discussions. Finally, Chapter 6 is focused on catalytic steam gasification studies (Paper IV), seeking H_2-enrichement in the biomass-derived gas by the contribution of water gas shift and CO_2 adsorption. The author was the main person responsible for the publications presented in Chapter 3 to 6. The author designed and performed most of the experimental work related to the preparation, characterization and activity studies of the catalysts. The author also performed all the theoretical calculations and part of the thermodynamic analysis presented. In addition, the author was the main responsible for the formal analysis of the results and writing the articles. Concluding remarks and recommendations for future work are given in Chapter 7.

For convenience reasons, other related papers published as a co-author during the course of the doctorate are also provided as appendix. Though these studies are not the main body of the present thesis, their execution were the bases for the concepts explored in Chapters 3 to 6. The author contributed to the characterization of the studied materials and execution of the gasification experiments, as well as writing and reviewing.

3. CATALYTIC UPGRADING OF BIOMASS-DERIVED GAS

3.1. Thermodynamic Guidelines for Improved Operation of Iron-based Catalysts in Gasification of Biomass

Luís Ruivo, Tiago Silva, Daniel Neves, Luís Tarelho, Jorge Frade
University of Aveiro (CESAM and CICECO)
Currently submitted in the Energy Journal

Abstract

The present work intended the development of a graphical approach to support the operation of conventional iron-based catalysts under gasification conditions. A combination of experimental data and thermodynamic modelling was used as guidelines to elucidate the dependence of catalyst performance on the thermochemical conditions of producer gas. The outcomes are represented by stability diagrams in a form of planar representations for easier identification of appropriate operating windows. Attention was focused not only on potential deactivation mechanisms resulting from gas-solid interactions, but also on the stability of relevant catalytic phases when exposed to biomass-derived gas atmospheres at temperatures in the range 600-900 ºC. The results suggest that controlled process parameters contributes to enhance the tolerance of iron-based materials to deactivation by carbon deposition, H_2S poisoning and/or carbonation. Selected examples also show that the redox potential imposed by producer gas can have a significant impact on the stability of relevant active phases, with subsequent impact on catalyst performance. To overcome these constrains, one should considerer suitable composition changes to enhance their redox properties, possibly combined with microstructural or nanostructural development during materials processing.

Keywords: Biomass, Gasification, Iron Catalysts, Thermodynamics, Stability Diagrams

3.1.1. Introduction

Considering the current status of the global energy policy, the coming years will be marked by important challenges, associated with the desired energy transition to a circular bioeconomy. In this scenario, gasification of biomass is of particular interest since it can convert a variety of low-value feedstocks into a valuable gas product, providing a flexible renewable source for the production of baseload electricity, transportation fuels and various chemicals [1–3]. During biomass thermal conversion, additional contaminants are also produced which require cleaning and conditioning of the raw gas.

Despite the recognized potential of biomass gasification, its transition to an industrial context still faces technical shortcomings, mostly resulting from the formation of undesired tar which causes several operating problems [4,5]. In addition, the H_2:CO molar ratio of the biomass-derived gas shows typical values < 2.0, which implies further adjustments to fulfil the quality demands of different end-use applications [6]. Accordingly, the integration of heterogeneous catalysts as a part of the gasification concept is crucial to connect the divergence between the conversion of biomass-derived gas with profitable products.

Catalytic hot gas upgrading has been widely investigated, as reported in previous reviews provided by e.g. Guan et al. [7], Sutton et al. [8], Zhang et al. [9] and Shahbaz et al. [10]. Ni-based materials revealed greater activity for the conversion of tar to CO and H_2 but are relatively expensive and require continuous regeneration. In addition, deactivation by sulphur chemisorption on Ni active sites and microstructural ageing are other recognized limitations [11,12], making these type of materials unattractive in an industrial context that present severe process conditions.

On the other hand, Fe-based materials has shown a growing interest for gasification applications because of their low-cost, lower environmental impact and effective performance toward tar cracking and H_2 production [13,14]. However, complications resulting from carbon deposition is expected for in-situ applications due to unconverted char in the gasifier bed and the catalytic mechanisms involving tar side reactions [15]. There is also evidence that redox changes of iron active sites, induced by the thermochemical conditions of the biomass-derived raw gas, might result in a progressive decline of catalytic activity [16]. Gas-solid interactions with S-containing compounds may also have implications on the selectivity of chemical reactions [17]. The design of suitable operating conditions is therefore crucial for extending catalyst lifetime, which is a crucial issue in the context of process economics.

Thermodynamic modelling has been extensively applied to support the optimization of biomass gasification technologies [18–22], giving qualitative and quantitative information about the operational limits. Though the relevance of such approach, theoretical analysis specifically addressing catalyst performance are limited in literature. Studies are mostly focused on the evaluation of specific reactor parameters, such as the gasifier agent, temperature and composition of biomass feedstocks, with the objective of improving producer gas quality and overall gasification efficiency. Subsequently, there is a particular need of understanding the interactions of iron-based materials with biomass-derived gas within the gasifier, as well as simplified modelling approaches to evaluate the operating conditions required for efficient operation.

Therefore, the present study aimed to develop a graphical approach to support the operation of iron-based materials during biomass gasification. A combination of experimental data and thermodynamic modelling was applied as guidelines to elucidate the dependence of catalyst performance on the process conditions. This is expected to provide comprehensive guidelines for the selection of proper operating conditions for catalysts, which is still dictated mainly by empiricism, and to minimize the impact of some underestimated deactivation mechanisms. In addition, a mathematical model for gasification of biomass is provided by applying mass balances, energy balances and thermodynamic equilibrium predictions, aiming to establish appropriate conditions for the betterment of carbon conversion. Though the fundamentals discussed here are of general applicability, the work is focused on autothermal gasification of biomass, where primary measures are preferable to enhance process efficiency.

3.1.2. Thermodynamic Assessment

3.1.2.1. Fundamentals of Temperature Diagrams

A biomass gasification model was employed to support the design of temperature diagrams. It was based on thermodynamic equilibrium approach that consists in evaluating the composition of the biomass-derived products using minimization Gibbs energy. The proposed model is based on steady-state calculations of energy associated with all the intervenient species and includes the following general assumptions: i) perfect mixing and uniform temperature and pressure; ii) heat losses through the gasifier are neglected; iii) the biomass feedstock is represented by an equivalent molecule comprising carbon (C), hydrogen (H) and oxygen (O). The presence of nitrogen (N) and sulfur (S) is neglected, and the fraction of ashes in the biomass feedstock is only considered for its impact on the overall mass balance; iv) the model assumes that gasification reaction rates are fast and residence time is long enough to reach chemical equilibrium; v) reaction products mainly consist of H_2, CO, CO_2, CH_4, H_2O, N_2 and unconverted carbon (char). Details concerning the thermodynamic equilibrium approach was provided in previous investigations [18,19].

Based on the aforementioned considerations, mass and energy balances, per unit of biomass on a dry and ash-free basis (daf), were implemented. The principle of mass conservation applied to the gasification process can be described by a single global equation and expressed as follows:

$$\left(\frac{1}{1-\mathrm{W_w}}\right)\cdot\left(1+\frac{\mathrm{W_A}}{1-\mathrm{W_A}}\right)+\mathrm{W_{GA}}-\mathrm{Y_{Char}}-\mathrm{Y_{Gas}}=0 \qquad \text{Eq. 3.1-1}$$

where W_w is the fraction of moisture in biomass ($\mathrm{kg_{H_2O}}\cdot\mathrm{kg_{fuel}^{-1}}$), W_A is the fraction of ash in dry biomass ($\mathrm{kg_{Ash}}\cdot\mathrm{kg_{dry,fuel}^{-1}}$), W_{GA} is the ratio between the gasifier agent and biomass on a dry and ash-free basis ($\mathrm{kg_{GA}}\cdot\mathrm{kg_{daf,fuel}^{-1}}$), $\mathrm{Y_{Char}}$ and $\mathrm{Y_{Gas}}$ are the mass yields of char and producer gas, respectively. The $\mathrm{W_{GA}}$ may comprise different components, being formulated according to the following equation:

$$\mathrm{W_{GA}}=\mathrm{ER}\cdot\mathrm{W_s}\cdot\left[1+\frac{\mathrm{M_{N_2}}}{\mathrm{M_{O_2}}}\cdot\left(\frac{1}{\mathrm{X_{O_2,GA}}}-1\right)\right]+\mathrm{W_{H_2O}} \qquad \text{Eq. 3.1-2}$$

where ER is the equivalence ratio, W_s and W_{steam} are the stoichiometric amount of gas mixture required for a complete combustion of biomass ($\mathrm{kg_{Air/O_2}}\cdot\mathrm{kg_{daf,fuel}^{-1}}$) and the steam to biomass mass ratio ($\mathrm{kg_{H_2O}}\cdot\mathrm{kg_{daf,fuel}^{-1}}$), respectively, $\mathrm{X_{O_2,GA}}$ is the molar fraction of O_2 in $\mathrm{W_s}$, $\mathrm{M_{N_2}}$ and $\mathrm{M_{O_2}}$ are the molar mass ($\mathrm{kg}\cdot\mathrm{mol^{-1}}$) of N_2 and O_2, respectively. The $\mathrm{Y_{Gas}}$ and $\mathrm{Y_{Char}}$ relates to the abundances of the biomass-derived products and can be defined as follows:

$$\mathrm{Y_{Char}}=1-\mathrm{Y_{Gas}} \qquad \text{Eq. 3.1-3}$$

$$\mathrm{Y_{Gas}}=\sum_{i}^{n}\mathrm{Y_{i,Gas}} \qquad \text{i = } H_2\text{, CO, } CO_2\text{, } CH_4\text{, } N_2 \text{ and } H_2O \qquad \text{Eq. 3.1-4}$$

Energy calculations take into account reference conditions, at normal room temperature (T_{ref} = 298 K) and pressure (P_{ref} = 1 atm). Considering the biomass on a dry and ash-free basis, one easily obtains the following relation for the enthalpy balance:

$$\Delta H_{products} - \Delta H_{reactants} - Q = 0 \qquad \text{Eq. 3.1-5}$$

where $\Delta H_{products}$ and $\Delta H_{reactants}$ denote the enthalpy changes of biomass-derived products and reactants ($kJ \cdot kg_{daf,fuel}^{-1}$) at reference conditions, according to:

$$\Delta H_{reactants} = \left(\overline{cp}_{fuel} + ER \cdot W_s \cdot \overline{cp}_s + W_{H_2O} \cdot \overline{cp}_{H_2O}\right) \cdot (T_{adb} - T_{ref}) + LHV_{fuel} \qquad \text{Eq. 3.1-6}$$

$$\Delta H_{products} = \Delta H_{p,Gas} + \Delta H_{p,Char} \qquad \text{Eq. 3.1-7}$$

$$\Delta H_{p,Gas} = Y_{Gas} \cdot [\overline{cp}_{Gas} \cdot (T_{adb} - T_{ref}) + LHV_{Gas}] \qquad \text{Eq. 3.1-8}$$

$$\Delta H_{p,Char} = Y_{Char} \cdot [\overline{cp}_{Char} \cdot (T_{adb} - T_{ref}) + LHV_{Char}] \qquad \text{Eq. 3.1-9}$$

The parameter Q denotes the heat exchanged between the reactor and the environment, being negative, positive or zero in cases where the gasification process is exothermic, endothermic or adiabatic, respectively. The thermodynamic data, such as the average specific heat ($\overline{cp}$) and the lower heating value (LHV) of reactants and products, was obtained through empirical formulas [23]. In the case of the W_s and Y_{Gas} parameters, the $\overline{cp}$ values were determined as follows:

$$\overline{cp}_{W_s} = \frac{1}{M_{W_s}} \cdot \left(\overline{cp}_{O_2} \cdot X_{O_2,GA} \cdot M_{O_2} + \overline{cp}_{N_2} \cdot (1 - X_{O_2,GA}) \cdot M_{N_2}\right) \qquad \text{Eq. 3.1-10}$$

$$\overline{cp}_{Gas} = \sum_i \overline{cp}_i \cdot X_{i,Gas} \qquad \text{Eq. 3.1-11}$$

3.1.2.2. Oxygen Potential and Carbon Activity in Producer Gas

Depending on the reaction to be promoted, oxidation or reduction of the active sites can significantly affect the performance of metal catalysts; this can be described by reaction (3.1-12), for a generic metal active site, which depends on partial pressure of oxygen (pO_2). Based on this principle, the behaviour of the metal active sites under gasification conditions will depend on the redox conditions imposed by the biomass-derived gas.

$$2\left(\frac{x}{y}\right) Me + O_2 \rightleftharpoons \left(\frac{2}{y}\right) M_xO_y \qquad \text{Eq. 3.1-12}$$

The partial conversion of biomass through gasification involves a set of parallel reactions, including onset of fully oxidized species (reactions 3.1-13 and 3.1-14), whose extension is dictated by the working conditions of the gasifier [24]. The WGS reaction (3.1-15) may also play a role in the pO_2 associated with biomass-derived. WGS reaction can be expressed as the sum of reaction (3.1-13) and (3.1-14) and, although it suggests the absence of oxygen, kinetic restriction may affect this redox-type mechanisms [18].

$$2CO + O_2 \rightleftharpoons 2CO_2$$ Eq. 3.1-13

$$2H_2 + O_2 \rightleftharpoons 2H_2O$$ Eq. 3.1-14

$$CO + H_2O \rightleftharpoons CO_2 + H_2$$ Eq. 3.1-15

Still, one may estimate ideal redox conditions and dependence of pO_2 on temperature or producer gas composition on assuming gas phase equilibrium. An ideal condition may be defined in the gas phase, as follows:

$$\frac{p_{CO}}{p_{CO_2}} = \frac{1}{\sqrt{K_{13} \cdot p_{O_2}}}$$ Eq. 3.1-16

$$\frac{p_{H_2}}{p_{H_2O}} = \frac{1}{\sqrt{K_{14} \cdot p_{O_2}}}$$ Eq. 3.1-17

where p_i (i = CO, CO_2, H_2 and H_2O) represents the partial pressure of gas species, K_{13} and K_{14} denote the equilibrium constants of reaction (3.1-13) and (3.1-14), respectively, calculated from thermodynamic data ($K_i = \exp[-\Delta G_i/RT]$). On the other hand, to analyse risks of carbon precipitation on catalyst surface, or onset of metal carbides at sufficiently high temperatures, one should consider the carbon activity (a_C) in the gas phase which is mainly imposed by the Boudouard reaction and described as follows:

$$2CO \rightleftharpoons C + CO_2$$ Eq. 3.1-18

$$a_C = K_{18} \cdot \frac{p_{CO}^2}{p_{CO_2}}$$ Eq. 3.1-19

Risks of carbon deposition correspond to conditions when $a_C \geq 1$ or $K_{18} \cdot p_{CO}^2 \geq p_{CO_2}$, i.e. for CO-rich conditions, and/or low temperatures, as K_{18} rises with decreasing temperature. Onset of the carbide phase may also occur at the onset of carbon (reaction 3.1-20) or on reaching sufficiently high activity of carbon (reaction 3.1-21), mainly at relatively high temperatures. Though this may be interpreted as a negative impact on catalytic performance, carbide catalysts have also been proposed for relevant gas phase processes, namely Mo carbides proposed as catalysts for reverse water gas shift [25] or utilization of CO_2 [26]. Note also that this concept has been extended to the so-called MXenes, after previous functionalization of carbides of different transition metal elements (Ti, V, Cr, …) [27]. Thus, one must also examine the thermochemical conditions when the carbide phase may be present in biomass gasification.

$$3Fe + C \Leftrightarrow Fe_3C$$ Eq. 3.1-20

$$3FeO + C \Leftrightarrow Fe_3C + 1.5O_2$$ Eq. 3.1-21

The experimental data used to determine the a_C and pO_2 values associated with biomass derived gas was compiled by collecting and organizing experimental results from the literature [14,28–53], regarding gasification experiments with distinct biomass feedstocks and different operation conditions.

3.1.2.3. Fundamentals of Phase Stability Diagrams

Thermodynamic calculations were applied as guidelines to investigate the stability range of iron-based catalysts and their compatibility with the thermochemical conditions of biomass gasification. The analysis was performed on assuming simplified model systems and computing diagrams in a form of planar representations [54]; this is based on derivation of representative reactions for 2-phase equilibria, and then extracting the relevant values of oxygen partial pressure (pO_2), carbon dioxide partial pressure (pCO_2), water partial pressure (pH_2O), hydrogen sulphide partial pressure (pH_2S) and/or activity values (a_i) to establish stability ranges for expected phases. For example, interactions of iron oxides with biomass-derived contaminants such as H_2S corresponds to a quaternary system Fe-O-S-H and phase equilibrium at constant temperature and total pressure will still depend simultaneously on H_2S, pO_2 and pH_2 (or pH_2O). Early studies of the mechanism of reaction of iron with H_2S at high temperatures [55] reported linear dependence on time and suggested that kinetics relies on mixed transport of cation vacancies and holes in a dense non-stoichiometric $Fe_{1-\delta}S$ scale, combined on migration of H_2 in a top porous layer. One may then assume ready re-equilibration with H_2O, under the thermochemical conditions of gasification, depending on oxygen partial pressure (3.1-14). Direct formation of H_2O is expected for reaction of H_2O_2 with iron oxides, as depicted for FeO. Thus, one analysed the relevant 2-phase equilibrium reactions vs pO_2, to account for changes in redox conditions and vs the $pH_2S{:}\,pH_2O$ ratio, to account for the combined effects of other gases. The corresponding reactions are shown in Table 3.1.1.

In the case of solid carbon interactions (graphite is the stable carbon form) involving metallic iron, its carbide Fe_3C and oxides (FeO, Fe_3O_4, Fe_2O_3), one may describe the corresponding 2-phase equilibrium as a function of carbon activity (Table 3.1-2).

The dependence of $pH_2S{:}\,pH_2O$ ratio and pO_2, or on a_C and pO_2 are determined numerically for given values of pO_2, being the outcomes used to plot the corresponding stability diagrams. Log scales are applied for their closer relation with corresponding chemical potential differences from the reference state $\Delta\mu O_2 = RTln(pO_2)$ and $\Delta\mu_C = RTln(a_C)$. The same approach was applied to obtain the equilibrium conditions for other iron-containing catalytic systems. The FactSage software package (version 7.3) has been used to support the development of the stability diagrams. The thermodynamic properties required for the analysis, such as standard enthalpies of formation (ΔH_i°), standard entropies (S_i°), and specific heat (cp_i), were taken from the FactPS, SGTE 2017 and FToxide databases. The thermodynamic analysis was conducted at a temperature range of 600–1000 ºC that is typical for biomass gasification processes.

Table 3.1-1: Thermodynamic predictions for interactions of H_2S in the Fe-O-S-H system.

Boundary	Reaction	Relation
Fe/FeS	$2H_2S + 2Fe + O_2 \Leftrightarrow 2FeS + 2H_2O$	$\log(p_{O_2}) = \frac{\Delta G}{2.30RT} - 2\log\left(\frac{p_{H_2S}}{p_{H_2O}}\right)$
FeO/FeS	$H_2S + FeO \Leftrightarrow FeS + H_2O$	$\log\left(\frac{p_{H_2S}}{p_{H_2O}}\right) = \frac{\Delta G}{2.30RT}$
Fe_3O_4/FeS	$6H_2S + 2Fe_3O_4 \Leftrightarrow 6FeS + 6H_2O + O_2$	$\log(p_{O_2}) = 6\log\left(\frac{p_{H_2S}}{p_{H_2O}}\right) - \frac{\Delta G}{2.30RT}$
Fe_2O_3/FeS	$4H_2S + 2Fe_2O_3 \Leftrightarrow 4FeS + 4H_2O + O_2$	$\log(p_{O_2}) = 4\log\left(\frac{p_{H_2S}}{p_{H_2O}}\right) - \frac{\Delta G}{2.30RT}$
FeO/Fe_3O_4	$6FeO + O_2 \Leftrightarrow 2Fe_3O_4$	$\log(p_{O_2}) = \frac{\Delta G}{2.30RT}$
Fe/FeO	$2Fe + O_2 \Leftrightarrow 2FeO$	$\log(p_{O_2}) = \frac{\Delta G}{2.30RT}$
Fe_3O_4/Fe_2O_3	$4Fe_3O_4 + O_2 \Leftrightarrow 6Fe_2O_3$	$\log(p_{O_2}) = \frac{\Delta G}{2.30RT}$
FeS/FeS_2	$2H_2S + 2FeS + O_2 \Leftrightarrow 2FeS_2 + 2H_2O$	$\log(p_{O_2}) = \frac{\Delta G}{2.30RT} - 2\log\left(\frac{p_{H_2S}}{p_{H_2O}}\right)$
$FeSO_4$/FeS_2	$2/3H_2S + 2/3FeSO_4 \Leftrightarrow 2/3FeS_2 + 2/3H_2O + O_2$	$\log(p_{O_2}) = 2/3\log\left(\frac{p_{H_2S}}{p_{H_2O}}\right) - \frac{\Delta G}{2.30RT}$
$FeSO_4$/FeS	$0.75H_2S + Fe_3O_4 + O_2 \Leftrightarrow Fe_2S_3 + O_2 + 0.4H_2O$	$\log(p_{O_2}) = 0.4\log\left(\frac{p_{H_2S}}{p_{H_2O}}\right) - \frac{\Delta G}{2.30RT}$
Fe/FeS	$2H_2S + 2Fe + O_2 \Leftrightarrow 2FeS + 2H_2O$	$\log(p_{O_2}) = \frac{\Delta G}{2.30RT} - 2\log\left(\frac{p_{H_2S}}{p_{H_2O}}\right)$
$FeSO_4$/$Fe_2(SO_4)_3$	$0.5H_2S + FeSO_4 + O_2 \Leftrightarrow 0.5Fe_2(SO_4)_3 + 0.5H_2O$	$\log(p_{O_2}) = \frac{\Delta G}{2.30RT} - 0.5\log\left(\frac{p_{H_2S}}{p_{H_2O}}\right)$
FeS/$FeSO_4$	$0.5FeS + O_2 \Leftrightarrow 0.5FeSO_4$	$\log(p_{O_2}) = \frac{\Delta G}{2.30RT}$
FeS_2/$FeSO_4$	$2/3FeS_2 + 2/3H_2O + O_2 \Leftrightarrow 2/3H_2S + 2/3FeSO_4$	$\log(p_{O_2}) = \frac{\Delta G}{2.30RT}$

Table 3.1-2: Thermodynamic predictions for interaction of carbon in the Fe-O-C system.

Boundary	Reaction	Relation
FeO/Fe_3C	$3FeO + C \Leftrightarrow Fe_3C + 1.5O_2$	$\log(a_C) = \frac{\Delta G}{2.30RT} + 1.5\log(p_{O_2})$
Fe_3O_4/Fe_3C	$Fe_3O_4 + C \Leftrightarrow Fe_3C + 2O_2$	$\log(a_C) = \frac{\Delta G}{2.30RT} + 2\log(p_{O_2})$
Fe/Fe_3C	$3Fe + C \Leftrightarrow Fe_3C$	$\log(a_C) = \frac{\Delta G}{2.30RT}$
Fe_2O_3/Fe_3C	$1.5Fe_2O_3 + C \Leftrightarrow Fe_3C + 2.25O_2$	$\log(a_C) = \frac{\Delta G}{2.30RT} + 2.25\log(p_{O_2})$
Fe_3O_4/Fe_2O_3	$4Fe_3O_4 + O_2 \Leftrightarrow 6Fe_2O_3$	$\log(p_{O_2}) = \frac{\Delta G}{2.30RT}$
FeO/Fe_3O_4	$6FeO + O_2 \Leftrightarrow 2Fe_3O_4$	$\log(p_{O_2}) = \frac{\Delta G}{2.30RT}$
Fe/FeO	$2Fe + O_2 \Leftrightarrow 2FeO$	$\log(p_{O_2}) = \frac{\Delta G}{2.30RT}$

3.1.2.4. Reduction Factor

Under direct gasification conditions, where air is used to partially convert the biomass feedstock, p_{O_2} will be mainly dictated by the CO:CO_2 molar ratio (Eq. 3.1-16) in the producer gas. A higher contribution of the H_2:H_2O molar ratio to the pO_2 (Eq. 3.1-17) is expected for biomass steam gasification. In this case, steam will behave as a mild oxidant and promotes both the conversion of CO and higher yield of H_2. Thus, a commonly used parameter to characterize the redox environment of a catalytic process is the reduction factor [56], which is defined as the quotient between the contents of both reductive gases and the contents of fully oxidized gases, as follows:

$$R = \frac{p_{CO} + p_{H_2}}{p_{CO_2} + p_{H_2O}} \qquad \text{Eq. 3.1-22}$$

3.1.3. Results and Discussion

3.1.3.1. Optimization of Char Conversion

Iron-based materials tend to lose activity over operation time due to carbon deposition which leads to blocking of active sites and, eventually formation of iron carbide (Fe_3C), with consequent deterioration of catalyst performance by metal dusting [57]. In the case of primary catalysts, these phenomena can be controlled to some extent by the betterment of carbon conversion, which is strongly affected by the biomass properties and the gasifier operating parameters such as residence time, bed temperature, gasification agent and equivalence ratio [58]. Although residence time cannot be directly controlled, the bed temperature and amount of oxidant are monitoring during operation and can be adjusted to guarantee thermodynamic conditions for complete carbon conversion. Note that the discrepancies between theoretical and experimental measurements decreases in the case of solid carbon [59], suggesting that the accumulation of carbon in the gasifier bed can be predicted with a reasonable accuracy.

Figure 3.1-1 shows the evolution of the gasification adiabatic temperature (T_{adb}) and minimum temperature for complete conversion of carbon ($T_{0,Char}$), as a function of the equivalence ratio (ER). The analysis was performed for atmospheric air, using model biomass compounds (cellulose and lignin) and real biomass feedstocks (eucalyptus and rape seed). The crossing of both temperatures in the diagrams allows the definition of different operating windows for the gasifier. The conversion of biomass under carbon-free conditions is achievable for zones II and III, avoiding excessive carbon precipitation on the surface of catalysts. Actually, gasification should be driven across Zone III, where autothermal conditions are guaranteed.

It is also clear from the results that the conversion of carbon is affected by the O:C molar ratio associated with the biomass feedstock. The minimum ER required to attain complete conversion of cellulose (O:C = 0.83) inside the gasifier is ER ≈ 0.085 (Figure 3.1-1a); this value increases to ER ≈ 0.33 in the case of lignin (O:C = 0.22), because the low O:C molar ratio requires additional supply of oxygen, to reach the stoichiometric ratio, and shifts the carbon-free operating windows to higher equivalence ratio. A similar behaviour is observed when eucalyptus (O:C = 0.73) and rape seed (O:C = 0.30) are considered as biomass feedstocks. Note that direct gasification of biomass is typically carried out at temperatures between 700 and 900 ºC with ER ranging from 0.15 to 0.30 (shaded area on diagrams) [3]; this means that the use of lignin-rich feedstocks will result in higher accumulation of unwanted carbon in the gasifier bed, with subsequent negative impact on gasification efficiency. Higher tar content can also be expected in biomass-derived gas, consisting of more stable compounds such as polyaromatic hydrocarbons, since lignin is more difficult to decompose compared to other biomass components (cellulose and hemicellulose) [60,61]. Accordingly, the selection of proper gasification conditions, as well as suitable biomass feedstocks, are critical to minimize the formation of unwanted products. In this regard, it should also be taken into consideration that performance indexes are in trade-off relationship. For example, increasing the ER to improve carbon conversion will reduce the cold gas efficiency, due to increasing fractions of fully oxidized gases (Eq. 3.1-13 and 3.1-14). A reasonable compromise can be obtained by driving the process through Zone 3 (Figure 3.1-1), near the intersection between T_{adb} and $T_{0,Char}$.

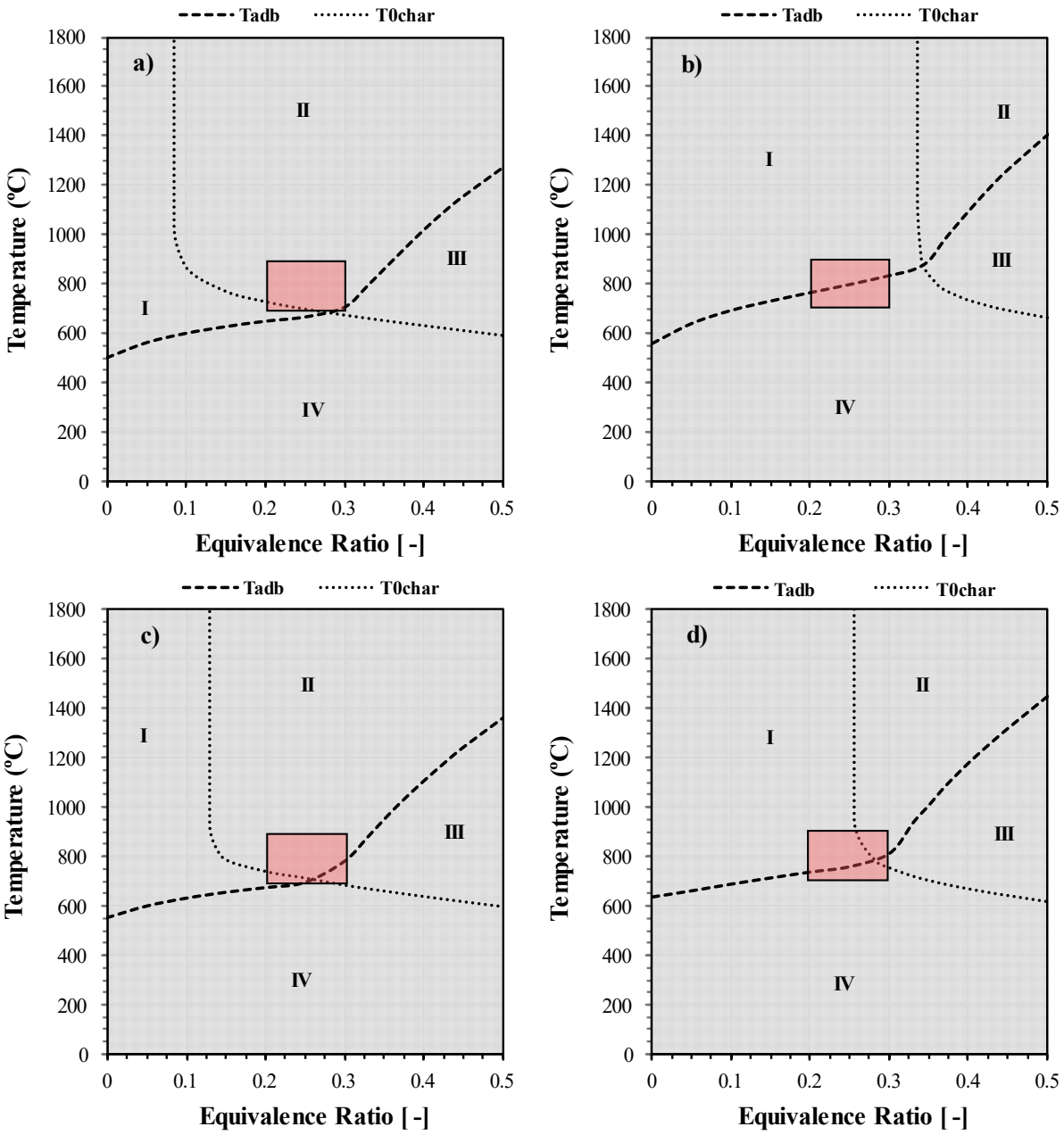

Figure 3.1-1: Thermodynamic predictions of temperature diagrams for gasification of biomass in adiabatic conditions and in char-free conditions as a function of the equivalence ratio for representative compositions of biomass: a) cellulose; b) lignin; c) eucalyptus and d) rape seed.

3.1.3.2. Catalytic Properties of Iron Species and Carbide Formation

Iron-based materials can exhibit distinct catalytic behavior during biomass gasification due to the variable oxidation state of their active sites. Previous studies have reported metallic iron (Fe) as the main active phase for tar decomposition [28,62] because of its higher ability to break C−C and C−H bonds in aromatic hydrocarbon compounds compared to the corresponding iron oxides. Still, when the purpose of the catalyst is to increase the production of H_2 through the WGS reaction, the spinel magnetite (Fe_3O_4) shows enhanced catalytic activity, which relies on the reducibility of the $Fe^{3+} \leftrightarrow Fe^{2+}$ redox couple in the octahedral sites of Fe_3O_4 [56,63]. In the case of chemical looping gasification, where transition metal oxides are applied as oxygen carriers to promote oxidation reactions, performance of Fe-based catalysts relies on cycling between oxidation to hematite (Fe_2O_3), which provides higher oxygen storage, and reduction to lower valence states in the gasifier [64,65]. Figure 3.1-2 shows thermodynamic predictions for the Fe-O-C system, which is presented vs p_{O_2} and a_C. The corresponding thermochemical conditions of biomass gasification were calculated from experimental data, and were superimposed in this diagram (symbols); this comprises gasification experiments with different gasification agents (air, steam and O_2-steam mixtures). Note that relatively small variations of pO_2 in the gasifier atmosphere can have practical consequences on the prevailing phase of Fe-based catalysts, ranging from a prevailing relevance of wustite (FeO) for gasification at the highest temperatures, and gradual shift to a distribution from magnetite (Fe_3O_4), wustite and metallic Fe at lower temperatures.

Risks of carbon deposition at relatively low temperatures (600 ºC) may be minimized by maintaining the redox conditions in the Fe_3O_4 range, which also lowers the risk of collapse by excessive volume changes on reducing magnetite to wustite (-16 %) or wustite to metallic Fe (-42 %). Fe_3O_4 shows the widest redox window, whereas the redox window of wustite (FeO) narrows with decreasing temperature [66]. The reduction factor of the producer gas (R) is shown in the secondary vertical axis and is also a useful guideline to prevent deposition of carbon, by keeping R > 1, as shown in Figure 3.1-2 for 600 ºC. Otherwise, one may design structural changes in the active sites of magnetite-based catalysts, as pointed out for WGS catalysts [56]. One may also consider the incorporation of promoters (e.g. La, Sr, Ce, ...) into iron oxides catalysts for H_2-enriched gas production, mainly when it is unfeasible to adjust R, and to seek enhanced oxygen storage [67].

Risks of carbon deposition decrease with increasing temperatures, as shown in Figure 3.1-2, at the highest temperatures. Note that the chemical potential differences $\Delta\mu_C = RTln(a_C)$ and $\Delta\mu_{O_2} = RTln(pO_2)$ which separate the average experimental conditions from onset of carbon (at a_C = 1) increase with temperature. In fact, carbon deposition is not expected at temperatures ≥ 900 ºC, even when the reducing factor is high. Onset of carbide (Fe_3C) also seems unlikely under typical conditions of gasification because the activity of carbon is shifted to sufficiently low values below the Fe/Fe_3C equilibrium. Still, the experimental conditions may reach the Fe/Fe_3C boundary at intermediate temperatures, as shown for 700 ºC in Figure 3.1-2. Thus, unconverted char in the gasifier bed may still shift the a_C to higher values, raising concerns about their impact on Fe_3C formation. The tendency to carbon precipitation with decreasing operating temperature may contribute to the formation of iron carbide (Fe_3C) resulting from interactions of carbon with metallic iron

[68]. The risk of metal dusting and their negative effects on catalytic activity during long-term operation might be minimized by alloying Fe with other elements, promoting the formation of a protective oxide layer [69]. Formation of iron carbonate ($FeCO_3$) is unlikely under biomass gasification conditions, since $FeCO_3$ is unstable at temperatures above ≈ 600 K, even in pCO_2-rich atmospheres [57].

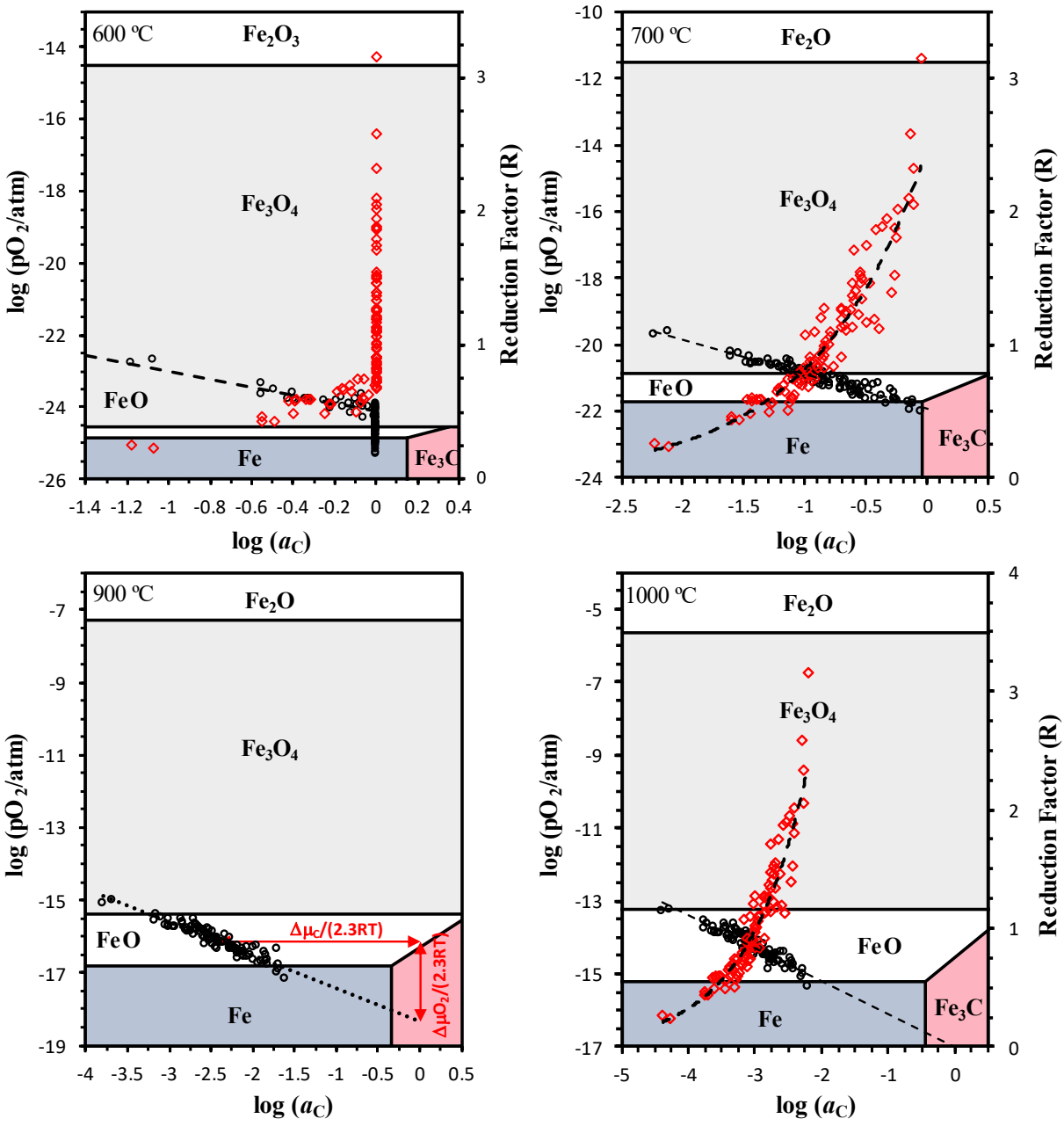

Figure 3.1-2: Thermodynamic predictions for the Fe-O-C system and superimposed calculations for a_C vs pO_2 values (black dots) associated with producer gas compositions from biomass gasification experiments with distinct feedstocks and different operating conditions. Experimental results of reducing factor (R) are shown in the secondary axis (red dots).

3.1.3.3. Tolerance of Fe-based catalysts to Sulfur Poisoning

It is well-know that sulfur impurities in biomass-derived gas is one of the major concerns associated with the use of metal-based catalysts. Though some mechanistic investigations showed that adsorption of H_2S onto iron surface can induce oxide-metal bond scission with negative impact on WGS performance [70], the influence of gas-phase sulfur on the catalytic behaviour of iron species during exposure to biomass-derived gas is still poorly understood. The poisoning effect of sulfur on the catalytic activity of iron active sites was generally explained by a simple site-blocking mechanism, leading to formation of iron sulphide (FeS) which causes a sharp drop in the rate of catalytic conversion, as well as poorer product selectivity [17].

Figure 3.1-3 shows gas-solid thermodynamic predictions for the sulfur tolerance of iron species, and superimposed calculations for $\mathrm{H_2S:H_2O}$ vs $\mathrm{pO_2}$ values associated with producer gas compositions. The phase stability diagrams are analysed for the combined effects of hydrogen sulphide and water vapour ($\mathrm{pH_2S:pH_2O}$), at fixed temperatures, for complete description of the quaternary system Fe-O-S-H. In this case, the analysis is not restricted to specific values of pH_2O, as proposed earlier to assess the sulphur tolerance of Fe-based oxygen storage materials for chemical looping combustion [71]. Dependence on ($\mathrm{pH_2S:pH_2O}$) also allows one to emphasize that operation in steam-rich conditions offer prospects to upgrade sulphur tolerance in biomass gasification, as found on comparing the average results from air gasification (black triangles in Figure 3.1-3) and results from steam gasification (green squares) or oxy-steam gasification (red diamonds). Thus, one may expect substantial gains in tolerance to H_2S when the fraction of $\mathrm{pH_2O}$ in the producer gas is high. For example, sulfur tolerance up to $\mathrm{pH_2S} \approx$ 30 ppm is expected at 800 ºC and $\log(\mathrm{pO_2}) =$ -17.8 atm if one assumes a gas composition with $\mathrm{pH_2O} = 0.10$ atm, whereas this value increases to $\mathrm{pH_2S} \approx$ 75 ppm when $\mathrm{pH_2O} = 0.25$ atm.

Figure 3.1-3 also suggests that sulphur tolerance is poorest for wustite (FeO) and may the optimized for Fe_3O_4-based catalysts, mainly in the intermediate range of $\mathrm{pO_2}$. However, this does not translate in real advantages if one considers biomass gasification catalysts, since most operation conditions fall in a narrow range of redox conditions, usually near the FeO/Fe_3O_4 borderline; this conclusion may also be extended for potential applications in chemical looping gasification, since the oxidising step requires complete conversion to Fe_2O_3, under conditions when sulphates become highly stable, even for sulphur contents below the ppm range. Note that a typical standard for atmospheric air quality is in the order of 0.2 ppm of SO_2, at room temperature, and this corresponds to similar contents of H_2S at higher temperatures [72]. Thus, one should not expect regeneration on cycling between H_2S-contaminated reducing producer gas and the oxidising step in fairly cleaner air.

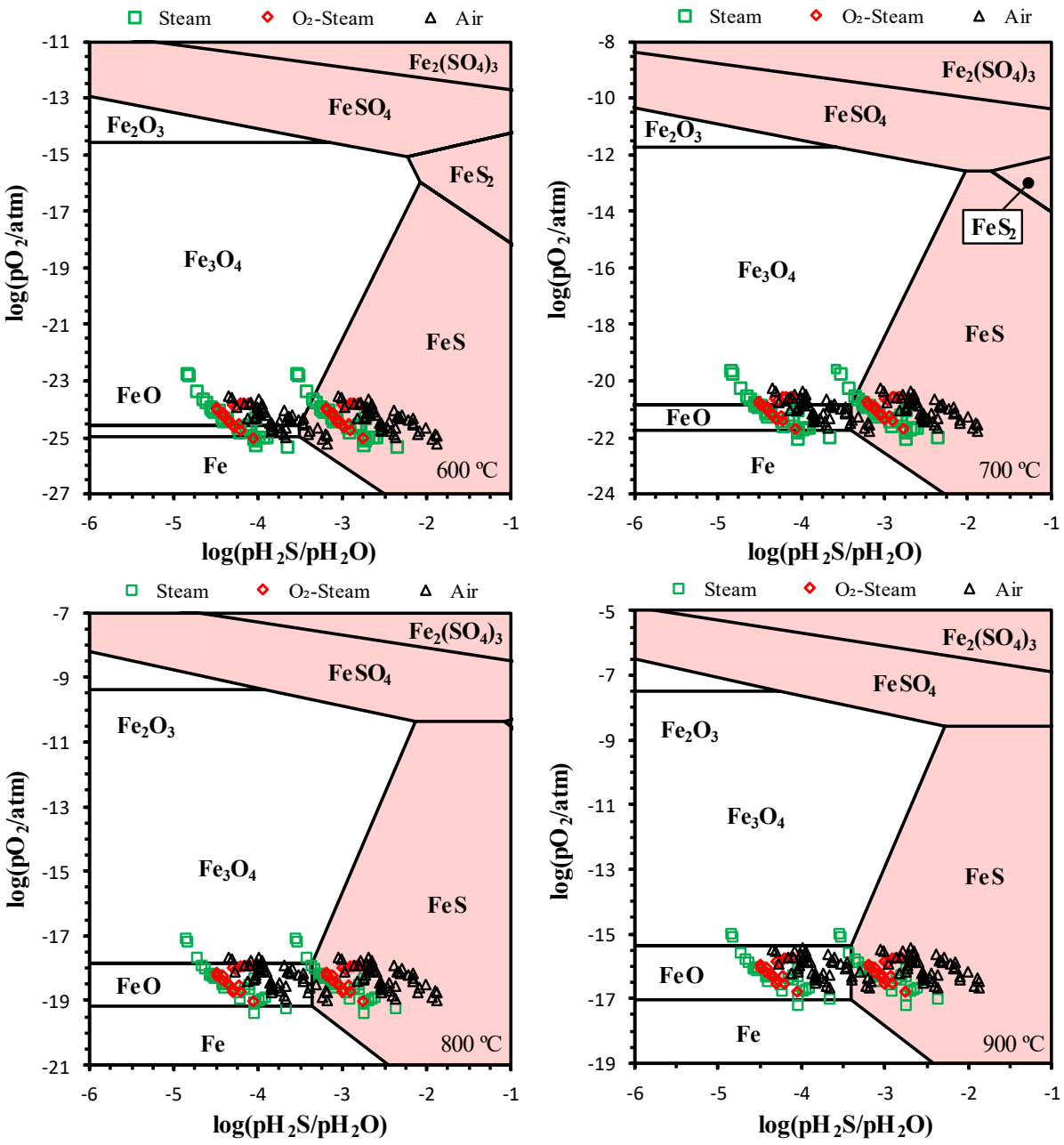

Figure 3.1-3: Thermodynamic predictions for the Fe-O-S system and superimposed calculations for H_2S:H_2O vs pO_2 values (dots) associated with producer gas compositions from biomass gasification experiments with distinct feedstocks and different operating conditions.

3.3.1.4. Fe-Ca-O-C Catalysts for H_2 Promotion and Tar Reduction

The so-called Fe/CaO catalysts in the Fe-Ca-O-C system have received special attention because of their high activity towards tar conversion and H_2 promotion during steam gasification. It is often based on the activity of Fe_3O_4 for the enhancement of WGS reaction [56], combined with the ability of calcium oxide (CaO) to favour in-situ CO_2 absorption, shifting the reaction equilibrium to higher H_2 yields. The CaO is also active in reforming reactions but is easily deactivated by biomass tar, resulting in the decline of catalytic performance [73]. Thus, significant cumulative formation of calcium carbonate ($CaCO_3$) results in the suppression of the CO_2-sorption ability, requiring regeneration cycles at high temperatures, which causes particle coarsening or agglomeration and severe pore blockage [74]. To overcome these constraints, the promotion of brownmillerite phase ($Ca_2Fe_2O_5$) is a proposed option, which is expected to retain the catalyst performance by enhancing its thermal stability and redox tolerance over multiple operation cycles.

Catalytic performance of $Ca_2Fe_2O_5$ has been ascribed to co-existence of octahedral and tetrahedral sites of the brownmillerite structure, and the lower coordination was interpreted as O-vacancies facilitating the mobility of oxygen [75]. However, this interpretation is somewhat arguable taking into account that direct measurements of oxygen permeability are lower than for ferrite perovskites and also because significant changes in oxygen stoichiometry are related mainly to reductive decomposition rather than changes in occupation of the structural tetrahedral positions of $Ca_2Fe_2O_5$ [76]. Therefore, one revised the extended phase stability of the Ca-Fe-O-C system (Figure 3.1-4) as a guideline for coexistence of $Ca_2Fe_2O_5$ with other phases, and oxygen storage or CO_2 storage ability related to onset of secondary phases, including formation of carbonate.

Ready onset of $CaCO_3$ at 600 ºC implies greater risks of CaO deactivation for $\log(pCO_2) > -0.86$ atm, due to the limited thermodynamic stability of the brownmillerite structure ($A_2B_2O_5$). Higher pO_2 values results in improved CO_2 tolerance relative to carbonation of CaO, but these gains are insufficient to guarantee $Ca_2Fe_2O_5$ stability under typical gasification gas compositions, as indicated by the experimental data points (symbols). Increasing the gasification temperature ($T \geq 700$ ºC) provides CO_2 tolerance of $Ca_2Fe_2O_5$, even in CO_2-rich atmospheres, and minimize the risks of massive decomposition of the brownmillerite structure when exposed to biomass-derived gas, in close agreement with evidence in relevant literature [77].

The wide redox range for $Ca_2Fe_2O_5$ extends from the actual range of biomass-derived gas up to oxidising conditions. In fact, the compiled information from a wide variety of experimental data on biomass gasification falls almost entirely within the thermochemical phase boundary of the brownmillerite phase, even at 700 ºC. Thus, the $Ca_2Fe_2O_5$ phase allows prospective operation under much wider redox ranges, compared to pure metallic Fe or its oxides (FeO or Fe_3O_4). Note that the Fe/FeO and FeO/Fe_3O_4 boundaries are clearly located inside the stability range of $Ca_2Fe_2O_5$. Thus, this phase delays onset of metallic Fe, and minimizes its catalytic promotion of carbon deposition, raising prospects for higher H_2 production at moderate reaction temperatures (≈ 700 ºC), enhanced gasification efficiency [78] and catalyst stability during long-term operation.

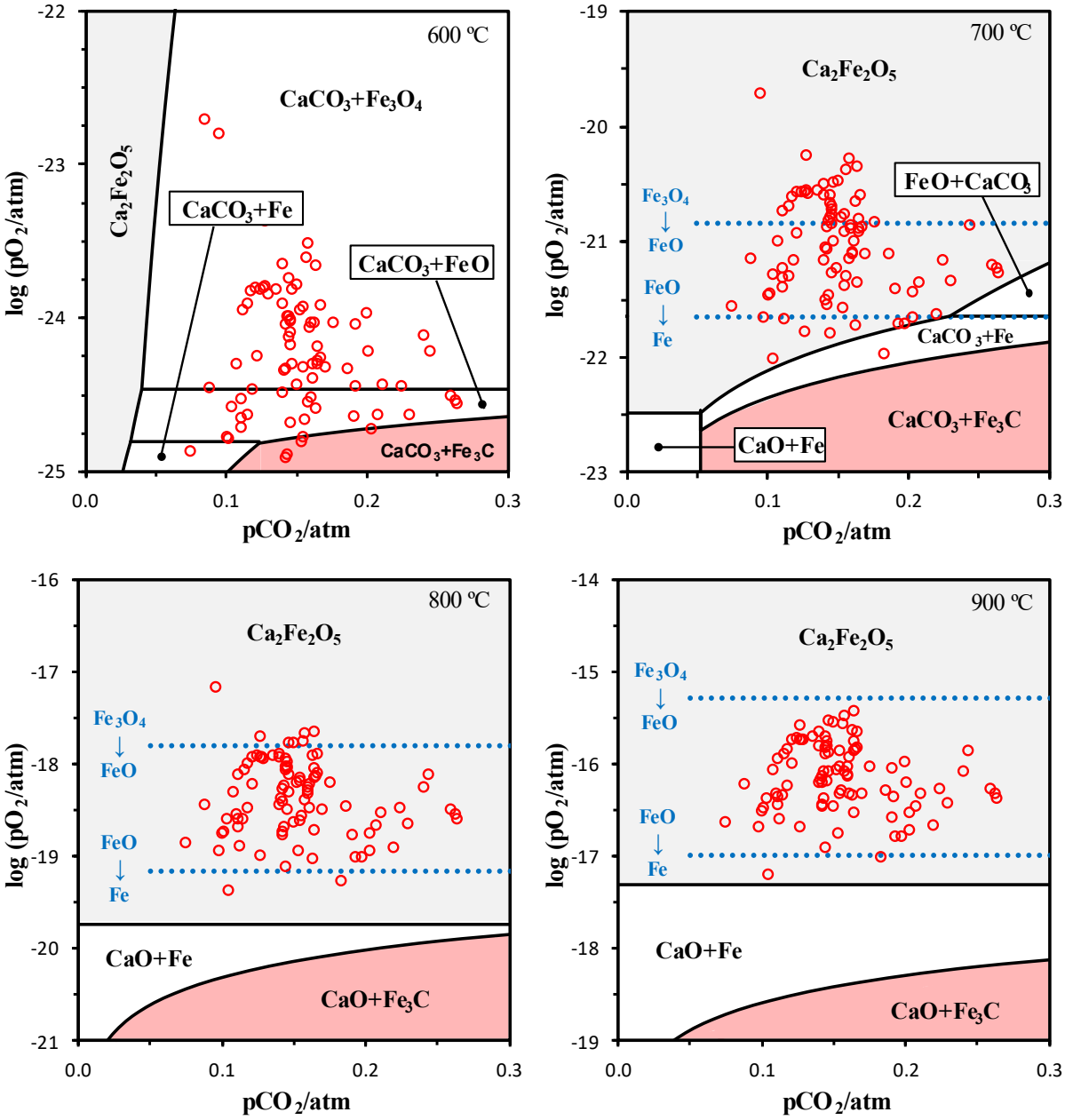

Figure 3.1-4: Phase stability diagrams for the Fe-O-Ca-C system and superimposed calculations for pCO_2 vs pO_2 values (black dots) associated with producer gas compositions from biomass gasification experiments with distinct feedstocks and different operating conditions.

3.1.3.5. Other Iron-Containing Catalytic Systems

Chemical looping gasification by means of transition metal oxides provides an alternative option for biomass thermal conversion. Biomass is partially converted by the lattice oxygen of metal oxide and steam, aiming to obtain N_2-free producer gas with a low tar content [79]. Tar conversion through oxidation reactions is also expected, namely earlier precipitation of metallic particles and their impact on C-C bonds, increasing the carbon conversion efficiency. Particular attention has been given to the application of ferrite materials such as $NiFe_2O_4$, $CuFe_2O_4$, $MnFe_2O_4$ and $CoFe_2O_4$, as oxygen carriers, [80,81]. Ni- and Co-based compounds are known for their higher catalytic activity but also raise the highest environmental concerns during operation [81], including carcinogenic effects at least in the case of Ni. Ni- and Co-based compounds are also less affordable than corresponding Mn-based compounds. Manganese ferrite is less expensive and also raises lower concerns about safety. Reduced $(Mn,Fe)_xO_y$ nanoparticles were successfully tested in biomass gasification with impact on tar conversion [14].

The reducibility of spinels and their reversibility in reduction/reoxidation cycles can be related to the high flexibility of the AB_2O_4 spinel structure which allows incorporation of diverse combinations of divalent and trivalent transition metal ions in both tetrahedral A-sites and octahedral B-sites.

Thermodynamic modelling of the Cu-Fe-O, Ni-Fe-O, Co-Fe-O and Mn-Fe-O systems (Figure 3.1-5) show that the stability windows of spinels, in terms of temperature-pO_2 ranges differ significantly but does not reach the conditions of biomass gasification (circles); these results combine a wide range of experimental data of producer gas compositions, obtained by gasification at different temperatures, using air, steam and O_2-steam mixtures as gasifying agent. Thus, one observes a significant gap between the redox conditions of producer gas and the phase boundary of ferrites in the reducing side, and the widest gap is observed for $CuFe_2O_4$.

Decomposition of ferrites under conditions of biomass gasification is a gradual multistep process, as detailed for $CoFe_2O_4$:

$$CoFe_2O_4 \rightarrow CoO + 2/3Fe_3O_4 + x_1O_2 \uparrow$$

$$\rightarrow (1+\delta)(Co,Fe) + (2/3-\delta)Fe_3O_4 + x_2O_2 \uparrow$$

$$\rightarrow (1+\delta)(Co,Fe) + (2-\delta)FeO + x_2O_2 \uparrow$$

$$\rightarrow 3(Co,Fe) + x_3O_2 \uparrow \qquad \text{Eq. 3.1-22}$$

Volume changes induced by these reduction steps are relatively high (Table 3.1-3), with corresponding risks of mechanical disintegration upon redox cycling, mainly if one considers complete reduction of both oxide components. These risks are somewhat minimized if one considers only reduction of cobalt, while retaining magnetite as the main oxide phase; this minimizes the volume changes and also maintains structural similarity between magnetite and $CoFe_2O_4$. However, this step of reduction only covers a relatively small fraction of the experimental results reported for biomass gasification, as shown in Figure 3.1-5. The effective oxygen supply in this early reduction step is also relatively small.

Table 3.1-3: Predicted relative volume on redox cycling ferrite catalysts with gradual reduction steps, based on the thermodynamic predictions shown in Figure 5.

Transformation	O_2 Loss (%)	$\Delta V/V_0$ (%)
$CuFe_2O_4 \longrightarrow Cu + 2Fe + 2O_2$	26	-54
$CuFe_2O_4 \longrightarrow Cu + 2FeO + O_2$	13	-30
$CuFe_2O_4 \longrightarrow Cu + 2/3Fe_3O_4 + 2/3O_2$	9	-19
$NiFe_2O_4 \longrightarrow Ni + 2Fe + 2O_2$	26	-54
$NiFe_2O_4 \longrightarrow Ni + 2FeO + O_2$	13	-30
$NiFe_2O_4 \longrightarrow Ni + 2/3Fe_3O_4 + 2/3O_2$	9	-19
$CoFe_2O_4 \longrightarrow Co + 2Fe + 2O_2$	26	-55
$CoFe_2O_4 \longrightarrow Co + 2FeO + O_2$	13	-32
$CoFe_2O_4 \longrightarrow Co + 2/3Fe_3O_4 + 2/3O_2$	9	-21
$MnFe_2O_4 \longrightarrow MnO + 2/3Fe_3O_4 + 2/3O_2$	2	-10
$MnFe_2O_4 \longrightarrow MnO + 2FeO + 1/2O_2$	7	-21
$MnFe_2O_4 \longrightarrow MnO + 2Fe + 3/2O_2$	20	-43
$0.5Mn_2O_3 + Fe_2O_3 \longrightarrow MnO + 2/3Fe_3O_4 + 5/6O_2$	6	-10
$0.5Mn_2O_3 + Fe_2O_3 \longrightarrow MnO + 2FeO + 5/4O_2$	17	-20
$0.5Mn_2O_3 + Fe_2O_3 \longrightarrow MnO + 2Fe + 1.75O_2$	23	-43

Decomposition of other ferrites follow a similar sequence of decomposition steps, except for the first step which only occurs at sufficiently high temperatures in the case of $NiFe_2O_4$ (> 800 ºC) and is not observed in the case of $CuFe_2O_4$. The final stage yields complete reduction to a bimetallic alloy and is slightly displaced from the corresponding conditions for reduction of pure wustite (FeO) to metallic Fe, as shown by a dotted blue line for the Ni-Fe-O and Co-Fe-O systems. In these cases, one observes a significant fraction of gasification experiments within the redox range of complete reduction; this indicates higher oxygen supply ability for chemical looping within the redox range of gasification. Thus, one cannot find a clear advantage of $CuFe_2O_4$ relative to other ferrites, in what concerns the oxygen storage ability and redox conditions for charge/discharge. Effective application of Cu-based materials as oxygen carriers should also take into consideration greater risks of microstructural ageing derived from the low melting point of metallic Cu (≈ 1085 ºC) and readier sintering. Greater risks of microstructural degradation may also be caused by contaminants such as alkaline, which may induce low melting eutectics [82]. Thus, gasification temperatures should be limited to minimized these risks [83].

Ni- and Co-based compounds also offer greater catalytic potential for a wide variety of processes, such as the production of H_2 through the promotion of WGS reaction and degradation of tar compounds [84], except possibly for their simultaneous promotion of carbon deposition.

$MnFe_2O_4$ follows a somewhat different multistep reduction, mainly because MnO is hardly reduced by fuels:

$$MnFe_2O_4 \rightarrow MnO + \left(\frac{2}{3} - \delta\right) Fe_3O_4 + x_1O_2 \uparrow$$

$$\rightarrow MnO + 2FeO + x_2O_2 \uparrow$$

$$\rightarrow 2Fe + MnO + x_2O_2 \uparrow$$

$$\rightarrow (2 + \delta)(Mn, Fe) + (1 - \delta)MnO + x_3O_2 \uparrow \qquad \text{Eq. 3.1-23}$$

In addition, $MnFe_2O_4$ shows limited stability under oxidising conditions, undergoing complete oxidation to trivalent state of both oxide components, as follows:

$$MnFe_2O_4 \overset{O_2}{\rightarrow} 1/3Mn_3O_4 + Fe_2O_3 \overset{O_2}{\rightarrow} 0.5Mn_2O_3 + Fe_2O_3 \qquad \text{Eq. 3.1-24}$$

Thus, the spinel phase is not retained in both limiting conditions of chemical looping cycles, except possibly for less common processes when a specific redox pair (e.g. CO_2/CO) may still allow an oxidation step within the intermediate redox range. For example, $MnFe_2O_4$ was proposed for a chemical looping reaction between methane and CO_2 [85].

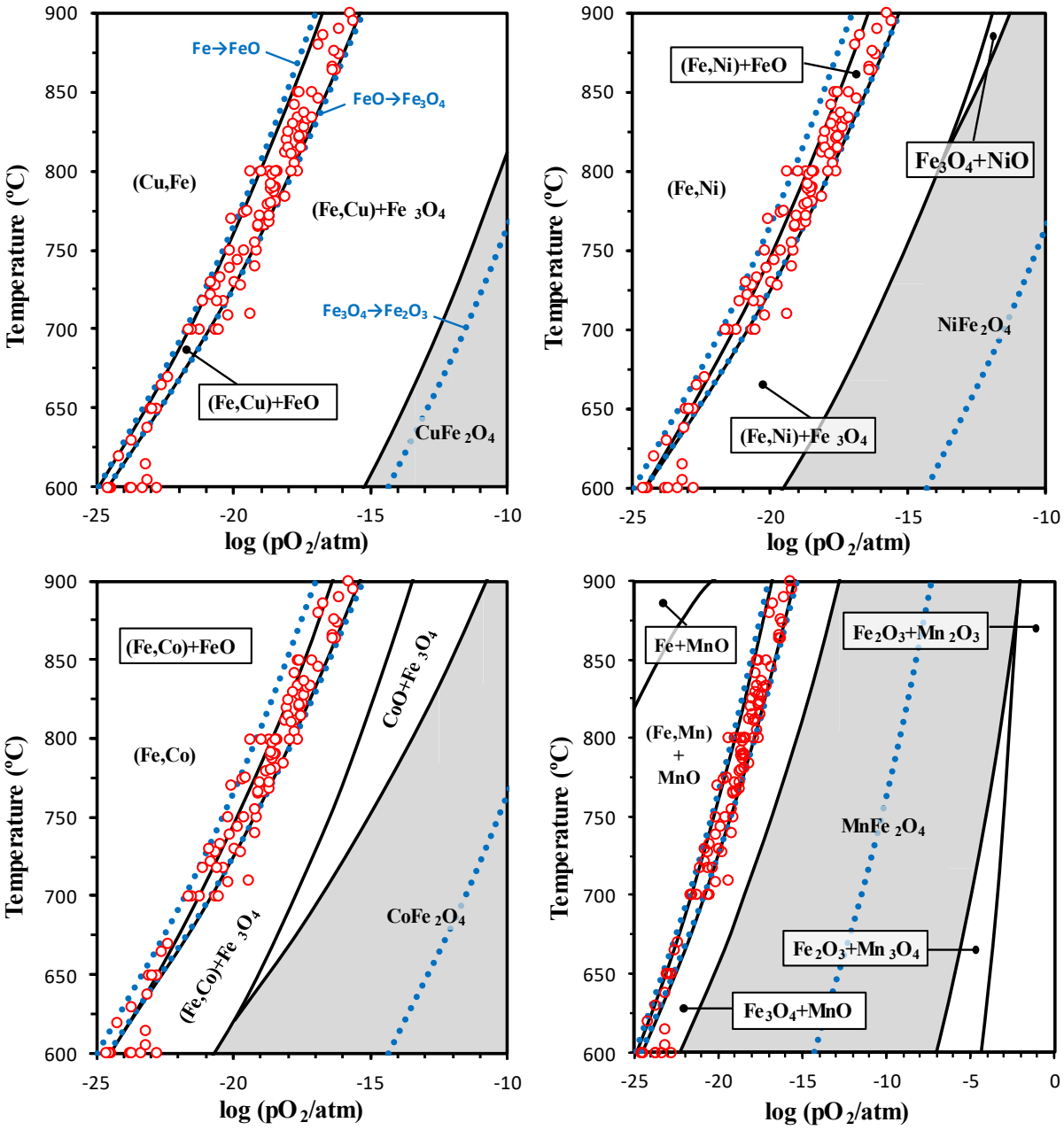

Figure 3.1-5: Phase stability diagrams for ferrite materials ($CuFe_2O_4$, $NiFe_2O_4$, $CoFe_2O_4$ and $MnFe_2O_4$) as a function of temperature and pO_2. Dotted blue lines show the redox equilibria for pure iron oxides, and red circles represent the pO_2 range associated with producer gas from experiments with distinct feedstocks and different operating conditions.

3.1.4. Conclusions

In the present study, one re-examined the thermodynamics of iron-based catalysts under the experimental conditions of biomass gasification. A combination of experimental data and thermodynamic modelling allows one to assess the dependence of catalyst performance on the thermochemical conditions of biomass gasification, by superimposing these results on phase stability diagrams of Fe-based catalysts. Thermodynamic modelling of biomass conversion showed that conversion of carbon inside the reactor is strongly dependent on the O:C molar ratio associated with the biomass feedstock and gasifier temperature. Lignin-rich feedstocks lead to higher accumulation of unconverted carbon in the gasifier bed, with expected negative impact on catalyst stability and process efficiency. This risk can be minimized with sufficient equivalence ratio to ensure operation of the gasifier at a temperature slightly above the theoretical value required for complete carbon conversion, and by selecting appropriate biomass feedstocks.

Thermodynamic predictions for the Fe-O-C system indicated that changes in the redox atmosphere of the gasifier can have significant impact on the catalytic behavior of Fe active sites. Greater redox tolerance of Fe_3O4 phase is expected at 600 ºC. At higher gasification temperatures, the catalytic promotion of H_2 through the WGS reaction requires precise control of the reduction factor (R < 1), and modification of Fe-based catalysts to retain the redox tolerance of active sites. Conversion of tars over metallic Fe is challenging because the required oxygen partial pressure may cause reoxidation.

Coke deposition and sulfur contamination of iron active sites can be assessed by suitable stability diagrams, with planar representations in pO_2 vs activity of carbon or vs the partial pressure ratio pH_2S: pH_2O in the gas atmosphere. Experimental conditions of biomass gasification were superimposed in the diagrams, and confirm that carbon precipitation on Fe surface is expected under gasification conditions at relatively low temperatures. Accumulation of unwanted carbon in the reactor bed may raise concerns about the impact of Fe_3C formation at higher temperatures. Thermodynamic modelling of the Fe-O-S system revealed that poisoning by H_2S can cause degradation of Fe-based catalysts, with tolerance limits differing according to process conditions, including significant differences between gasification with air and with steam.

The Ca-Fe-O-C system was examined as guideline for $Ca_2Fe_2O_5$; this shows ready carbonation at 600 ºC, while enhancing the stability at higher temperatures. The corresponding results suggest that thermodynamic stability of brownmillerite phase at 600 ºC requires higher redox potential in the biomass-derived gas to avoid decomposition of $Ca_2Fe_2O_5$ structure, with subsequent formation of carbonate phases. Accordingly, the in-situ application of those materials may involve higher gasification temperatures, as suggested by the wide gap between the upper and lower limits of resistance to CO_2 for the $Ca_2Fe_2O_5$ phase at temperatures above 700 ºC.

Stability phase diagrams of typical ferrites (AB_2O_4, with A = Cu, Ni, Co and Mn) were also computed to evaluate their reactivity at gasification conditions, and prospects for chemical looping. These systems provide conditions for onset of bimetallic (Fe,Cu), (Fe.Ni) or (Co,Fe) particles. Similar conditions were also observed in terms of reduction steps and corresponding oxygen supply, except for slight differences in the conditions for complete

reduction of both oxide components, and greater risks of microstructural ageing of oxygen storage materials in the Cu-Fe-O system. The Mn-Fe-O system shows a more complex sequence of reduction/oxidation steps in chemical looping.

Acknowledgments

The authors acknowledge the financial support through projects NOTARGAS (ref. POCI-01-0145-FEDER-030661) and CHARCLEAN (PCIF/GVB/0179/2017). Thanks to the Portuguese Foundation for Science and Technology (FCT) / Ministry of Science, Technology and Higher Education (MCTES) for the financial support to CESAM (UIDP/50017/2020, UIDB/50017/2020, LA/P/0094/2020), and CICECO – Aveiro Institute of Materials (UIDB/50011/ 2020, UIDP/50011/2020 & LA/P/0006/2020), through national funds. The authors also acknowledge the Portuguese Foundation for Science and Technology for providing financial support to the PhD scholarship granted to Luís Ruivo (ref. SFRH/BD/129901/2017).

References

[1] Sikarwar VS, Zhao M, Clough P, Yao J, Zhong X, Memon MZ, et al. An overview of advances in biomass gasification. Energy Environ Sci 2016;9:2939–77. https://doi.org/10.1039/c6ee00935b.

[2] Huber GW, Iborra S, Corma A. Synthesis of transportation fuels from biomass: Chemistry, catalysts, and engineering. Chem Rev 2006;106:4044–98. https://doi.org/10.1021/cr068360d.

[3] Pio DT, Tarelho LAC, Matos MAA. Characteristics of the gas produced during biomass direct gasification in an autothermal pilot-scale bubbling fluidized bed reactor. Energy 2017;120:915–28. https://doi.org/10.1016/j.energy.2016.11.145.

[4] Abu El-Rub Z, Bramer EA, Brem G. Review of catalysts for tar elimination in biomass gasification processes. Ind Eng Chem Res 2004;43:6911–9. https://doi.org/10.1021/ie0498403.

[5] Xu C, Donald J, Byambajav E, Ohtsuka Y. Recent advances in catalysts for hot-gas removal of tar and NH3 from biomass gasification. Fuel 2010. https://doi.org/10.1016/j.fuel.2010.02.014.

[6] Ruivo L, Oliveira H, Gomes H, Cruz N, Yaremchenko A, Tarelho LAC, et al. Siderite/Concrete catalysts for H2-enriched gas production from biomass steam gasification. Energy Convers Manag 2022;255:115280. https://doi.org/10.1016/j.enconman.2022.115280.

[7] Guan G, Kaewpanha M, Hao X, Abudula A. Catalytic steam reforming of biomass tar: Prospects and challenges. Renew Sustain Energy Rev 2016;58:450–61. https://doi.org/10.1016/j.rser.2015.12.316.

[8] Sutton D, Kelleher B, Ross JRH. Review of literature on catalysts for biomass gasification. Fuel Process Technol 2001;73:155–73. https://doi.org/10.1016/S0378-3820(01)00208-9.

[9] Zhang Z, Liu L, Shen B, Wu C. Preparation, modification and development of Ni-based catalysts for catalytic reforming of tar produced from biomass gasification. Renew Sustain Energy Rev 2018;94:1086–109. https://doi.org/10.1016/j.rser.2018.07.010.

[10] Shahbaz M, yusup S, Inayat A, Patrick DO, Ammar M. The influence of catalysts in biomass steam gasification and catalytic potential of coal bottom ash in biomass steam gasification: A review. Renew Sustain Energy Rev 2017. https://doi.org/10.1016/j.rser.2017.01.153.

[11] Moud PH, Andersson KJ, Lanza R, Engvall K. Equilibrium potassium coverage and its effect on a Ni tar reforming catalyst in alkali- and sulfur-laden biomass gasification gases. Appl Catal

B Environ 2016;190:137–46. https://doi.org/10.1016/j.apcatb.2016.03.007.
[12] Moud PH, Andersson KJ, Lanza R, Pettersson JBC, Engvall K. Effect of gas phase alkali species on tar reforming catalyst performance: Initial characterization and method development. Fuel 2015;154:95–106. https://doi.org/10.1016/j.fuel.2015.03.027.
[13] Zou J, Oladipo J, Fu S, Al-Rahbi A, Yang H, Wu C, et al. Hydrogen production from cellulose catalytic gasification on CeO2/Fe2O3 catalyst. Energy Convers Manag 2018;171:241–8. https://doi.org/10.1016/j.enconman.2018.05.104.
[14] Ruivo LCM, Gomes H, Lopes D V, Yaremchenko AA, Vilas-boas C, Tarelho LAC, et al. Catalytic O2-steam gasification of biomass over Fe2-xMnxO3 oxides supported on ceramic foam filters. Fuel 2022;324:124566. https://doi.org/10.1016/j.fuel.2022.124566.
[15] Gómez-barea A, Ollero P, Leckner B. Optimization of char and tar conversion in fluidized bed biomass gasifiers. Fuel 2013;103:42–52. https://doi.org/10.1016/j.fuel.2011.04.042.
[16] Tamhankar SS, Tsuchiya K, Riggs JB. Catalytic cracking of benzene on iron oxide-silica: catalyst activity and reaction mechanism. Appl Catal 1985;16:103–21. https://doi.org/10.1016/S0166-9834(00)84073-7.
[17] Arabczyk W, Moszyński D, Narkiewicz U, Pelka R, Podsiadły M. Poisoning of iron catalyst by sulfur. Catal Today 2007;124:43–8. https://doi.org/10.1016/j.cattod.2007.02.003.
[18] Puig-Arnavat M, Bruno JC, Coronas A. Review and analysis of biomass gasification models. Renew Sustain Energy Rev 2010;14:2841–51. https://doi.org/10.1016/j.rser.2010.07.030.
[19] La Villetta M, Costa M, Massarotti N. Modelling approaches to biomass gasification: A review with emphasis on the stoichiometric method. Renew Sustain Energy Rev 2017. https://doi.org/10.1016/j.rser.2017.02.027.
[20] Safarian S, Unnþórsson R, Richter C. A review of biomass gasification modelling. Renew Sustain Energy Rev 2019;110:378–91. https://doi.org/10.1016/j.rser.2019.05.003.
[21] Atikah A, Abdullah N, Ha F, Inayat A. Assessing the gasification performance of biomass : A review on biomass gasification process conditions, optimization and economic evaluation. Renew Sustain Energy Rev 2016;53:1333–47. https://doi.org/10.1016/j.rser.2015.09.030.
[22] Pio DT, Tarelho LAC. Empirical and chemical equilibrium modelling for prediction of biomass gasi fi cation products in bubbling fl uidized beds. Energy 2020;202:117654. https://doi.org/10.1016/j.energy.2020.117654.
[23] Moran MJ, Shapiro HN. Fundamentals of Engineering Thermodynamics, 5th Edition. 2006. https://doi.org/10.1038/1811028b0.
[24] Heidenreich S, Foscolo PU. New concepts in biomass gasification. Prog Energy Combust Sci 2015;46:72–95. https://doi.org/10.1016/j.pecs.2014.06.002.
[25] Zhang Q, Pastor-Pérez L, Jin W, Gu S, Reina TR. Understanding the promoter effect of Cu and Cs over highly effective B-Mo2C catalysts for the reverse water-gas shift reaction. Appl Catal B Environ 2019;244:889–98. https://doi.org/10.1016/j.apcatb.2018.12.023.
[26] Zhang Q, Pastor-Pérez L, Gu S, Reina TR. Transition metal carbides (TMCS) catalysts for gas phase CO2 upgrading reactions: A comprehensive overview. Catalysts 2020;10. https://doi.org/10.3390/catal10090955.
[27] Morales-Salvador R, Gouveia JD, Morales-García Á, Viñes F, Gomes JRB, Illas F. Carbon Capture and Usage by MXenes. ACS Catal 2021;11:11248–55. https://doi.org/10.1021/acscatal.1c02663.
[28] Nordgreen T, Nemanova V, Engvall K, Sjöström K. Iron-based materials as tar depletion catalysts in biomass gasification: Dependency on oxygen potential. Fuel 2012;95:71–8. https://doi.org/10.1016/j.fuel.2011.06.002.
[29] Lim MT, Alimuddin Z. Bubbling fluidized bed biomass gasification-Performance, process findings and energy analysis. Renew Energy 2008;33:2339–43. https://doi.org/10.1016/j.renene.2008.01.014.
[30] Li J, Liu J, Liao S, Yan R. Hydrogen-rich gas production by air-steam gasification of rice husk

using supported nano-NiO/γ-Al2O3 catalyst. Int J Hydrogen Energy 2010. https://doi.org/10.1016/j.ijhydene.2010.04.108.

[31] Di Carlo A, Borello D, Sisinni M, Savuto E, Venturini P, Bocci E, et al. Reforming of tar contained in a raw fuel gas from biomass gasification using nickel-mayenite catalyst. Int J Hydrogen Energy 2015. https://doi.org/10.1016/j.ijhydene.2015.05.128.

[32] Campoy M, Gómez-Barea A, Vidal FB, Ollero P. Air-steam gasification of biomass in a fluidised bed: Process optimisation by enriched air. Fuel Process Technol 2009;90:677–85. https://doi.org/10.1016/j.fuproc.2008.12.007.

[33] Andrés JM De, Narros A, Rodríguez ME. Air-steam gasi fi cation of sewage sludge in a bubbling bed reactor : Effect of alumina as a primary catalyst. Fuel Process Technol 2011;92:433–40. https://doi.org/10.1016/j.fuproc.2010.10.006.

[34] Nacken M, Baron G V, Heidenreich S, Rapagnà S, Orazio AD, Gallucci K, et al. New DeTar catalytic fi lter with integrated catalytic ceramic foam : Catalytic activity under model and real bio syngas conditions. Fuel Process Technol 2015;134:98–106. https://doi.org/10.1016/j.fuproc.2015.01.020.

[35] Huang BS, Chen HY, Chuang KH, Yang RX, Wey MY. Hydrogen production by biomass gasification in a fluidized-bed reactor promoted by an Fe/CaO catalyst. Int J Hydrogen Energy 2012;37:6511–8. https://doi.org/10.1016/j.ijhydene.2012.01.071.

[36] Lv P, Yuan Z, Ma L, Wu C, Chen Y, Zhu J. Hydrogen-rich gas production from biomass air and oxygen/steam gasification in a downdraft gasifier. Renew Energy 2007;32:2173–85. https://doi.org/10.1016/j.renene.2006.11.010.

[37] Turn S, Kinoshita C, Zhang Z, Ishimura D, Zhou J. An experimental investigation of hydrogen production from biomass gasification. Int J Hydrogen Energy 1998;23:641–8. https://doi.org/10.1016/s0360-3199(97)00118-3.

[38] Rapagnà S, Jand N, Kiennemann A, Foscolo PU. Steam-gasification of biomass in a fluidised-bed of olivine particles. Biomass and Bioenergy 2000;19:187–97. https://doi.org/10.1016/S0961-9534(00)00031-3.

[39] Luo S, Xiao B, Hu Z, Liu S, Guo X, He M. Hydrogen-rich gas from catalytic steam gasification of biomass in a fixed bed reactor: Influence of temperature and steam on gasification performance. Int J Hydrogen Energy 2009;34:2191–4. https://doi.org/10.1016/j.ijhydene.2008.12.075.

[40] Li XT, Grace JR, Lim CJ, Watkinson AP, Chen HP, Kim JR. Biomass gasification in a circulating fluidized bed. Biomass and Bioenergy 2004;26:171–93. https://doi.org/10.1016/S0961-9534(03)00084-9.

[41] Behainne JJR, Martinez JD. Performance analysis of an air-blown pilot fluidized bed gasifier for rice husk. Energy Sustain Dev 2014;18:75–82. https://doi.org/10.1016/j.esd.2013.11.008.

[42] Kim YD, Yang CW, Kim BJ, Kim KS, Lee JW, Moon JH, et al. Air-blown gasification of woody biomass in a bubbling fluidized bed gasifier. Appl Energy 2013;112:414–20. https://doi.org/10.1016/j.apenergy.2013.03.072.

[43] Mansaray KG, Ghaly AE, Al-Taweel AM, Hamdullahpur F, Ugursal VI. Air gasification of rice husk in a dual distributor type fluidized bed gasifier. Biomass and Bioenergy 1999;17:315–32. https://doi.org/10.1016/S0961-9534(99)00046-X.

[44] Subramanian P, Sampathrajan A, Venkatachalam P. Fluidized bed gasification of select granular biomaterials. Bioresour Technol 2011;102:1914–20. https://doi.org/10.1016/j.biortech.2010.08.022.

[45] Sarker S, Bimbela F, Sánchez JL, Nielsen HK. Characterization and pilot scale fluidized bed gasification of herbaceous biomass: A case study on alfalfa pellets. Energy Convers Manag 2015;91:451–8. https://doi.org/10.1016/j.enconman.2014.12.034.

[46] Li J, Yin Y, Zhang X, Liu J, Yan R. Hydrogen-rich gas production by steam gasification of palm oil wastes over supported tri-metallic catalyst. Int J Hydrogen Energy 2009;34:9108–15.

https://doi.org/10.1016/j.ijhydene.2009.09.030.
[47] Devi L, Ptasinski KJ, Janssen FJJG, Van Paasen SVB, Bergman PCA, Kiel JHA. Catalytic decomposition of biomass tars: Use of dolomite and untreated olivine. Renew Energy 2005;30:565–87. https://doi.org/10.1016/j.renene.2004.07.014.
[48] D'Orazio A, Rapagnà S, Foscolo PU, Gallucci K, Nacken M, Heidenreich S, et al. Gas conditioning in H2 rich syngas production by biomass steam gasification: Experimental comparison between three innovative ceramic filter candles. Int J Hydrogen Energy 2015;40:7282–90. https://doi.org/10.1016/j.ijhydene.2015.03.169.
[49] Zhang Z, Pang S. Experimental investigation of tar formation and producer gas composition in biomass steam gasification in a 100 kW dual fluidised bed gasifier. Renew Energy 2019;132:416–24. https://doi.org/10.1016/j.renene.2018.07.144.
[50] Xiao Y, Xu S, Song Y, Shan Y, Wang C, Wang G. Biomass steam gasification for hydrogen-rich gas production in a decoupled dual loop gasification system. Fuel Process Technol 2017;165:54–61. https://doi.org/10.1016/j.fuproc.2017.05.013.
[51] Barisano D, Canneto G, Nanna F, Alvino E, Pinto G, Villone A, et al. Steam/oxygen biomass gasification at pilot scale in an internally circulating bubbling fluidized bed reactor. Fuel Process Technol 2016;141:74–81. https://doi.org/10.1016/j.fuproc.2015.06.008.
[52] Zhang B, Zhang L, Yang Z, He Z. An experiment study of biomass steam gasification over NiO/Dolomite for hydrogen-rich gas production. Int J Hydrogen Energy 2017;42:76–85. https://doi.org/10.1016/j.ijhydene.2016.10.044.
[53] Kulkarni A, Baker R, Abdoulmomine N, Adhikari S. Experimental study of torrefied pine as a gasification fuel using a bubbling fluidized bed gasifier. Renew Energy 2016;93:460–8. https://doi.org/10.1016/j.renene.2016.03.006.
[54] Brandão A, Monteiro JF, Kovalevsky A V., Fagg DP, Kharton V V., Frade JR. Guidelines for improving resistance to CO2 of materials for solid state electrochemical systems. Solid State Ionics 2011;192:16–20. https://doi.org/10.1016/j.ssi.2010.02.006.
[55] Arm H, Delahay P, Hudgins C, Hügli F, Hulett L, Qureshi M. Mechanism of the Iron-Hydrogen Sulfide Reaction at Elevated Temperatures. J Electrochem Soc 1960;107:264. https://doi.org/10.1149/1.2427676.
[56] Lee DW, Lee MS, Lee JY, Kim S, Eom HJ, Moon DJ, et al. The review of Cr-free Fe-based catalysts for high-temperature water-gas shift reactions. Catal Today 2013;210:2–9. https://doi.org/10.1016/j.cattod.2012.12.012.
[57] Svoboda K, Slowinski G, Rogut J, Baxter D. Thermodynamic possibilities and constraints for pure hydrogen production by iron based chemical looping process at lower temperatures. Energy Convers Manag 2007;48:3063–73. https://doi.org/10.1016/j.enconman.2007.05.019.
[58] Devi L, Ptasinski KJ, Janssen FJJG. A review of the primary measures for tar elimination in biomass gasification processes. Biomass and Bioenergy 2003;24:125–40. https://doi.org/10.1016/S0961-9534(02)00102-2.
[59] Miccio F, Piriou B, Ruoppolo G, Chirone R. Biomass gasification in a catalytic fluidized reactor with beds of different materials. Chem Eng J 2009;154:369–74. https://doi.org/10.1016/j.cej.2009.04.002.
[60] Font Palma C. Modelling of tar formation and evolution for biomass gasification: A review. Appl Energy 2013. https://doi.org/10.1016/j.apenergy.2013.04.082.
[61] Yu H, Zhang Z, Li Z, Chen D. Characteristics of tar formation during cellulose, hemicellulose and lignin gasification. Fuel 2014. https://doi.org/10.1016/j.fuel.2013.10.080.
[62] Nordgreen T, Liliedahl T, Sjöström K. Elemental iron as a tar breakdown catalyst in conjunction with atmospheric fluidized bed gasification of biomass: A thermodynamic study. Energy and Fuels 2006;20:890–5. https://doi.org/10.1021/ef0502195.
[63] Zhu M, Wachs IE. Iron-Based Catalysts for the High-Temperature Water-Gas Shift (HT-WGS) Reaction: A Review. ACS Catal 2016;6:722–32. https://doi.org/10.1021/acscatal.5b02594.

[64] Huang Z, Zhang Y, Fu J, Yu L, Chen M, Liu S, et al. Chemical looping gasification of biomass char using iron ore as an oxygen carrier. Int J Hydrogen Energy 2016;41:17871–83. https://doi.org/10.1016/j.ijhydene.2016.07.089.

[65] Hu J, Li C, Guo Q, Dang J, Zhang Q, Lee DJ, et al. Syngas production by chemical-looping gasification of wheat straw with Fe-based oxygen carrier. Bioresour Technol 2018;263:273–9. https://doi.org/10.1016/j.biortech.2018.02.064.

[66] Pineau A, Kanari N, Gaballah I. Kinetics of reduction of iron oxides by H2. Part I: Low temperature reduction of hematite. Thermochim Acta 2006;447:89–100. https://doi.org/10.1016/j.tca.2005.10.004.

[67] Reddy GK, Gunasekara K, Boolchand P, Smirniotis PG. Cr- and Ce-doped ferrite catalysts for the high temperature water-gas shift reaction: TPR and mossbauer spectroscopic study. J Phys Chem C 2011;115:920–30. https://doi.org/10.1021/jp102959p.

[68] Zhang J, Schneider A, Inden G. Characterisation of the coke formed during metal dusting of iron in CO-H2-H2O gas mixtures. Corros Sci 2003;45:1329–41. https://doi.org/10.1016/S0010-938X(02)00251-2.

[69] Grabke HJ, Krajak R, Nava Paz JC. On the mechanism of catastrophic carburization: “metal dusting.” Corros Sci 1993;35:1141–50. https://doi.org/10.1016/0010-938X(93)90334-D.

[70] Hla SS, Duffy GJ, Morpeth LD, Cousins A, Roberts DG, Edwards JH. Investigation into the performance of a Co-Mo based sour shift catalyst using simulated coal-derived syngases. Int J Hydrogen Energy 2011;36:6638–45. https://doi.org/10.1016/j.ijhydene.2011.02.075.

[71] Pishahang M, Larring Y, Adánez J, Gayán P, Sunding M. Fe2O3–Al2O3 oxygen carrier materials for chemical looping combustion, a redox thermodynamic and thermogravimetric evaluation in the presence of H2S. J Therm Anal Calorim 2018;134:1739–48. https://doi.org/10.1007/s10973-018-7422-5.

[72] Cabibil H, Kelber JA. Oxidation of S at Fe metal and oxide surfaces and interfaces. Surf Sci 1997;373:257–74. https://doi.org/10.1016/S0039-6028(96)01169-7.

[73] Zhang X, Yang S, Xie X, Chen L, Sun L, Zhao B, et al. Stoichiometric synthesis of Fe/CaxO catalysts from tailored layered double hydroxide precursors for syngas production and tar removal in biomass gasification. J Anal Appl Pyrolysis 2016;120:371–8. https://doi.org/10.1016/j.jaap.2016.06.005.

[74] Sun Z, Chen S, Russell CK, Hu J, Rony AH, Tan G, et al. Improvement of H2-rich gas production with tar abatement from pine wood conversion over bi-functional Ca2Fe2O5 catalyst: Investigation of inner-looping redox reaction and promoting mechanisms. Appl Energy 2018;212:931–43. https://doi.org/10.1016/j.apenergy.2017.12.087.

[75] Zamboni I, Courson C, Kiennemann A. Fe-Ca interactions in Fe-based/CaO catalyst/sorbent for CO2 sorption and hydrogen production from toluene steam reforming. Appl Catal B Environ 2017;203:154–65. https://doi.org/10.1016/j.apcatb.2016.10.024.

[76] Shaula AL, Pivak Y V., Waerenborgh JC, Gaczyñski P, Yaremchenko AA, Kharton V V. Ionic conductivity of brownmillerite-type calcium ferrite under oxidizing conditions. Solid State Ionics 2006;177:2923–30. https://doi.org/10.1016/j.ssi.2006.08.030.

[77] Sun Z, Chen S, Hu J, Chen A, Rony AH, Russell CK, et al. Ca2Fe2O5: A promising oxygen carrier for CO/CH4 conversion and almost-pure H2 production with inherent CO2 capture over a two-step chemical looping hydrogen generation process. Appl Energy 2018;211:431–42. https://doi.org/10.1016/j.apenergy.2017.11.005.

[78] Zamboni I, Zimmermann Y, Kiennemann A, Courson C. Improvement of steam reforming of toluene by CO2 capture using Fe/CaO-Ca12Al14O33 bi-functional materials. Int J Hydrogen Energy 2015;40:5297–304. https://doi.org/10.1016/j.ijhydene.2015.01.065.

[79] Yin S, Shen L, Dosta M, Hartge EU, Heinrich S, Lu P, et al. Chemical Looping Gasification of a Biomass Pellet with a Manganese Ore as an Oxygen Carrier in the Fluidized Bed. Energy and Fuels 2018;32:11674–82. https://doi.org/10.1021/acs.energyfuels.8b02849.

[80] Chen J, Zhao K, Zhao Z, He F, Huang Z, Wei G. Identifying the roles of MFe 2 O 4 (M=Cu, Ba, Ni, and Co) in the chemical looping reforming of char, pyrolysis gas and tar resulting from biomass pyrolysis. Int J Hydrogen Energy 2019;44:4674–87. https://doi.org/10.1016/j.ijhydene.2018.12.216.

[81] Adanez J, Abad A, Garcia-Labiano F, Gayan P, De Diego LF. Progress in chemical-looping combustion and reforming technologies. Prog Energy Combust Sci 2012;38:215–82. https://doi.org/10.1016/j.pecs.2011.09.001.

[82] Coursol P, Pelton AD, Zamalloa M. Phase Equilibria and Thermodynamic Properties of the Cu 2O-CaO-Na2O system in equilibrium with copper. Metall Mater Trans B Process Metall Mater Process Sci 2003;34:631–8. https://doi.org/10.1007/s11663-003-0033-x.

[83] Mattisson T, Järdnäs A, Lyngfelt A. Reactivity of some metal oxides supported on alumina with alternating methane and oxygen - Application for chemical-looping combustion. Energy and Fuels 2003;17:643–51. https://doi.org/10.1021/ef020151i.

[84] Kumar P V, Short MP, Yip S, Yildiz B. High Surface Reactivity and Water Adsorption on NiFe 2 O 4 (111) Surfaces. J Phys Chem C 2013;117:5678–83.

[85] Zhou H, Yi Q, Wei G, Zhang Y, Hou Y, Huang Z, et al. Reaction performance and lattice oxygen migration of MnFe2O4 oxygen carrier in methane-carbon dioxide reaction system. Int J Hydrogen Energy 2020;45:30254–66. https://doi.org/10.1016/j.ijhydene.2020.08.103.

3.2. Iron-Based Catalyst ($Fe_{2-x}Ni_xTiO_5$) for Tar Decomposition in Biomass Gasification

L.C.M. Ruivo[1], D.T. Pio[1], A.A. Yaremchenko[1], L.A.C. Tarelho[1], J.R. Frade[1], E. Kantarelis[2], K. Engvall[2]

[1] University of Aveiro (CESAM and CICECO)

[2] KTH Royal Institute of Technology (Stockholm, Sweden)

Published in Fuel, 2021, 300, 120859.

Abstract

In this study, a novel $Fe_{2-x}Ni_xTiO_5$ catalyst for potential applications in biomass gasification gas cleaning/upgrading was investigated. The material was successfully synthesized through combined mechanical activation and microwave firing. Catalytic steam reforming was studied in a fixed bed tubular reactor, using a mixture of toluene and naphthalene as model tar compounds as well as downstream a fluidized bed gasifier. $Fe_{2-x}Ni_xTiO_5$ catalyst showed high activity in converting the model compounds at temperatures higher than 700 ºC. The catalyst exhibited a tar conversion of 78 % at 800 ºC when exposed to biomass-derived gas from a bubbling fluidized bed gasifier. Nevertheless, the catalytic activity declined with increased time on stream due to structural changes in iron active phases, caused by redox conditions of the producer gas. Furthermore, thermodynamic calculations suggest that sulfur chemisorption on the nickel surface, may also contribute to the catalyst deactivation.

Keywords: Biomass, Gasification, Tar reforming, Iron Catalysis, Ilmenite

3.2.1. Introduction

Biomass has proved to be an effective contribution to future energy demand, principally in societies with high forestry resources. Gasification is an attractive technology, involving partial oxidation of solid carbonaceous materials such as biomass, into a gas mixture, mainly composed of CO, H_2, CO_2, CH_4 and H_2O [1,2]. However, other gases and impurities are also formed during the process, which require cleaning and upgrading of the producer gas depending on the gas end-use [3]. The cleaned and upgraded producer gas can be used in applications, such as heat and power generation (e.g. boilers, gas turbines or engines), biofuel or other chemicals production [4,5].

Despite the recognized potential of biomass gasification, commercialization of industrial-scale technologies still faces technical challenges due to operational constraints, caused by the presence of tar in the producer gas, a mixture of condensable organic compounds with molecular weight greater than benzene, resulting in blocking and fouling of engines, filter and pipe plugging and catalysts deactivation in downstream processing [6,7]. In case of fluidized bed (FB) gasifiers, the tar content in the raw synthetic gas varies from 1 up to 100 $g \cdot Nm^{-3}$, requiring a upgrading meeting the required quality as a commodity for the different energy applications [8]. Several tar mitigation techniques have been the subject of intense research, such as thermal cracking or physical separation [9,10]. Although these methods have proven to be effective in tar removal, they involve significant energy penalties, decreasing both the economic and energy performance of the process. A more interesting option is based on thermocatalytic tar decomposition, wherein the catalyst converts the tar to syngas components (i.e. CO and H_2), and also may promote the

reforming reactions of light hydrocarbons, increasing the carbon conversion efficiency without severe heat penalties [11].

Research on catalytic hot gas cleaning for removal of tar has mainly been stipulated by low cost criteria and empiricism, focusing on two types of catalysts: primary catalysts used inside the gasifier; and secondary catalysts applied mainly in downstream fixed-bed reactors. The use of catalysts as primary measure for tar abatement is promising because it can take advantage of using the sensible heat of the raw producer gas, thus contributing to higher efficiency of the catalytic process and consequently reducing the needs of downstream cleaning equipment; this can be highly relevant to avoid excessive plant costs [12]. In this regard, catalytic materials can be used as a bed material or as integrated catalytic reactor within the freeboard section of the FB gasifier [8]. Particular attention has been given to the use of low-cost catalysts such as olivine, limestone, dolomite, concrete, fayalite, ashes, chars, among others [12–15]. Nevertheless, the application of catalysts as primary control measures may not be sufficient to achieve complete tar removal and the desired producer gas upgrade. In these cases, a combination of primary and secondary measures can be a promising strategy [16]. Processes utilizing secondary catalysts have mainly focused on nickel-based materials [17–19]. These catalysts generally perform better than primary catalysts in tar conversion but are expensive, requiring previous gas cleaning and catalyst regeneration. Sulfur poisoning, deactivation by carbon diffusion through Ni crystallites and sintering are other limitations [17]. Alternatively, iron-based materials have gained a growing interest due to their appreciable activity in tar conversion, low cost and environmental impact [20].

Ilmenite ($FeTiO_3$) has been proposed as low-cost iron-based material for catalytic upgrading of biomass-derived raw gas. The use of ilmenite as a catalyst for the steam reforming of biomass tar has shown that its application implied an activation step in order to increase the reduced forms of the iron-containing species on the particle surface [21]. This is in accordance with other studies, indicating that metallic iron exhibits catalytic activity in tar conversion, compared to corresponding iron oxides [20,22]. Without reduction, it is expected that ilmenite works as an oxygen carrier increasing the conversion of tar by partial oxidation [23]. Previous works demonstrated that ilmenite has a high activity for water-gas shift reactions, but its catalytic activity for tar conversion is limited and has to be improved [24,25]. This can be achieved by optimizing their structure type, since the Fe-Ti-O system can take several phases, from $FeTi_2O_5$ to Fe_2TiO_5, depending on the stoichiometry between iron and titanium oxides and oxidation state of Fe^{n+} ions [26]. Therefore, this system is very flexible for compositional, structural and redox changes, with expected impact on catalytic activity and other relevant properties for prospective catalysts with additional functionalities such as ability for magnetic separation from ashes and char or self-heating ability to sustain the required temperatures and to assist endothermic reactions in secondary cleaning methods.

The addition of secondary transition metal is another attractive approach to enhance performance. In particular, Fe-Ni bimetallic systems are comprised of two metals that are independently active and can exhibit a substantial synergistic effect [27]. The interactions between Ni and Fe atoms significantly change both the physical and chemical properties of the metals. Higher catalytic activity in reforming reactions and improved resistance against carbon deposition are attributed to the existence of the large interface between the Ni metal

and the Fe oxide surface [28]. The interaction between metal particles and the support is also believed to be critical in preventing Ni sintering [29], which is a remarkable challenge under gasification conditions. Therefore, the Ni-Fe system is considered to be promising, since it results in superior activity and stability compared to correspondent monometallic catalysts [27]. Furthermore, compared to typical Ni-based catalytic materials, the preparation cost and toxicity are reduced by Fe addition. Although Fe-Ni bimetallic systems have been investigated for various reactions, only a few studies are reported about tar reforming [15,28,30]. Moreover, these studies mainly considered the analysis of Ni-rich bimetallic systems, which highlights the need for extended activity studies focused on Fe-rich bimetallic catalysts with lower Ni loadings.

In the present study, the catalytic performance of a novel $Fe_{2-x}Ni_xTiO_5$ catalyst, with low Ni content, towards tar reforming reactions is investigated. A simple and cost-effective procedure based on mechanical activation and microwave firing for the preparation of the catalytic materials was developed, followed by detailed characterization of the produced catalysts.

3.2.2. Materials and Methods

3.2.2.1. Catalyst Preparation

$Fe_{2-x}Ni_xTiO_5$ catalysts were prepared by combining mechanical activation and solid-state synthesis with microwave firing. A ternary mixture of powder precursors composed of nickel (II) oxide (Alfa Aesar, 99% pure), iron (III) oxide (abcr, 99.8% pure) and titanium (IV) oxide (Sigma-Aldritch, 99.8% pure) are taken in stoichiometric atomic ratios (Fe+Ni):Ti = 2 and Ni:(Fe+Ni) = 0, 5 and 10%. This formulation relates to a maximum Ni loading of 2.5 wt.%, which is considerably lower than the typical Ni-based catalysts found on the literature with Ni loading ranging from 5 to 40 wt% [18]. The precursors were balled-milled for 4h at 500 rpm, using zirconia vial and zirconia grinding media in a Retsch PM 100 planetary mill, resulting in an average powder particle size below 0.6 μm. After drying the resulting mixture in an oven at 60 ºC for 12h, disk-shaped pellets (Ø 20 mm, 1.5 g) were compacted by uniaxial pressing (F = 10 kN) to enhance the interdiffusion of the cations during heat treatment. The pellets were then calcined at 1000 ºC in air for 2h by microwave irradiation, using a PYRO T480 heating system, to promote the formation of pseudobrookite crystalline phase Fe_2TiO_5 and the subsequent incorporation of NiO into the support. The temperature was increased at a rate of 15 ºC/min from room temperature up to the desired temperature. The Ni-free sample was used as a reference, and the catalysts samples were denoted by 0%Ni-FT, 5%Ni-FT and 10%Ni-FT.

3.2.2.2. Catalyst Characterization

The physicochemical properties of the catalyst were evaluated employing structural (XRD) and microstructural (SEM/TEM/EDS) studies, thermal analysis (TGA, TPO) and surface characterization (BET).

Surface area and pore characteristics of both calcined and reduced catalysts were measured via nitrogen adsorption at 77K, using a Quantachrome Nova Series instrument. Prior to measurements, the samples were degassed under vacuum at 140 ºC for 12 hours.

The surface area was analyzed using the Brunauer–Emmett–Teller (BET) method [31]. Pore volumes (vp) and average pore size (d_p) were estimated by Barrett, Joyner, and Halenda method (BJH).

Phase composition of fresh, reduced and tested catalyst was obtained by X-ray diffraction carried out on a Rigaku D/MAX-B diffractometer with monochromatic Cu Kα radiation (k = 1.5405 Å). Diffraction patterns were recorded in a step-scan mode between 10º and 80º 2θ values, with a step size of 0.02º, a counting time of 5 s per step and the receiving slit fixed at 0.2 mm. Diffraction patterns were indexed using the International Center for Diffraction Data (ICDD). The average grain size was calculated using the Scherrer formula by measuring the full width at half maximum of peaks [32].

Catalyst reducibility was investigated by thermogravimetric analysis (TGA) of calcined sample employing Setaram SetSys 16/18 analyzer (sensitivity 0.4 µg, initial sample weight ~ 470 mg). TGA was conducted in a reductive 10% H_2/N_2 gas mixture running through the catalyst with a flow of 25 $cm^3 \cdot min^{-1}$. The temperature was ramped at 5 °C·min^{-1} from room temperature up to 700 °C and then kept stable for 10 hours.

The microstructure and elemental distribution in the catalyst were investigated by scanning electron microscopy (SEM, Hitachi, TM4000 Plus) and transmission electron microscopy (TEM/STEM–JEOL 2200FS), equipped with energy dispersive X-Ray spectroscopy (EDS Oxford Inca TEM250). The analysis was performed for catalyst samples in the form of pellets (SEM) or fine powder (TEM/ EDS) deposited on a copper grid covered by a perforated carbon membrane.

The amount of carbonaceous species, accumulated on the surface of the spent catalyst, was measured by a thermo-optical system. The method is based on a volatilization of the carbon deposits and its differentiation into several fractions by means of controlled heating, with subsequent conversion by oxidation to CO_2 for detection. A sample of 100 mg was placed in a quartz reactor and exposed to 200 mL·min^{-1} of a gas mixture consisting of 4 vol.% O_2/N_2. The temperature was ramped at 10 ºC·min^{-1} from room temperature to 850 ºC and then remain stable for 5 minutes. The CO_2 concentration was continuously monitored by an on-line analyzer and the carbon deposits ($\mu g_C \cdot g_{cat}^{-1}$) were calculated based on CO_2 transient response curves.

3.2.2.3. Catalytic Activity Studies

Reforming of Model Tar Compounds

Catalyst performance was studied through steam reforming of C_7H_8 and $C_{10}H_8$ which were used as model tar compounds. The experiments were conducted at a temperature range of 700-900 ºC that is typical for reforming reactions and similar to those referred in the literature [10]. The experimental set-up consists of an atmospheric fixed bed reactor, consisting of a stainless-steel tube (length 500 mm, 15 mm ID) placed within an electric furnace. Prior to testing, the catalyst was crushed and sieved to 300-400 µm and reduced in-situ at 700 ºC in a 10%v H_2/N_2 atmosphere. The temperature was increased at a rate of 10 ºC·min^{-1} from room temperature up to the desired temperature and then kept stable for 4 hours to guarantee simultaneously the complete reduction of Ni and the partial decomposition of the Fe_2TiO_5 phase into metallic Fe and $FeTiO_3$. All the experiments were initiated following the same procedure: 15 g of catalyst supported on a layer of quartz wool

was loaded into the fixed-bed reactor and heated at 15 °C·min^{-1} in N_2 atmosphere (750 mL_{STP}·min^{-1}) to the desired reaction temperature ranging from 700 to 900 °C. Once the reaction temperature was reached, the gas flow was switched to 1000 mL_{STP}·min^{-1} (GHSV ≈ 48,500–58,500 h^{-1}) of a mixture containing ~12 ± 1.4 g·Nm^{-3} of tar model compounds (24 mol.% naphthalene and 76 mol.% toluene), 20 vol% H_2O and N_2 (balance). The reaction temperature was measured by a K-type thermocouple placed in the middle of the catalyst bed. The water and tar mixture were injected into the evaporator by an HPLC pump (Gilson 307) and carried by N_2 gas into the reactor. During testing, N_2 was feed by a mass flow controller (Bronkhorst, EL-Flow Select F-200CV). To prevent tar condensation, all lines were heated above 350 ºC. At the reactor outlet, the gas flow passed through an isopropanol and P_2O_5 trap, which collected the unconverted model tar and moisture. The composition of the dry tar-free gas was measured online using a micro-GC (Thermo Scientific, C2V-200). The tar composition of the reformed gas was determined by collecting a series of samples before and after the catalytic bed, according to the solid phase adsorption (SPA) method [33]. The collected tar samples were analyzed using a gas chromatograph (Varian CP 3800). Figure 3.2-1 shows a schematic representation of the bench scale facility used during the activity tests.

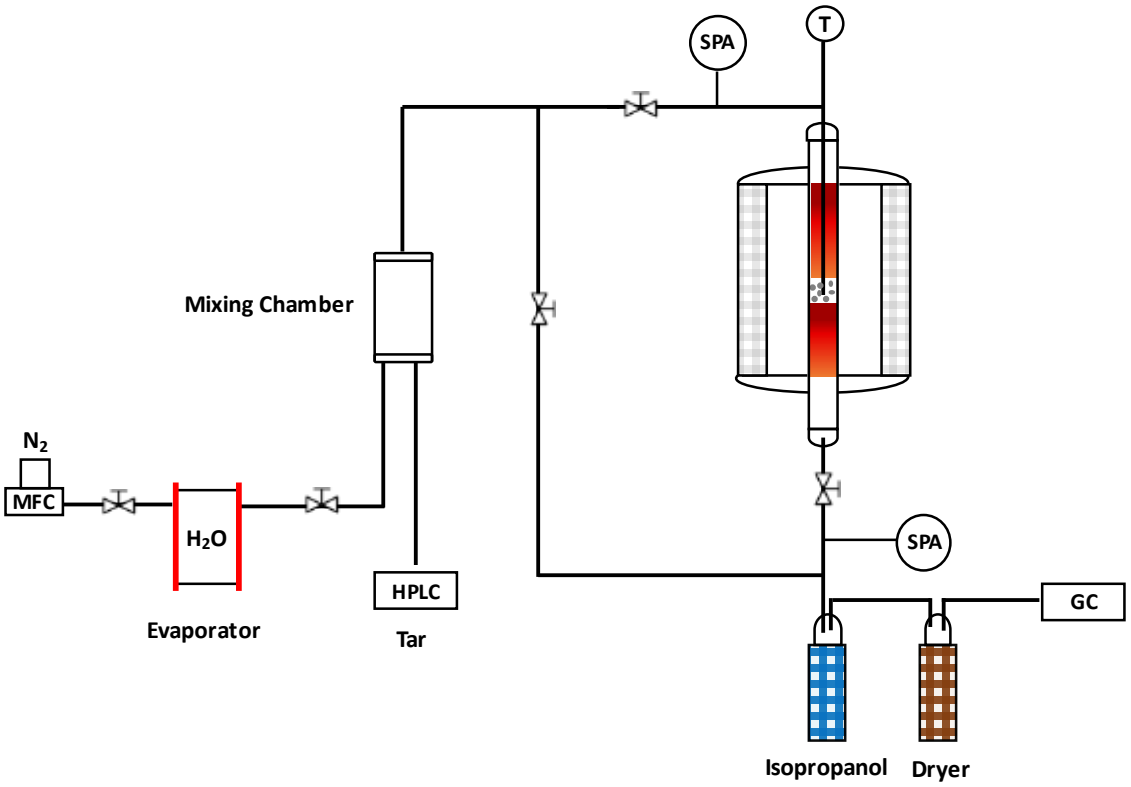

Figure 3.2-1: Schematic diagram of the experimental system used during activity tests.

The tar conversion (X_C), normalized distribution of carbon-containing species at the reactor outlet (X_i) and hydrogen yield (Y_{H_2}), were calculated based on the following Equations (3.2-1), (3.2-2) and (3.2-3), respectively:

$$X_{tar}(\%) = (1 - \frac{m_{tar}^{out}}{m_{tar}^{in}}) \times 100 \quad \text{Eq. 3.2-1}$$

$$X_i(\%) = (\frac{\dot{n}_i \cdot \gamma_i}{(7 \cdot \dot{n}_{C_7H_8} + 10 \cdot \dot{n}_{C_{10}H_8})^{in}}) \times 100 \quad \text{Eq. 3.2-2}$$

$$Y_{H_2}(\%) = (\frac{2 \cdot \dot{n}_{H_2}}{8 \cdot (\dot{n}_{C_7H_8} + \dot{n}_{C_{10}H_8})^{in} + 2 \cdot \dot{n}_{H_2O}}) \times 100 \quad \text{Eq. 3.2-3}$$

Where m_{tar} is the mass of tar, $\dot{n}_{C_7H_8}$ and $\dot{n}_{C_{10}H_8}$ are the molar flow rate (mol·min^{-1}) of toluene and naphthalene, respectively, $\dot{n}_i$ and γ_i are the partial molar flow rate and the number of carbon atoms in the component *i* at the reactor outlet (i = CO, CO_2, CH_4, C_6H_6, C_7H_8 and $C_{10}H_8$), respectively, $\dot{n}_{H_2O}$ and $\dot{n}_{H_2}$ are the steam and hydrogen molar flow rate at the entrance and reactor outlet, respectively.

Biomass-Derived Tar

The catalytic activity for decomposing tar was further tested for one of the synthesized catalysts in experiments using biomass-derived tar in a real gas produced in a 5 kW_{th} FB system. The experimental set-up is located at KTH and incorporates a bubbling fluidized bed reactor, a ceramic filter and a secondary catalytic fixed bed reactor. The gasification reactor is composed by a bottom bed of 50 mm inner diameter and 300 mm height, and a freeboard of 104 mm inner diameter and 450 mm height. Both the ceramic filter and the catalytic fixed bed reactor have a length of 700 mm and an inner diameter of 50 mm. A detailed description of the experimental facility is found in the literature [22].

The fuel fed to the gasifier was residual forest biomass from eucalyptus with a composition as presented in Table 3.2-1. The operating conditions were defined following previous studies made with eucalyptus in the gasification system [34]. Thereby, the gasification temperature and equivalence ratio (ER) were fixed at 800 ºC and 0.2, respectively. The resulting producer gas was cleaned from soot and bed particles in a ceramic filter at 800 ºC before it passed through the catalytic fixed bed reactor.

Prior to the gasification experiment, the fresh catalyst was crushed and sieved to 300-400 µm and reduced at 700 ºC in a 10%v H_2/N_2 atmosphere. Afterward, 150 g of reduced catalyst (GHSV ≈ 78,100 h^{-1}) was introduced in the secondary catalytic reactor and heated in N_2 atmosphere to the desired temperature, defined according to the results obtained in the experiments with model tar compounds. When stable gasification conditions were achieved, the biomass-derived gas was gradually replacing the N_2 in the catalytic fixed bed reactor. Subsequently, the tar concentration in the producer gas was measured both before and after the catalytic fixed bed, according to the methods described in previously. In order to eliminate possible thermal effects of the catalytic reactor on tar reduction, an experiment with inert material (alumina), under the same conditions, was performed. The obtained results were used as a reference condition in evaluating the catalytic tar conversion.

Table 3.2-1: Proximate and elemental analysis of residual forest biomass from eucalyptus.

Ultimate Analysis (wt.%, daf)	
Carbon	53.0
Hydrogen	6.3
Nitrogen	1.2
Oxygen (by difference)	38.1
Sulfur	0.003
Proximate Analysis (wt.%, db)	
Moisture	6.7
Volatile Matter	74.6
Fixed Carbon	15.5
Ash	3.2
LHV ($MJ/kg_{F,db}$)	19.4

db – dry basis, daf – dry ash free, wb – wet basis

3.2.2.4. Thermodynamic Calculations for Fe-Ti-O System

Thermodynamic calculations based on activity diagrams [35] were applied as guidelines to investigate catalyst redox stability range and their compatibility with the thermochemical conditions of biomass gasification. The method is based on the derivation of representative reactions for 2-phase equilibria and then extracting the corresponding phase stability ranges vs oxygen partial pressure (pO_2) and iron-titanium activity ratio (aFe:aTi), from the relevant mass action constant. The thermodynamic properties required for the analysis (standard enthalpies of formation, standard entropies, and specific heat capacities) were retrieved from the FACTSAGE v.5.5 software package with the FToxid database. Furthermore, thermodynamic equilibrium calculations were also performed to determine the most abundant equilibrium sulfur compounds in the producer gas, assuming all sulfur in the biomass is converted to gas-phase species. The calculations are based on the biomass composition and gasification conditions used in the experiment with biomass-derived tar.

3.2.3. Results and Discussion

3.2.3.1. Characterization of Fresh Catalysts

The XRD patterns of non-reduced catalysts are shown in Figure 3.2-2. The calcination of precursors by microwave irradiation under air atmosphere at 1000 ºC for 2h imposes suitable conditions to promote the formation of the orthorhombic iron titanate phase with space group *Pbnm* (Fe_2TiO_5; PDF card no. 01-076-1158). In case of the 10%Ni-FT sample, inspection of the XRD data showed a presence of rhombohedral nickel titanate as a secondary phase ($NiTiO_3$; PDF card no. 01-075-3757) and also a possible modification of Fe_2TiO_5 structure by nickel additions. Slight deviation towards lower angles suggests lattice expansion by incorporation of Ni^{2+} ions in the pseudobrokite structure of $(Fe,Ni)_2TiO_5$, as given by differences between unit cell parameters of samples 0%Ni-FT (*a* = 9.802 Å, *b* =

9.944 Å and *c* = 3.725 Å) and 10%Ni-FT (*a* = 9.807 Å, *b* = 10.046 Å and *c* = 3.732 Å). The comparison of calculated parameters of the orthorhombic lattice demonstrate an expansion of the unit cell along the *b*-axis for 10%Ni-FT sample in agreement with a larger ionic radius of Ni^{2+} cations with respect to that of Fe^{3+} [36].

However, the average crystallite size for samples 0%Ni-FT (41 nm) and 10%Ni-FT (43 nm) are within the experimental error and insufficient to confirm potential effects of Ni addition on average size of $(Fe,Ni)_2TiO_5$ crystallites [37].

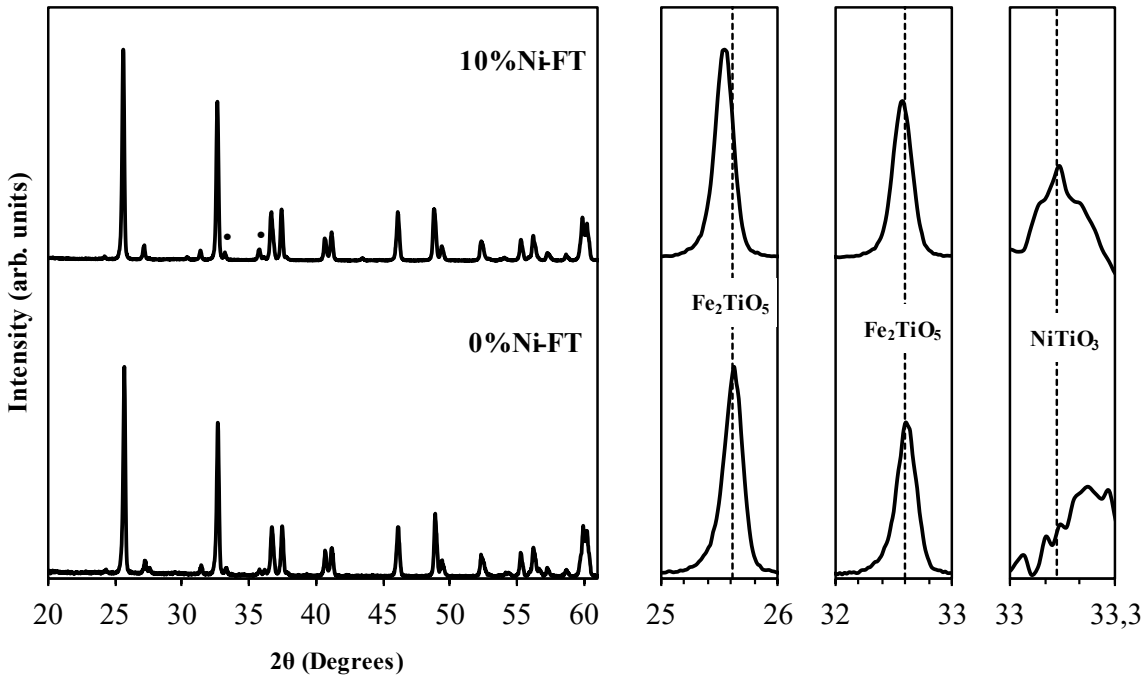

Figure 3.2-2: X-ray diffraction patterns of the calcined 0%Ni-FT and 10%Ni-FT samples, ascribed to the orthorhombic phase Fe_2TiO_5, with traces of secondary phase (● – $NiTiO_3$) for 10%Ni-FT.

In order to evaluate the reducibility of calcined 10%Ni-FT sample, isothermal TGA experiments were performed with heating rate of 5 ºC/min to an upper temperature plateau of 700 ºC (Figure 3.2-3) this shows an initial stage on heating up to about 700 ºC, yielding weight losses up to about 5.6 %, a second stage with weight losses up to about 12.7 %, and a final stage with much slower losses. The loss in the first stage is consistent with early transformation to the ilmenite phase, combined with segregation of magnetite and metallic Ni:

$$(1-x)Fe_{2-y}Ni_yTiO_5 + xNiTiO_3 \rightarrow FeTiO_3 + (0.8/3)Fe_3O_4 + 0.2Ni + \delta O_2 \qquad \text{Eq. 3.2-4}$$

where $y = (0.2-x)/(1-x)$. The corresponding losses are marked by the upper dotted line in Figure 3.2-3. Losses up to about 12.7% by the end of the second are consistent with complete reduction of the magnetite phase to metallic Fe, as marked by the lower dotted line. At last, the residual losses in the third stage may be related to deviations from the nominal stoichiometry of the ilmenite phase ($Fe_{1-x}Ti_{1+x}O_3$) and additional segregation of additional Fe, possibly combined with partial reduction of titanium ions to trivalent Ti^{3+}.

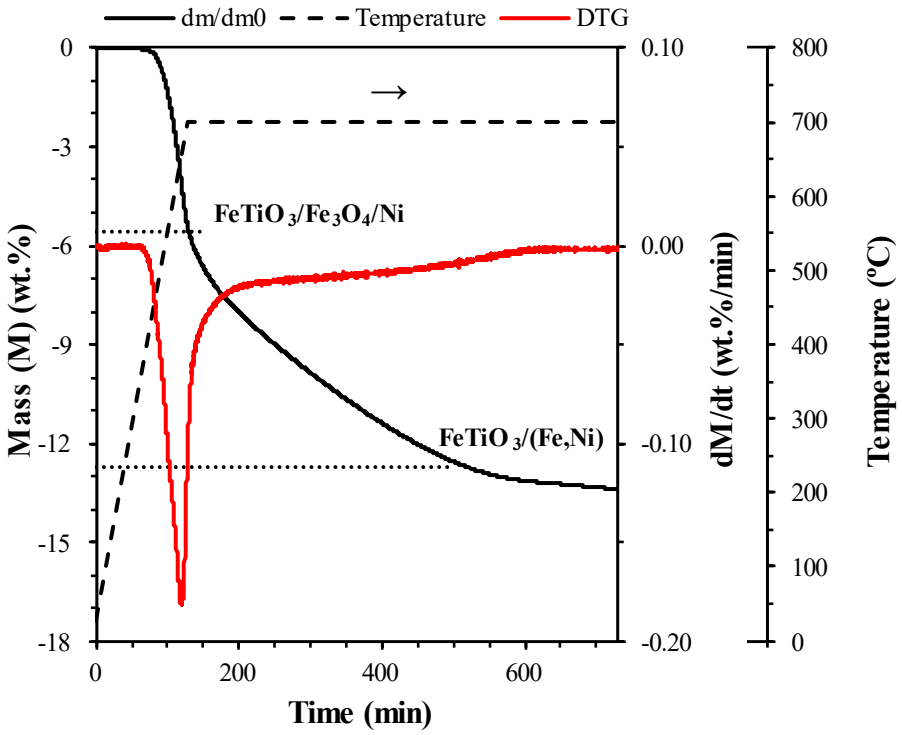

Figure 3.2-3: Relative weight change of calcined 10%Ni-FT sample in 10% H_2/N_2 atmosphere, on heating at 5 ºC/min and subsequent isothermal treatment at 700 ºC.

The expected changes at the end of stage 2 are confirmed by XRD (Figure 3.2-4), which shows co-existence of the ilmenite phase with the Fe-based phase revealed by (110) and (200) reflections of a bcc phase, at about 44.7º and 65.0º, and weaker (111) and (200) reflections of a Ni-based fcc phase, at about 43.9º and 51.1º. Still, these reflections are shifted to lower angles, relative to the expected reflections of pure Ni, at about 44.7º and 51.8, indicating lattice expansion by alloying with Fe [38]. It is expected that Fe-Ni alloys may result in better catalytic performance in reforming reactions and increased resistance against carbon deposition due to dilution effect. The addition of Fe increases the coverage of oxygen atoms on the Fe-Ni alloy surface due to its higher oxygen affinity than Ni, enhancing the suppression of carbon deposits by oxidation of the coke precursors [27].

The physical properties of the synthesized catalysts are summarized in Table 3.2-2. The catalysts surface area increased after reduction at 700 ºC in 10% H_2/N_2 atmosphere (10%Ni-FT increased from 2.98 $m^2 \cdot g^{-1}$ to 6.75 $m^2 \cdot g^{-1}$ and 0%Ni-FT from 1.63 $m^2 \cdot g^{-1}$ to 5.55 $m^2 \cdot g^{-1}$). Additionally, the total pore volume of the catalysts also increased, promoting the residual appearance of micropores (V_{micro} = 5.7 % for 0%Ni-FT and 10.1 % for 10%Ni-FT). In case of the 10%Ni-FT sample, the Ni loading increased the surface area of the reduced catalyst, which is dominated by mesopores (2-50 nm) with a total pore volume of 0.014 $cm^3 \cdot g^{-1}$. The average pore size obtained for reduced samples is 16.6 Å for 10%Ni-FT and 15.2 Å for 0%Ni-FT. A comparison of these values with the kinetic diameter of naphthalene ($\emptyset_{C_{10}H_8}$ = 6.2 Å), shows that the pore diameter of the reduced catalysts is far larger, allows for reduced Knudsen diffusion limitations and overall enhanced mass transfer properties [39].

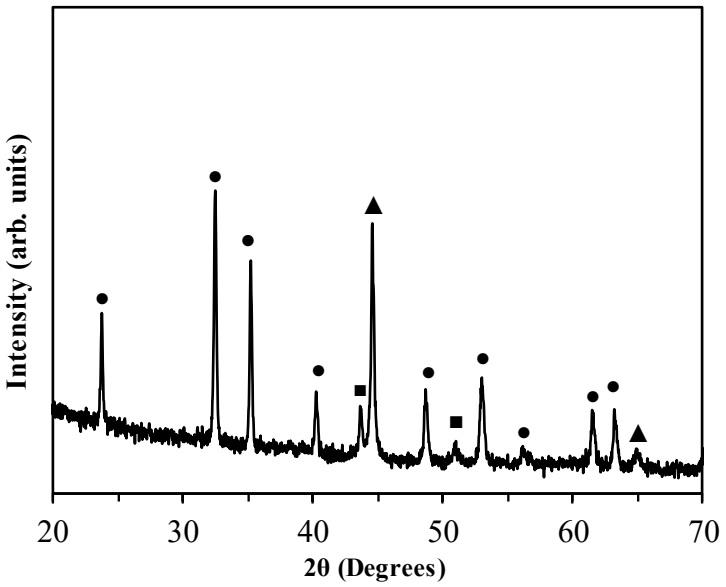

Figure 3.2-4: X-ray diffraction pattern of the calcined 10%Ni-FT sample after TGA analysis at 700 ºC in 10% H_2/N_2 atmosphere (● – $FeTiO_3$; ▲ – Fe; ■ – Fe or Fe-Ni alloy).

Table 3.2-2: Physical properties of calcined and activated catalyst samples.

Sample	BET ($m^2 \cdot g^{-1}$)	Vp (cm^3/g)	d_P (Å)	Mesopores (%)	Micropores[a] (%)	True Density (g/cm^3)
0%Ni-FT (Calcined)	1.63	0.001	11.1	100	-	
0%Ni-FT (Reduced)	5.55	0.021	15.2	94.3	5.70	4.93
10%Ni-FT (Calcined)	2.98	0.001	11.4	100	-	-
10%Ni-FT (Reduced)	6.75	0.014	16.6	89.9	10.1	5.02

a - determined by t-plot method

Scanning electron microscopy (SEM) was used to inspect relevant microstructural features of the reduced 10%Ni-FT sample (Figure 3.2-5). The results showed that catalyst particles present an irregular shape, with typical particle sizes in the micrometer range.

Catalyst reduction in H_2/N_2 promotes formation of metallic precipitates, by decomposition of Fe_2TiO_5 and $NiTiO_3$, as identified by XRD and also evidenced by TEM/EDS studies (Figure 3.2-6), revealing uniform dispersion of Fe (blue dots) and Ni (green dots) elements on the surface of catalyst; this provides potential active sites for tar conversion. Though STEM/EDS micrograph suggests potential aggregation of Ni particles, gaussian analysis indicates the presence of nano particles of various dimensions, with more than 70% below 60 nm.

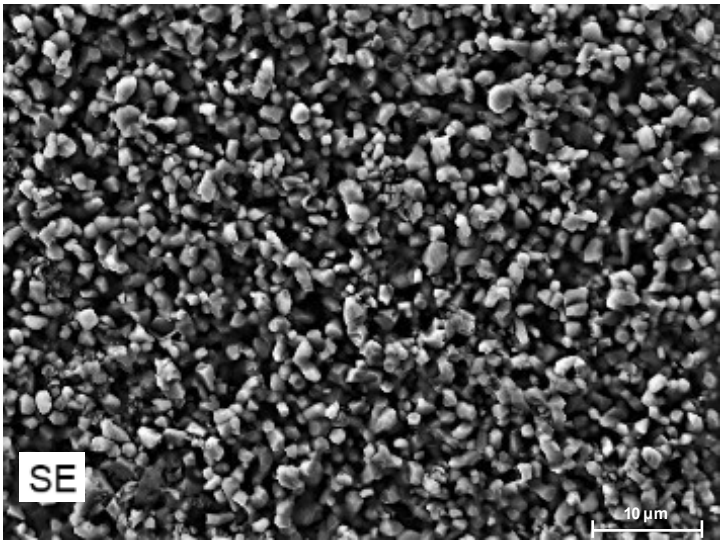

Figure 3.2-5: SEM micrograph of 10%Ni-FT sample after reduction in H_2/N_2 atmosphere.

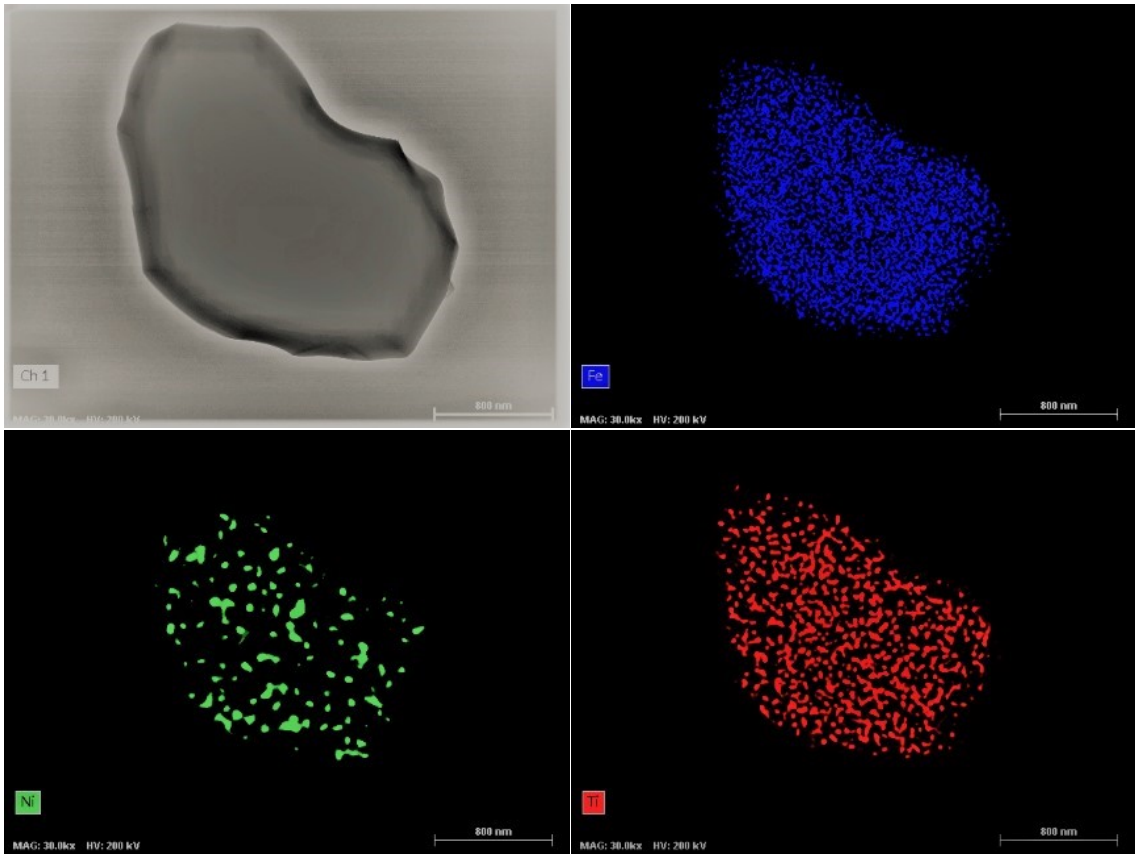

Figure 3.2-6: STEM micrograph and elemental mapping of 10%Ni-FT sample after reduction in H_2/N_2 atmosphere. The horizontal bar shows an 800 nm scale.

3.2.3.2. Catalytic Activity Studies

Conversion of Model Tar Compounds

The model tar conversion was determined after 15 min on reaction stream when steady state conditions were achieved. A reference condition experiment in the presence of inert material was also conducted for comparison purposes and to evaluate the relevance of thermal conversion of model tar compounds. The results showed a conversion of tar compounds lower than 4 wt.% in the 700–900 ºC temperature range. Thus, the contribution of thermal effects for tar decomposition was considered negligible.

Steam reforming of aromatic hydrocarbons is typically presented as the steam reforming reaction (3.2-5), whereas the water gas shift (WGS) reaction (3.2-6) contributes to increase the $H_2/(CO+CO_2)$ ratio. High temperatures are expected to promote thermal cracking of tar compounds (3.2-7) with a subsequent preponderance in the gas composition (H_2, CH_4, and others ligh C_nH_m). The non-catalytic reactions (3.2-8) and (3.2-9) can also contribute to increase the gas yield by carbon gasification.

$$C_nH_m + nH_2O \rightarrow nCO + (0.5m + n)H_2 \quad \text{Eq. 3.2-5}$$

$$CO + H_2O \leftrightarrows CO_2 + H_2 \quad \text{Eq. 3.2-6}$$

$$C_nH_m \rightarrow C_{n-x}H_{m-y} + xC + yH_2 \quad \text{Eq. 3.2-7}$$

$$C\ (s) + H_2O \rightarrow CO + H_2 \quad \text{Eq. 3.2-8}$$

$$C(s) + CO_2 \rightarrow 2CO \quad \text{Eq. 3.2-9}$$

The reforming results with model tar compounds for the different catalyst samples are presented in Table 3.2-3. As expected, the catalytic activity was enhanced at higher reaction temperature. The 10%Ni-FT sample exhibited higher catalytic activity in converting tar compounds, ranging from 42 to 99 % for temperatures between 700 and 900 ºC, respectively. In contrast, the 0%Ni-FT sample achieved the lowest tar decomposition rate and the largest shift from 3 to 70 %, after increasing temperature from 700 to 900 ºC, respectively. Under the same reaction conditions, the conversion for the 5%Ni-FT sample ranges 30 and 85 % in the same temperature range.

It is clear from the results that the tar conversion was significantly enhanced by Ni promotion, due to the presence and strong interaction of Fe-Ni intermetallic precipitates on the catalyst support. At an intermediate temperature (800 ºC), tar reduction of the 10%Ni-FT catalyst was around 88 %, which is significantly higher than achieved for the 0%Ni-FT catalyst with only 28 %. Though the metallic surface of Fe reveals a higher dissociative adsorption of steam, the activation and dissociation of C–H and C–C bonds in carbonaceous intermediates are quite higher on the surface of Ni [40], and subsequently the conversion of model tar is enhanced. However, reforming activity of Ni-FT catalysts was considerably lower at 700 ºC, which suggest deactivation by carbon deposition. It should be noted that the rate of Boudouard reaction (3.2-9) is insignificant at 700 °C [41]. Therefore, increasing the reaction temperature above 700 ºC can promote coke gasification, minimizing its deposition over the Ni-FT catalysts. This trend on tar conversion with

increasing temperature has been reported in the literature on steam reforming of tar compounds over Ni-based catalysts [42,43]. These studies also show that an increase in temperature above 700 ºC has a larger impact on the coke gasification rate than on the tar decomposition at Ni active sites. Another important aspect is the effect of Ni loading on naphthalene decomposition, since it is one of the major tar compounds and also considered the most difficult to decompose in a raw produced gas from biomass gasification [44]. At reaction temperatures above 700 ºC, a large naphthalene conversion was obtained with both the 5%Ni-FT (86-90 %) and the 10%Ni-FT (85-100 %) samples, suggesting a substantial activity towards cracking of multiple ring aromatic compounds. In contrast, the conversion of naphthalene for the 0%Ni-FT catalyst was quite lower in the same temperature range (31-33 %). The results emphasize that naphthalene catalytic decomposition is enhanced by the presence of Ni and synergetic effect of Fe-Ni alloy, showing superior activity than Ni-free species on the 0%Ni-FT catalyst. The synergetic effect of Ni-Fe alloy has been reported in previous studies on steam reforming of model tar compounds over Ni-Fe alloy catalysts [45,46], where the adsorption of aromatics or their carbonaceous derivatives on Ni-Fe bimetallic surface becomes stronger than that on monometallic Ni and Fe, promoting higher conversion rates.

Table 3.2-3: Model tar compounds conversion (%) over Ni–FT catalysts as a function of temperature. The total tar conversion means the cumulative conversion of C_7H_8 and $C_{10}H_8$ ($m_{tar} = m_{C_7H_8} + m_{C_{10}H_8}$).

	700 ºC			800 ºC			900 ºC		
Sample	Total	C_7H_8	$C_{10}H_8$	Total	C_7H_8	$C_{10}H_8$	Total	C_7H_8	$C_{10}H_8$
0%Ni-FT	2.5	2.6	2.2	27.8	27.5	30.7	70.3	87.5	32.6
5%Ni-FT	29.8	31.5	22.1	77.8	76.1	85.5	84.6	83.5	89.9
10%Ni-FT	41.5	44.0	26.9	87.9	88.4	85.1	99.0	98.8	100

Figure 3.2-7 depicts the influence of the prepared catalysts on the distribution of carbon-containing species and H_2 yield. An increase in reaction temperature led to higher contents of permanent gases. The addition of Ni reforms the formed light hydrocarbons, as the CH_4 molar fraction was not detected for 5%Ni-FT and 10%Ni-FT, whereas 0%Ni-FT yielded up to 6.0 ± 0.7 %v at 900 ºC. In addition to the partial conversion of model tar compounds to permanent gases, one finds significant changes in the fraction of remaining aromatic compounds, with emphasis on the onset of benzene formation. Comparing to the 5%Ni-FT and 10%Ni-FT catalysts, the 0%Ni-FT mainly catalyzed the conversion of toluene to benzene at reaction temperature higher than 800 ºC, which can be explained by an increased hydrodealkylation activity, a hypothesis supported by previous studies on the steam reforming of toluene with iron-based materials [47]. Moreover, other investigations also concluded that the activity of iron-based materials results in the decomposition of larger tar compounds into smaller fragments of carbon species, subsequently forming benzene [20]. Therefore, it can be concluded that the increased benzene content is a combined effect of cracking of naphthalene molecules and increased toluene dealkylation activity over Fe active sites. Though the 0%Ni-FT catalyst presented high conversion of toluene to benzene with increasing reaction temperature, further decomposition of benzene was not achieved. In case of the samples with Ni loading benzene was formed but subsequently decomposed,

showing a negligible amount for the 10%Ni-FT catalyst. The obtained results suggest that benzene adsorption is thermodynamically more favorable on the Ni surface This has been also proposed by Schravendijk et al. [48], investigating the interaction of benzene with metal surfaces in explicit water, concluding that a strong affinity of water for the hydrophilic surfaces such as Fe makes benzene adsorption thermodynamically unfavorable, while on Ni there is no preference due to the lower reactivity of steam.

On the other hand, H_2:($CO+CO_2$) ratio remains slightly higher than predicted by reforming reactions, even at 900ºC, with H_2:($CO+CO_2$) ≈ 2.13 for 10%Ni-FT and ≈ 2.74 for the 0%Ni-FT catalyst. According to thermodynamic equilibrium calculations, on combining the model tar compounds composition and assuming mass conservation only for reactions (3.2.5) and (3.2.6), one would expect values of H_2:($CO+CO_2$) ranging from 1.83 to 1.74 for the studied temperature range. The lower $CO:CO_2$ ratio achieved for the bimetallic catalysts indicates that the addition of Ni promoted the WGS reaction. The changes in the electronic and geometric properties of the homogeneous bimetallic particles induced by Ni addition promotes bridged CO adsorption on Fe-Ni surface, which enhanced WGS activity and methane conversion [49].

Analysis of the catalyst BET surface area (Figure 3.2-8) was carried out after the reforming experiments. The results show a consistent loss in surface area with increasing temperature. The 10%Ni-FT sample achieved the highest reduction rate, ranging from 0.8 to 4.2 %, while the 0%Ni-FT sample showed a minor decrease from 0.5 to 2.8 %, with increasing temperature from 700 to 900 ºC, respectively. Moreover, the 10%Ni-FT sample showed the highest loss in surface area at 900 ºC, compared to the catalyst without Ni loading. However, this phenomenon did not cause observable reduction in the catalyst performance, as can be observed from the results previously reported (see Table 3.2-3). Therefore, the decrease of surface area should be related to the catalyst support, but this subject should be further analyzed in future work.

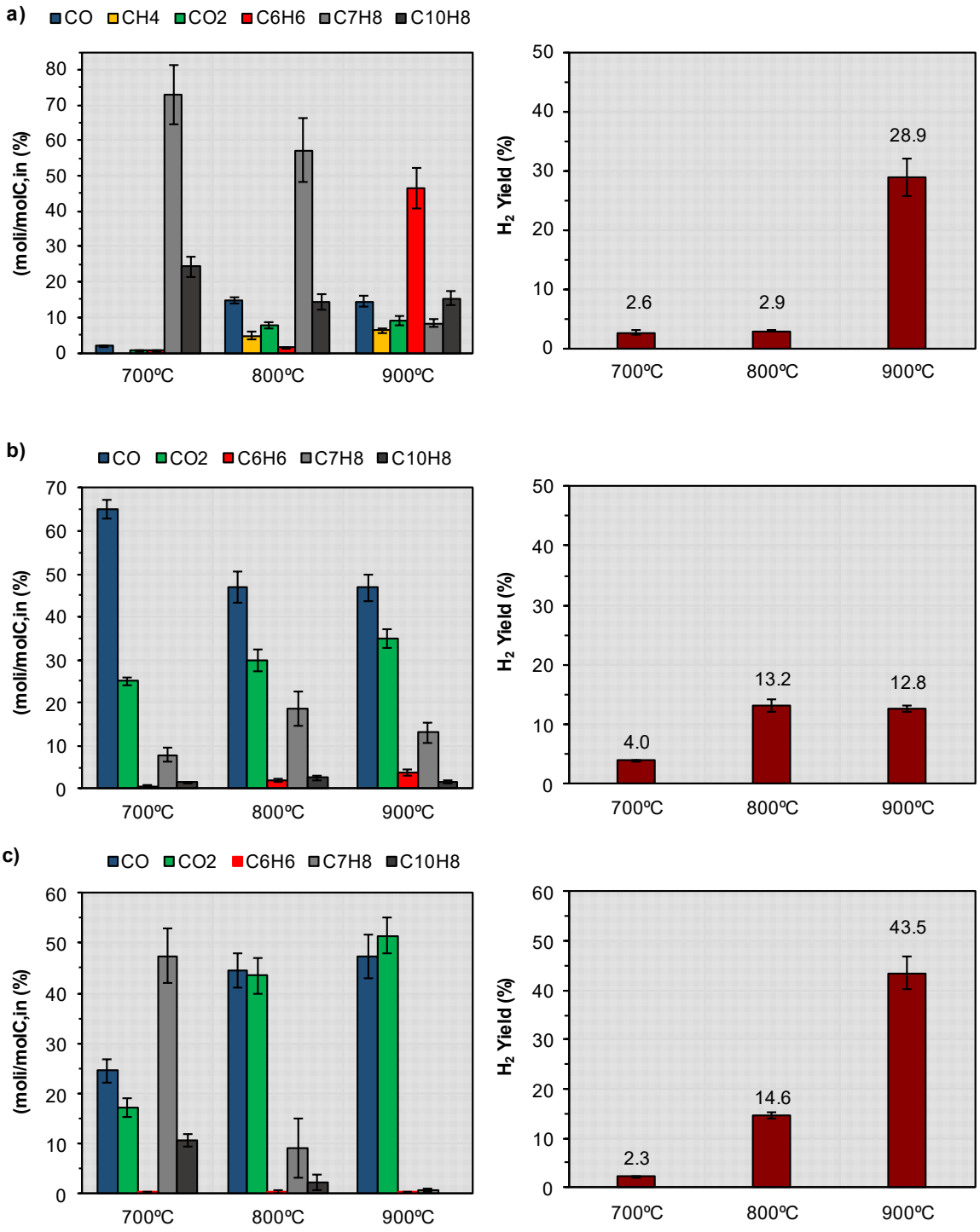

Figure 3.2-7: Normalized distribution of carbon-containing species and H_2 production at reactor outlet for a) 0%Ni-FT, b) 5%Ni-FT and c) 10%Ni-FT samples.

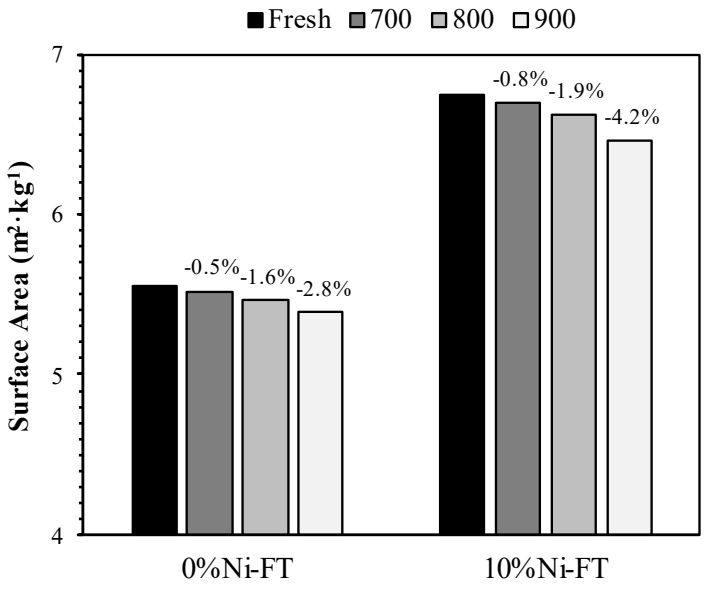

Figure 3.2-8: BET surface analysis of the Ni-FT catalysts after the tar reforming experiments at different reaction temperatures (700, 800 and 900 ºC), and its comparison with fresh catalyst.

Thermocatalytic Conversion of Biomass-Derived Tar

The thermocatalytic decomposition of biomass-derived tar was analyzed during biomass gasification experiments in a bench-scale atmospheric fluidized bed system. Based on the previous results obtained with model tar compounds and to reduce catalyst sintering, the catalytic bed temperature was fixed at 800 ºC. The experiment was performed using the 10%Ni-FT because it had the best performance on model tar compounds decomposition. The typical tar composition in the raw gas resulting from direct gasification of eucalyptus at 800 ºC is presented in Figure 3.2-9. The obtained tar concentration in the raw producer gas before the catalytic bed was 5.4 $g \cdot Nm^{-3}$. The main tar compounds (benzene not included) were toluene, naphthalene, indene and some residual hydrocarbons with higher molecular weight (C_{18+}). On N_2-free dry gas basis, the average composition of the main gas components was 30.1 ± 0.2 % CO, 30.4 ± 0.3 % CO_2, 28.5 ± 0.5 % H_2 and 11.0 ± 0.3 % of light hydrocarbons (e.g. CH_4, C_2H_2, C_2H_4 and C_2H_6).

Results from the thermocatalytic reduction of biomass-derived tar are presented in Figure 3.2-10. Compared to the reference condition (inert material), the tar reduction promoted by 10%N-FT catalyst was about 78 %. Moreover, the decrease in concentration of naphthalene and toluene was around 73 % and 42 %, respectively. The formation of Fe-Ni intermetallic alloy and the uniform dispersion of Fe^0 active sites after catalyst reduction are considered key factors for the thermocatalytic performance of 10%Ni-FT.

Nevertheless, a significant decay in tar cracking capacity of the catalyst after 120 minutes in the gas stream was observed. The formation of carbon deposits on the catalyst surface may explain the breakdown in tar decomposition, since it is a typical phenomenon of the endothermic decomposition of aromatic hydrocarbons [50]. Nevertheless, thermal programmed oxidation measurements performed for the used 10%Ni-FT catalyst (Figure 3.2-11) indicates a carbon deposit of about 1.25 $\mu gC \cdot g_{cat}^{-1}$, suggesting that carbon deposition was not the main cause of catalysts deactivation. The oxidation of carbon

deposits occurred mainly at temperatures below 450 ºC indicating the presence of alpha carbon [51]. Similar results were observed by Xie et al. [52], investigating the performance of Fe-Ni/carbon nanofibers composite as a tar breakdown catalyst in biomass gasification. The effective suppression of carbon deposits from the surface of Ni-Fe bimetallic catalysts was attributed to the higher oxygen affinity of Fe species that leads to a fast removal of carbon substrates during tar decomposition.

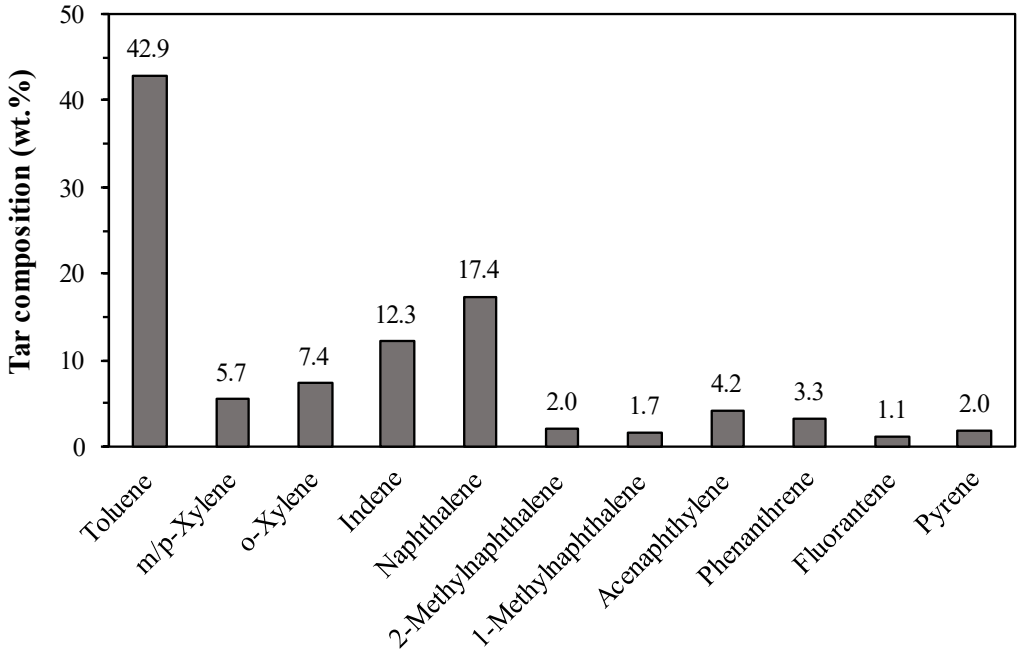

Figure 3.2-9: Tar composition (wt.%) in the producer gas before the catalytic bed, during eucalyptus gasification with ER = 0.2 and bed temperature of 800 ºC.

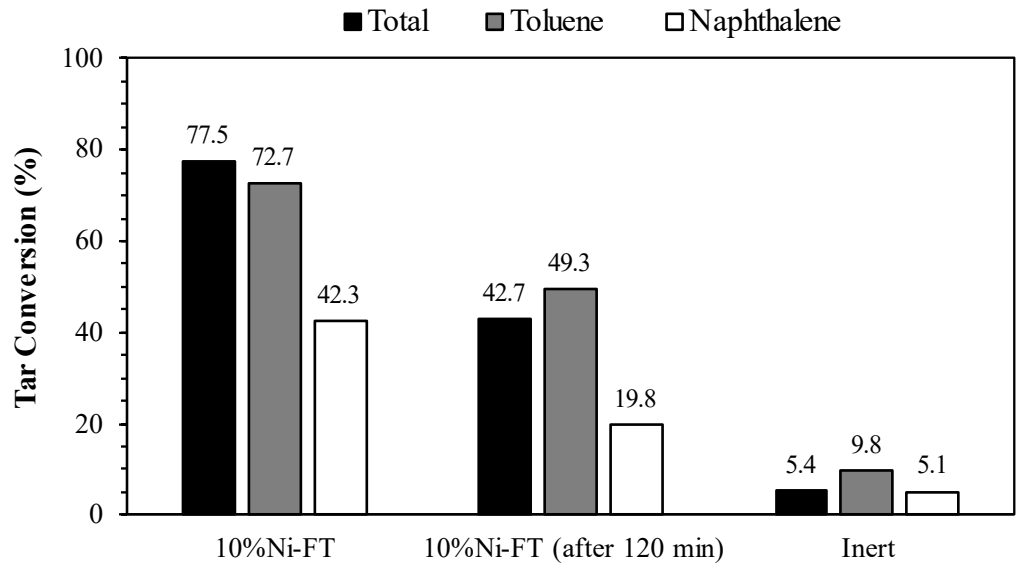

Figure 3.2-10: Thermocatalytic conversion of biomass-derived tar of the 10%Ni-FT catalyst at 800 ºC and for different time of operation. Biomass gasification at 800 ºC.

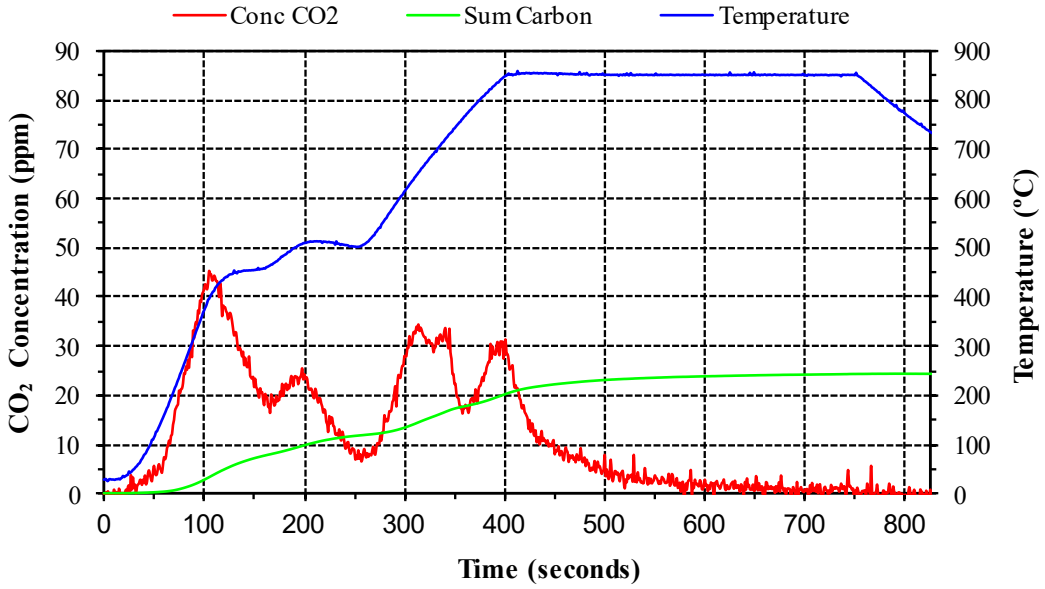

Figure 3.2-11: Thermogram of 10%Ni-FT catalyst under 4%v O_2/N_2 atmosphere, after exposed to biomass-derived tar in the catalytic reactor.

On the other hand, it is well-know that sulfur containing compounds in the biomass-derived raw gas is a severe poison for Ni active sites, even at low ppm level [53]. The poisoning effect of sulfur on Ni surface is explained by a simple site-blocking mechanism (Ni-S) that results in a substantial loss of activity toward tar molecules [54]. Gas-phase thermodynamic equilibrium calculations were performed to estimate the main sulfur compounds presented in the producer gas (Figure 3.2-12). The calculations showed that H_2S is the most abundant specie. Based on the results obtained, the actual sulfur coverage (θ_S), at the catalytic reactor temperature (800 ºC) and sulfidation conditions (H_2S/H_2 = 6.29 $\times$ 10^{-5}) would yield a sulfur coverage of ~0.90 [55] of the Ni sites (assuming no sorption on Fe sites), which is a plausible explanation for the decrease in catalyst activity.

Note that the naphthalene conversion for the 10%Ni-FT catalyst is strongly dependent of Ni promotion (see section 3.2.3.2), whereat the decrease in naphthalene conversion with increasing time on stream (from 42 to 20 %) suggest intra-particle diffusion limitations due to sulfur coverage on Ni active sites. This has been proposed by Moud et al. [56,57], investigating the combined effect of biomass-derived gas phase alkali together with sulfur on Ni/$MgAl_2O_4$ catalyst. It was observed in these studies a large drop in naphthalene conversion due to severe intra-particle diffusion limitations caused by sulfur passivation on Ni surface.

XRD is also likely to provide clearer explanations for the degradation of catalysts, based on significant structural changes. Figure 3.2-13 shows the XRD pattern of the spent 10%Ni-FT catalyst after 120 min of gasification test. Considerable phase transformation was observed, with emphasis on depletion of the main reflections of the Fe-based bcc phase, and corresponding onset of the magnetite phase. Through Fe^{2+} and Fe^{3+} species were recognized as active phases for improving WGS reaction [59,60], metallic iron (Fe^0) exhibits better activity in breaking C-C and C-H bonds, contributing to a higher tar conversion. This has been proposed by Nordgreen et al. [58], investigating the

decomposition of biomass-derived tar over iron-based catalysts. It was concluded that the oxidation of metallic iron negatively affects the tar decomposition rate. Min et al. [21], arrived at similar results from their studies on steam reforming of tar over $FeTiO_3$ catalyst. The authors stated that the reduced form of iron-containing species would have higher activity for tar decomposition than iron oxides. Therefore, one should not underestimate the catalytic role of the Fe-based bcc phase. Note also that the relative intensity of reflections ascribed to the Ni-based fcc phase is less affected, probably because it displays greater redox tolerance.

Thermodynamic calculations were performed as guidelines to evaluate potential structural changes in the catalyst imposed by thermochemical conditions of biomass-derived raw producer gas. This analysis relies on activity ratio (aFe:aTi) vs oxygen partial pressure (pO_2), to establish stability ranges for expected phases. Figure 3.2-14 shows thermodynamic predictions for redox stability of relevant phases in the Fe-Ti-O system, at 800ºC, and corresponding changes in CO_2:CO ratio in the atmosphere. In the gasification experiment performed with 10%Ni-FT catalyst, raw gas composition showed a CO_2:CO molar ratio ≈ 1, which is equivalent to $\log(pO_2/atm) \approx -18$. This indicates that redox conditions imposed by biomass-derived raw producer gas promoted the oxidation of Fe^0 species to a higher oxidative states (Fe^{2+}/Fe^{3+}), and onset of magnetite (Fe_3O_4) as demonstrated also by XRD (Figure 3.2-13). Therefore, it is possible to conclude that oxidation of Fe^0-free species on 10%Ni-FT catalyst by biomass-derived raw gas was a factor with influence in decreasing tar cracking ability with operation time. Moreover, definition of optimal conditions for application of catalyst in upgrading producer gas from biomass gasification is a critical parameter to achieve higher catalyst performance.

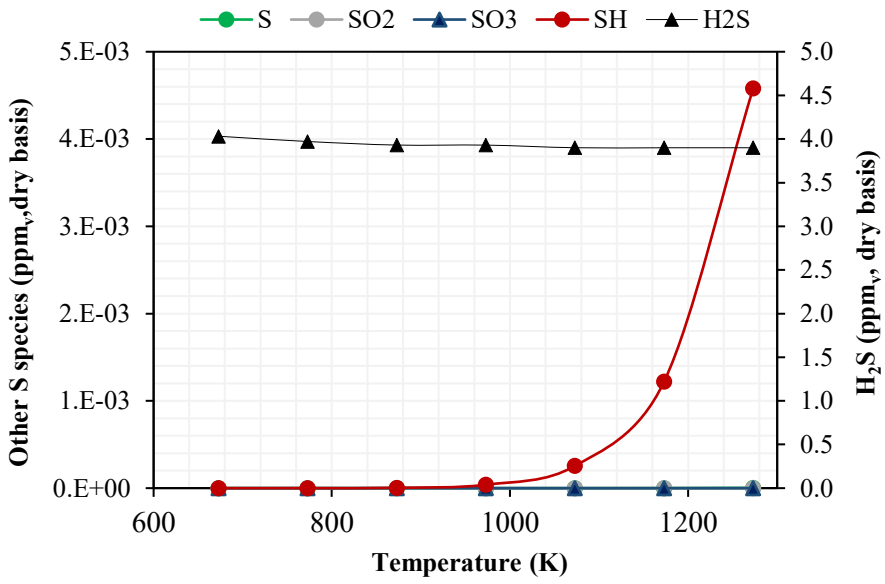

Figure 3.2-12: Thermodynamic predictions of sulfur compounds concentration in the biomass-derived raw gas as a function of temperature (ER = 0.2).

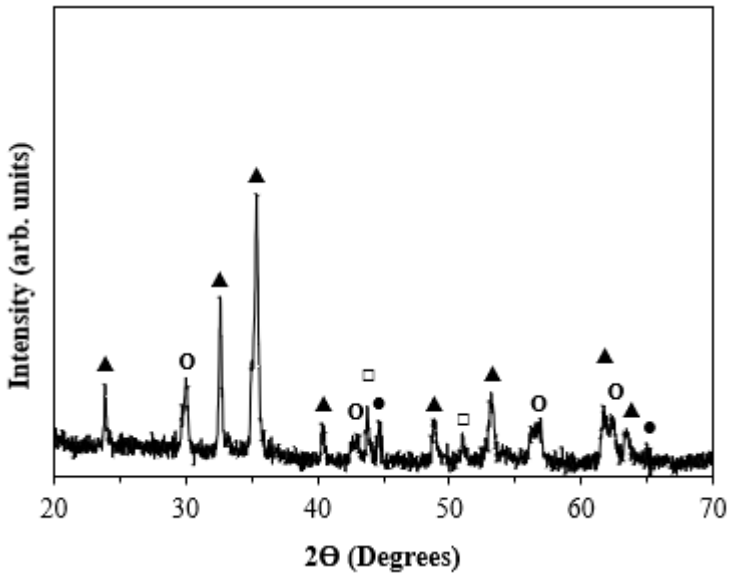

Figure 3.2-13: X-ray diffraction patterns of the 10%Ni-FT catalyst, after exposed to biomass-derived tar in the catalytic reactor at 800 ºC (● – Fe ▲ – $FeTiO_3$ o – Fe_3O_4 □ – Fe-Ni).

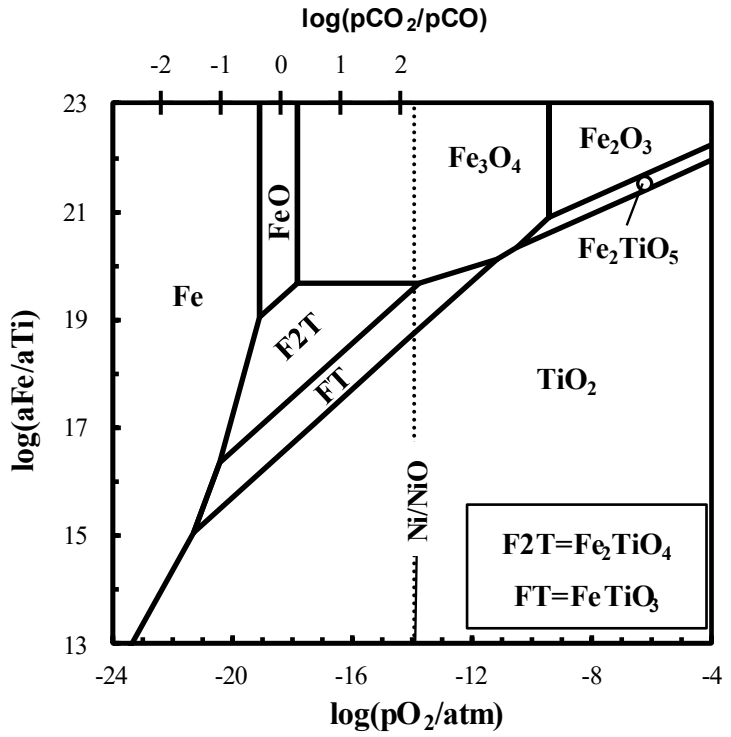

Figure 3.2-14: Thermodynamic predictions for redox stability of different phases in Fe-Ti-O and superimposed calculations for $CO:CO_2$ atmosphere at 800 ºC.

3.2.4. Conclusions

The $Fe_{2-x}Ni_xTiO_5$ catalyst was successfully prepared through combined mechanical activation and microwave firing methods. The XRD suggest a strong metal-support interaction between Ni and pseudobrokite structure. The TGA results also demonstrated a great reducibility of the catalyst at 700 ºC. A uniform distribution of active species and formation of Fe-Ni alloy were observed after reduction.

The steam reforming experiments with model tar compounds provided a high conversion for reaction temperatures above 700 ºC. The addition of Ni to the iron-based catalyst promoted both steam reforming and water-gas-shift reaction, increasing H_2 content in the producer gas. Based on the studies with model tar compounds, the 10%Ni-FT catalyst was chosen for tar cracking experiments in a fixed bed reactor, located downstream of a bench-scale fluidized bed gasifier. The results showed 78 % decrease in the total tar concentration, with 73 % decrease in toluene concentration and 42 % decrease in naphthalene concentration.

Nevertheless, during gasification experiment a significant decline in catalyst activity was observed at longer times on stream, due to structural changes in iron active sites imposed by redox conditions of biomass gasification, which need to be considered a critical parameter in enhancing catalyst performance. Moreover, thermodynamic equilibrium calculations suggest the deactivation of Ni active sites as a result of sulfur poisoning, which may also explain the decrease in catalyst activity. Future research on catalyst recovering, including a more thorough analysis of regeneration mechanisms to suppress sulphur compounds will therefore be of great interest.

Acknowledgments

The authors acknowledge the the financial support through projects NOTARGAS (ref. POCI-01-0145-FEDER-030661) and “SusPhotoSolutions - Soluções Fotovoltaicas Sustentáveis”, PO Centro 2020 (ref. CENTRO-01-0145-FEDER-000005). Thanks are due to Portuguese Foundation for Science and Technology (FCT) / Ministry of Science, Technology and Higher Education (MCTES) for the financial support to CESAM (UIDP/50017/2020+UIDB/50017/2020), and CICECO (UIDB/50011/2020 & UIDP/50011/2020), through national funds, and BRISK 2 funded by EU Horizon 2020.The authors also acknowledge the Portuguese Foundation for Science and Technology and The Navigator Company for providing financial support to the PhD scholarship granted to Daniel Pio (ref. PD/BDE/128620/2017) and Luís Ruivo (ref. SFRH/BD/129901/2017). Part of this work was carried out with the support of the Swedish Gasification Centre (SFC). Funding from the Swedish Energy Agency (34721-2), academic and industrial partners is gratefully acknowledged.

References

[1] Sikarwar VS, Zhao M, Clough P, Yao J, Zhong X, Memon MZ, et al. An overview of advances in biomass gasification. Energy Environ Sci 2016;9:2939–77. https://doi.org/10.1039/c6ee00935b.

[2] Khodaei H, Al-Abdeli YM, Guzzomi F, Yeoh GH. An overview of processes and considerations in the modelling of fixed-bed biomass combustion. Energy 2015;88:946–72. https://doi.org/10.1016/j.energy.2015.05.099.

[3] Abu El-Rub Z, Bramer EA, Brem G. Review of catalysts for tar elimination in biomass gasification processes. Ind Eng Chem Res 2004;43:6911–9. https://doi.org/10.1021/ie0498403.

[4] Huber GW, Iborra S, Corma A. Synthesis of transportation fuels from biomass: Chemistry, catalysts, and engineering. Chem Rev 2006;106:4044–98. https://doi.org/10.1021/cr068360d.

[5] Li C, Suzuki K. Tar property, analysis, reforming mechanism and model for biomass gasification-An overview. Renew Sustain Energy Rev 2009;13:594–604. https://doi.org/10.1016/j.rser.2008.01.009.

[6] Devi L, Ptasinski KJ, Janssen FJJG, Van Paasen SVB, Bergman PCA, Kiel JHA. Catalytic decomposition of biomass tars: Use of dolomite and untreated olivine. Renew Energy 2005;30:565–87. https://doi.org/10.1016/j.renene.2004.07.014.

[7] Evans RJ, Milne TA. Chemistry of Tar Formation and Maturation in the Thermochemical Conversion of Biomass. Dev Thermochem Biomass Convers 1997:803–16. https://doi.org/10.1007/978-94-009-1559-6_64.

[8] Devi L, Ptasinski KJ, Janssen FJJG. A review of the primary measures for tar elimination in biomass gasification processes. Biomass and Bioenergy 2003;24:125–40. https://doi.org/10.1016/S0961-9534(02)00102-2.

[9] Yung MM, Jablonski WS, Magrini-Bair KA. Review of catalytic conditioning of biomass-derived syngas. Energy and Fuels 2009. https://doi.org/10.1021/ef800830n.

[10] Anis S, Zainal ZA. Tar reduction in biomass producer gas via mechanical, catalytic and thermal methods: A review. Renew Sustain Energy Rev 2011. https://doi.org/10.1016/j.rser.2011.02.018.

[11] Abdoulmoumine N, Adhikari S, Kulkarni A, Chattanathan S. A review on biomass gasification syngas cleanup. Appl Energy 2015;155:294–307. https://doi.org/10.1016/j.apenergy.2015.05.095.

[12] Cortazar M, Lopez G, Alvarez J, Amutio M, Bilbao J, Olazar M. Behaviour of primary catalysts in the biomass steam gasification in a fountain confined spouted bed. Fuel 2019;253:1446–56. https://doi.org/10.1016/j.fuel.2019.05.094.

[13] Heidenreich S, Foscolo PU. New concepts in biomass gasification. Prog Energy Combust Sci 2015;46:72–95. https://doi.org/10.1016/j.pecs.2014.06.002.

[14] Pio DT, Tarelho LAC, Pinto RG, Matos MAA, Frade JR, Yaremchenko A, et al. Low-cost catalysts for in-situ improvement of producer gas quality during direct gasification of biomass. Energy 2018;165:442–54. https://doi.org/10.1016/j.energy.2018.09.119.

[15] Shahbaz M, yusup S, Inayat A, Patrick DO, Ammar M. The influence of catalysts in biomass steam gasification and catalytic potential of coal bottom ash in biomass steam gasification: A review. Renew Sustain Energy Rev 2017. https://doi.org/10.1016/j.rser.2017.01.153.

[16] Valderrama Rios ML, González AM, Lora EES, Almazán del Olmo OA. Reduction of tar generated during biomass gasification: A review. Biomass and Bioenergy 2018;108:345–70. https://doi.org/10.1016/j.biombioe.2017.12.002.

[17] Guan G, Kaewpanha M, Hao X, Abudula A. Catalytic steam reforming of biomass tar: Prospects and challenges. Renew Sustain Energy Rev 2016;58:450–61. https://doi.org/10.1016/j.rser.2015.12.316.

[18] Zhang Z, Liu L, Shen B, Wu C. Preparation, modification and development of Ni-based catalysts for catalytic reforming of tar produced from biomass gasification. Renew Sustain Energy Rev 2018;94:1086–109. https://doi.org/10.1016/j.rser.2018.07.010.

[19] Sutton D, Kelleher B, Ross JRH. Review of literature on catalysts for biomass gasification. Fuel Process Technol 2001;73:155–73. https://doi.org/10.1016/S0378-3820(01)00208-9.

[20] Nordgreen T, Liliedahl T, Sjöström K. Metallic iron as a tar breakdown catalyst related to atmospheric, fluidised bed gasification of biomass. Fuel 2006;85:689–94.

https://doi.org/10.1016/j.fuel.2005.08.026.
[21] Min Z, Asadullah M, Yimsiri P, Zhang S, Wu H, Li CZ. Catalytic reforming of tar during gasification. Part I. Steam reforming of biomass tar using ilmenite as a catalyst. Fuel 2011;90:1847–54. https://doi.org/10.1016/j.fuel.2010.12.039.
[22] Nordgreen T, Liliedahl T, Sjöström K. Elemental iron as a tar breakdown catalyst in conjunction with atmospheric fluidized bed gasification of biomass: A thermodynamic study. Energy and Fuels 2006;20:890–5. https://doi.org/10.1021/ef0502195.
[23] Leion H, Lyngfelt A, Johansson M, Jerndal E, Mattisson T. The use of ilmenite as an oxygen carrier in chemical-looping combustion. Chem Eng Res Des 2008;86:1017–26. https://doi.org/10.1016/j.cherd.2008.03.019.
[24] Lind F, Berguerand N, Seemann M, Thunman H. Ilmenite and nickel as catalysts for upgrading of raw gas derived from biomass gasification. Energy and Fuels 2013;27:997–1007. https://doi.org/10.1021/ef302091w.
[25] Lind F, Seemann M, Thunman H. Continuous catalytic tar reforming of biomass derived raw gas with simultaneous catalyst regeneration. Ind Eng Chem Res 2011;50:11553–62. https://doi.org/10.1021/ie200645s.
[26] Guo WQ, Malus S, Ryan DH, Altounian Z. Crystal structure and cation distributions in the FeTi2O5 -Fe2TiO5 solid solution series. J Phys Condens Matter 1999;11:6337–6336.
[27] Tomishige K, Li D, Tamura M, Nakagawa Y. Nickel-iron alloy catalysts for reforming of hydrocarbons: Preparation, structure, and catalytic properties. Catal Sci Technol 2017. https://doi.org/10.1039/c7cy01300k.
[28] Ashok J, Dewangan N, Das S, Hongmanorom P, Wai MH, Tomishige K, et al. Recent progress in the development of catalysts for steam reforming of biomass tar model reaction. Fuel Process Technol 2020;199:106252. https://doi.org/10.1016/j.fuproc.2019.106252.
[29] Huang T, Huang W, Huang J, Ji P. Methane reforming reaction with carbon dioxide over SBA-15 supported Ni-Mo bimetallic catalysts. Fuel Process Technol 2011;92:1868–75. https://doi.org/10.1016/j.fuproc.2011.05.002.
[30] Li D, Tamura M, Nakagawa Y, Tomishige K. Metal catalysts for steam reforming of tar derived from the gasification of lignocellulosic biomass. Bioresour Technol 2015;178:53–64. https://doi.org/10.1016/j.biortech.2014.10.010.
[31] Brunauer S, Emmett PH, Teller E. Adsorption of Gases in Multimolecular Layers. J Am Chem Soc 1938;60:309–19. https://doi.org/10.1021/ja01269a023.
[32] Scherrer P. Determination of the internal structure and size of colloid particles by X-rays. Göttinger Nachrichten Gesell 1918;2:98–100.
[33] Brage C, Yu Q, Chen G, Sjöström K. Use of amino phase adsorbent for biomass tar sampling and separation. Fuel 1997. https://doi.org/10.1016/S0016-2361(96)00199-8.
[34] Pio DT, Ruivo LCM, Tarelho LAC, Frade JR, Kantarelis E, Engvall K. Tar formation during eucalyptus gasification in a bubbling fluidized bed reactor: Effect of feedstock and reactor bed composition. Energy Convers Manag 2021;229:113749. https://doi.org/10.1016/j.enconman.2020.113749.
[35] Vitorino NMD, Kovalevsky A V., Ferro MC, Abrantes JCC, Frade JR. Design of NiAl2O4 cellular monoliths for catalytic applications. Mater Des 2017;117:332–7. https://doi.org/10.1016/j.matdes.2017.01.003.
[36] Shannon RD. Revised effective ionic radii and systematic studies of interatomic distances in halides and chalcogenides. Acta Crystallogr Sect A 1976;A32:751–67. https://doi.org/10.1107/S0567739476001551.
[37] Lenin N, Karthik A, Sridharpanday M, Selvam M, Srither SR, Arunmetha S, et al. Electrical and magnetic behavior of iron doped nickel titanate (Fe3+/NiTiO3) magnetic nanoparticles. J Magn Magn Mater 2016;397:281–6. https://doi.org/10.1016/j.jmmm.2015.08.115.
[38] Glaubitz B, Buschhorn S, Brüssing F, Abrudan R, Zabel H. Development of magnetic moments in Fe1 - XNix-alloys. J Phys Condens Matter 2011;23. https://doi.org/10.1088/0953-8984/23/25/254210.
[39] Jae J, Tompsett GA, Foster AJ, Hammond KD, Auerbach SM, Lobo RF, et al. Investigation into the shape selectivity of zeolite catalysts for biomass conversion. J Catal 2011;279:257–68. https://doi.org/10.1016/j.jcat.2011.01.019.
[40] Koike M, Li D, Nakagawa Y, Tomishige K. A highly active and coke-resistant steam reforming catalyst comprising uniform nickel-iron alloy nanoparticles. ChemSusChem 2012;5:2312–4. https://doi.org/10.1002/cssc.201200507.

[41] Basu P. Biomass Gasification, Pyrolysis and Torrefaction: Practical Design and Theory. 2013. https://doi.org/10.1016/C2011-0-07564-6.
[42] Furusawa T, Saito K, Kori Y, Miura Y, Sato M, Suzuki N. Steam reforming of naphthalene/benzene with various types of Pt- and Ni-based catalysts for hydrogen production. Fuel 2013;103:111–21. https://doi.org/10.1016/j.fuel.2011.09.026.
[43] Artetxe M, Nahil MA, Olazar M, Williams PT. Steam reforming of phenol as biomass tar model compound over Ni/Al2O3 catalyst. Fuel 2016;184:629–36. https://doi.org/10.1016/j.fuel.2016.07.036.
[44] Devi L, Ptasinski KJ, Janssen FJJG. Decomposition of naphthalene as a biomass tar over pretreated olivine: Effect of gas composition, kinetic approach, and reaction scheme. Ind Eng Chem Res 2005;44:9096–104. https://doi.org/10.1021/ie050801g.
[45] Koike M, Li D, Watanabe H, Nakagawa Y, Tomishige K. Comparative study on steam reforming of model aromatic compounds of biomass tar over Ni and Ni-Fe alloy nanoparticles. Appl Catal A Gen 2015;506:151–62. https://doi.org/10.1016/j.apcata.2015.09.007.
[46] Ashok J, Kawi S. Nickel-iron alloy supported over iron-alumina catalysts for steam reforming of biomass tar model compound. ACS Catal 2014;4:289–301. https://doi.org/10.1021/cs400621p.
[47] Morin M, Nitsch X, Pécate S, Hémati M. Tar conversion over olivine and sand in a fluidized bed reactor using toluene as model compound. Fuel 2017;209:25–34. https://doi.org/10.1016/j.fuel.2017.07.084.
[48] Schravendijk P, Van Der Vegt N, Delle Site L, Kremer K. Dual-scale modeling of benzene adsorption onto Ni(111) and Au(111) surfaces in explicit water. ChemPhysChem 2005;6:1866–71. https://doi.org/10.1002/cphc.200400591.
[49] Ashok J, Wai MH, Kawi S. Nickel-based Catalysts for High-temperature Water Gas Shift Reaction-Methane Suppression. ChemCatChem 2018;10:3927–42. https://doi.org/10.1002/cctc.201800031.
[50] Park C, Rodriguez NM, Baker RTK. Carbon Deposition on Iron–Nickel during Interaction with Carbon Monoxide–Hydrogen Mixtures. J Catal 1997;169:212–27. https://doi.org/https://doi.org/10.1006/jcat.1997.1691.
[51] Figueiredo; JL ;C. ABTKBJH. Carbon Fibers Filaments and Composites. Springer, Dordrecht; 1990. https://doi.org/10.1007/978-94-015-6847-0.
[52] Xie Y, Su Y, Wang P, Zhang S, Xiong Y. In-situ catalytic conversion of tar from biomass gasification over carbon nanofibers- supported Fe-Ni bimetallic catalysts. Fuel Process Technol 2018;182:77–87. https://doi.org/10.1016/j.fuproc.2018.10.019.
[53] Claude V, Courson C, Köhler M, Lambert SD. Overview and Essentials of Biomass Gasification Technologies and Their Catalytic Cleaning Methods. Energy and Fuels 2016;30:8791–814. https://doi.org/10.1021/acs.energyfuels.6b01642.
[54] Jiang X, Wayne Goodman D. The effect of sulfur on the dissociative adsorption of methane on nickel. Catal Letters 1990;4:173–80. https://doi.org/10.1007/BF00765701.
[55] Alstrup I, Rostrup-Nielsen JR, Røen S. High temperature hydrogen sulfide chemisorption on nickel catalysts. Appl Catal 1981;1:303–14. https://doi.org/10.1016/0166-9834(81)80036-X.
[56] Moud PH, Andersson KJ, Lanza R, Engvall K. Equilibrium potassium coverage and its effect on a Ni tar reforming catalyst in alkali- and sulfur-laden biomass gasification gases. Appl Catal B Environ 2016;190:137–46. https://doi.org/10.1016/j.apcatb.2016.03.007.
[57] Moud PH, Andersson KJ, Lanza R, Pettersson JBC, Engvall K. Effect of gas phase alkali species on tar reforming catalyst performance: Initial characterization and method development. Fuel 2015;154:95–106. https://doi.org/10.1016/j.fuel.2015.03.027.
[58] Nordgreen T, Nemanova V, Engvall K, Sjöström K. Iron-based materials as tar depletion catalysts in biomass gasification: Dependency on oxygen potential. Fuel 2012;95:71–8. https://doi.org/10.1016/j.fuel.2011.06.002.
[59] Virginie M, Courson C, Kiennemann A. Toluene steam reforming as tar model molecule produced during biomass gasification with an iron/olivine catalyst. Comptes Rendus Chim 2010;13:1319–25. https://doi.org/10.1016/j.crci.2010.03.022.
[60] Azhar Uddin M, Tsuda H, Wu S, Sasaoka E. Catalytic decomposition of biomass tars with iron oxide catalysts. Fuel 2008;87:451–9. https://doi.org/10.1016/j.fuel.2007.06.021.

Supplementary Material

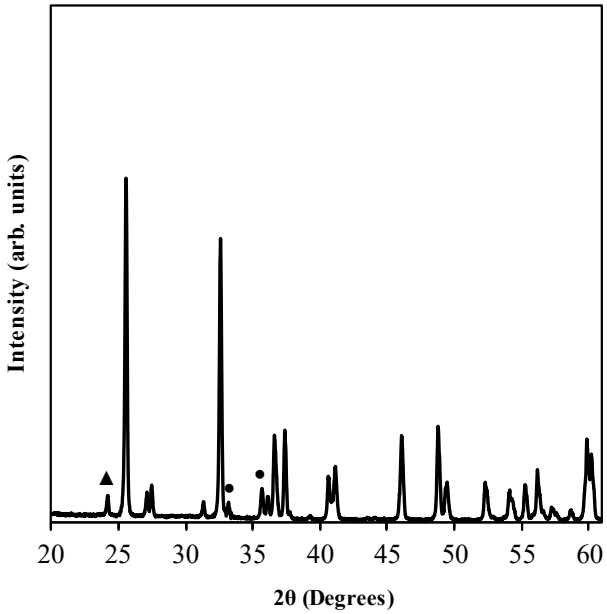

Figure S1 – X-ray diffraction patterns of the calcined 5%Ni-FT sample, ascribed to the orthorhombic phase Fe_2TiO_5, with traces of secondary phase (● – $NiTiO_3$ ▲ – TiO_2).

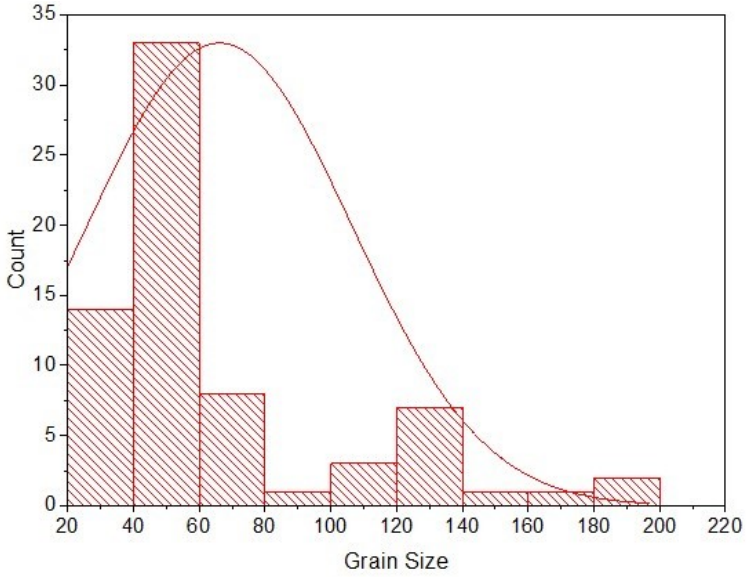

Figure S2 – Gaussian distribution of Ni grain size for the 10%Ni-FT sample.

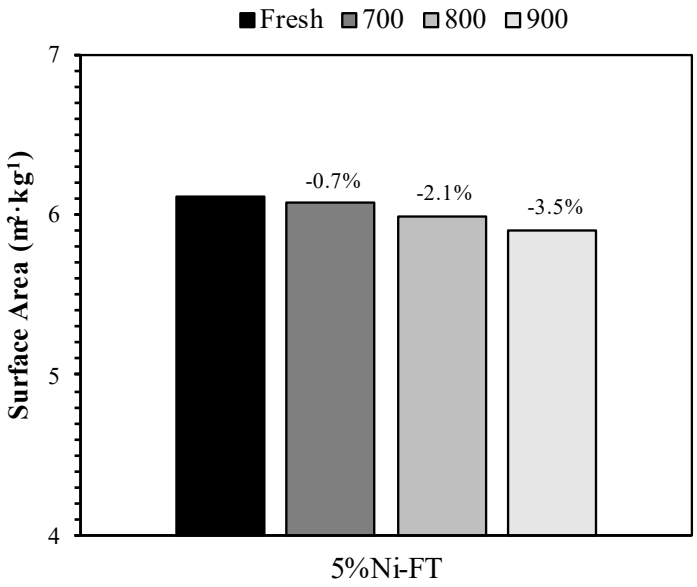

Figure S3 – BET analysis of the 5%Ni-FT catalyst after the reforming experiments.

Table S1 – Physical properties of calcined and activated 5%Ni-FT sample.

Sample	BET ($m^2 \cdot g^{-1}$)	Vp (cm^3/g)	d_P (Å)	Mesopores (%)	Micropores[a] (%)	True Density (g/cm^3)
5%Ni-FT (Calcined)	1.70	0.001	8.8	100	-	
5%Ni-FT (Reduced)	5.97	0.015	14.7	95.2	4.80	4.94

a - determined by t-plot method

3.3. Catalytic O_2-Steam Gasification of Biomass over $Fe_{2-x}Mn_xO_3$ Oxides Supported on Ceramic Foam Filters

Luís C. M. Ruivo, Helena Gomes, Daniela V. Lopes, Aleksey A. Yaremchenko, Catarina Vilas-Boas, Luís A. C. Tarelho, Jorge R. Frade

University of Aveiro (CESAM and CICECO)

Published in Fuel, 2022, 324, 124566.

Abstract

In the present study, catalytic gasification of biomass was investigated by incorporation of a supported $Fe_{2-x}Mn_xO_3$ catalyst into the freeboard zone of a bubbling fluidized bed gasifier. The material was processed by combining incipient wetness impregnation with microwave-assisted firing methods. These catalysts were characterized by elemental, structural and microstructural analyses, and redox testing by thermogravimetry. Catalytic performance was assessed by comparison with blank tests and used to study the influence of the catalyst temperature, equivalence ratio and gas hourly space velocity on tar decomposition. The catalyst revealed higher activity in converting tar compounds with increasing temperature and equivalence ratio, while increasing the gas hourly space velocity showed a negative impact on catalyst performance. Under optimal operating conditions, the catalyst exhibited a significant impact on tar conversion (83 %) and gasification parameters, such as the gas yield (0.81 to 0.93 $\mathrm{Nm^3_{dry,gas}\cdot kg^{-1}_{dry,fuel}}$), carbon conversion efficiency (55.3 to 65.1 %) and cold gas efficiency (50.7 to 61.6 %). Post-mortem analysis of the tested catalyst provided further information on redox changes and their dependence on temperature, which were co-related with catalytic performance. Elemental mapping showed traces of sulphur, which increased with temperature and did not correlate with the catalytic performance; this was interpreted by thermodynamic modelling, based on the wide redox stability range of divalent manganese oxide and its enhanced tolerance to hydrogen sulphide.

Keywords: Biomass, Gasification, Tar, Catalyst, Iron Oxide, Manganese Oxide

3.3.1. Introduction

Gasification of biomass is a flexible, reliable, and sustainable thermochemical route to convert a variety of low-value feedstocks into a high-value gas mixture, mainly composed of CO, H_2, CO_2, CH_4 and H_2O. The resulting producer gas can be applied in various end-use applications, such as electricity generation in combustion engines or gas turbines, and as a feedstock for the synthesis of biofuels or other valuable chemicals (e.g. synthetic methane, ammonia or methanol).

Despite the potential of biomass gasification, the presence of undesired tar in the producer gas has been the main challenge for large-scale applications. Tar is commonly defined as a complex mixture of organic compounds with molecular weight greater than benzene, which comprises single to multiple ring aromatic compounds along with other oxygenated hydrocarbons [1]. Tar concerns are related to its condensation at temperatures < 400 ºC, causing blocking and fouling of engines, filter and pipe plugging and

contamination of downstream equipment [2]. Based on this, gas conditioning for tar abatement is needed to ensure the required gas quality for subsequent applications.

Research on tar removal has mainly been focused on catalytic hot gas cleaning, aiming to convert tar components to additional H_2 and CO products. This method involves a set of parallel reactions whose extension is limited by the operating conditions and the type of catalyst applied [3]. The H_2O content of the biomass-derived raw gas will promote steam reforming reactions (3.3-1), while CO_2 content will induce dry reforming reactions (3.3-2). Thermal cracking of tar compounds (3.3-3) is also expected at higher temperatures. Furthermore, oxidation reactions (3.3-4) and (3.3-5) can have a significant preponderance on tar decomposition during gasifier operation if the type of catalyst employed shows oxygen storage ability. Additional reactions such as carbon gasification (3.3-6)-(3.3-7), water-gas-shift (3.3-8) and methanation (3.3-9) can also be promoted, contributing to increase the overall gasification efficiency.

$$C_nH_m + n \cdot H_2O \rightarrow n \cdot CO + (0.5m + n) \cdot H_2 \quad \text{Eq. 3.3-1}$$

$$C_nH_m + n \cdot CO_2 \rightarrow 2n \cdot CO + 0.5m \cdot H_2 \quad \text{Eq. 3.3-2}$$

$$C_nH_m \rightarrow C_{n-x}H_{m-y} + x \cdot C + y \cdot H_2 \quad \text{Eq. 3.3-3}$$

$$C_nH_m + (n/2) \cdot O_2 \rightarrow n \cdot CO + (m/2) \cdot H_2 \quad \text{Eq. 3.3-4}$$

$$C_nH_m + (n + m/4) \cdot O_2 \rightarrow n \cdot CO_2 + (m/2) \cdot H_2O \quad \text{Eq. 3.3-5}$$

$$C(s) + H_2O \rightarrow CO + H_2 \quad \text{Eq. 3.3-6}$$

$$C(s) + CO_2 \rightarrow 2CO \quad \text{Eq. 3.3-7}$$

$$CO + H_2O \rightleftarrows CO_2 + H_2 \quad \text{Eq. 3.3-8}$$

$$CO + 3H_2 \leftrightarrow CH_4 + H_2O \quad \text{Eq. 3.3-9}$$

Iron-based catalysts have showed promising results when applied as primary catalysts in biomass gasification processes. Particular attention has been given to the development of FeO/CaO bi-functional materials due to their high activity towards tar cracking and H_2 promotion [4,5]. The enhanced activity of FeO/CaO catalysts in tar conversion is attributed to the formation of the $Ca_2Fe_2O_5$ phase that decomposes polyaromatic hydrocarbons, despite the lower performance in char gasification reactions [4]. The main drawbacks of FeO/CaO-based catalysts are the decline in activity due to repeated operation cycles and interactions between Ca and Cl, yielding a $CaCl_2$-rich outer layer, which causes catalyst depletion [5]. Another attractive approach to promote tar conversion is based on Fe-Ni bimetallic systems. Higher catalytic activity in tar reforming reactions and improved resistance against carbon deposition are attributed to the synergetic effect of Fe-Ni alloy [6]. Still, the environmental implications of Ni (e.g. contamination of air, water, and soil) have motivated the research of alternative promotors [7]. The adoption of Ni-Fe catalysts is also hindered by the vulnerability of the catalysts to deactivate when low

concentrations of sulfur compounds are present in the biomass-derived gas. The poisoning effect of sulfur was generally explained by a simple site-blocking mechanism [8], which can induce oxide-metal bond scission with negative impact on the rate of catalytic conversion. Therefore, the development of sulfur-tolerant catalysts is of primary importance for efficient conversion of biomass to syngas. Other Fe-based materials, such as Fe_xO_y, $CuFe_2O_4$ and $CoFe_2O_4$, have also been tested as oxygen carriers because of their reactivity during oxidation and reduction over several operating cycles [9–11]. Higher thermal and mechanical stability, proper fluidization properties and resistance to attrition and agglomeration are other important characteristics associated with these materials.

On the other hand, the development of Fe-based catalysts by incorporation of Mn appears to be an interesting approach for the abatement of tar compounds because of their low toxicity and excellent redox properties [12]. Previous studies have reported high catalytic activity of Mn oxides for oxidation of aromatic hydrocarbons, such as benzene [13], toluene [14], naphthalene [15] and o-xylene [16]. Higher performance in oxidation reactions was attributed to the nature of Mn active sites, as well as their surface lattice oxygen mobility and reducibility. The conversion of tar compounds over Fe-Mn catalysts have also been investigated [17,18], revealing that the addition of Mn provides higher catalytic activity for tar conversion due to the synergetic effect of Fe-Mn binary oxides. Although the relevance of the aforementioned studies, none of them were carried out under realistic biomass gasification conditions, where the catalyst was continuously exposed to the biomass-derived raw gas, as well as to erosion and ageing mechanisms caused by the dynamic conditions of gasification under high gas flows. Moreover, these studies mainly considered the analysis of Fe/Mn mixed oxides, which highlights the need for extended activity studies focused on Fe-Mn solid solutions.

Therefore, the present work investigated the performance of a supported porous $Fe_{2-x}Mn_xO_3$ catalyst during biomass gasification in a 3 kW_{th} bench-scale bubbling fluidized bed system. The main challenge was to improve tar conversion by catalytic oxidation reactions without affecting the overall efficiency of the gasification process. For this purpose, catalyst samples were prepared by combining incipient wetness impregnation with microwave-assisted firing methods, followed by their detailed characterization. Gasification experiments were designed to investigate the influence of catalyst temperature, equivalence ratio and gas hourly space velocity on tar decomposition. Then, the impact of the catalyst on the efficiency parameters of gasifier was evaluated for optimal operating conditions.

3.3.2. Materials and Methods

3.3.2.1. Catalyst Preparation

Catalysts were prepared by combining incipient wetness impregnation method with microwave-assisted firing. Ceramic foam filters (10 ppi of porosity, 20 mm outer diameter and 10 mm length), supplied by Pyrotek, were impregnated with manganese (II) and iron (III) salts by capillary pressure and roasting. The filters (~1.4 g each) were previously washed with distilled water and oven dried. The impregnation solution was prepared by adding 10 wt.% of $Mn(NO_3)_2{\cdot}4H_2O$ and 32 wt.% of $Fe(NO_3)_3{\cdot}9H_2O$ into distilled water, both reagents from Sigma-Aldrich. This formulation corresponds to the atomic ratio Fe:Mn =

1.99:1, being the stoichiometric quantities required to promote the formation of spinel manganese ferrite in which Mn and Fe display tetrahedral and octahedral cation sites, respectively. Initially, the carriers were immersed in the Mn-Fe salts solution overnight at room temperature, followed by capillary pressure. Samples were roasted for 30 min at 200 °C followed by 30 min of capillary pressure impregnation in a vacuum desiccator. The procedure was repeated 10 times before calcination at 700 °C for 1 hour by microwave irradiation. The Fe/Mn-free sample was used as a reference, and the catalyst sample was denoted by Fe-Mn. Figure 3.3-1 shows the ceramic foam filters before and after the preparation procedure.

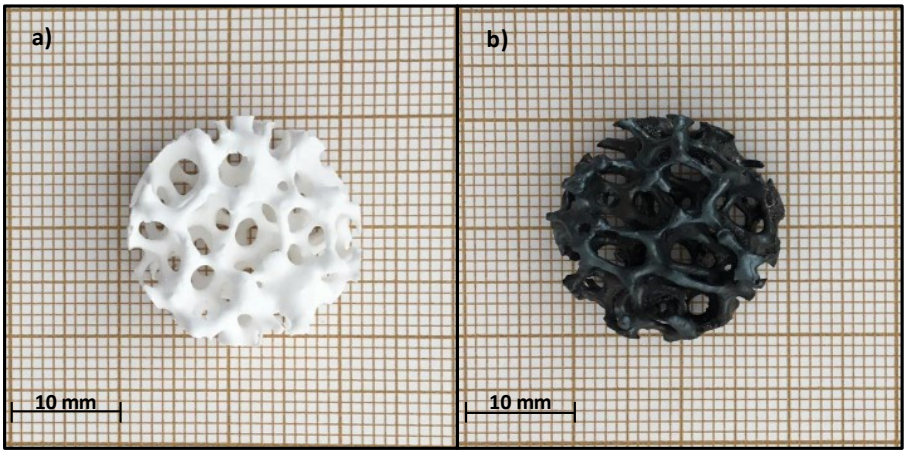

Figure 3.3-1: Ceramic foam filters before (a) and after (b) the preparation procedure.

3.3.2.2. Catalyst Characterization

Analysis of the elemental composition of the fresh catalyst was performed by X-ray fluorescence (XRF), using a Philips X'Pert PRO MPD spectrometer. Powder X-ray diffraction (XRD) measurements were carried out on a PANalytical X'Pert Pro^3 diffractometer equipped with a CuK_α radiation source. Diffraction patterns were recorded between 2θ values of 10 and 80º, with a scan step of 0.02º and exposition time of 200 s. Phase identification was ascertained by PANalytical High Score Plus 4.7 (PDF-4) software. Microstructural and elemental distribution studies were conducted by scanning electron microscopy (SEM, Hitachi, TM4000 Plus) and transmission electron microscopy (TEM/STEM–JEOL 2200FS), equipped with energy dispersive X-Ray spectroscopy (EDS Oxford Inca TEM250). The analysis was performed for bulk samples (SEM), mounted on aluminum sample holders and coated with carbon using a sputter coater, or fine powders (TEM/ EDS) deposited on a copper grid covered by a perforated carbon membrane. Thermal analysis was performed in a Setaram SetSys 16/18 thermogravimetric analyzer (TGA) to investigate the redox ability of the catalyst. The experiments were performed in 10%H_2-90%N_2 atmosphere flowing through the fresh catalyst with a flow of 25 $cm^3 \cdot min^{-1}$. The temperature was increased from room temperature up to 900 °C at a constant heating rate of 5 °C·min^{-1}. Post-mortem analyses of the spent catalysts were also performed by Fourier-transform infrared spectroscopy (FTIR). The spectra of the samples were recorded by accumulating 64 scans at 4 cm^{-1} resolution in the spectral range of 500−4000 cm^{-1} using a GALAXY SERIES FT-IR 7000 spectrometer equipped with a DTGS CsI detector.

3.3.2.3. Catalytic Gasification Experiments

Feedstock Material

Residual forest biomass from pine (*Pinus Pinaster*) was used as feedstock in the investigation. The proximate and ultimate analyses were performed following the corresponding CEN/TS standard for solid biofuels. The lower heating value of the feedstock (LHV_F) was determined using the correlation developed by Channiwala et al. [19], whereas the bulk density was estimated by determining the weight of fuel in a given volume. Prior to the gasification experiments, the feedstock was ground and sieved to a size of 2-4 mm in diameter to meet the requirements of the fuel feeding system. The physicochemical properties of the biomass feedstock are provided in Table 3.3-1.

Table 3.3-1: Characteristics of the pine feedstock used in the gasification experiments.

Ultimate Analysis (wt.%, daf)	
Carbon	51.9
Hydrogen	6.4
Nitrogen	0.5
Sulfur	0.03
Oxygen (by difference)	41.2
Proximate Analysis (wt.%, wb)	
Moisture	9.0
Volatile Matter	71.6
Fixed Carbon	18.4
Ash	1.0
LHV_F ($MJ \cdot kg_{F,db}^{-1}$)	19.4
Bulk Density ($kg_F \cdot m^{-3}$)	308.4 ± 0.2

db – dry basis, daf – dry ash-free basis, wb – wet basis

Experimental Apparatus and Procedure

Catalyst performance was evaluated through O_2/steam gasification experiments in a bench-scale infrastructure (Figure 3.3-2). The system consists of a bubbling fluidized bed (BFB) gasifier, a fuel feeding unit and a downstream section for raw gas cleaning, sampling and analysis. The BFB reactor is heated by an external electric furnace, and the bottom bed and freeboard can be temperature-controlled separately. The BFB reactor also incorporates an in-situ catalytic fixed-bed reactor located on the freeboard zone (L, Figure 3.3-2), consisting of a sampling probe with an inner diameter of 22 mm and a heigh of 100 mm, through which the raw producer gas was forced to pass. The operating temperature is measured using a K-type thermocouple placed in the middle of the catalyst bed. Details concerning the experimental set-up configuration was described in previous studies [20].

Prior to each gasification experiment, 10 g of fresh catalyst was loaded on a porous ceramic wool involved in a wire mesh placed at the bottom of the catalytic reactor and heated in N_2 atmosphere up to the desired temperature. Subsequently, the biomass-derived gas was gradually replacing the inert atmosphere in the catalytic fixed bed reactor. Once the catalyst reactivity stabilized (after ≈ 30 min), the biomass-derived gas was sampled through a set of isopropanol impingers partially immersed in an ice bath at ≈ 0 ºC, for the unconverted tar and moisture collection, with a total sampling time of approximately 45 minutes. The composition of the dry tar-free gas (N_2, H_2, CO, CO_2, CH_4, C_2H_4, C_2H_6 and C_3H_8) was characterized by means of an off-line gas analyser (micro-GC). The producer gas was collected in 10-minute periods using gas sample bags (FlexFoil). The condensed species were quantitatively determined by weighing the impingers before and after the experiment. The water content was measured by means of a volumetric Karl Fischer equipment (SI Analytics Automatic Titrator TitroLine 7500), being the weight of tar (m_{tar}) determined by difference. Afterward, the tar yield (Y_{tar}) was normalized with reference to the consumption of biomass during the sampling time ($m_{F,t}$):

$$Y_{tar}\ (g_{tar} \cdot kg_F^{-1}) = \frac{m_{tar}}{m_{F,t}} \qquad \text{Eq. 3.3-10}$$

The experimental conditions of the catalytic gasification experiments performed are presented in Table 3.3-2. The average steam to carbon molar ratio (S/C) and bed temperature (T_{bed}) were maintained at 0.5 and 795 ± 10 ºC, respectively. These values were chosen following guidelines resulting from previous studies performed by the authors, which suggest that an optimal balance between producer gas quality and process efficiency and stability [21]. The operating parameters investigated were the catalyst temperature (T_{cat} – 700 to 800 ºC), equivalence ratio (ER – 0.10 to 0.15), and gas hourly space velocity (GHSV – 2500 to 5000 h^{-1}). In order to eliminate possible thermal effects of the catalytic fixed bed reactor, experiments with inert material (ceramic foam filters) under the same conditions were performed (Table S1 – Supplementary Material). The obtained results were used as a reference case in evaluating the catalyst performance.

Table 3.3-2: Operating conditions of the catalytic gasification experiments (biomass feeding = 87.8 g·h^{-1}, steam feeding = 33.5 g·h^{-1} and bed temperature = 795 ± 10 ºC).

Test	O_2 (L_{STP}·h^{-1})	ER (-)	T_{cat} (ºC)	GHSV (h^{-1})
E1	81.0	0.100	700 ± 5	2500
E2	81.0	0.100	750 ± 5	2500
E3	81.0	0.100	800 ± 5	2500
E4	78.7	0.125	800 ± 5	2500
E5	76.5	0.150	800 ± 5	2500
E6	76.5	0.150	800 ± 5	3750
E7	76.5	0.150	800 ± 5	5000

*STP – Refers to L at normal pressure (1.013×10^5 Pa) and temperature (0 ºC).

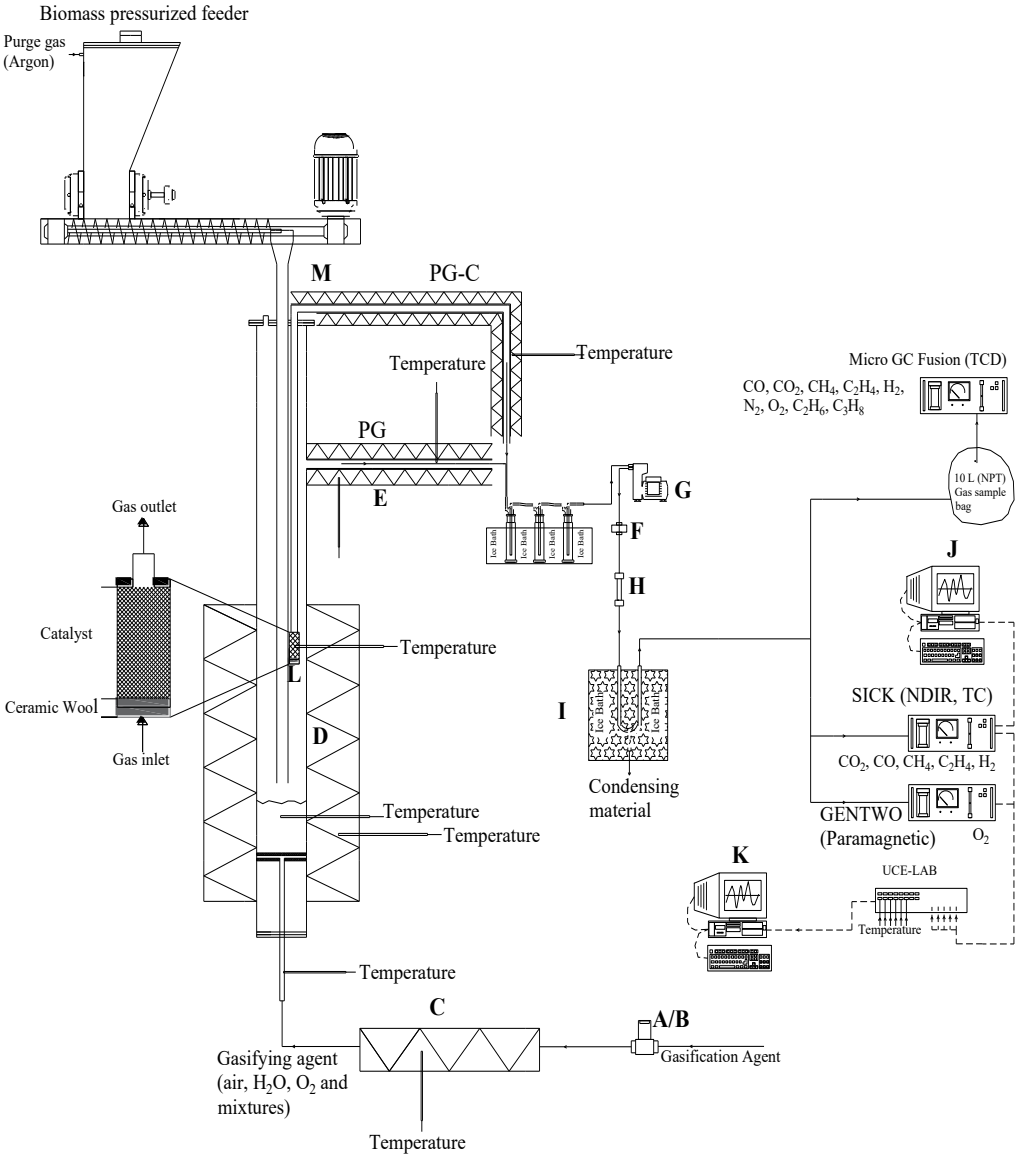

Figure 3.3-2: Schematic layout of the experimental infrastructure used during gasification experiments. Dashed Line - Electric Circuit, Continuous Line - Pneumatic Circuit, A/B – Mass-flow Controller, C – Evaporator, D – External Electric Furnace, E – Raw PG Exhaust, F – Quartz Filter G – Gas Sampling Pump, H – Gas Flow Meter, I - Gas Condensation Unit for Residual Moisture J - Computer for Data Acquisition from SICK Analyzer, K - Computer for Data Acquisition, L – Catalytic Fixed Bed Reactor, M - Probe Heated at 450 ºC, T – K-type thermocouple, PG – Raw Producer Gas, PG-C – Upgraded Producer Gas, GENTWO – O_2 Paramagnetic Online Gas Analyzer, UCE-LAB - Electronic Command Unit, Micro GC - Gas Chromatograph with TCD, SICK – NDIR and TC Online Gas Analyzer.

Data Analysis

The performance of the catalyst was evaluated based on the impact on gas composition, tar reduction and gasification performance. The lower heating value of the dry producer gas (LHV_G) was estimated based on the concentration of the combustible gases and their respective LHV at standard conditions (P_N = 101325 Pa and T_N = 273.15 K). Tar conversion (X_{tar}) was expressed as the ratio of difference between the tar yield obtained with and without the catalyst under the same operating conditions. Cold gas efficiency (CGE) was defined as the ratio between the chemical energy present in the producer gas and the potential energy input. Carbon conversion efficiency (CCE) was calculated as the ratio of carbon in the producer and the carbon present in the feedstock. Finally, gas yield (Y_{Gas}) has been evaluated on the basis of a mass balance, assuming the conservation of N_2 and was expressed as mass of gas produced per mass of dry biomass. The tar conversion and performance parameters were calculated as follow:

$$X_{tar}\ (\%) = 1 - \frac{Y_{tar,cat}}{Y_{tar,inert}} \qquad \text{Eq. 3.3-11}$$

$$Y_{Gas}\ (Nm^3_{dry\ gas} \cdot kg_F^{-1}) = \frac{G_{v,gas}}{G_{m,fuel}} \qquad \text{Eq. 3.3-12}$$

$$CCE\ (\%) = \frac{G_{v,gas} \times \frac{P_N}{R \times T_N} \times M_C \times \sum \varepsilon_{C,i} \times y_i}{G_{m,fuel} \times w_{C,F}} \times 100 \qquad \text{Eq. 3.3-13}$$

$$CGE\ (\%) = \frac{Y_{Gas} \times LHV_{Gas}}{LHV_{fuel}} \times 100 \qquad \text{Eq. 3.3-14}$$

Where $Y_{tar,cat}$ and $Y_{tar,inert}$ denotes the tar yield ($g_{tar} \cdot kg_F^{-1}$) obtained with and without catalyst under the same operating conditions, respectively, $G_{m,fuel}$ and $G_{v,gas}$ are the dry biomass feeding rate ($\mathrm{kg_F \cdot h^{-1}}$) and the dry producer gas flow rate ($\mathrm{Nm^3_{dry\ gas} \cdot h^{-1}}$), respectively, y_i and $\varepsilon_{C,i}$ are the molar fraction and the number of carbon atoms in component i (i = CO_2, CO, CH_4, C_2H_4, C_2H_6 and C_3H_8), respectively, M_C and $w_{C,F}$ are the molecular weight of carbon and the mass fraction of carbon in the dry biomass, respectively, LHV_{Gas} and LHV_{fuel} are the lower heating value of the dry producer gas ($\mathrm{MJ \cdot Nm^{-3}_{dry\ gas}}$) and dry biomass ($\mathrm{MJ \cdot kg_F^{-1}}$), respectively.

3.3.3. Results and Discussion

3.3.3.1. Characterization of the Fresh Catalyst

The elemental composition of the ceramic support before and after impregnation is summarized in Table 3.3-3. XRF results indicate that Fe and Mn can be effectively supported on the ceramic foam filters. The weight percentage of Fe and Mn were found to be 14.7 and 6.5 wt.% in the calcined Fe-Mn catalyst, which corresponds to the atomic ratio Fe:Mn = 2.22, and deviates slightly from the target ratio in the nitrate precursors (Fe:Mn = 1.99). The ceramic support mainly contains Al (42.7 wt.%) and Si (8.5 wt.%), with residual contents of Fe (0.2 wt.%) and without detection of Mn.

The effectiveness of the preparation method is also confirmed in Figure 3.3-3, which shows the surface and cross-sectional EDS mapping of the as-prepared Fe-Mn catalyst. A homogeneous distribution of Fe and Mn on the outer surface of Fe-Mn catalyst is observed, as well as a proper integration of these elements inside the ceramic support. It should be noted that the Mn/Fe atomic ratio on the catalyst surface (0.42) is higher than inside the ceramic foam filter (0.32), suggesting the enrichment of O-vacancies on the surface of catalyst after calcination. Subsequently, it is expected the improvement of the catalyst performance since the abundant O-vacancies can facilitate the active oxygen mobility and promote the evolution of lattice oxygen favouring to tar oxidation reactions [22]. On the other hand, TEM studies of the crushed catalyst after calcination (Figure 3.3-4) indicated the presence of Fe-Mn nano particles of different shapes and dimensions. According to Gaussian analysis in Figure S1, around 80 % of the bimetallic particles are below 35 nm.

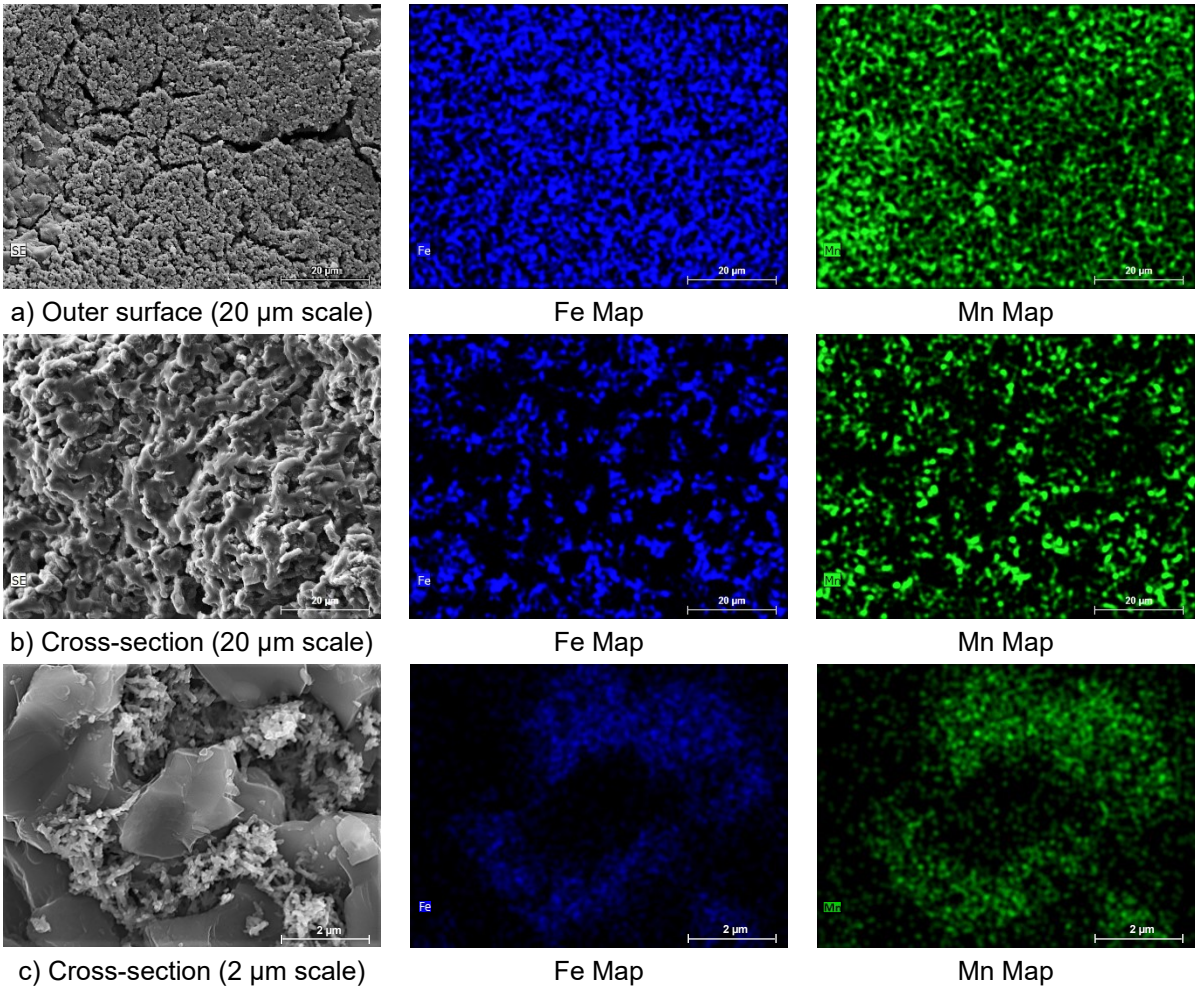

Figure 3.3-3: SEM micrographs of Fe-Mn supported catalyst, and corresponding elemental maps of Fe and Mn. The micrographs are related to the outer surface (a) and cross-section (b and c) of catalyst sample.

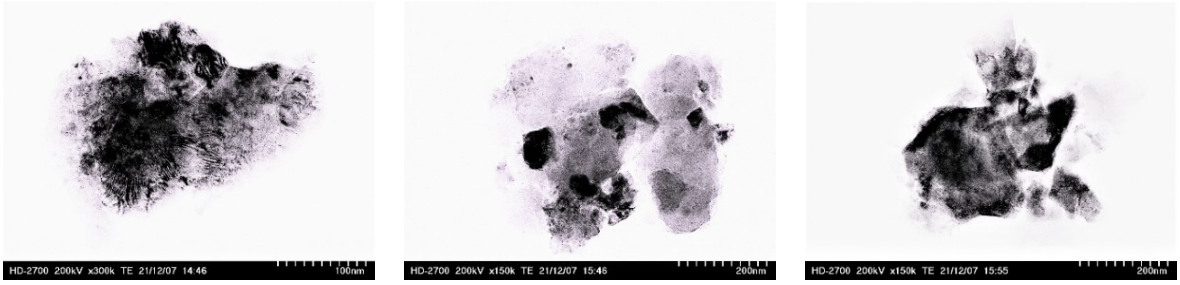

200 kV – 100 nm scale | 200 kV – 200 nm scale | 200 kV – 200 nm scale

Figure 3.3-4: TEM images of the crushed Fe-Mn catalyst after calcination at 700 °C for 1 hour.

Table 3.3-3: Elemental analysis (wt.%) of the ceramic foam filter and calcined Fe-Mn catalyst, determined by the XRF. Other elements include Mg, Na, P, Cl, K, Ca and Ti.

Elements	Ceramic Foam	Fe-Mn Catalyst
O	48.0	42.0
Al	42.7	30.3
Si	8.5	5.5
Fe	0.2	14.7
Mn	n.d	6.5
S (ppm)	n.d	n.d
Others	0.5	1.0

The XRD patterns of the ceramic support and calcined Fe-Mn catalyst are shown in Figure 3.3-5. The results indicate that corundum (Al_2O_3, PDF # 00-010-0173) is the main crystalline phase in the ceramic support, followed by traces of mullite as a secondary phase ($(Al_2O_3)_x(SiO_2)_y$). In case of the Fe-Mn catalyst sample, inspection of the XRD data shows that calcination by microwave irradiation promoted the formation of mixed Fe-Mn oxides, accompanied by the decomposition of the NO_3 anions associated with the precursors. The diffraction peaks at 2θ = 23.13°, 32.94°, 38.22°, 45.14°, 55.15°, 65.75° and 67.42° can be indexed to the crystallographic planes of the cubic bixbyite phase ($Mn_{1-x}Fe_{1+x}O_3$). Presence of a rhombohedral hematite-based phase (Fe_{2-x} Mn_xO_3) was also detected at 2θ = 24.16°, 33.17°, 35.63°, 40.87°, 49.48°, 54.09°, 62.45° and 64.03°, with partial overlapping of some peaks (red symbols) with the ceramic support phases. These phases are consistent with the $MnO_x - FeO_x$ phase diagram [23] for the actual atomic ratio (Fe:Mn = 2.22:1), and firing at 700 ºC. Partial interchange is expected for both phases, based on similarity of ionic radius of Mn^{3+} and Fe^{3+} cations. The expected phase compositions predicted by the phase diagram are in the order of $Mn_{1.1}Fe_{0.9}O_3$ for the bixbyite phase and $Fe_{1.88}Mn_{0.12}O_3$ hematite at 700 ºC; this may enable bimetallic interactions in FeMn-based catalysts [24].

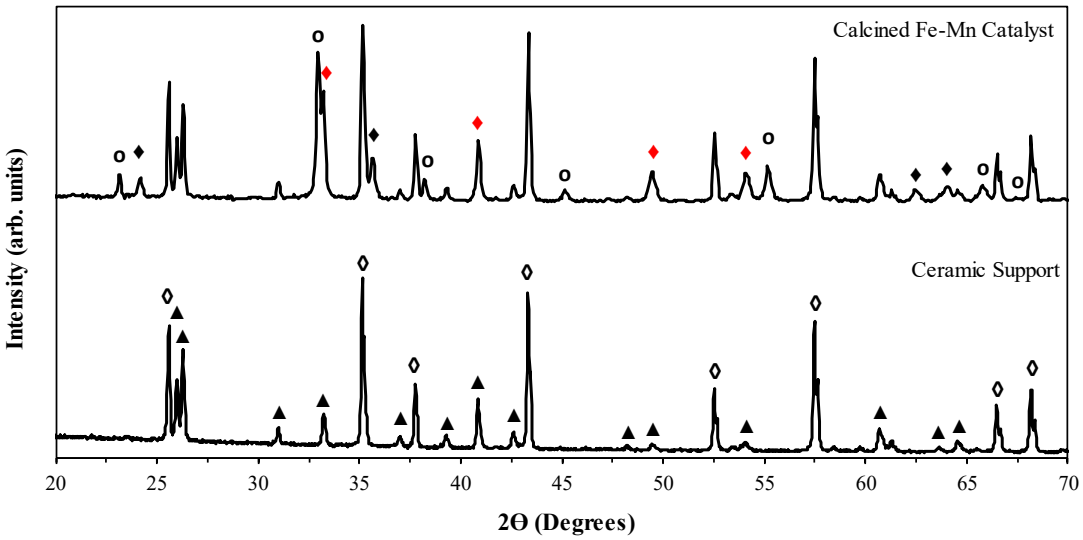

Figure 3.3-5: X-ray diffraction patterns of the ceramic foam filters before and after impregnation (▲ – $(Al_2O_3)_x(SiO_2)_y$ ◊ – Al_2O_3 ♦ – $Mn_xFe_{2-x}O_3$ o – $Mn_{1-x}Fe_{1+x}O_3$).

Thermogravimetry (Figure 3.3-6) was performed with heating at 5 ºC·min^{-1} in 10%H_2-N_2 atmosphere to investigate the redox ability of Fe-Mn catalyst. The results showed two reduction peaks located at 460 ºC and ~ 610 ºC, corresponding to an initial reduction stage yielding weight losses up to about 1.8 wt.% and a second stage with weight losses up to about 2.5 wt.%, respectively. The losses in the first exceed those expected by reduction of $(Fe,Mn)_2O_3$ to $(Fe,Mn)_3O_4$ (≈ 1 wt.%), and suggest also partial reduction of $(Fe,Mn)_3O_4$ to (Fe,Mn)O, in close agreement with other studies [25], as well as thermodynamic modelling of the Fe-Mn-O system in moderately reducing conditions [26]. Losses of about 2.5 wt.% at the end of the second stage suggest complete reduction of iron oxide to a divalent FeO-based phase while retaining a Mn_3O_4-based spinel (≈ 2.4 wt.%); this is consistent with segregation of Mn on the catalyst surface, reported in relevant literature [27], with expected impact on H_2 chemisorption and ability to prevent reduction to metallic Fe. Still, losses attained at higher temperatures (e.g. ≈ 4.2 wt.% at 1000 ºC) exceed the level expected for reduction to wustite-type (Mn,Fe)O divalent oxides (≈ 3.0 wt.%) and indicate that a fraction of iron is also reduced to metallic state. In addition, one may expect deviations from the ideal stoichiometries of wustite, spinel or hematite phases, with prevailing cation vacancies in the wustite $Fe_{1-\delta}O$ [28] or spinel $Fe_{3-\delta}O_4$ [29] phases, and prospects for either oxygen vacancies $Fe_{2-\delta}O_3$ or cation vacancies $Fe_2O_{3-\delta}$ in the hematite phase [30]. Moreover, the XRD pattern of the tested Fe-Mn catalyst sample (Figure S2 – Supplementary Material) indicates the formation of silicate phase $(Mn,Fe)_2SiO_4$ phase, which may stabilize the divalent state of Fe and Mn [31].

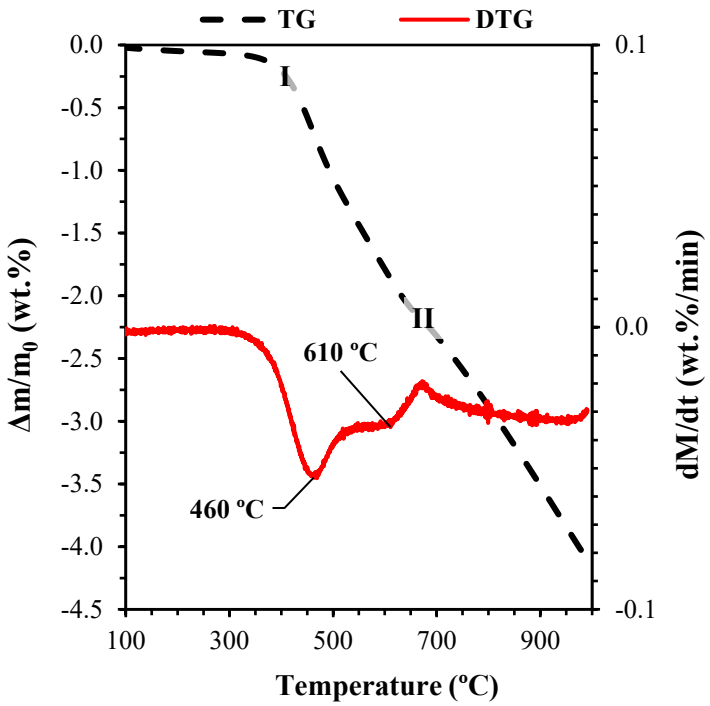

Figure 3.3-6: Thermogravimetric (TG) and differential thermogravimetric analysis (DTG) curves for the Fe-Mn catalyst in 10% H_2-N_2 atmosphere at 5 ºC·min^{-1}.

3.3.3.2. Catalytic Gasification Experiments

Effect of Experimental Parameters on Tar Decomposition

The influence of the catalyst temperature on tar conversion is presented in Figure 3.3-7a. As expected, higher catalytic activity was obtained at higher temperature and around of 72.5 % tar conversion was reached at 800 ºC. Moderate activity was found at lower temperature (31.8 %), suggesting catalyst deactivation by coke deposition, possibly catalysed by onset of metallic Fe. In fact, the rate of Boudouard reaction (3.3-7) is insignificant at 700 ºC which may promote the formation of carbon deposits on active sites [32]. This temperature dependence is confirmed by analysis of the producer gas composition (Figure 3.3-7b), where an increase in the catalyst temperature led to higher CO content (19.4 to 33.9 vol.%) with subsequent decline in CO_2 content (37.2 to 24.6 vol.%). Additionally, H_2 content varied slightly (19.1 to 18.2 $g_{H_2} \cdot kg_{dry,fuel}^{-1}$) when temperature increased, suggesting higher rates of dry carbon gasification (3.3-7) rather than steam gasification (3.3-6), and/or dry reforming (3.3-2) relative to steam reforming (3.3-1). Note that carbon conversion is expected to be inhibited by the formation of C-H surface complexes during steam gasification [33]. Variable oxygen stoichiometry of $(Fe, Mn)O_x$ oxide structures also allows oxygen storage ability [34]; this may contribute to minimize restrictions on gasification by removing H_2 efficiently from the reaction zone.

Similar tendencies on tar decomposition over the Fe-Mn catalyst were observed for the variation of equivalence ratio from 0.10 to 0.15 (Figure 3.3-7c). An increase of this ratio from 0.10 to 0.15 led to higher catalytic activity in converting tar compounds, ranging from 72.5 to 82.8 %, respectively. At intermediate equivalence ratio (ER = 0.125), catalytic tar

reduction ability was around 79.5 %. Higher ratio also impacts considerably the producer gas composition (Figure 3.3-7d), with emphasis on the onset of CO_2 formation. This effect can be attributed to the mobility of lattice oxygen in the Fe/Mn catalyst, which favors the conversion of combustible species, as revealed by the decreased in both CO (33.9 to 22.4 vol.%) and C_xH_y (4.6 to 2.3 vol.%) contents. Furthermore, H_2 and CH_4 contents showed fluctuations with increasing equivalence ratio, suggesting occurrence of parallel reactions such as water-gas-shift (3.3-8) and/or methanation (3.3-9).

Regarding the influence of gas hourly space velocity (GHSV) on the catalytic performance, one observed a minor impact of this parameter for values between 2500 and 5000 h^{-1} (Figure 3.3-7e). Tar decomposition over the Fe-Mn catalyst (79.5 and 80.9 %) showed comparable activity for GHSV values between 2500 and 3750 h^{-1}, respectively. A slight decrease in catalytic activity was found at 5000 h^{-1}, probably due to lower contact time between the active sites and tar compounds. The stable performance of the Fe-Mn catalyst as a function of GHSV was confirmed by the producer gas composition (Figure 3.3-7f) since no relevant changes were observed for the main components.

The effective performance of the Fe-Mn catalyst in converting tar compounds can be ascribed to substantial activity towards oxidation reactions. Post-mortem analysis by FTIR (Figure 3.3-8) showed evidence of oxidized species on the surface of Fe-Mn catalysts, as revealed by the CO_2 double peak at ~ 2361 cm^{-1} and 2335 cm^{-1} [35]. It should be noted that stronger CO_2 bands were obtained with increasing catalyst temperature (Figure 3.3-8a), which may be related to the observed tar breakage ability. A similar relation between the CO_2 band intensities and tar decomposition over the Fe-Mn catalyst was obtained for the variation of equivalence ratio (Figure 3.3-8b), suggesting gas-phase oxygen as an important factor for the decomposition of tar species on the catalyst active sites. Peaks in the range 500-700 cm^{-1} are consistent with the presence of Fe-Mn spinel oxides [36], probably superimposed on α-Al_2O_3 vibrational modes where Al takes octahedral coordination [37]. Other bands may be related to the actual catalyst support, namely tetrahedral Al-O stretching at 830 cm^{-1}, and a double peak ascribed to Si-O-Si asymmetric stretching in mullite at ~ 1162 cm^{-1} and 1113 cm^{-1} [38].

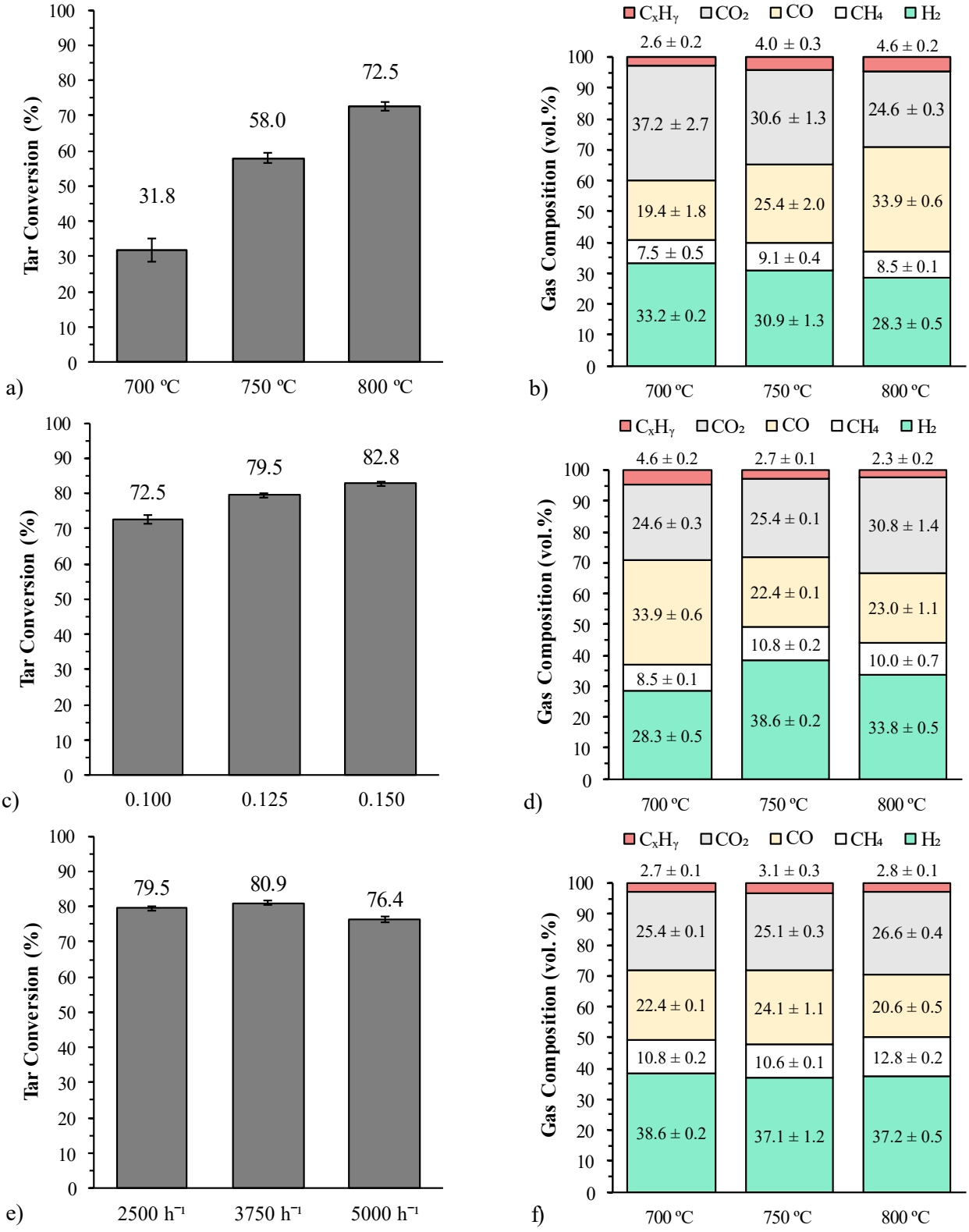

Figure 3.3-7: Tar conversion and producer gas composition as a function of reaction temperature (a-b, ER = 0.100 and GHSV = 2500 h^{-1}), equivalence ratio (c-d, T = 800 ºC and GHSV = 2500 h^{-1}) and gas hourly space velocity (e-f, T = 800 ºC and ER = 0.150).

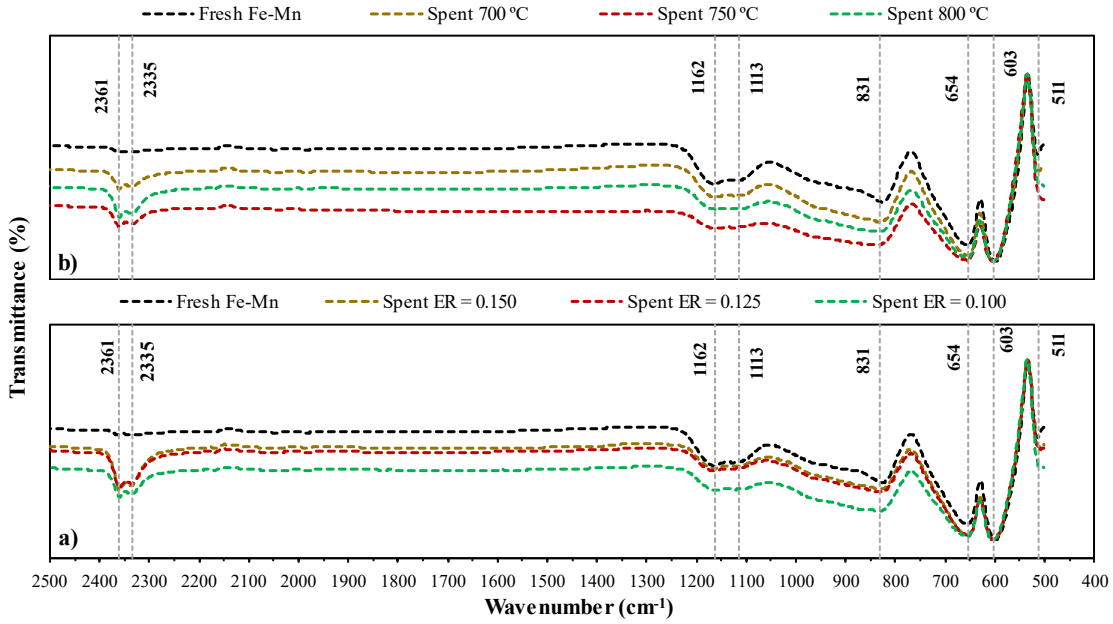

Figure 3.3-8: FTIR spectra of the spent Fe-Mn catalyst as a function of the equivalence ratio inside the gasifier (a) and the catalyst temperature (b).

XRD patterns of the spent catalysts (Figure 3.3-9a) showed a phase transition from $(Fe,Mn)_2O_3$ to $(Fe,Mn)_3O_4$ when exposed to biomass-derived raw gas. Also, partial reduction of $(Fe,Mn)_3O_4$ spinel oxide to wustite (Fe,Mn)O was observed at catalyst temperatures above 700 ºC, in close agreement with increasing $CO:CO_2$ ratio (Figure 3.3-7b); this suggest that higher activity towards oxidation reactions was attained by the reducibility of Fe^{3+}/Fe^{2+} or Mn^{4+}/Mn^{3+} and corresponding changes in oxygen stoichiometry, in close agreement with relevant literature [39,40]. The wustite:spinel peak ratios decrease with increasing equivalence ratio, indicating greater redox tolerance of the $(Fe,Mn)_3O_4$ spinel phase, and suggesting direct correlation with the catalyst activity (Figure 3.3-7c).

Thermogravimetric reduction of the spent catalysts in $10\%H_2$-$90\%N_2$ atmosphere (Figure S3) also allows to determine variations in the oxygen stoichiometry ($\Delta\delta$) compared to the fresh catalyst. It was assumed that only oxygen is released from the samples during TGA experiments, being the basis for determining the $\Delta\delta$-values. The corresponding results (Table S2) showed a suitable matching with the structural changes observed in the spent catalysts (Figure 3.3-9). Note that the maximum $\Delta\delta$-value for the catalyst temperature was exhibited at 800 ºC (866 $\mu mol_{O_2} \cdot g_{sample}^{-1}$), showing that ability of the catalyst to donate lattice oxygen increases with temperature. In contrast, the catalyst revealed a reduction of $\Delta\delta$ from 866 to 523 $\mu mol_{O_2} \cdot g_{sample}^{-1}$ when exposed to higher equivalence ratios, suggesting that gas-phase O_2 might play a key role in the regeneration of lattice oxygen. Based on those results, one may assume that tar decomposition over the Fe-Mn catalyst followed a redox-type mechanism [41], consisting in the adsorption of tar on catalyst surface to form intermediates, with subsequent oxidation to by-products, and further re-oxidation of the active sites by gas-phase O_2 interactions.

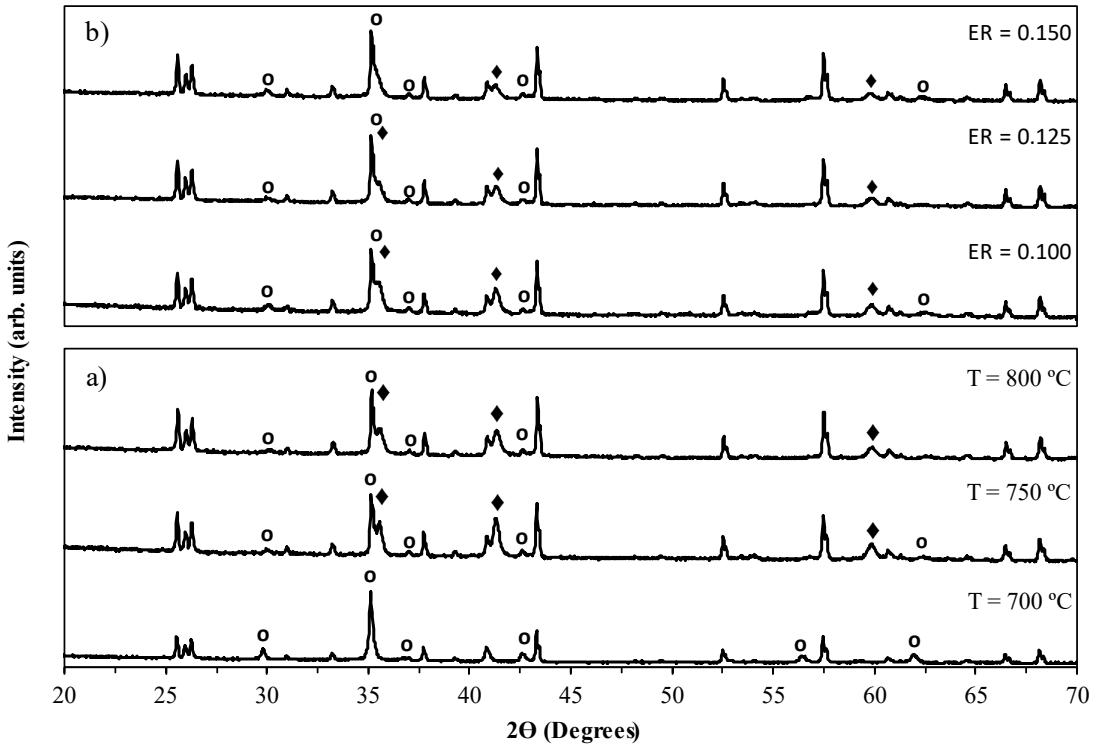

Figure 3.3-9: XRD patterns of the spent Fe-Mn catalysts as a function of the catalyst temperature and the equivalence ratio inside the gasifier (♦ – (Mn,Fe)O o – $(Mn,Fe)_3O_4$). The unidentified peaks are related to Al_2O_3 and aluminosilicate support phases.

TEM/EDS analysis of the spent Fe-Mn catalyst (Figure 3.3-10) showed evidence of sulphur coverage with increasing temperature, which may poison Mn-based catalysts, such as Fe-Mn catalysts for NO_x conversion [42]. Potential S-Metal interactions was also confirmed by chemical analysis of the spent catalysts (Table S3 – Supplementary Material), which revealed sulfur deposits between 115 and 412 $mg_S \cdot kg_{cat}^{-1}$. However, this phenomenon did not seem to cause obvious decrease in catalytic activity under conditions of gasification, as indicated by the previous results presented in Figure 3.3-7; this indicates that operating conditions may determine sulphur tolerance, possibly combined with interactions between the catalytic layer and alumina-based supports, as reported for Fe-based catalysts intended for propane de-hydrogenation and tested after exposition to H_2S [43]. Those results indicated that interaction of the thin Fe layer with the $\gamma - Al_2O_3$ support minimized risks of complete conversion of the active layer to FeS. Thus, gas-solid thermodynamic equilibrium calculations was performed to provided guidelines for reactivity of the Fe-Mn catalyst with H_2S, which is the expected most abundant sulfur-containing specie in the biomass-derived gas.

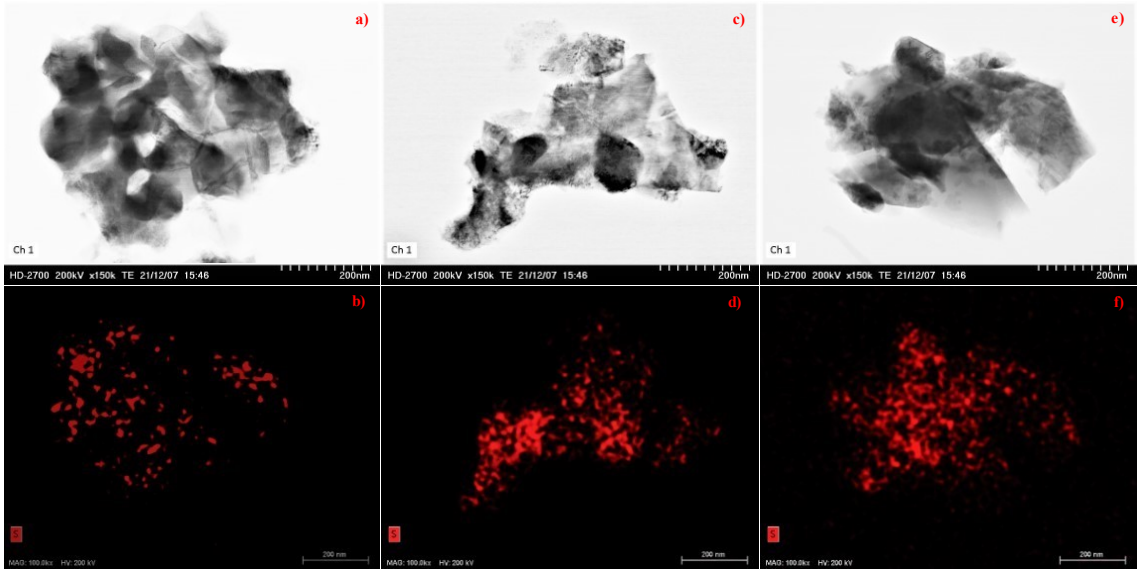

Figure 3.3-10: TEM micrographs of the spent Fe-Mn catalyst tested at different temperatures, and corresponding elemental maps of sulfur (a,b – 700 ºC, c,d – 750 ºC and e,f – 800 ºC).

Figure 3.3-11 shows thermodynamic predictions for interactions of H_2S with Fe or Mn and their oxides. Relevant reactions for Fe species may be ascribed as:

$$H_2S + Fe + 0.5O_2 \Leftrightarrow FeS + H_2O \quad \text{Eq. 3.3-15}$$

$$H_2S + FeO \Leftrightarrow FeS + H_2O \quad \text{Eq. 3.3-16}$$

$$H_2S + 1/3Fe_3O_4 \Leftrightarrow FeS + H_2O + 1/6O_2 \quad \text{Eq. 3.3-17}$$

$$H_2S + 0.5Fe_2O_3 \Leftrightarrow FeS + H_2O + 0.25O_2 \quad \text{Eq. 3.3-18}$$

Note that corresponding mass action constants yield equilibrium lines as functions of the pH_2S:pH_2O ratio and oxygen partial pressure. Note that the logarithmic scale is a suitable measure of chemical potential differences, relative equilibrium:

$$\Delta\mu_{H_2S} - \Delta\mu_{H_2O} = RTln\left(\frac{pH_2S}{pH_2O}\right) - RTln\left(\frac{pH_2S}{pH_2O}\right)_{eq} \quad \text{Eq. 3.3-19}$$

Thus, this may be taken as guideline for reactivity. Transitions from metallic Fe to FeO ($O_2 + 2Fe \Leftrightarrow FeO$) and FeO to Fe_3O_4 ($6FeO + O_2 \Leftrightarrow 2Fe_3O_4$) occur in a relatively short range, which is also close to conditions expected for biomass gasification. In fact, these redox conditions can also be expressed as function of $pH_2:pH_2O$ or $pCO:pCO_2$ ratio on assuming gas phase equilibrium, as indicated in the secondary horizontal axis. Thus, from the actual CO and CO_2 contents in Figure 3.3-7 one expects a relatively short redox range $0.5 < pCO:pCO_2 < 2$, which is consistent with transition from prevailing spinel to co-existence of spinel and wustite phases at higher gasification temperatures (Figure 3.3-9). This transition is even more likely under conditions imposed by the $pH_2:pH_2O$ redox pair, which tend to evolve faster with increasing temperatures, from less reducing conditions, in the stability range of magnetite, and through intermediate reducing conditions, in the stability range of wustite, in close agreement with thermogravimetry with a flowing 10%H_2-90%N_2 atmosphere.

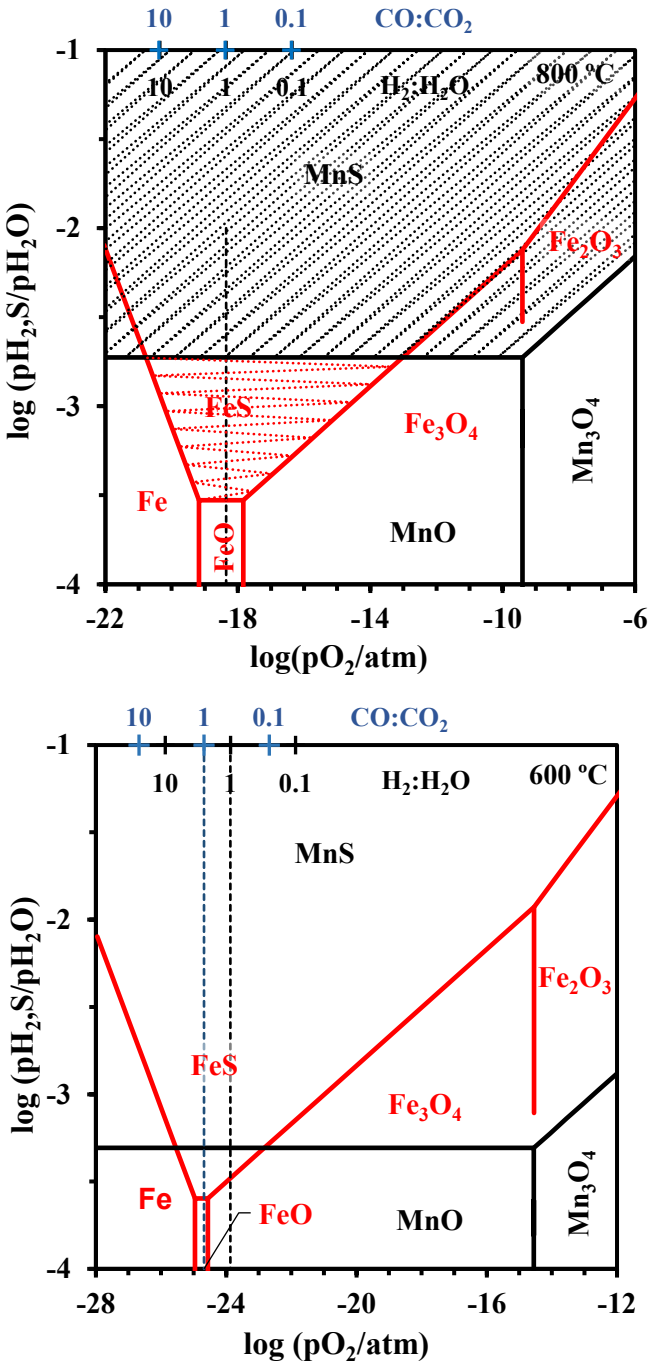

Figure 3.3-11: Thermodynamic predictions for sulphur and redox tolerance of Fe and Mn at 600 ºC and 800 ºC, as marked by shaded areas for the diagram at 800 ºC. The secondary horizontal axis shows typical redox ranges for gasification based on the expected range of $CO:CO_2$ or $H_2:H_2O$.

The stability range of metallic Fe is likely to require a combination of still higher temperatures and sufficiently dry H_2, which may not be fully attained in the actual experimental conditions. Figure 3.3-11 also shows that divalent manganese shows higher tolerance to hydrogen sulphide and much wider redox stability, greatly exceeding the range expected for gasification. Thus, the detected traces of sulphur (Figure 3.3-10) may be related mainly to the highest sensitivity of divalent iron oxide, whereas the fraction of manganese oxide provides greater tolerance. From Figure 3.3-11 at 800 ºC, one predicts tolerance up to $\mathrm{H_2S{:}\,H_2O} \approx 0.002$ and $\mathrm{pH_2S}$, and up to 2×10^{-4} atm (200 ppm) if one assumes a slightly humid producer gas ($\mathrm{pH_2O} \approx 0.1\ \mathrm{atm}$). Thus, one may assume that the apparent sulfur tolerance of the Fe-Mn catalyst results from the formation of the $(Fe,Mn)_xO_y$ oxides with positive impact on the sulfur resistance. Furthermore, it has also been reported that sulfur poisoning over Fe-Mn spinel oxides is a reversible deactivation mechanism and thus the catalyst can be regenerated to their initial activity using H_2O [44]. Still, future research on catalyst recovering, including a more comprehensive analysis of regeneration mechanisms to suppress sulfur compounds will be of major interest.

Biomass Gasification Performance

The influence of the Fe-Mn catalyst on gasification performance was assessed for the catalyst temperature at 800 ºC, equivalence ratio at 0.150 and GHSV at 3750 h^{-1} since those operating conditions were found to promote higher catalytic activity. The main gas components yield, such as H_2, CH_4, CO, CO_2 and light hydrocarbons C_xH_y (C_2H_4, C_2H_6, and C_3H_6) are presented in Figure 3.3-12. Compared to the reference condition (inert material), upgrading of the biomass-derived gas over the Fe-Mn catalyst led to an increase in the contents of CO (219.7 to 281.3 $\mathrm{g_{CO}} \cdot \mathrm{kg_{dry,fuel}^{-1}}$) and CO_2 (438.6 to 460.6 $\mathrm{g_{CO_2}} \cdot \mathrm{kg_{dry,fuel}^{-1}}$).

Although the Fe-Mn catalyst was expected to promote oxidation reactions under gasification conditions, H_2 yield slightly increased from 27.7 to 31.1 $\mathrm{g_{H_2}} \cdot \mathrm{kg_{dry,fuel}^{-1}}$, suggesting synergistic effects between Fe and Mn active sites. Note that WGS activity of Fe-based catalysts is promoted by redox mechanisms, resulting from the charge transfer between Fe^{2+} and Fe^{3+} cations [45], which may have contributed to mitigate the inhibitory effect of Mn species on H_2 production. Moreover, a substantial increase in both CH_4 (58.6 to 70.8 $\mathrm{g_{CH_4}} \cdot \mathrm{kg_{dry,fuel}^{-1}}$) and C_xH_y (27.3 to 37.0 $\mathrm{g_{C_xH_y}} \cdot \mathrm{kg_{dry,fuel}^{-1}}$) yields were observed, suggesting the hydrogenation of carbon oxides (CO_x) over the Fe-Mn catalyst. This has been also proposed by Shadravan et al. [46], investigating the selective hydrogenation of CO_x over Mn-promoted catalysts. The authors concluded that the affinity of Mn species toward oxidation reactions stabilize the CO dissociation products, providing a thermodynamic driving force that promotes C−O bond cleavage, with subsequent improvement in the conversion of CO_x to CH_4 and C_xH_y.

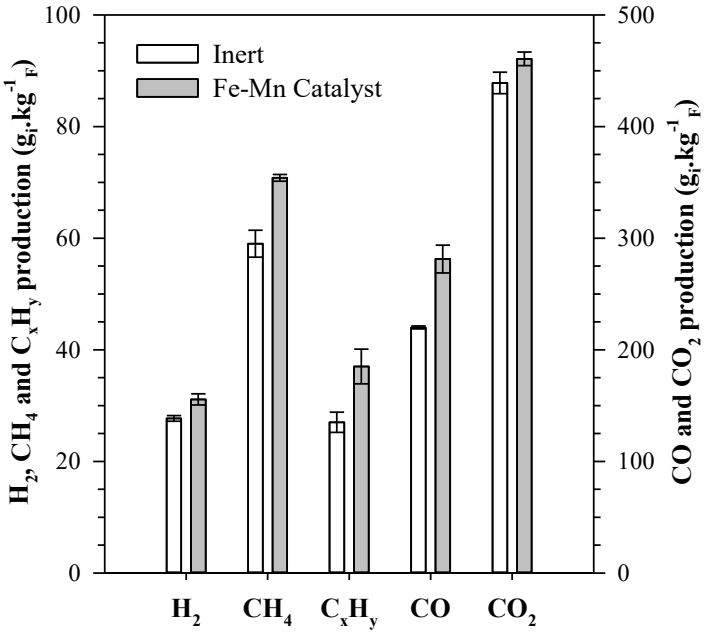

Figure 3.3-12: Yields of H_2, CH_4, CO, CO_2, and C_xH_y for the experiments performed with inert material and the Fe-Mn catalyst (T_{cat} = 800 ºC, ER = 0.150 and GHSV = 3750 h^{-1}).

Figure 3.3-13 shows the impact of the Fe-Mn catalyst on the lower heating value of the producer gas (LHV_G) and gasification process parameters, such as the specific dry gas production (Y_{Gas}), carbon conversion efficiency (CCE) and cold gas efficiency (CGE). It can be seen that the Y_{Gas} increased from 0.80 to 0.93 $\mathrm{Nm^3_{dry,gas} \cdot kg_F}$ when the Fe-Mn was employed. This increase is mainly associated with the catalytic conversion of tar compounds into permanent gases since the Fe-Mn catalyst was placed on the freeboard zone of the gasifier where char-related reactions have a minor impact on gas production. Furthermore, a relative increase of about 5.5 % was observed for the LHV_G of the producer gas which is consistent with the higher yields obtained for combustible products (Figure 3.3-12). The Fe-Mn catalyst also showed positive effects on CCE and CGE, with relative increases of 17.7 % and 21.6 %, respectively. Table 3.3-4 summarized the performance of different primary catalysts during gasification of biomass. It can be observed that tar conversion over the $Fe_{2-x}Mn_xO_3$ catalyst was equivalent to conventional Ni-based catalysts found in literature. However, comparison of these materials must be careful because the different reaction conditions (e.g. temperature, equivalence ratio, steam to carbon molar ratio, tar content…) were proven to affect catalyst activity.

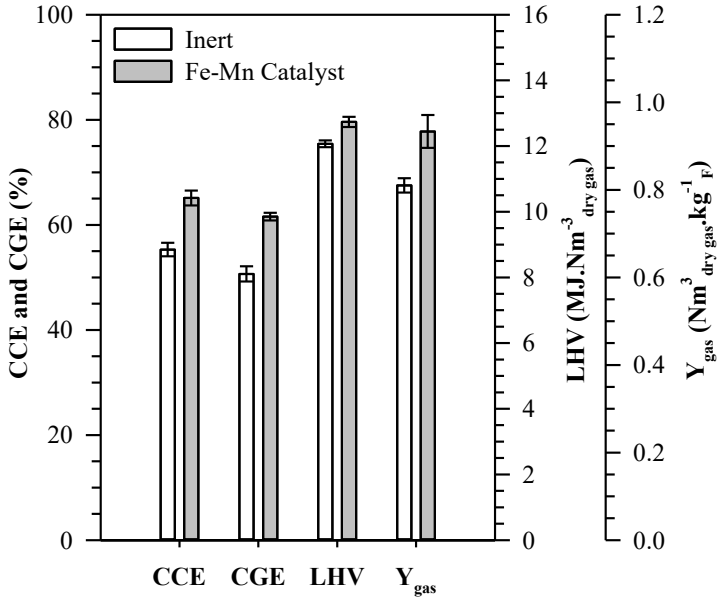

Figure 3.3-13: Y_{Gas}, CCE, CGE and LHV_G for the experiments performed with inert material and the Fe-Mn catalyst (T_{cat} = 800 ºC, ER = 0.150 and GHSV = 3750 h^{-1}).

Table 3.3-4: Performance of different primary catalysts under biomass gasification conditions.

Catalyst	T_{cat} (ºC)	ER (-)	S/C (-)	X_{Tar} (%)	CCE Increase (%)	CGE Increase (%)	Ref
$Fe_{2-x}Mn_xO_3$	800	0.15	0.5	83	17.7	21.6	This Work
Olivine	800	0.30	-	45	22.4	43.3	[47]
Fe/Olivine	800-850	-	1.3	78-81	-	-	[48,49]
Ni/Olivine	680	-	0.7	93	19.9	14.5	[50]
Dolomite	800	0.14	0.5	58	17.4	18.2	[51]
Fe-Ni/Olivine	850	0.28	-	90	17.3	5.6	[52]
Y-Al_2O_3	900	-	1.0	84	25.7	-	[53]
NiO/Y-Al_2O_3	800	0.22	1.3	99	-	-	[54]
Ni/Mayenite	800	-	0.7	90	-	-	[55]
CaO/Al_2O_3	860	-	2.0	58	17.0		[56]

3.3.4. Conclusion

A facile method to process porous and highly gas permeable $Fe_{2-x}Mn_xO_3$ catalysts was developed by combining incipient wetness impregnation of porous alumina-based supports with microwave-assisted firing. The performance of these catalysts was demonstrated by comparing with blank biomass gasification tests, and used to evaluate the influence of the catalyst temperature, equivalence ratio and gas hourly space velocity on tar decomposition. The results revealed that the catalyst temperature and equivalence ratio had a positive impact on the abatement of tar compounds, whereas increasing the gas hourly space velocity led to a decline in catalytic activity. Catalytic conversion of tar compounds followed a redox-type mechanism, facilitated by the variable oxygen stoichiometry of mixed Fe/Mn oxides, which promoted oxidation reactions.

Under optimal operating conditions, the catalyst promoted a significant increase in the tar conversion (83 %), gas yield (0.81 to 0.93 $\mathrm{Nm^3_{dry,gas}} \cdot \mathrm{kg^{-1}_{dry,fuel}}$), carbon conversion efficiency (55.3 to 65.1 %) and cold gas efficiency (50.7 to 61.6 %). Although post-mortem analysis of the spent catalyst showed presence of sulfur and increasing contents with rising temperature, this does not prevent enhanced catalytic activity, probably due to wide redox stability of divalent manganese oxide and its greater sulphur tolerance in gasification conditions, relative to corresponding iron oxides. Still, future research on catalyst poisoning is needed for more detailed analysis of prospective mechanisms and to minimize sulphur poisoning of gasification catalysts.

Acknowledgments

The authors acknowledge the financial support through projects NOTARGAS (ref. POCI-01-0145-FEDER-030661). Thanks to the Portuguese Foundation for Science and Technology (FCT) / Ministry of Science, Technology and Higher Education (MCTES) for the financial support to CESAM (UIDP/50017/2020+UIDB/50017/2020), and CICECO (UIDB/50011/2020 & UIDP/50011/2020), through national funds. The authors also acknowledge the Portuguese Foundation for Science and Technology for providing financial support to the PhD scholarship granted to Luís Ruivo (ref. SFRH/BD/129901/2017) and Helena Gomes (ref. 2020.09864.BD). Daniela V. Lopes acknowledges the support of her research fellow grant (ref. BI/UI50/9051/2020) withing the SIDERWIN project (SIDERWIN-DLV-768788 - Horizon 2020/SPIRE10).

References

[1] Milne T a, Evans RJ. Biomass Gasifier " Tars ": Their Nature , Formation , and Conversion. Constraints 1998. https://doi.org/10.2172/3726.

[2] Yung MM, Jablonski WS, Magrini-Bair KA. Review of catalytic conditioning of biomass-derived syngas. Energy and Fuels 2009. https://doi.org/10.1021/ef800830n.

[3] De Lasa H, Salaices E, Mazumder J, Lucky R. Catalytic steam gasification of biomass: Catalysts, thermodynamics and kinetics. Chem Rev 2011;111:5404–33. https://doi.org/10.1021/cr200024w.

[4] Huang BS, Chen HY, Chuang KH, Yang RX, Wey MY. Hydrogen production by biomass gasification in a fluidized-bed reactor promoted by an Fe/CaO catalyst. Int J Hydrogen Energy 2012;37:6511–8. https://doi.org/10.1016/j.ijhydene.2012.01.071.

[5] Zamboni I, Zimmermann Y, Kiennemann A, Courson C. Improvement of steam reforming of toluene by CO2 capture using Fe/CaO-Ca12Al14O33 bi-functional materials. Int J Hydrogen Energy 2015;40:5297–304. https://doi.org/10.1016/j.ijhydene.2015.01.065.

[6] Ruivo LCM, Pio DT, Yaremchenko AA, Tarelho LAC, Frade JR, Kantarelis E, et al. Iron-based catalyst (Fe2-xNixTiO5) for tar decomposition in biomass gasification. Fuel 2021;300:120859. https://doi.org/10.1016/j.fuel.2021.120859.

[7] Zou J, Oladipo J, Fu S, Al-Rahbi A, Yang H, Wu C, et al. Hydrogen production from cellulose catalytic gasification on CeO2/Fe2O3 catalyst. Energy Convers Manag 2018;171:241–8. https://doi.org/10.1016/j.enconman.2018.05.104.

[8] Moud PH, Andersson KJ, Lanza R, Pettersson JBC, Engvall K. Effect of gas phase alkali species on tar reforming catalyst performance: Initial characterization and method development. Fuel 2015;154:95–106. https://doi.org/10.1016/j.fuel.2015.03.027.

[9] Huang Z, Zhang Y, Fu J, Yu L, Chen M, Liu S, et al. Chemical looping gasification of biomass char using iron ore as an oxygen carrier. Int J Hydrogen Energy 2016;41:17871–83. https://doi.org/10.1016/j.ijhydene.2016.07.089.

[10] Hu J, Li C, Lee DJ, Guo Q, Zhao S, Zhang Q, et al. Syngas production from biomass using Fe-based oxygen carrier: Optimization. Bioresour Technol 2019;280:183–7. https://doi.org/10.1016/j.biortech.2019.02.012.

[11] Chen J, Zhao K, Zhao Z, He F, Huang Z, Wei G. Identifying the roles of MFe 2 O 4 (M=Cu, Ba, Ni, and Co) in the chemical looping reforming of char, pyrolysis gas and tar resulting from biomass pyrolysis. Int J Hydrogen Energy 2019;44:4674–87. https://doi.org/10.1016/j.ijhydene.2018.12.216.

[12] Li WB, Wang JX, Gong H. Catalytic combustion of VOCs on non-noble metal catalysts. Catal Today 2010;148:81–7. https://doi.org/10.1016/j.cattod.2009.03.007.

[13] Yang L, Bukhovko MP, Malek A, Li L, Jones CW, Agrawal PK, et al. Steam reforming kinetics of olefins and aromatics over Mn-Cr-O spinel oxides. J Catal 2021;404:964–76. https://doi.org/10.1016/j.jcat.2021.05.034.

[14] Tomishige K, Li D, Tamura M, Nakagawa Y. Nickel-iron alloy catalysts for reforming of hydrocarbons: Preparation, structure, and catalytic properties. Catal Sci Technol 2017. https://doi.org/10.1039/c7cy01300k.

[15] Garcia T, Sellick D, Varela F, Vázquez I, Dejoz A, Agouram S, et al. Total oxidation of naphthalene using bulk manganese oxide catalysts. Appl Catal A Gen 2013. https://doi.org/10.1016/j.apcata.2012.10.029.

[16] Wu Y, Feng R, Song C, Xing S, Gao Y, Ma Z. Effect of reducing agent on the structure and activity of manganese oxide octahedral molecular sieve (OMS-2) in catalytic combustion of o-xylene. Catal Today 2017;281:500–6. https://doi.org/10.1016/j.cattod.2016.05.024.

[17] Ma WJ, Huang Q, Xu Y, Chen YW, Zhu SM, Shen SB. Catalytic combustion of toluene over Fe-Mn mixed oxides supported on cordierite. Ceram Int 2013;39:277–81.

https://doi.org/10.1016/j.ceramint.2012.06.022.
[18] Bendoni R, Miccio F, Medri V, Benito P, Vaccari A, Landi E. Geopolymer composites for the catalytic cleaning of tar in biomass-derived gas. Renew Energy 2019;131:1107–16. https://doi.org/10.1016/j.renene.2018.08.067.
[19] Channiwala SA, Parikh PP. A unified correlation for estimating HHV of solid, liquid and gaseous fuels. Fuel 2002;81:1051–63.
[20] Pio DT, Gomes HGMF, Ruivo LCM, Matos MAA, Monteiro JF, Frade JR, et al. Concrete as low-cost catalyst to improve gas quality during biomass gasification in a pilot-scale gasifier. Energy 2021;233:120931. https://doi.org/10.1016/j.energy.2021.120931.
[21] Pio DT, Gomes HGMF, Tarelho LAC, Vilas-Boas ACM, Matos MAA, Lemos FMS. Superheated steam injection as primary measure to improve producer gas quality from biomass air gasification in an autothermal pilot-scale gasifier. Renew Energy 2022;181:1223–36. https://doi.org/10.1016/j.renene.2021.09.083.
[22] Lin X, Li S, He H, Wu Z, Wu J, Chen L, et al. Evolution of oxygen vacancies in MnOx-CeO2 mixed oxides for soot oxidation. Appl Catal B Environ 2018;223:91–102. https://doi.org/10.1016/j.apcatb.2017.06.071.
[23] Crum J V., Riley BJ, Vienna JD. Binary phase diagram of the manganese oxide-iron oxide system. J Am Ceram Soc 2009;92:2378–84. https://doi.org/10.1111/j.1551-2916.2009.03230.x.
[24] Wang H, Yang Y, Xu J, Wang H, Ding M, Li Y. Study of bimetallic interactions and promoter effects of FeZn, FeMn and FeCr Fischer-Tropsch synthesis catalysts. J Mol Catal A Chem 2010;326:29–40. https://doi.org/10.1016/j.molcata.2010.04.009.
[25] Li T, Wang H, Yang Y, Xiang H, Li Y. Effect of manganese on the catalytic performance of an iron-manganese bimetallic catalyst for light olefin synthesis. J Energy Chem 2013;22:624–32. https://doi.org/10.1016/S2095-4956(13)60082-0.
[26] Kang YB, Jung IH. Thermodynamic modeling of oxide phases in the Fe–Mn–O system. J Phys Chem Solids 2016;98:237–46. https://doi.org/10.1016/j.jpcs.2016.07.017.
[27] Li T, Yang Y, Zhang C, Tao Z, Wan H, An X, et al. Effect of Manganese Incorporation Manner on an Iron-Based Catalyst for Fischer-Tropsch Synthesis. J Nat Gas Chem 2007;16:244–51. https://doi.org/10.1016/S1003-9953(07)60055-3.
[28] Berthon J, Revcolevschi A, Morikawa H, Touzelin B. LETTER TO THE EDITORS GROWTH OF WUSTITE (Fe1-xO)CRYSTALS OF VARIOUS STOICHIOMETRIES. J Cryst Growth 1979;47:736–8.
[29] Bliem R, McDermott E, Ferstl P, Setvin M, Gamba O, Pavelec J, et al. Subsurface cation vacancy stabilization of the magnetite (001) surface. Science (80-) 2014;346:1215–8. https://doi.org/10.1126/science.1260556.
[30] Da Silva Alvim R, Ribeiro FN, Dalpian GM. Iron and oxygen vacancies at the hematite surface: Pristine case and with a chlorine adatom. Phys Chem Chem Phys 2020;22:25380–9. https://doi.org/10.1039/d0cp03798b.
[31] Kolk B, Albers A, Leith IR, Howden MG. Mössbauer and x-ray studies of the structure of iron-manganese oxide catalyst precursors. Appl Catal 1988;37:57–74. https://doi.org/10.1016/S0166-9834(00)80751-4.
[32] Koike M, Li D, Watanabe H, Nakagawa Y, Tomishige K. Comparative study on steam reforming of model aromatic compounds of biomass tar over Ni and Ni-Fe alloy nanoparticles. Appl Catal A Gen 2015;506:151–62. https://doi.org/10.1016/j.apcata.2015.09.007.
[33] Hüttinger KJ, Merdes WF. The carbon-steam reaction at elevated pressure: Formations of product gases and hydrogen inhibitions. Carbon N Y 1992;30:883–94. https://doi.org/10.1016/0008-6223(92)90011-K.
[34] Arjmand M, Leion H, Mattisson T, Lyngfelt A. Investigation of different manganese ores as oxygen carriers in chemical-looping combustion (CLC) for solid fuels. Appl Energy

2014;113:1883–94. https://doi.org/10.1016/j.apenergy.2013.06.015.
[35] Lyu Y, Li C, Du X, Zhu Y, Zhang Y, Li S. Catalytic oxidation of toluene over MnO2 catalysts with different Mn (II) precursors and the study of reaction pathway. Fuel 2020;262:116610. https://doi.org/10.1016/j.fuel.2019.116610.
[36] Baldi M, Escribano VS, Amores JMG, Milella F, Busca G. Characterization of manganese and iron oxides as combustion catalysts for propane and propene. Appl Catal B Environ 1998;17:175–82. https://doi.org/10.1016/S0926-3373(98)00013-7.
[37] Nampi PP, Moothetty P, Berry FJ, Mortimer M, Warrier KG. Aluminosilicates with varying alumina-silica ratios: Synthesis via a hybrid sol-gel route and structural characterisation. Dalt Trans 2010;39:5101–7. https://doi.org/10.1039/c001219j.
[38] Nieto MI, Urretavizcaya G, Cavalieri AL, Pena P. Structural changes in colloidal and polymeric aluminosilicate gels with mullite composition. Br Ceram Trans 1998;97:17.
[39] Yang W, Su Z, Xu Z, Yang W, Peng Y, Li J. Comparative study of α-, β-, γ- and δ-MnO2 on toluene oxidation: Oxygen vacancies and reaction intermediates. Appl Catal B Environ 2020;260:118150. https://doi.org/10.1016/j.apcatb.2019.118150.
[40] Garcia T, Sellick D, Varela F, Vázquez I, Dejoz A, Agouram S, et al. Total oxidation of naphthalene using bulk manganese oxide catalysts. Appl Catal A Gen 2013;450:169–77. https://doi.org/10.1016/j.apcata.2012.10.029.
[41] Mars P, van Krevelen DW. Oxidations carried out by means of vanadium oxide catalysts. Chem Eng Sci 1954;3:41–59. https://doi.org/10.1016/S0009-2509(54)80005-4.
[42] Gao C, Shi JW, Fan Z, Gao G, Niu C. Sulfur and water resistance of mn-based catalysts for low-temperature selective catalytic reduction of NOx: A review. Catalysts 2018;8. https://doi.org/10.3390/catal8010011.
[43] Sharma L, Purdy SC, Page K, Rangarajan S, Pham H, Datye A, et al. Sulfur Tolerant Subnanometer Fe/Alumina Catalysts for Propane Dehydrogenation. ACS Appl Nano Mater 2021;4:10055–67. https://doi.org/10.1021/acsanm.1c01366.
[44] Zhihang C, Wang F, Li H, Wang L, Li X. Low-Temperature Selective Catalytic Reduction of NOx with NH3 over Fe_Mn Mixed-Oxide Catalysts Containing Fe3Mn3O8 Phase. Ind Eng Chem Res 2011;51:202–12.
[45] Popa T, Xu G, Barton TF, Argyle MD. High temperature water gas shift catalysts with alumina. Appl Catal A Gen 2010;379:15–23. https://doi.org/10.1016/j.apcata.2010.02.021.
[46] Shadravan V, Bukas VJ, Gunasooriya GTKK, Waleson J, Drewery M, Karibika J, et al. Effect of Manganese on the Selective Catalytic Hydrogenation of CO x in the Presence of Light Hydrocarbons over Ni/Al2O3: An Experimental and Computational Study. ACS Catal 2020;10:1535–47. https://doi.org/10.1021/acscatal.9b04863.
[47] Christodoulou C, Grimekis D, Panopoulos KD, Pachatouridou EP, Iliopoulou EF, Kakaras E. Comparing calcined and un-treated olivine as bed materials for tar reduction in fluidized bed gasification. Fuel Process Technol 2014;124:275–85. https://doi.org/10.1016/j.fuproc.2014.03.012.
[48] Pan Y, Abulizi A, Talifu D, Tursun Y, Xu S. Catalytic gasification of biomass and coal blend with Fe2O3/olivine in a decoupled triple bed. Fuel Process Technol 2019;194:106121. https://doi.org/10.1016/j.fuproc.2019.106121.
[49] Virginie M, Adánez J, Courson C, De Diego LF, García-Labiano F, Niznansky D, et al. Effect of Fe-olivine on the tar content during biomass gasification in a dual fluidized bed. Appl Catal B Environ 2012;121–122:214–22. https://doi.org/10.1016/j.apcatb.2012.04.005.
[50] Wang G, Xu S, Wang C, Zhang J, Fang Z. Desulfurization and tar reforming of biogenous syngas over Ni/olivine in a decoupled dual loop gasifier. Int J Hydrogen Energy 2017;42:15471–8. https://doi.org/10.1016/j.ijhydene.2017.05.041.
[51] Tian Y, Zhou X, Lin S, Ji X, Bai J, Xu M. Syngas production from air-steam gasification of biomass with natural catalysts. Sci Total Environ 2018;645:518–23.

https://doi.org/10.1016/j.scitotenv.2018.07.071.

[52] Meng J, Wang X, Zhao Z, Zheng A, Huang Z, Wei G, et al. Highly abrasion resistant thermally fused olivine as in-situ catalysts for tar reduction in a circulating fluidized bed biomass gasifier. Bioresour Technol 2018;268:212–20. https://doi.org/10.1016/j.biortech.2018.07.135.

[53] Erkiaga A, Lopez G, Amutio M, Bilbao J, Olazar M. Steam gasification of biomass in a conical spouted bed reactor with olivine and γ-alumina as primary catalysts. Fuel Process Technol 2013;116:292–9. https://doi.org/10.1016/j.fuproc.2013.07.008.

[54] Li J, Liu J, Liao S, Yan R. Hydrogen-rich gas production by air-steam gasification of rice husk using supported nano-NiO/γ-Al2O3 catalyst. Int J Hydrogen Energy 2010. https://doi.org/10.1016/j.ijhydene.2010.04.108.

[55] Di Carlo A, Borello D, Sisinni M, Savuto E, Venturini P, Bocci E, et al. Reforming of tar contained in a raw fuel gas from biomass gasification using nickel-mayenite catalyst. Int J Hydrogen Energy 2015. https://doi.org/10.1016/j.ijhydene.2015.05.128.

[56] Xie Y, Xiao J, Shen L, Wang J, Zhu J, Hao J. Effects of Ca-based catalysts on biomass gasification with steam in a circulating spout-fluid bed reactor. Energy and Fuels 2010;24:3256–61. https://doi.org/10.1021/ef100081w.

Supplementary Material

Table S1 – Experimental results obtained at the reactor outlet during biomass gasification experiments performed with inert material.

Experiment	*Experimental Conditions*			*Producer Gas Composition*					*Operating Parameters*				
	T_{cat} (ºC)	ER (-)	GHSV (h^{-1})	CO (vol.%)	H_2 (vol.%)	CO_2 (vol.%)	CH_4 (vol.%)	C_xH_y (vol.%)	Y_{Tar} $(g_{tar} \cdot kg_F)$	Y_{Gas} $(Nm^3 \cdot kg_F)$	LHV_{Gas} $(MJ \cdot Nm^{-3})$	*CCE (%)*	*CGE (%)*
Blank-E1	700	0.100	2500	21.4	37.7	32.6	6.1	2.3	313.9	0.536	10.4	36.7	29.0
Blank-E2	750	0.100	2500	23.2	38.0	28.2	6.8	2.9	244.7	0.796	11.5	53.0	47.3
Blank-E3	800	0.100	2500	28.8	36.3	24.7	7.4	2.8	207.0	0.802	11.9	56.4	49.6
Blank-E4	800	0.125	2500	22.3	38.2	27.5	9.7	2.4	143.2	0.812	11.9	55.6	50.4
Blank-E5	800	0.150	2500	21.1	36.5	29.2	10.8	2.4	119.0	0.831	12.0	57.9	51.5
Blank-E6	800	0.150	3750	21.5	36.1	29.8	10.3	2.3	136.7	0.830	11.8	57.9	50.4
Blank-E7	800	0.150	5000	20.8	35.8	30.3	10.3	2.8	148.5	0.833	12.0	59.2	51.6

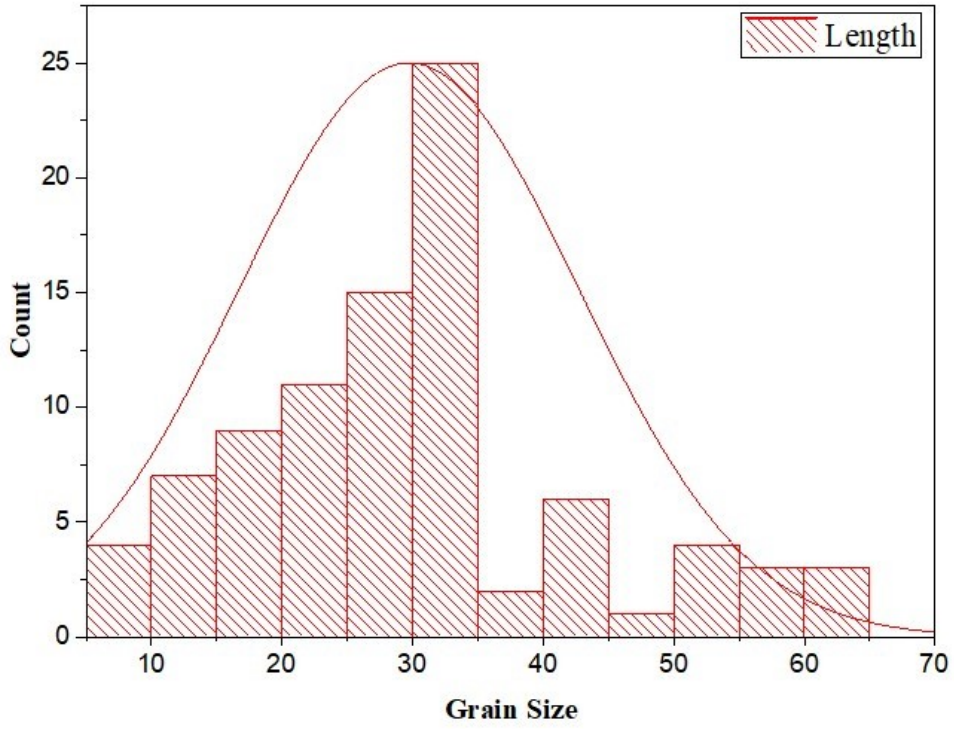

Figure S1 – Gaussian distribution of Fe-Mn grain size for the crushed catalyst sample.

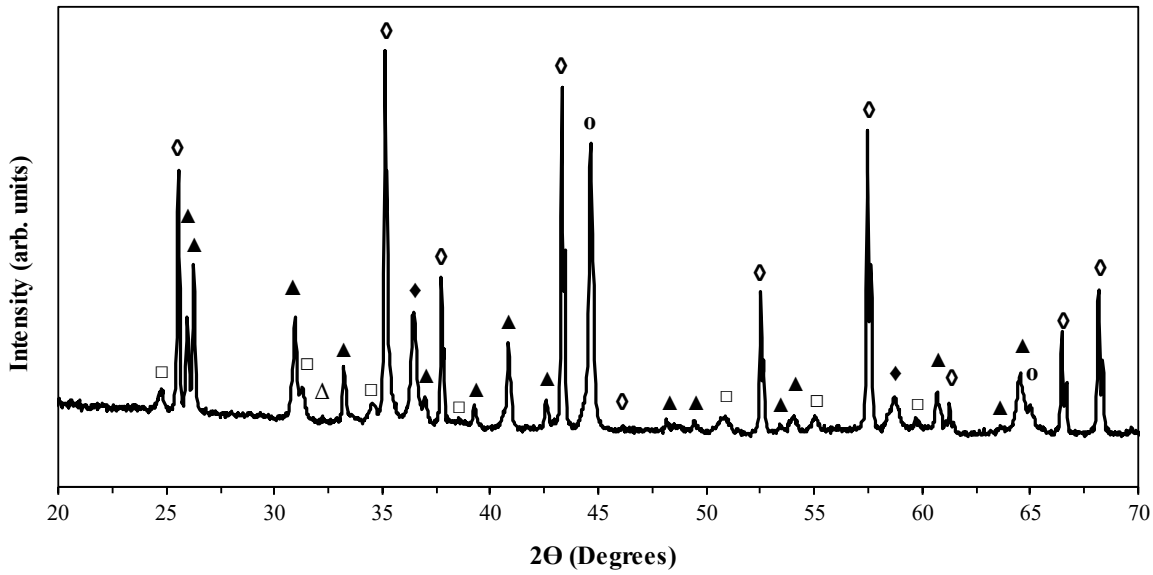

Figure S2 – X-ray diffraction pattern of the spent Fe-Mn catalyst sample after thermogravimetric studies in 10%H_2-N_2 atmosphere (▲ – $Al_{2.36}Si_{0.64}O_{4.82}$ ◊ – Al_2O_3 ♦ – $(Fe,Mn)_3O_4$ □ – $(Mn,Fe)_2SiO_4$ o – Fe).

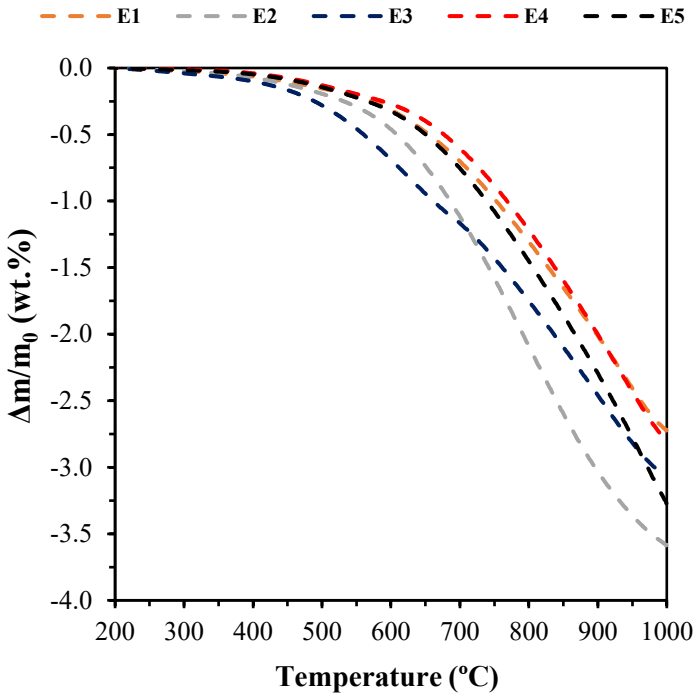

Figure S3 – Thermogravimetric (TG) curves of the spent Fe-Mn catalysts samples in 10%H_2-N_2 atmosphere at 5 ºC·min^{-1}.

Table S2 – Calculation of the changes in the oxygen stoichiometry of the spent catalysts ($\Delta\delta$) from the TGA curves shown in Figure S3.

Sample	Catalytic Experiments			TGA Results			
	Temperature (ºC)	ER (-)	GHSV (h^{-1})	$m_{initial}$ (mg)	m_{end} (mg)	δ_i (μmol·g^{-1})	$\Delta\delta$ (μmol·g^{-1})
Fresh Catalyst	-	-	-	472.87	453.44	2569	-
Spent Catalyst (E1)	700	0.100	2500	469.64	456.84	2242	-326
Spent Catalyst (E2)	750	0.100	2500	253.51	244.41	1920	-469
Spent Catalyst (E3)	800	0.100	2500	432.75	419.46	1703	-866
Spent Catalyst (E4)	800	0.125	2500	469.91	456.74	1752	-817
Spent Catalyst (E5)	800	0.150	2500	465.88	450.64	2046	-523

3.4. Siderite/Concrete Catalysts for H_2-enriched Gas Production from Biomass Steam Gasification

Luís Ruivo, Hortência Oliveira, Helena Gomes, Nuno Cruz, Aleksey Yaremchenko, Luís Tarelho, Jorge Frade
University of Aveiro (CESAM and CICECO)
Published in Energy Conversion and Management, 2022, 255, 115280.

Abstract

In this study, granulated siderite/concrete-based catalysts are proposed for in-situ applications in biomass steam gasification, seeking H_2-enrichement by the contribution of water gas shift and CO_2 adsorption. A cost-effective procedure has been applied for the preparation of granulated catalysts. Water Gas Shift reaction was studied in a fixed bed reactor and Taguchi experimental design was used to elucidate the relevance of experimental parameters on catalyst performance. The results show that the impact of reaction temperature, concrete/siderite ratio and steam to carbon molar ratio on H_2 promotion had the following order: reaction temperature (43.1 %), concrete/siderite ratio (30.2 %) and steam to carbon molar ratio (26.7 %). Additionally, the catalyst exhibited high activity when integrated into the freeboard zone of a bubbling fluidized bed gasifier. Compared to the reference condition, one observed significant impact at 700 ºC on the H_2:CO ratio (1.9 to 3.3), H_2 production (33.8 to 48.6 $g_{H_2} \cdot kg_{dry,fuel}^{-1}$), carbon conversion efficiency (54.1 to 58.6 %) and cold gas efficiency (55.0 to 60.9 %). Though the catalyst exhibited resistance to sintering, post-mortem analysis suggests loss of active species after repeated cycles of regeneration due to thermal-induced stresses, which caused gradual decrease in activity.

Keywords: Biomass, Gasification, Catalyst, Siderite, Concrete.

3.4.1. Introduction

Steam gasification of lignocellulosic biomass is considered an attractive route to promote the integration of bio-based fuels, produced from low-value or residual biomass sources by a circular economy perspective [1,2]. It can also be employed to enhance the efficiency of biomass-based energy by increasing H_2-rich natural gas in boilers or integrated gasification combined cycles for electricity generation. The process occurs at high temperatures and involves the partial conversion of a solid carbonaceous material such as biomass into a combustible gas through interaction with steam. The producer raw gas consist mainly of CO, H_2, CO_2, CH_4 and C_xH_y [3], but additional impurities and condensable compounds (tars) are also generated during the process, requiring the clean-up of the producer gas for further application [4,5].

One of the most demanding areas of current biomass gasification research is related to substitution of natural gas by synthetic gas (SNG) for end-use technologies such as gas turbines or transportation vehicles, taking advantage of the natural gas infrastructure for distribution and storage [6]. The SNG is produced by methanation reactions (3.4-1) and (3.4-2), in the presence of Ni-based catalysts. Though the producer gas is greatly influenced by gasification conditions, the H_2:CO molar ratio fluctuates in the range of 1.5-2.0 which favours a series of parallel reactions (3.4-3)-(3.4-5) and coke formation during methanation

[7]. Additionally, high contents of CO may promote exothermic reactions, causing sintering of catalyst particles by local overheating [8]. Therefore, the H_2/CO molar ratio of producer gas must be upgraded by catalytic Water Gas Shift (WGS) reaction (3.4-6) before methanation [9,10].

$$CO + 3H_2 \leftrightarrow CH_4 + H_2O \quad \text{Eq. 3.4-1}$$

$$CO_2 + 4H_2 \leftrightarrow CH_4 + 2H_2O \quad \text{Eq. 3.4-2}$$

$$CO + H_2 \leftrightarrow C + H_2O \quad \text{Eq. 3.4-3}$$

$$CO_2 + 2H_2 \leftrightarrow C + 2H_2O \quad \text{Eq. 3.4-4}$$

$$2CO \leftrightarrow C + CO_2 \quad \text{Eq. 3.4-5}$$

$$CO + H_2O \leftrightarrow H_2 + CO_2 \quad \text{Eq. 3.4-6}$$

Industrial WGS reaction processes are mainly focused on production of H_2 with low CO content, to prevent poisoning of catalysts, and two types of catalysts are applied in separate fixed-bed reactors: relatively high temperature (HTS, 350-500 ºC) and low temperature (LTS, 150-300 ºC) catalysts. Particular attention has been given to the use of Fe/Cr-based mixed oxides (HTS) and Cu/Zn mixed oxides (LTS) [11–13]. In the case of the Fe/Cr-based catalysts, the environmental implications of chromium have motivated the research of alternative promoters such as Mg, Co, Mo, Ce, Al, Mn or Zn [14–18]. Cu/Zn-based catalysts are also deactivated at low sulphur content (< 0.5 ppm), requiring previous gas cleaning [19]. Additionally, the operation of the WGS unit at high pressures penalizes notably the overall economic balance of the gasification plant [20].

A more interesting option is based on the integration of WGS catalysts in the gasifier unit, allowing to improve the economic viability by decreasing system and production costs [21]. In this case, higher gasification temperatures, often ≥ 700 ºC, and other operating conditions in gasifier units differ markedly from those of reactors for CO-lean H_2 production. Thus, different catalyst concepts are required with emphasis on widely available minerals or wastes, or low cost oxides such as CaO, with CO_2 sorption ability and prospects to reach higher H_2 yields [22,23].

The main drawbacks of CaO-based catalysts are the deactivation after carbonation, which requires continuous regeneration cycles, and its poor erosion resistance, which causes elutriation from the gasifier [24,25]. Alternatively, the use of so-called Fe/CaO bi-functional catalysts in gasification processes is gaining more attention, due to their thermal stability, low-cost and effective activity towards WGS and reforming reactions. Huang et al. [26] studied the performance of a $Ca_2Fe_2O_5$/CaO catalyst during biomass gasification and concluded that the promotion of H_2 is achieved by the contribution of $Ca_2Fe_2O_5$ to avoid deactivation of CaO. The O_2-storage ability of calcium ferrite $Ca_2Fe_2O_5$ also enhances the oxidation of CO. Ismail et al. [27] achieved similar results investigating the role of chemical looping of CaO/Fe_2O_3 mixed oxides during H_2 production. The authors observed that the addition of CaO gives cyclic stability and additional capacity to produce H_2. Zamboni et al. [28] prepared composite Fe/(CaO+$Ca_{12}Al_{14}O_{33}$) catalysts and tested their potential

application to produce H_2 via biomass steam gasification in a fixed-bed reactor. These multiphase catalysts were active for both tar steam reforming and WGS reactions enhanced by in-situ CO_2 capture. The results also suggested that H_2 yield is improved by the redox behavior of α-Fe_2O_3.

Previous research has demonstrated the importance of catalyst sustainability with respect to both the production costs and environmental implications [29]. Particular attention has been provided to the design of low-cost catalysts by using Fe-containing natural minerals such as ilmenite or large-scale industrial wastes [30,31]. In this context, concrete wastes from the construction sector can be widely available CaO-rich wastes with potential catalytic activity in biomass gasification processes. Annual world cement production is expected to grow from approximately 2540 million tons (Mt) in 2006 to around 4380 Mt in 2050 with corresponding impact on massive waste management [32]. The most common minerals in Portland cement mainly include di-calcium (Ca_2SiO_4) and tricalcium (Ca_3SiO_5) silicates, which react in the presence of H_2O to form portlandite ($Ca(OH)_2$) and hydrated calcium silicates [33]. Calcium aluminates in cement compositions (e.g. $Ca_{12}Al_{14}O_{33}$) also react readily. Thus, one considered cement or concrete wastes as alternative widely available sorbents for low cost catalysts.

The fraction of iron oxide in cement is usually low, requiring additional sources for composite catalysts. The most common Fe-based minerals (hematite and magnetite) are key raw materials for metallurgy, whereas other minerals such as pyrite (FeS_2) or molysite ($FeCl_3$) release corrosive gases and raise environmental concerns. Thus, relevant literature on catalytic gasification proposed mainly other Fe-containing minerals such as ilmenite or olivine. In the present work one proposes the use of siderite, which contains mainly $FeCO_3$. This phase undergoes thermal decomposition at typical temperatures of reforming or water gas shift reactions, yielding a dry reforming reactant (CO_2) and the resulting Fe oxides are likely to evolve from the unstable divalent state to higher oxidation. In fact, siderite has already been proposed as a catalyst for coal gasification [34], but its applicability in biomass gasification processes has never been assessed.

Therefore, the present work aimed to investigate the catalytic performance of novel composite catalysts, based on siderite/concrete precursor mixtures, towards gasification and WGS reaction. For that purpose, a cost-effective procedure based on mechanical granulation was developed for the preparation of these composite catalysts, followed by their detailed characterization. An experimental design based on the Taguchi method [35] was used to seek suitable conditions for H_2 promotion, by varying the catalyst composition, reaction temperature and steam to carbon molar ratio. Afterward, the catalytic activity for H_2 production was tested in a 3 kW_{th} bench-scale BFB gasifier. In addition to solving specific issues related to the quality improvement of the gas from biomass steam gasification, this work results are also expected to benefit both academic and engineering fields, creating prospects for the design of novel catalytic concepts inspired by large-scale materials that are often managed as waste, thus contributing to fulfill the goals of circular economy.

3.4.2. Materials and Methods

3.4.2.1. Catalyst Preparation

The composite catalysts were prepared from mixtures of siderite (SIDCO Minerals Inc.) and simulated concrete, using different concrete contents, i.e., 0 wt.%, 25 wt.% and 50 wt.%. The simulated concrete formulation was prepared with Portland cement (CIMPOR) and silica sand, with a mass ratio sand:cement = 3, and water:solid with ratio = 0.5. This mixture was stirred at 100 rpm, dried at 25 ºC for 24 h, then cured in autoclave at 180 ºC for 12 h, ground and aged for 1 month in ambient air. Additionally, a sample of concrete was aged for 1 year to simulate concrete wastes, in order to assess potential structural changes after long term storage. The catalyst samples were prepared by granulation from siderite and 1 month aged concrete, as follows: (i) the siderite and concrete powders precursors were mixed in an appropriate proportion with 5 wt.%. of H_2O, using a helical ribbon agitator; (ii) the resulting mixture was subsequently inserted in a rotary drum and 15 wt.% of H_2O was gradually added by atomization, until the formation of nearly spherical structured bodies; (iii) the granules were then dried at 110 ºC for 24h for the removal of moisture and subsequently sieved to 2-4 mm; (iv) the selected fraction of granules was then subjected to thermal treatment at 700 °C in N_2 atmosphere for 1h to attained adequate mechanical strength and promote the decomposition of $FeCO_3$ into Fe_3O_4 phase; the temperature was increased at a rate of 10 ºC·min^{-1} from room temperature up to the desired temperature. The concrete-free sample was used as a reference, and the resulting granulated catalysts were denoted as 0%C-Fe, 25%C-Fe and 50%C-Fe.

3.4.2.2. Catalyst Characterization

Analysis of the elemental composition of the fresh and spent catalysts was performed by X-ray fluorescence (XRF), using a Philips X′Pert PRO MPD spectrometer. The crystalline phases were assessed by X-ray diffraction (XRD) carried out on a Panalytical X'Pert Pro^3 diffractometer. Diffraction patterns were obtained between 2θ values of 10 and 80º, with a scan step of 0.02º and exposition time of 200 s. The International Center for Diffraction Data (ICDD) was used for diffraction assignments.

The scanning electron microscopy (SEM, Hitachi SU-70 operated at 15 kV) equipped with energy dispersive X-Ray spectroscopy (EDS, Bruker Quantax 400 detector) was used to investigate the surface morphology and elemental distribution of the fresh and spent granulated catalysts. The samples were mounted on aluminum sample holders and coated with carbon using a sputter coater to guarantee that the samples were conductive. The skeletal density of the granulated catalysts was determined by helium pycnometer, whereas total porosity was estimated according to the Archimedes method [36]. The Shimadzu apparatus (model AG-X/R refresh) was used for compressive strength tests. The side crushing strength (SCS) method [37] was applied for 5 specimens, with the results presented as the average value.

In order to investigate the CO_2 absorption capacity of concrete and to screen structural changes in siderite at gasification temperatures, thermal analysis was conducted using a Setaram SetSys 16/18 thermogravimetric analyzer (TGA). The experiments were performed in 10% H_2 – 90% N_2 and CO_2 atmospheres flowing through the siderite and

concrete samples, respectively, with a flow of 25 $cm^3 \cdot min^{-1}$. The temperature was ramped at 1-2 °C·min^{-1} from room temperature up to 1000 °C.

Post-mortem analysis of the granulated catalyst after the gasification experiments was also performed by Fourier-transform infrared spectroscopy (FTIR). The spectra of the samples were recorded by accumulating 64 scans at 4 cm^{-1} resolution in the spectral range of 500−4000 cm^{-1} using a GALAXY SERIES FT-IR 7000 spectrometer equipped with a DTGS CsI detector.

3.4.2.3. Water Gas Shift (WGS) Reaction

Taguchi-type Experimental Design

The catalyst activity on water gas shift reaction was evaluated at different sets of parametric conditions, following the design matrix developed by Taguchi [38]. An L9 orthogonal array was applied for the design of the experiments considering three design parameters at three different levels (Table 3.4-1). The parameters investigated were the mass fraction of concrete in the catalyst composition (X_{conc}= concrete/concrete+siderite), reaction temperature (T), and steam to carbon molar ratio (S/C). Based on the experimental data, the signal-to-noise ratio (3.4-7) was calculated to determine the optimal parameters combination. The analysis of variance (ANOVA) of the response data was also used to evaluate the contribution factor (3.4-8) and the statistical significance for the individual parameters.

$$SNR = \frac{1}{i}\left[-10\log\frac{1}{n}\left(\sum_{j=1}^{3}\frac{1}{y_{i,j}^2}\right)\right] \quad \text{Eq. 3.4-7}$$

$$CF\ (\%) = \frac{SS_f}{SS_T} \times 100 \quad \text{Eq. 3.4-8}$$

$$SS_f = \sum_{l=1}^{3} k\left[(SNR)_{f,l} - SNR_T\right]^2 \quad \text{Eq. 3.4-9}$$

$$SS_T = \sum_{i=1}^{9}(SNR_i - SNR_T)^2 \quad \text{Eq. 3.4-10}$$

where i is the number of experiments, n and j are the number of replications for each experiment and the replication number, respectively, $y_{i,j}$ is the value of response for replication j, SS_f and SS_T are the sum of the squares for parameter f and the total sum of squares of all the parameters, respectively, k and SNR_T are the number of experiments at level l of parameter f and the total sum of all SNR values, respectively.

Table 3.4-1: Taguchi experimental design (L9 orthogonal array with three parameters at three levels) of water gas shift reaction as a function of temperature (T), concrete fraction (X_{conc}) and steam to carbon mola ratio (S/C), and corresponding results of mean H_2 potential and mean conversion of CO (η_{CO}).

Experiment	T (ºC)	X_{conc}	S/C	H_2 Potential	η_{CO}
E1	500	0	1	7.7	12.9
E2	500	25	2	15.3	19.1
E3	500	50	3	43.4	48.5
E4	600	0	2	26.1	28.9
E5	600	25	3	41.3	46.6
E6	600	50	1	33.0	39.9
E7	700	0	3	40.3	45.4
E8	700	25	1	32.7	38.6
E9	700	50	2	55.7	60.8

Experimental Procedure

The assessment of catalyst performance was carried out in an atmospheric fixed-bed reactor (Figure 3.4-1), consisting of a quartz tube (L = 400 mm and ID = 22 mm) placed within an electric furnace. The system also incorporates a controlled evaporator chamber, externally heated by a heater tape. Each test was conducted following the same experimental protocol: 10 g of a catalyst supported on two layers of ceramic wool was loaded into the fixed-bed reactor and heated at 10 °C·min^{-1} in N_2 atmosphere to the desired reaction temperature (Table 3.4-1). Subsequently, distilled water was injected into the evaporator by an HPLC pump (Jasco, PV-980 model) and carried by a gas mixture containing 10 vol% CO and N_2 (balance) into the reactor. The gas hourly space velocity (GHSV) changed from 14,500 to 18,250 h^{-1} due to steam addition. The gas mixture was fed by a mass flow controller (MFC, Alicat, MCS Series), whereas the temperature of the catalyst bed was controlled by a K-type thermocouple connected to a PID controller (Eurotherm). At the reactor outlet, the gas product passed through a series of traps, which removed the unconverted water by condensation, before being collected in sample bags (FlexFoil) for analysis by gas chromatography (micro-GC). The gas was sampled in 5-minute periods, with a total sampling time of 30 minutes.

The performance of the WGS reaction was evaluated through H_2 potential and CO conversion (η_{CO}), using equations (3.4-11) and (3.4-12), respectively:

$$H_2\ Potential\ (\%) = \frac{\dot{n}_{H_2,out}}{\dot{n}_{H_2,st}} \times 100 \qquad \text{Eq. 3.4-11}$$

$$\eta_{CO}\ (\%) = (1 - \frac{n_{CO,out}}{n_{CO,in}}) \times 100 \qquad \text{Eq. 3.4-12}$$

where $\dot{n}_{H_2,out}$ and $\dot{n}_{H_2,st}$ are the molar flow rate of H_2 (mol·min^{-1}) at the reactor outlet and that theoretically produced following the reaction stoichiometry, respectively, whereas $\dot{n}_{CO,in}$ and $\dot{n}_{CO,out}$ are the molar flow rate of CO (mol·min^{-1}) at the reactor inlet and outlet,

respectively. Elemental mass balance was made based on the measured inlet and outlet gas compositions. The dry product gas was calculated from nitrogen balance, whereas the water content at the reactor outlet was estimated from hydrogen balance.

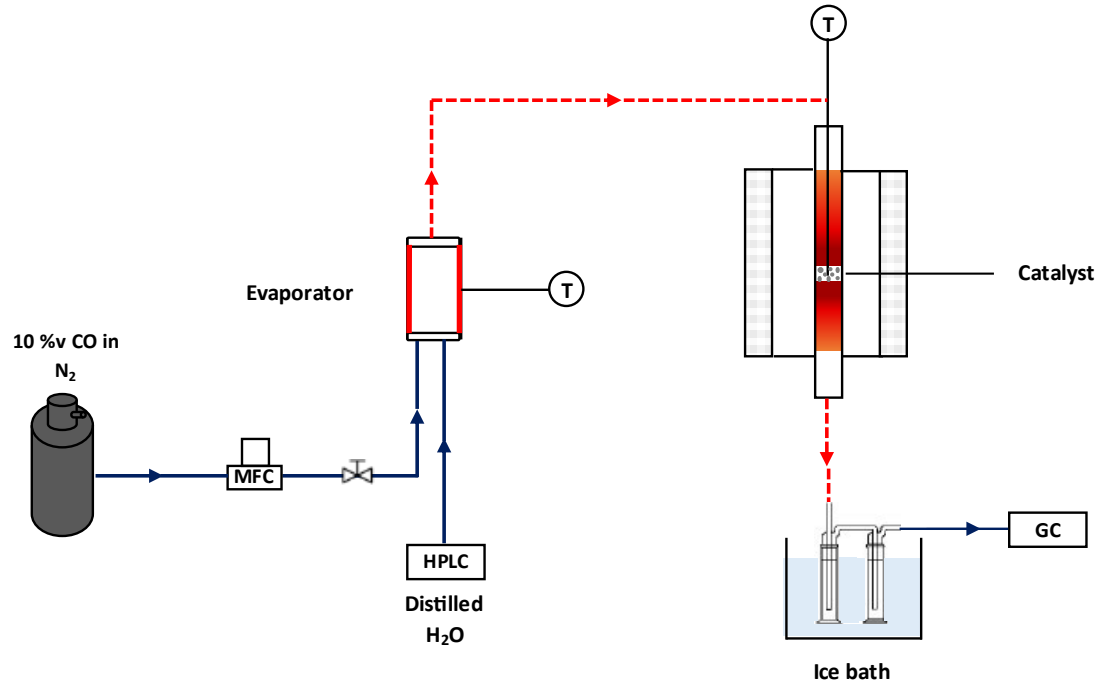

Figure 3.4-1: Schematic layout of the experimental system used in WGS experiments.

3.4.2.4. Catalytic Steam Gasification

Experimental Procedure

Selected granulated catalyst were tested for upgrading of biomass-derived raw gas in a bench-scale 3 kW_{th} gasification system (Figure 3.4-2). The experimental infrastructure is located at the University of Aveiro (Portugal) and comprises a fuel feeding system, a bubbling fluidized bed (BFB) reactor, and a downstream section for raw gas cleaning, sampling and analysis. The BFB reactor consists of a stainless-steel tube with an inner diameter of 49 mm and a height of 410 mm. The reactor is heated by an external electric furnace, and the bottom bed and freeboard can be temperature-controlled separately. The fluidizing gas is pre-heated using an electric evaporator and subsequently introduced at the bottom of the BFB reactor through a perforated distributor plate. The biomass feeding system is attached to the top of the gasifier and includes a screw feeder coupled to a feedstock hopper that modulates the feeding rate, and a discharge tube to add the biomass at the surface of the bottom bed. The BFB reactor also incorporates an in-situ catalytic fixed-bed reactor, with a height of 100 mm and an inner diameter of 16 mm, located on the freeboard zone at 50 mm above the bottom bed. Details concerning the experimental set-up configuration have been provided in a previous publication [39].

The biomass used in the gasification experiments was pellets produced from residual forest *Eucalyptus Globulus* (Table 3.4-2). The biomass properties were characterized by proximate and ultimate analysis, following the corresponding CEN/TS standard for solid

biofuels. The lower heating value (LHV_F) was calculated using the empirical correlation developed by Channiwala et al. [40], whereas the bulk density was estimated by determining the weight of fuel in a given volume. The experimental conditions of biomass steam gasification tests are summarized in Table 3.4-3. Nitrogen was added to the fluidizing steam as a carrier gas to assure the quantification of the dry producer gas through a mass balance across the reactive system.

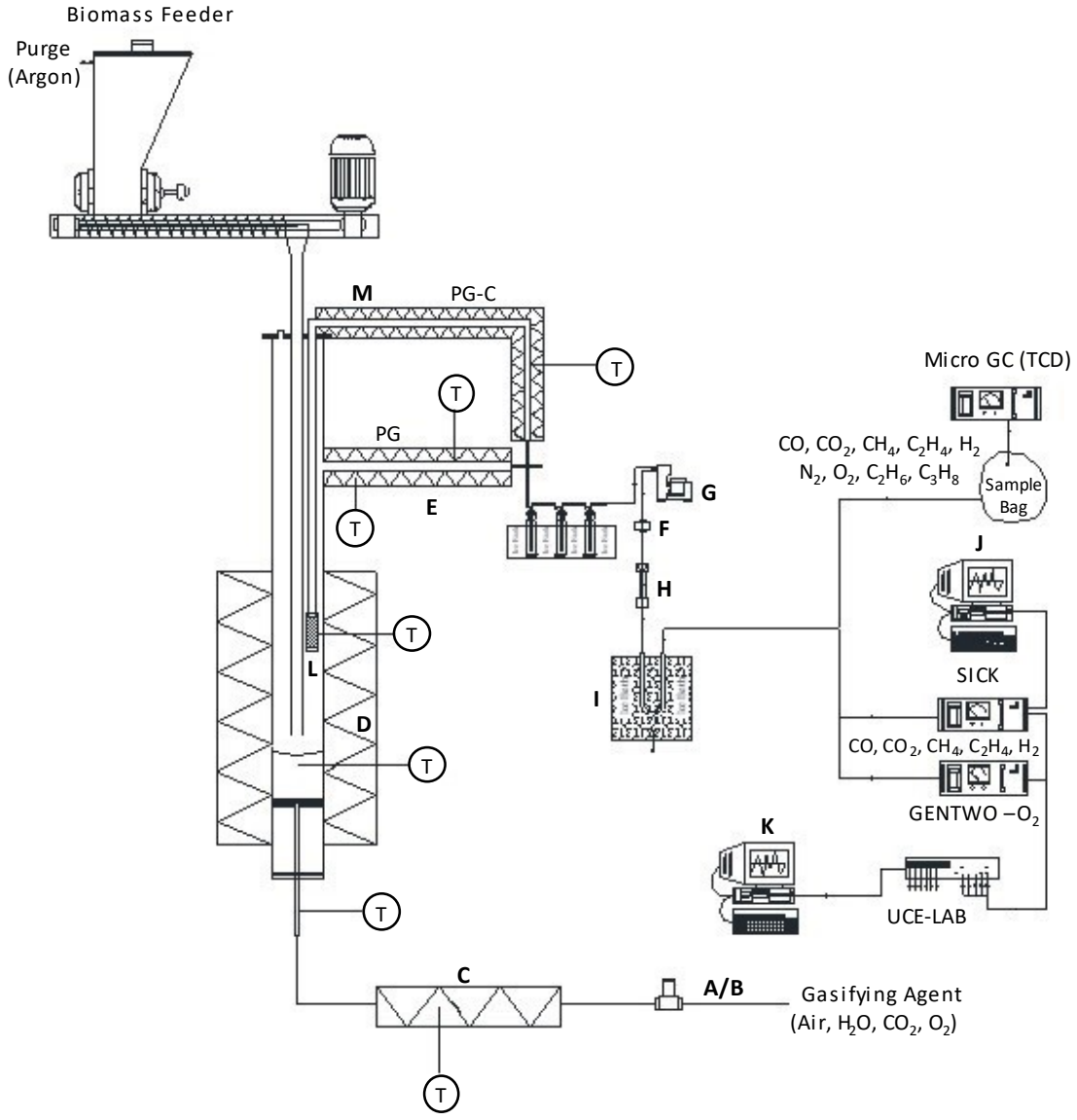

Figure 3.4-2: Schematic layout of the experimental infrastructure used during gasification experiments. Dashed Line - Electric Circuit, Continuous Line - Pneumatic Circuit, A/B – Mass-flow Controller, C – Evaporator, D – External Electric Furnace, E – Raw PG Exhaust, F – Quartz Filter G – Gas Sampling Pump, H – Gas Flow Meter, I - Gas Condensation Unit for Residual Moisture J - Computer for Data Acquisition from SICK Analyzer, K - Computer for Data Acquisition, L – Catalytic Fixed Bed Reactor, M - Probe Heated at 450 ºC, PG – Raw Producer Gas, PG-C – Upgraded Producer Gas, GENTWO – O_2 Paramagnetic Online Gas Analyzer, UCE-LAB - Electronic Command Unit, Micro GC - Gas Chromatograph with TCD, SICK – NDIR and TC Online Gas Analyzer.

Prior to the experiments, the fresh catalyst was loaded into the fixed-bed reactor and heated at 10 ºC/min in Ar atmosphere up to the desired temperature, defined according to the results obtained in the WGS experiments. When stable operating conditions were achieved, the producer gas from biomass gasification was made to pass through the catalytic fixed-bed reactor. Subsequently, the dry and clean producer gas composition (N_2, H_2, CO, CO_2, CH_4, C_2H_4, C_2H_6 and C_3H_8) was measured at distinct times, using an off-line gas analyzer (Micro-GC). The producer gas was sampled through the catalytic fixed-bed reactor in 10-minute periods using Tedlar bags (FlexFoil), with a total sampling time of approximately 90 minutes of steady-state operation. The lower heating value of the dry producer gas (LHV_G) was estimated based on the concentration of the combustible gases and their respective LHV at standard conditions (P_N = 101325 Pa and T_N = 273 K). Furthermore, four process parameters, namely specific H_2 production (Y_{H_2}), specific dry gas production (Y_{Gas}), carbon conversion efficiency (CCE) and cold gas efficiency (CGE), were calculated based on the equations (3.4-13), (3.4-14), (3.4-15) and (3.4-16), respectively:

$$Y_{H_2}\ (mol \cdot kg^{-1}) = \frac{n_{H_2,gas} \times M_{H_2}}{G_{m,fuel}} \qquad \text{Eq. 3.4-13}$$

$$Y_{Gas}\ (Nm^3 \cdot kg^{-1}) = \frac{G_{v,gas}}{G_{m,fuel}} \qquad \text{Eq. 3.4-14}$$

$$CCE\ (\%) = \frac{G_{v,gas} \times \frac{P_N}{R \times T_N} \times M_C \times \sum \varepsilon_{C,i} \times y_i}{G_{m,fuel} \times w_{C,F}} \times 100 \qquad \text{Eq. 3.4-15}$$

$$CGE\ (\%) = \frac{Y_{Gas} \times LHV_{Gas}}{LHV_{fuel}} \times 100 \qquad \text{Eq. 3.4-16}$$

Where $n_{H_2,gas}$ and M_{H_2} denotes the molar flow rate of H_2 ($mol \cdot h^{-1}$) at the catalytic reactor outlet and the molecular weight of hydrogen, respectively, $G_{m,fuel}$ and $G_{v,gas}$ are the dry biomass feeding rate ($kg \cdot h^{-1}$) and the dry producer gas flow rate ($Nm^3 \cdot h^{-1}$), respectively, y_i and $\varepsilon_{C,i}$ are the molar fraction and the number of carbon atoms in component i (i = CO_2, CO, CH_4, C_2H_4, C_2H_6 and C_3H_8), respectively, M_C and $w_{C,F}$ are the molecular weight of carbon and the mass fraction of carbon in the dry biomass, respectively, LHV_{Gas} and LHV_{fuel} are the lower heating value of the dry producer gas ($MJ \cdot Nm^{-3}$) and dry biomass ($MJ \cdot kg^{-1}$), respectively. In order to eliminate possible thermal effects of the catalytic fixed-bed reactor, an experiment with inert material (alumina) under the same conditions was performed. The obtained results of producer gas composition and process parameters of efficiency were used as a reference condition in evaluating the catalyst performance.

Table 3.4-2: Proximate and elemental analysis of residual forest biomass from eucalyptus.

Ultimate Analysis (wt.%, daf)	
Carbon	52.6
Hydrogen	6.3
Nitrogen	0.9
Sulfur	bd
Oxygen (by difference)	40.2
Proximate Analysis (wt.%, wb)	
Moisture	7.7
Volatile Matter	73.0
Fixed Carbon	16.3
Ash	3.0
LHV ($MJ \cdot kg_{F,db}^{-1}$)	19.3
Bulk Density ($kg_F \cdot m^{-3}$)	653 ± 30

db – dry basis, daf – dry ash-free basis, wb – wet basis, bd –bellow the detection limit (100 $mg \cdot kg^{-1}$)

Table 3.4-3: Operating conditions of catalytic biomass steam gasification tests.

Gasifier Operating Conditions	
Bed Material	Silica Sand
Bed Particle Diameter (μm)	180-250
Bed Material Loaded (g)	150
Biomass Flow Rate ($g \cdot min^{-1}$)	1.5
Fluidizing Gas	$H_2O + N_2$
Nitrogen Flow Rate ($L_{STP} \cdot min^{-1}$)	1.0
Steam Flow Rate ($g \cdot min^{-1}$)	1.1
Inlet Steam Temperature (ºC)	300
Steam to Carbon Molar Ratio (-)	1.0
Gasifier Bed Temperature (ºC)	800 ± 10
Catalyst Operation Parameters	
Duration of Test (min)	90
Catalyst Loaded (g)	25
Catalytic Bed Temperature (ºC)	700 ± 5
GHSV (h^{-1})	23,000

Catalyst Regeneration

To investigate the long-term stability of the granulated catalyst, a two-steps regeneration procedure was implemented: i) the initial spent catalyst was purged with 500 $mL_{STP}·min^{-1}$ of N_2 and heated at 10 °C·min^{-1} to 700 ºC. Afterward, the catalyst was exposed to atmospheric air for a period of 5 minutes to promote coke removal by exothermic oxidation; ii) once finished the oxidative regeneration step, N_2 was gradually replacing the atmospheric air in the fixed-bed reactor. Subsequently, the temperature was increase at 10 °C·min^{-1} from 700 to 900 ºC and then kept stable for 5 minutes to ensure the decomposition of $CaCO_3$ into CaO. The regeneration conditions were defined following previous studies performed by Acharya et al. [41]. The procedure was repeated for three consecutive gasification–regeneration cycles.

3.4.2.5. Thermodynamic Calculations

Thermodynamic calculations were applied as guidelines to investigate the stability range of the main catalyst compounds and their compatibility with the thermochemical conditions of biomass gasification. One developed phase stability diagrams for the system Fe-O-C vs CO and CO_2, and for CaO-SiO_2-CO_2 vs the aCaO:aSiO_2 ratio and pCO_2, extending methods proposed earlier [42]. Thermodynamic properties required for the analysis (standard enthalpies, standard entropies, and specific heat capacities) were obtained from the FACTSAGE v.5.5 software package with the FToxid database.

3.4.3. Results and Discussion

3.4.3.1. Characterization of Catalyst Precursors and Granulated Catalysts

Figure 3.4-3 shows XRD patterns of the synthetic concrete, siderite and granulated catalyst samples after thermal treatment at 700 ºC in N_2. The results indicate that quartz (SiO_2) is the main crystalline phase in concrete, directly related to the high fractions of sand used as filler, co-existing with much smaller contents of Ca-based phases (Ca_2SiO_4, $CaCO_3$ and $Ca(OH)_2$). Long term storage of fine ground concrete eliminates the contents of hydrated phase, probably by gradual carbonation in contact with atmospheric CO_2 [43]. This suggests that potential utilization of concrete waste in biomass gasification processes may require a de-carbonation step to increase CO_2 adsorption performance. In the case of the siderite sample, inspection of the XRD data showed $FeCO_3$ and SiO_2 as minor phase. The main phases are consistent with the corresponding elemental analyses (Table 3.4-4). Absence of alumina-based crystalline phases suggests that this is included in the amorphous fraction, and minor fractions of other elements may be incorporated in the main phases, as expected for small fractions of different carbonates ($CaCO_3$, $MgCO_3$ and $CaCO_3$) in $FeCO_3$-based solid solution or may also be present in the amorphous fraction.

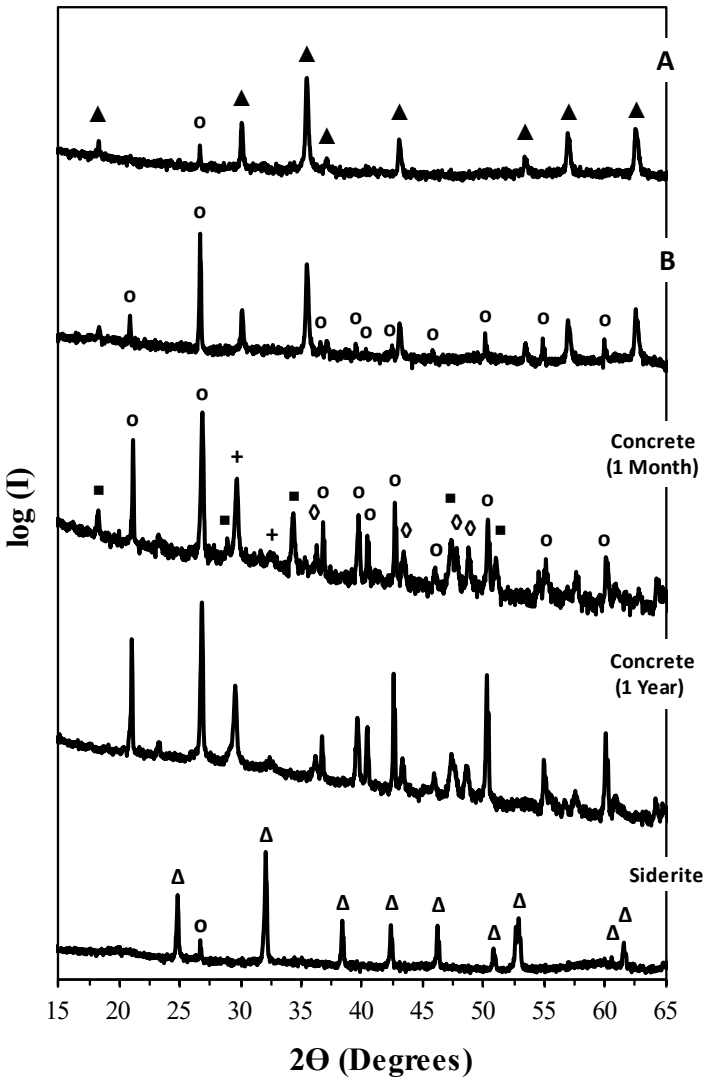

Figure 3.4-3: X-ray diffractograms of siderite, concrete (aged for 1 month or 1 year), and fired granulated catalysts prepared from siderite with 0 wt% concrete (A) and 50 wt% concrete (B). The following symbols are used for different phases: ▲Fe_3O_4, Δ $FeCO_3$, **o** SiO_2, **+** Ca_2SiO_4, ■ $Ca(OH)_2$ and ◊ $CaCO_3$.

Table 3.4-4: Cation elemental analyses (at.%) of siderite and concrete.

Element	Siderite	Concrete
Fe	80.8	0.8
Si	10.8	69.6
Ca	0.9	26.1
Al	6.2	1.7
Mg	0.9	0.9
Ti	0.2	0.1
Mn	0.2	-
K	-	0.6
Na	-	0.2

Table 3.4-5 shows relevant macroscopic properties of granulated catalysts after calcination in N_2 atmosphere at 700 ºC. Porosity and skeletal density vary significantly with the contents of concrete, and this also implies negative impact on crushing strength. Thus, one expects opposite effects on short term catalytic performance of composite catalysts and their long term ability to minimize erosion and ageing in the dynamic conditions of gasification under high gas flows.

Table 3.4-5: Physical and mechanical properties of granulated catalyst samples.

Wt.% Concrete	Skeletal Density ($g \cdot cm^{-3}$)	Total Porosity (%)	Crushing Strength (MPa)
0 %	3.489	24.0 ± 0.2	0.894 ± 0.08
25 %	3.323	30.3 ± 0.3	0.180 ± 0.04
50 %	3.145	30.6 ± 0.5	0.152 ± 0.03

SEM micrographs of granulated catalysts show sphere-like shape with diameter ranging from 3.2 to 3.6 mm (Figure 3.4-4). The concrete-free sample shows smoother surface morphology, whereas additions of concrete (50 wt.% concrete) yield rougher surfaces. In this case, the surface shows dark depressed regions, ascribed to decomposition of siderite-rich regions, and white concrete-rich regions, revealed by Ca- and Si-enriched elemental maps, as marked by circles in Figure 3.4-4. In addition, elemental maps show differences between the elemental maps of Ca and Si (squares in Figure 3.4-4), probably originated from heterogeneities in the distribution of cement and sand in the concrete precursor.

The granulated catalyst based on siderite without concrete (Figure 3.4-3a) shows decomposition of the main carbonate phase of siderite precursor after firing at 700 ºC in N_2 atmosphere, yielding magnetite (Fe_3O_4); this indicates moderately reducing conditions, as expected for conditions when the released gases remains close to the stoichiometric ratio $CO_2/CO \approx 2:1$:

$$3FeCO_3 \rightarrow Fe_3O_4 + 2CO_2 + CO \qquad \text{Eq. 3.4-17}$$

In fact, limited porosity of granulated samples and pore sizes in the micrometre range (Figure 3.4-4) may prevent dilution of the neutral carrier gas (N_2) inside internal pores. Thermodynamic examination of the Fe-O-C system (Figure 3.4-5) also emphasizes the CO_2-CO ranges for decomposition of $FeCO_3$ to Fe (3.4-18), FeO (3.4-19), Fe_3O_4 (3.4-17) or Fe_2O_3 (3.4-20), and corresponding 2 phase equilibria vs CO and CO_2:

$$FeCO_3 + CO \rightarrow Fe + 2CO_2 \qquad \text{Eq. 3.4-18}$$

$$FeCO_3 + CO \rightarrow FeO + CO_2 \qquad \text{Eq. 3.4-19}$$

$$2FeCO_3 + CO \rightarrow Fe_2O_3 + 2CO_2 + CO \qquad \text{Eq. 3.4-20}$$

Similarly, redox equilibria involving metallic Fe and different oxides can be related to CO and CO_2 ranges:

$$Fe + CO_2 \rightarrow FeO + CO \quad \text{Eq. 3.4-21}$$

$$3Fe + 4CO_2 \rightarrow Fe_3O_4 + 4CO \quad \text{Eq. 3.4-22}$$

$$3FeO + CO_2 \rightarrow Fe_3O_4 + CO \quad \text{Eq. 3.4-23}$$

$$2Fe_3O_4 + CO_2 \rightarrow 3Fe_2O_3 + CO \quad \text{Eq. 3.4-24}$$

Thermodynamic predictions in Figure 3.4-5 also show differences between operating conditions of WGS reactors intended for CO-free hydrogen production (< 500 ºC) and biomass gasification at higher temperatures. $FeCO_3$ is observed only under conditions of low temperature WGS (at T < 300 ºC), except possibly under pressurized conditions. These major differences in stability of carbonate may play a relevant role on WGS mechanisms catalysed by Fe-based catalysts, which involve redox changes and possibly also adsorption of carbonate groups [44]. Thus, incorporation of a basic component (CaO) is needed to assist the CO_2 sorbent capacity of WGS catalysts at higher temperatures.

Low temperature WGS also involves greater risks of carbon deposition by onset of Boudouard reaction (3.4-5), represented by the shaded area in Figure 3.4-5; this is shifted to lower CO:CO_2 ratio with decreasing temperature. Thus, Figure 3.4-5 also shows expected conditions for gradual conversion of CO to CO_2 (dashed line), after thermal decomposition of $FeCO_3$ to Fe_3O_4. Note that the stoichiometric ratio CO:CO_2 = 1:2 prevents carbon deposition by Boudouard reaction at T ≥ 700 ºC. In addition, Fe_3O_4/FeO-based catalysts may still hinder carbon deposition at intermediate temperatures by acting as a redox buffer and preventing onset of Fe^0, which would catalyse the Boudouard reaction.

Thermogravimetry (Figure 3.4-6) provides further insight on thermochemical and redox changes of siderite-based catalysts. Weight losses in flowing CO_2-rich atmosphere remain negligible for temperatures up to about 350 ºC and increase sharply above 400 ºC, reaching maximum rate at about 425 ºC. These temperatures are significantly higher than predicted by thermodynamics (Figure 3.4-5), probably due to kinetic delay on heating. Weight losses converge to a limiting value between the plateaus predicted for decomposition to magnetite (3.4-17) and to hematite (3.4-20), possibly because the flowing 25%CO_2-75%N_2 atmosphere mixes readily with the CO+CO_2 gas mixtures which evolves by decomposition of siderite powder; this differs from the calcination of siderite-based granulated catalysts, which yielded magnetite phase (Figure 3.4-3), due to major differences in morphology. Note that the loose siderite powder used in TG experiments allows ready mixing with the flowing CO_2-based atmosphere whereas internal porosity of granulated samples maintains conditions which are close to the stoichiometric ratio CO:CO_2 ≈ 1:2.

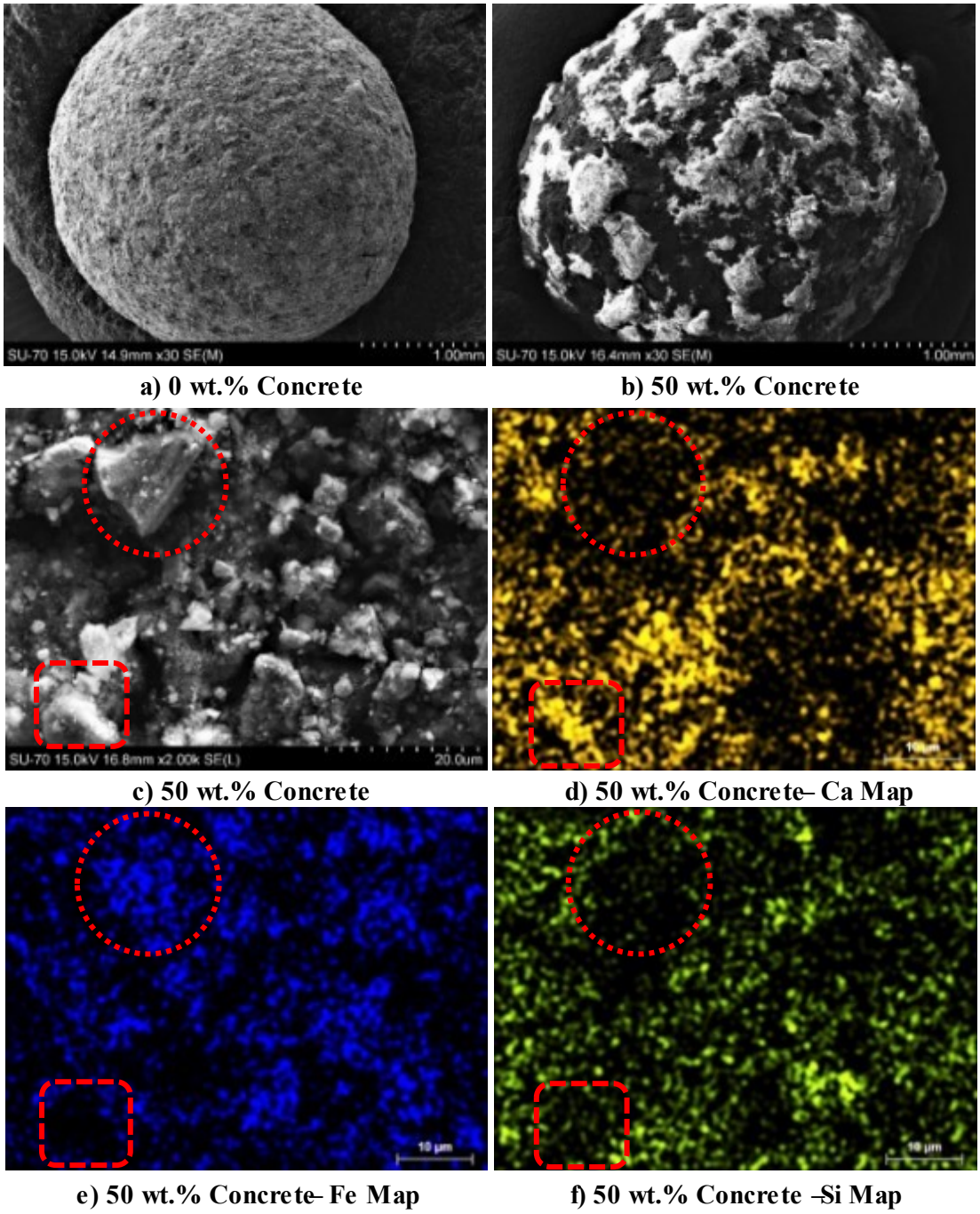

Figure 3.4-4: SEM microstructures of granulated catalyst without concrete and with 50 % concrete, and corresponding elemental maps of Ca, Fe and Si.

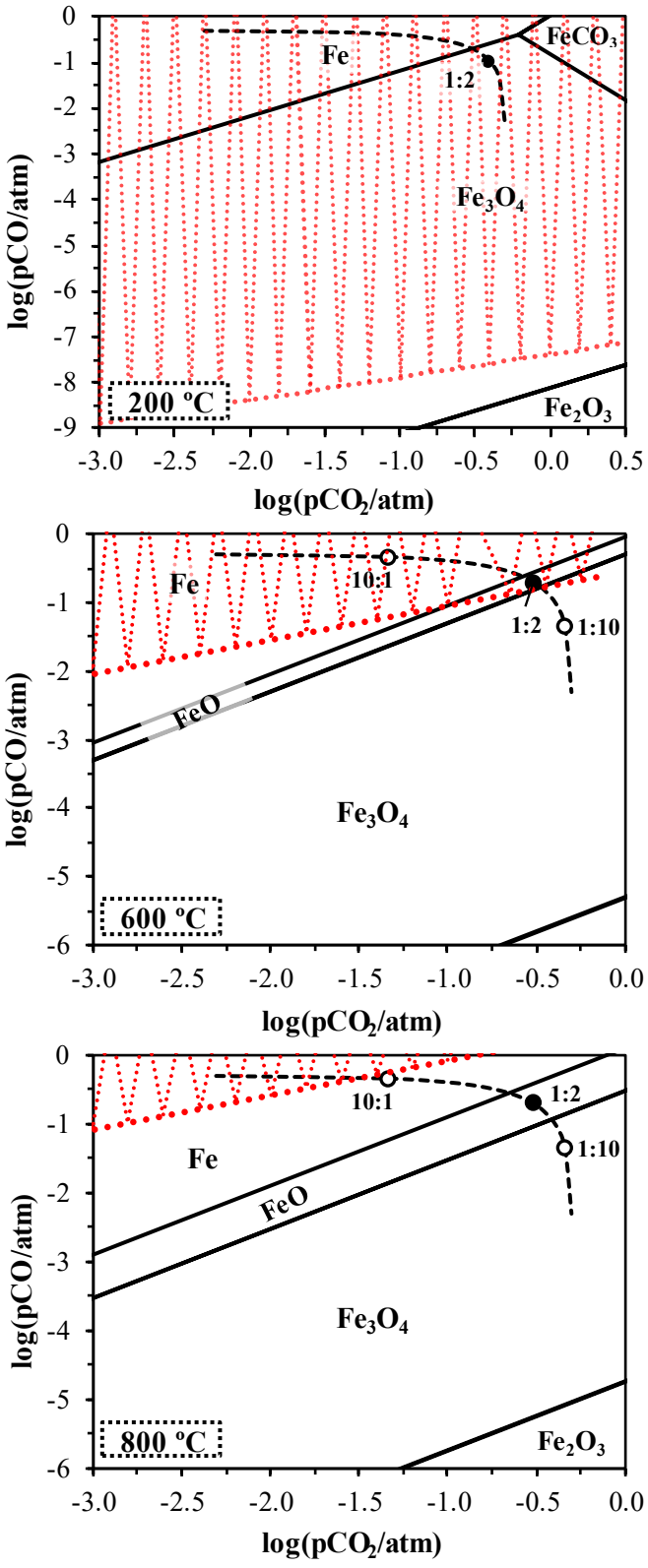

Figure 3.4-5: Thermodynamic guidelines of phase stability condition for the system Fe-O-C vs the CO_2 and CO ranges at 200 ºC, 600 ºC and 800 ºC. The shaded area shows the range of conditions which may cause onset of carbon and the dashed curve shows gradual conversion of CO to CO_2, with steam to carbon ratio = 1:1 (for $pCO+pCO_2 \approx 0.5$).

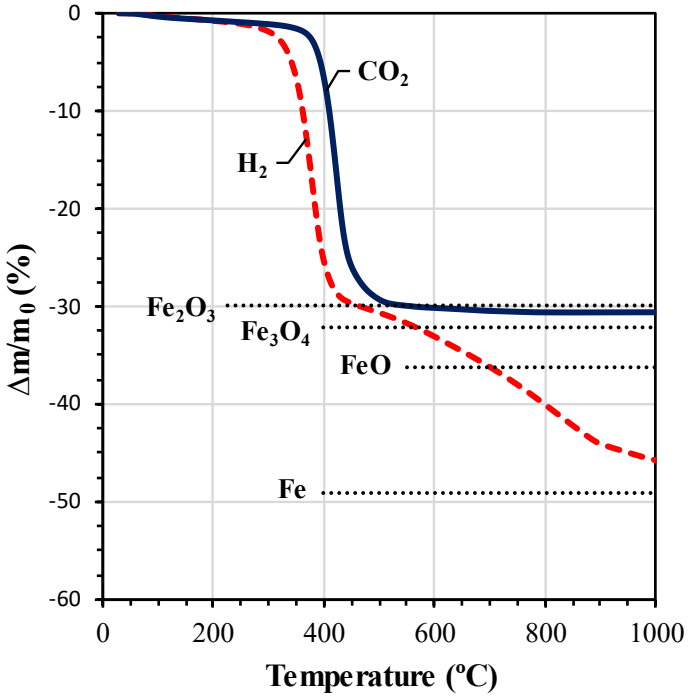

Figure 3.4-6: Thermogravimetry of siderite samples on heating in 25%CO_2-75%N_2 or 10% H_2-90%N_2 atmospheres, at 10 ºC·min^{-1}. Dotted lines show the expected losses on assuming conversion of $FeCO_3$ to different oxides or metallic Fe.

Decomposition of siderite in the reducing atmosphere (Figure 3.4-6) starts at slightly lower temperature (by 300 ºC) and reaches maximum rate at 381 ºC. Weight losses are higher than for decomposition in 25%CO_2-75%N_2, with a first step up to about 450 ºC, when cumulative losses correspond to conversion to Fe_2O_3, and subsequent losses indicate further reduction to FeO and Fe at higher temperatures. Calcination in N_2 at 700 ºC also yields complete decomposition of $FeCO_3$ in the granulated composite catalyst B, which was prepared with 50 wt.% concrete (Figure 3.4-3). In addition, XRD does not detect any traces of CaO-based crystalline phases ($Ca(OH)_2$, $CaCO_3$ and Ca_2SiO_4), suggesting their incorporation in the amorphous fraction, possibly combined with other oxides such as silica, iron oxide and alumina.

Therefore, further information was needed to clarify the thermochemical changes of the concrete precursor, as revealed by thermogravimetry. In fact, TG in 25%CO_2-75%N_2 atmosphere (Figure 3.4-7) shows direct evidence of both de-hydration and de-carbonation of aged concrete samples. De-hydration comprises early loss of adsorbed humidity, below 200 ºC (≈ 1 wt.%), and then gradual additional loss for up to about 500 ºC (≈ 2.2 wt.%), though without the sharp peak expected for decomposition of $Ca(OH)_2$ [43]; this is consistent with XRD evidence that this phase is absent after long term ageing (Figure 6.3). Additional weight loss (≈ 7.2 wt.%) is ascribed to decarbonation, which corresponds to a relatively high fraction of the upper limit of carbonation if one considered complete conversion of the total contents of CaO, MgO, Na_2O and K_2O (≈ 18.3 wt.%) in the concrete composition (Table 3.4-4). Thus, one may assume that previous long term storage of ground concrete converted at least most of the contents of highly reactive phases (Ca_3SiO_5), and possibly also a fraction of Ca_2SiO_4, probably by earlier hydration and subsequent

carbonation. The double peaks of decarbonation (at ≈ 615 ºC and ≈ 705ºC) are within the range expected for decomposition of $CaCO_3$, mainly for conditions when the previous $Ca(OH)_2$ peak vanishes [43]. In addition, a final sharp peak is observed at unusually high temperatures (≈ 920 ºC), and is reverted at ≈ 870 ºC), on cooling; this suggests onset of carbonated calcium silicate phases, by analogy with the temperature range reported for synthesis of spurrite ($Ca_5Si_2O_9.CO_3$) in CO_2-rich atmospheres [45]. However, experimental conditions for synthesis of this phase often require additions of a mineralizer (e.g. CaF_2) to reacting Ca_2SiO_4+$CaCO_3$ mixtures and/or use of an unstable and Ca-rich precursor (Ca_3SiO_5) [46].

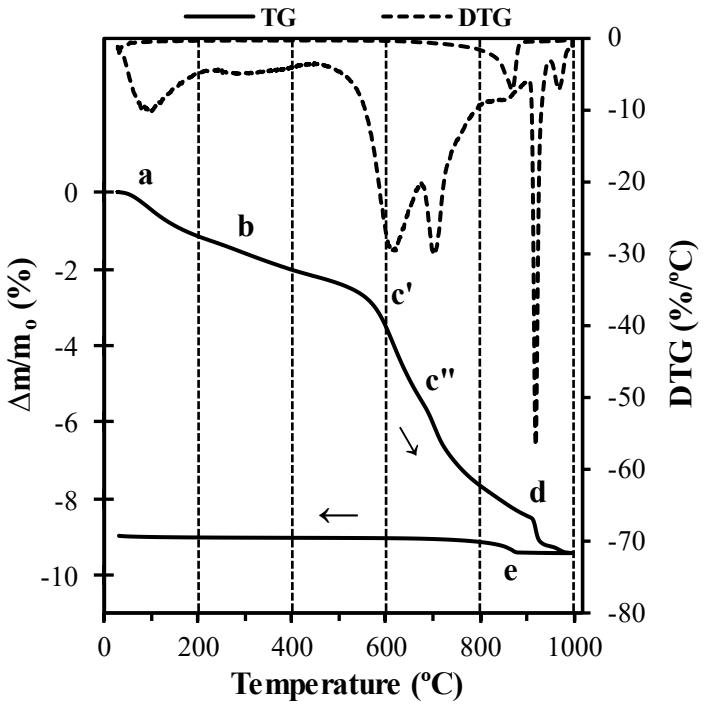

Figure 3.4-7: Thermogravimetry of concrete samples in CO_2 at 1°C/min after ageing for 1 year.

Thermodynamic simulations were also performed to confirm the expected conditions for carbonation/decarbonation of relevant phases in the ideal CaO-SiO_2-CO_2 system (Figure 3.4-8), using the classical notation in cement chemistry C≡CaO, S≡SiO_2 and ċ≡CO_2; this predicts stability of carbonated phases in cement (or concrete) samples at temperatures close to 500 ºC, in CO_2-rich atmosphere. The secondary vertical axis shows the thermodynamic driving force (i.e. chemical potential) for onset of carbonated phases in CO_2 atmosphere (pCO_2 ≈ 1 atm). Still, these predictions also indicate that calcium carbonate ($CaCO_3$) and spurrite ($Ca_5Si_2O_9.CO_3$) may decompose in air (pCO_2 ≈ 0.0004 atm) at lower temperatures. Note differences between carbonation of the metastable phase Ca_3SiO_5 (represented by dotted lines in Figure 3.4-8), and carbonation of decomposition products (CaO+Ca_2SiO_4). Figure 3.4-8 also predicts gradual decomposition of the carbonated phases with increasing temperature, with complete decarbonization on approaching 700 ºC; this is consistent with peaks c' and c" in Figure 3.4-7, with slight displacement to higher temperatures on thermal cycling.

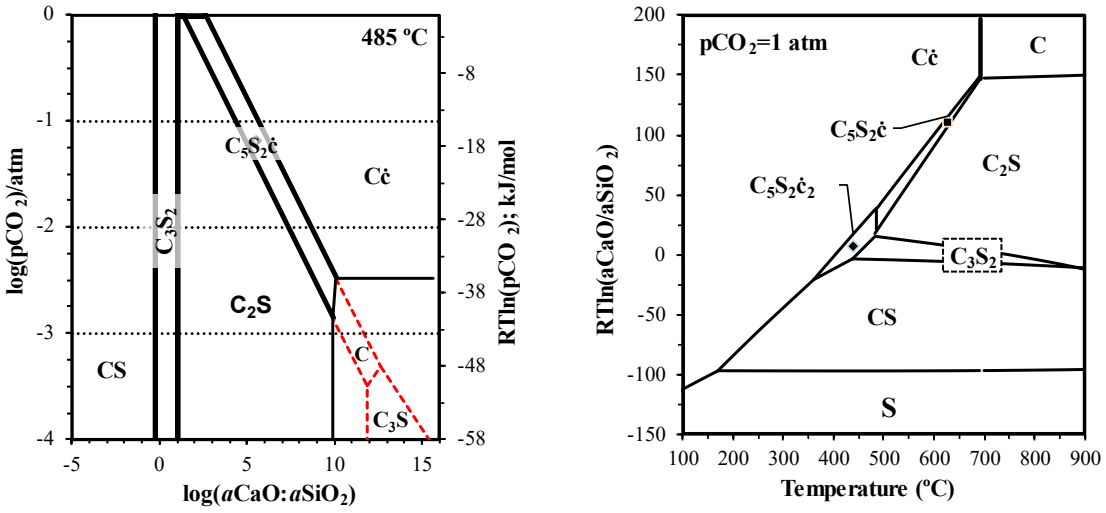

Figure 3.4-8: Activity phase stability diagrams for the CaO-SiO_2 system vs CO_2 chemical potential, at 485 ºC, and vs temperature, in CO_2 atmospheres.

Thermodynamic predictions in Figure 3.4-8 only show a narrow temperature range for onset of spurrite and fail to account for the final loss at 920 ºC, and its reversion at 870 ºC; this may be ascribed to amorphization, as suggested by absence of XRD reflections of Ca-based phases (Figure 3.4-3) or complex structural changes revealed by in real time changes observed during gradual decomposition of calcium carbonate [47]. Similarly, Ca_2SiO_4 may undergo transformation to different polymorphs, with expected impact on its stability range. In fact, the actual CO_2-rich atmospheres may promote transformation to $\beta - Ca_2SiO_4$ [46], and one also expects the additional contribution of Fe-additions [48], by ready decomposition of siderite to mixed valence oxides. Thus, one may assume that composite catalysts derived from siderite/concrete mixtures combine the catalytic activity of redox changes of iron oxides with corresponding O_2 storage ability, and CO_2-storage by decarbonisation/carbonization over wide temperature ranges, as required for CO_2 capture by treatment of producer gases obtained by biomass gasification.

3.4.3.2. Optimization of WGS Reaction Parameters

An inert material (Al_2O_3) was used as a reference to evaluate the conversion of CO by thermal reactions. The results showed a conversion of CO around 6 % at 500 ºC for the steam to carbon ratio (S/C) ranging from 1 to 3; this is much smaller than corresponding thermodynamic equilibrium calculations (Figure 3.4-9), which predict above 90% CO conversion at 500 °C for the same S/C range; this shows that thermal conversion of CO is sluggish and requires catalytic promotion. The molar flow rate obtained for the compounds in WGS experiments is presented in Table S1 – Supplementary Material.

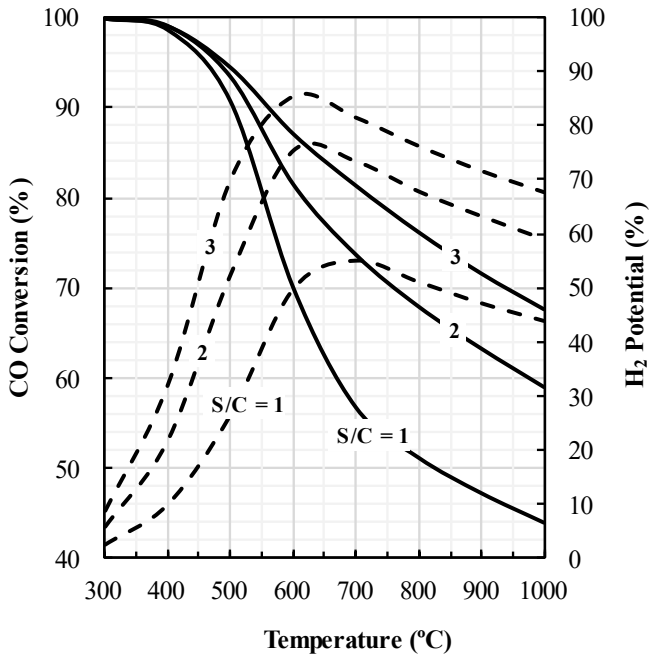

Figure 3.4-9: Thermodynamic equilibrium calculations for WGS performance at different temperatures and S/C molar ratio (--- H_2 potential, — CO conversion).

Taguchi planning was used to seek optimised catalytic promotion of WGS, and the designed orthogonal array and their results are presented in Table 3.4-1. All the experiments were performed in duplicate with standard deviation ranging from 0.1 to 11.1 %. The highest values of CO conversion and H_2 potential of 60.8 % and 55.7 %, respectively, were attained with experiment L9 (T = 700 ºC, X_{conc} = 50 wt.% and S/C = 2), and the lowest values of CO conversion (12.9 %) and H_2 potential (7.7 %), were achieved with experiment L1 (T = 500 ºC, X_{conc} = 0 wt.% and S/C = 1). The mean level of signal to noise ratio (SNR_L) has been calculated as the algebraic mean of all the SNRs of an individual parameter at a specific level, to assess the optimal level for each parameter. The H_2 potential was selected as the optimization criteria and the results are shown in Figure 3.4-10. The fluctuations (noise) associated with each individual parameter became higher at lower levels, revealing additional contributions of the other design parameters. Still, the SNR_L value denotes the ratio of the mean response value to the noise variance and subsequently these additional contributions were taken into account.

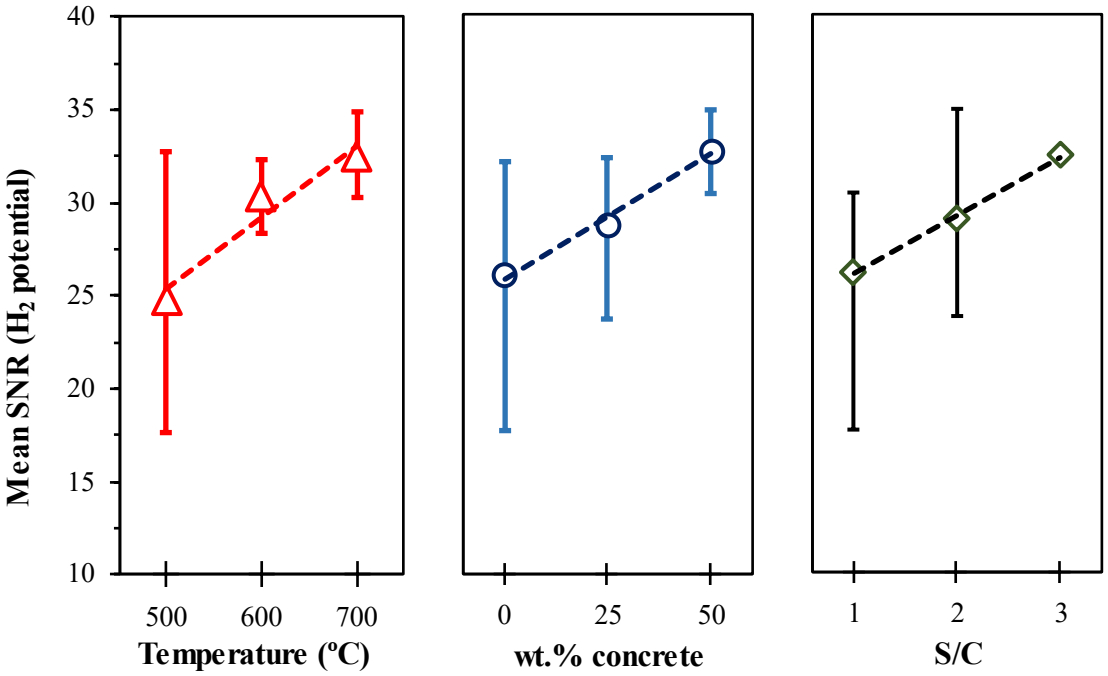

Figure 3.4-10: Mean SNR for each parameter at different levels.

The maximum SNR_L for the reaction temperature was exhibited at level 3 (T = 700 ºC, SNR_L = 32.4), showing that H_2 production increases with temperature. It should be noted that the WGS activity of Fe-based catalysts is typically understood as a redox mechanism, facilitated by the charge transfer between Fe^{2+} and Fe^{3+} in the octahedral site of magnetite (Fe_3O_4) [49]. In fact, magnetite should be the prevailing phase by decomposition of siderite as shown by thermodynamic predictions (Figure 3.4-5) and also thermogravimetry (Figure 6.6). Though thermodynamics favors WGS reaction at low temperature (Figure 3.4-9), application of catalyst increased the production of H_2 when temperature increased, since the reaction rate is thermally activated. This tendency on H_2 production with increasing temperature has been reported in the literature on WGS reaction over Fe-based catalysts [12,49,50]. A similar trend on activity of WGS catalysts was observed for the variation of catalyst composition. The composite catalyst with 50 wt.% concrete exhibits the highest SNR_L (32.7), whereas the concrete-free sample achieved the lowest SNR_L (26.0) for the production of H_2. These results show that the WGS reaction was enhanced by the presence of CaO-rich phases in the concrete fraction. The catalytic effect of CaO on the WGS reaction has been attributed to the promotion of the carboxyl mechanism [51]. The alkaline nature of CaO promotes the dissociative adsorption of H_2O and makes the surface rich with hydroxyl species (OH* and H*), which is the rate-determining step of the WGS reaction. The resulting species will interact with CO*, which is preferentially adsorbed on Fe-based active sites, generating surface formates (COOH*) which will be further decomposed to form CO_2 and H_2. Another important aspect is the CO_2 absorption capacity of CaO-based phases, since this can shift the WGS reaction equilibrium to higher H_2 yield [52].

Gradual carbonation/decarbonation (Figure 3.4-7) combined with thermodynamic analysis (Figure 3.4-8) of the $CaO\text{-}SiO_2\text{-}CO_2$ system in CO_2-rich atmospheres, possibly

connected with previous de-hydration, is consistent with prospective interaction with intermediate species in WGS (CO*, COOH*,…) in the actual temperature range (500 ºC to 700 ºC). In addition, the composite composition of the actual catalysts, possibly combined with dynamic conditions [47], may shift the carbonation/decarbonation cycles to still higher temperatures. as required for gasification, whereas subsequent CO_2 absorption at lower temperatures raises prospects for upgrading the producer gas. Thus, one would expect simultaneous H_2O dissociation and onset of carbonation for the studied temperature range, which is in close agreement with evidence in relevant literature [53].

On the other hand, the maximum SNR_L for the S/C molar ratio was obtained at level 3 (S/C = 3, SNR_L = 32.4), whereas the lowest value was achieved at level 1 (S/C = 1, SNR_L = 26.1). The improvement in H_2 yield with increasing S/C molar ratio can be ascribed to distinct factors. First, the equilibrium CO conversion and subsequent H_2 production improve with increasing S/C molar ratio > 1 (see Figure 3.4-9). Furthermore, the rate of Boudouard reaction (3.4-5) is insignificant at reaction temperatures below 700 °C [54], which means that increasing the S/C molar ratio can promote coke gasification, minimizing risks of carbon deposition over active sites. Steam also behaves as an oxidizing agent, preventing over-reduction and subsequent activity loss of Fe active species during the WGS reaction [55,56].

Based on the aforementioned results, the optimum level of each parameter is reaction temperature at level 3 (700 ºC), concrete fraction at level 3 (50 wt.%) and S/C molar ratio at level 3 (3). The analysis of variance (Table 3.4-6) was applied not only to assess the fitness of the experimental results but also to determine the contribution of each parameter for increasing H_2 production. The F-value of 24.2 implies that the results are significant, with only a 0.2 % chance that this F-value could be due to noise. All the process parameters show statistical significance (p-value ≤ 0.05). Moreover, the regression coefficient showed relatively good correlation, specifying that 93.5 % of the total variation on H_2 production is ascribed to the studied parameters. The obtained results of the ANOVA analysis are also confirmed by estimating the contribution factor for individual parameters. The results confirm that the reaction temperature was the most significant parameter influencing H_2 production with a contribution of 43.1 %, followed by the concrete fraction with 30.2 % contribution. The S/C molar ratio was the least influencing parameter with a contribution factor of 26.7 %.

Table 3.4-6: Statistical parameters obtained from ANOVA.

Source	Sum of Squares	df	F-value	P-value
Model	214.62	3	24.16	0.0021
Reaction Temperature	92.57	1		0.0027
Concrete/$FeCO_3$	64.77	1		0.0052
S/C Molar Ratio	57.28	1		0.0066
Residual	14.80	5		
Total	229.42	8		

R^2 = 0.935; Adjusted R^2 = 0.914; Standard Deviation = 5.05; SRN = 29.16; Coefficient of Variance = 17.3%; df = degree of freedom; P ≤ 0.05 = Significant

3.4.3.3. Biomass Steam Gasification

Based on the previous results obtained in section 3.4.3.2, the catalyst with 50 wt.% concrete was selected for steam gasification experiments. The influence of this catalyst on the main gas components, such as H_2, CH_4, CO, CO_2, and light hydrocarbons C_xH_y (C_2H_4, C_2H_6, and C_3H_6) is presented in Figure 3.4-11. Compared to the reference condition, in-situ application of the granulated catalyst led to substantial increment in both H_2 (43.7 to 50.4 vol.%) and CO_2 (22.1 to 25.8 vol.%) concentrations, whereas the concentration of CO decreases (23.6 to 15.4 vol.%). The specific H_2 production (Y_{H_2}) was around 48.5 $g_{H_2} \cdot kg_{dry,fuel}^{-1}$, which is significantly higher than achieved for the reference condition with only 33.6 $g_{H_2} \cdot kg_{dry,fuel}^{-1}$. Subsequently, the H_2:CO molar ratio of the producer gas increased from 1.9 to 3.3, reaching the established limits for SNG production by methanization reaction (3.4-1). The performance of different metal-based catalysts for H_2-enriched gas production during gasification of biomass has been reported in previous studies (Table 3.4-7). It can be seen that H_2 promotion by the siderite/concrete composite was close to other catalysts found in literature. Still, comparison of these materials and their effects must be careful because the different operating conditions applied in the experiments, such as temperature and steam to carbon molar ratio, were proven to influence catalyst activity.

It is clear from the results that the WGS reaction was significantly enhanced by the presence of the granulated composite catalyst with 50 wt.% concrete. Its performance can be attributed to synergistic effects between Fe-based and Ca-based species under gasification conditions. Though Ca-based crystalline phases could not be detected by XRD (Figure 3.4-3), post-mortem analysis of this spent catalyst by FTIR (Figure 3.4-12) showed evidence of calcium silicates, as revealed by the broad band in the range 800-1200 cm^{-1}, ascribed to asymmetrical stretching of Si-O bond of calcium silicates [61], whereas onset of carbonation is indicated by the broad band in the 1300-1500 cm^{-1} [62,63]. In addition, the FTIR spectrum shows symmetric stretching of carbonate groups at ~1080 cm^{-1}, probably superimposed on Si-O-Si asymmetric stretching of quartz (~1098 cm^{-1}) [64]. Note also that the double peak at ~780-800 cm^{-1} is consistent with Si-O-Si symmetrical stretching [64]. Other peaks ascribed to carbonate include degenerate planar bending (~ 695 cm^{-1}) and out of plane bending (~ 870 cm^{-1}). Moreover, the CO_2 double peak at ~ 2358 cm^{-1} indicates CO_2-adsorption ability [65]. This is supported by TG profile of the simulated concrete aged for 1 month in CO_2 atmosphere (Figure S1 – Supplementary Material), showing that the relevant temperature range for carbonation of concrete is within prospective conditions for biomass gasification processes. Thus, one may assume that Fe species promote CO oxidation, enhancing WGS activity and contributing to H_2 production, whereas Ca-containing species from concrete promote CO_2 sorption, in close agreement with previous literature [66,67].

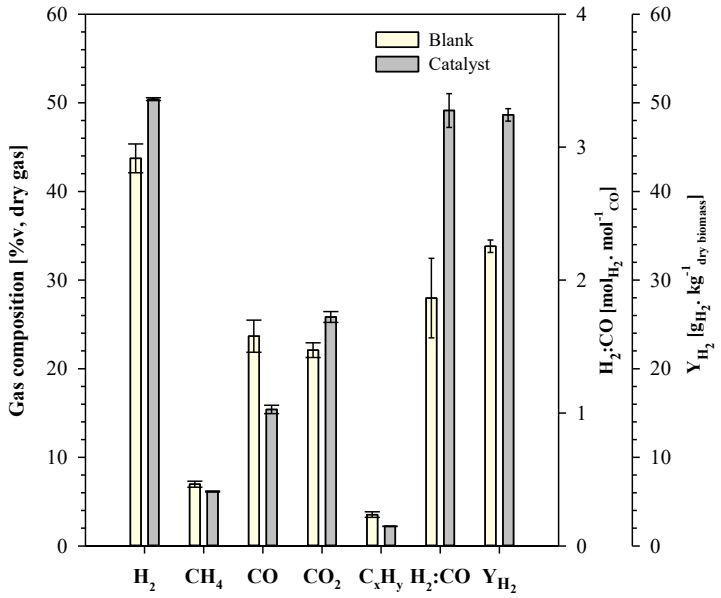

Figure 3.4-11: Gas composition in terms of H_2, CH_4, CO, CO_2, and C_xH_y concentration, H_2:CO molar ratio and Y_{H_2} for the experiments performed without (blank) and with the catalyst.

Table 3.4-7: Performance of different primary catalysts for H_2 production from biomass gasification.

Catalyst	T_{cat} (ºC)	S/C	Y_{H_2} ($g_{H_2} \cdot kg_F$)	H_2 Increase (%)	H_2:CO	Ref.
Siderite/Concrete	700	1.0	48.6	43.8	3.3	This Work
CaO	660	-	21.0	28.4	0.5	[26]
Fe_2O_3	800	3.0	34.6	25.4	0.4	[18]
$(Mg,Fe)SiO_4$	850	3.0	50.0	11.1	1.4	[57]
$MgCO_3 \cdot CaCO_3$	850	3.0	75.0	66.7	4.3	[57]
Fe/Olivine	850	3.0	62.5	38.9	3.3	[58]
CaO/Al_2O_3	860	3.8	54.9	20.4	2.8	[59]
Fe/CaO	660	-	27.9	70.5	0.6	[26]
Fe-Ni/CaO	500	5.0	21.7	20.9	6.8	[60]

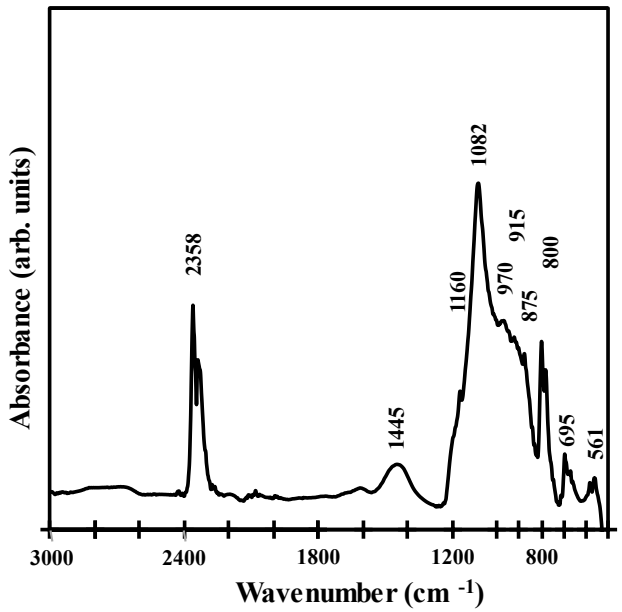

Figure 3.4-12: FTIR spectrum of the 50%C-Fe catalyst after the gasification experiment.

Figure 3.4-13 shows the impact of the composite catalyst (X_{conc} = 50 %) on the Lower Heating Value (LHV_G) of the producer gas and process efficiency parameters, namely specific dry gas production (Y_{Gas}), carbon conversion efficiency (CCE), and cold gas efficiency (CGE). Compared to the reference condition, a relative decrease of about 11.8 % was observed for the LHV_G. This trend can be explained by the decrease in the CO content with a major impact on the LHV_G. In contrast, the composite catalyst showed positive effects on Y_{Gas}, CCE, and CGE, with relative increases of 25.4 %, 8.3 %, and 10.6 %, respectively. The specific production of carbon in the producer gas increased from 275.0 to 298.5 $g_C \cdot kg_{dry,fuel}^{-1}$, suggesting a positive effect of the composite catalyst on tar decomposition. It should be noted that char-related reactions did not play a role in this matter since the catalyst was placed on the freeboard zone of the gasifier where gas-solid interactions should have a negligible effect on gas composition. Furthermore, one finds significant changes in the content of hydrocarbons, with emphasis on the onset of CH_4 formation. Though the specific production of C_xH_y decrease from 40.3 to 31.3 $g_{C_xH_y} \cdot kg_{dry,fuel}^{-1}$ after application of the 50%C-Fe catalyst, the production of CH_4 was higher than the reference condition (42.6 to 47.0 $g_{CH_4} \cdot kg_{dry,fuel}^{-1}$), suggesting decomposition of heavier hydrocarbons or other compounds. For example, hydrodealkylation of toluene was proposed in previous studies with Fe/CaO-based steam reforming catalyst [68,69]. Those authors suggested that Ca and Fe active sites promote dissociation of H-H and H-O bonds into intermediates, which react with C_7H_8 to form C_6H_6 and methyl (CH_3) and desorb as CH_4. Others concluded that the activity of Fe/CaO-based catalysts convert hydrocarbons to CO and H_2 by steam reforming reactions, which may also explain the observed decrease in C_xH_y compounds [70]. However, the scope of this work is still mainly to demonstrate catalytic activity of catalysts based on siderite/concrete wastes for WGS and tar decomposition, rather than a detailed study of corresponding mechanisms.

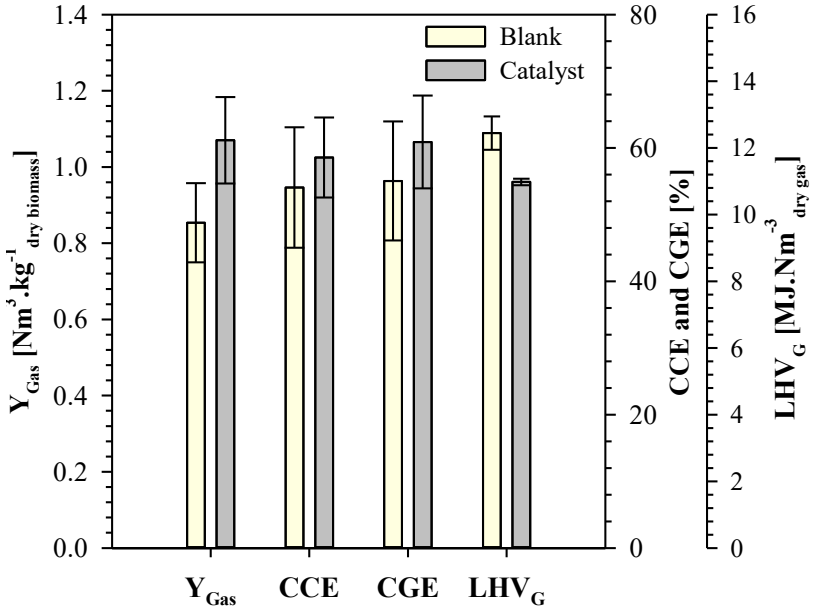

Figure 3.4-13: Y_{Gas}, CCE, CGE and LHV_G for the experiments performed without (blank) and with catalyst.

In the performed gasification experiments, raw gas composition presented a reduction factor ($R = \frac{P_{CO}+P_{H_2}}{P_{CO_2}+P_{H_2O}}$) ≈ 1.43; this indicates that reducing species prevail in the producer gas composition, promoting partial reduction of the Fe_3O_4 phase, as shown by the thermodynamic predictions in Figure 6.5, with potential impact on catalytic activity. It should be noted that the performance of Fe-based materials in WGS reaction is associated with the electronic nature of the Fe^{3+} cations, whereas Fe^{2+} and Fe^0 showed marginal contribution to catalytic activity [18,71]. Still, post-mortem analysis of the spent catalyst shows co-existence of the magnetite (Fe_3O_4) and wustite (FeO) phases (Figure 3.4-14), with potential oxygen storage ability, while acting also as a redox buffer, with coexistence of Fe^{3+} and Fe^{2+}. Additionally, XRD shows the prevailing phase (quartz), from the concrete precursor, without any evidence of crystalline Ca-containing phases. Thus, it seems that onset of carbonation, demonstrated by FTIR (Figure 3.4-12), occurs as amorphous carbonated phase [72] under the operating conditions of the gasification experiments.

3.4.3.4. Catalyst Regeneration Cycles

Ageing after repeated cycles of catalytic testing and regeneration was also assessed. These results revealed a decrease in the H_2 production from 48.6 to 42.6 $g_{H_2} \cdot kg^{-1}_{dry,fuel}$ after three regeneration cycles (Figure 3.4-15) with corresponding decrease in the H_2:CO molar ratio of the biomass-derived gas from 3.3 to 3.0. Though the activity of the catalyst progressively declines with continuous gasification/regeneration cycles, the H_2:CO molar ratio of the producer gas still reaches the established limits for the synthesis of synthetic natural gas (SNG). Compared to the reference condition, the composite catalyst with 50 wt.% concrete yielded more than 26 % of H_2 production after continuous operational cycles.

SEM measurements (Figure 3.4-16) have been carried out for the 50 wt.% concrete catalyst in order to examine the surface morphology after repeated cycles of regeneration at a higher temperature. Comparing with the fresh sample (Figure 3.4-4c), the spent 50 wt.% concrete catalyst did not show evidence of sintering after three consecutive gasification-regeneration cycles. However, a gradual appearance of microcracks was observed on the surface, which is a typical indicator of catalyst damage [73]. Degradation of catalytic activity may also be ascribed to loss of Ca active species due to thermal-induced stresses, as revealed by chemical analysis of the spent catalyst (Table S2 – Supplementary Material), which showed a reduction of Ca content from 7.63 to 4.71 wt.% after consecutive regeneration cycles. Detection of chlorine (≈ 0.04 wt.%) may also be ascribed to reaction with Ca, yielding a $CaCl_2$-rich outer layer, which may be easily abraded [74]. In addition, strong Si-Metal interactions have been suggested to negatively affect catalyst activity due to the migration of Si species to the surface of metal particles, covering and blocking the active sites [75]. Though adsorbed Si is difficult to remove, it is a reversible deactivation mechanism and thus the catalyst can be regenerated from this aspect. Still, further work is needed for a detailed understanding of deactivation mechanisms and to study the effects of relevant factors (e.g. porosity, contents of cement) on mechanical properties of granulated catalysts.

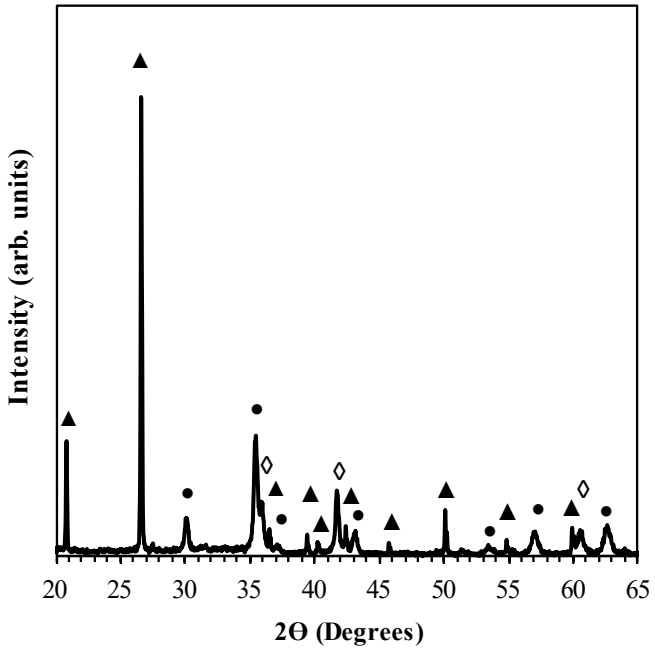

Figure 3.4-14: X-ray diffraction pattern of the 50%C-Fe catalyst after exposure to biomass-derived gas at 800 ºC (● – Fe_3O_4 ▲ – SiO_2 ◊ – FeO).

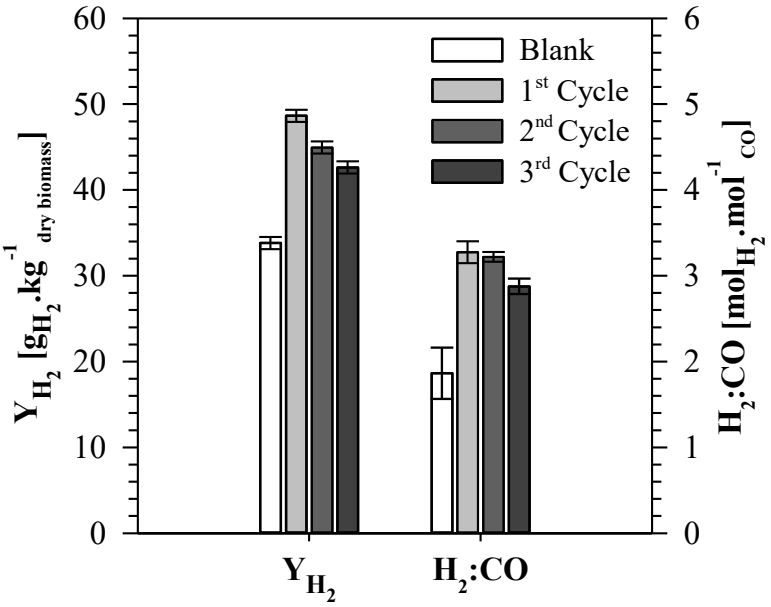

Figure 3.4-15: Specific production of H_2 and H_2:CO molar ratio for three consecutive gasification-regeneration cycles.

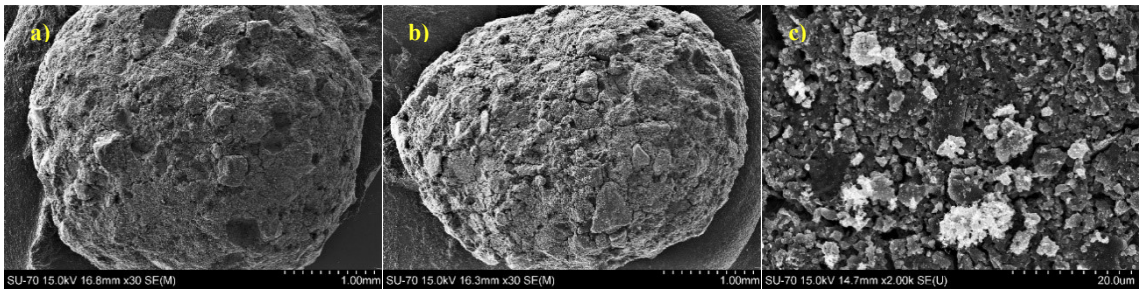

Figure 3.4-16: Microstructural evolution of the spent 50%C-Fe catalyst after the first (a) and third (b and c) gasification-regeneration cycle.

3.4.4. Conclusion

The present study proposed granulated siderite/concrete-based catalysts to promote the WGS reaction for H_2-enriched gas production from biomass steam gasification. The influence of wt.% concrete, reaction temperature and steam to carbon molar ratio on H_2 promotion were assessed by a Taguchi-type experimental design. The results indicated that the impact of the experimental parameters on H_2 promotion had the following order: reaction temperature (43.1 %), concrete mass ratio (30.2 %), and steam to carbon molar ratio (26.7 %). These contributions may be related to the redox behaviour of iron oxides with mixed valence, derived from the siderite precursor, with corresponding oxygen storage ability, and extended conditions for carbonation/decarbonation of the concrete precursor, which may provide catalytic active sites for intermediate species and CO_2 storage ability.

Based on the WGS reaction studies, the catalyst with 50 wt.% concrete was chosen for steam gasification experiments in a fixed bed reactor, located in the freeboard zone of a bench-scale fluidized bed gasifier. The results revealed significant increase in the H_2/CO molar ratio (1.9 to 3.3), H_2 yield (33.8 to 48.6 $g_{H_2} \cdot kg_{dry,fuel}^{-1}$), carbon conversion efficiency (54.1 to 58.6 %) and cold gas efficiency (55.0 to 60.9 %).

Post-mortem analysis suggests the loss of active species due to thermal-induced stresses during continuous regeneration cycles, causing gradual decline of catalytic activity. Nevertheless, the upgraded gas still complied with the H_2:CO requirements for the generation of synthetic natural gas. Thus, future research on the thermomechanical properties of the granulated catalyst is required to improve long-term performance.

Acknowledgment

The authors acknowledge the financial support through projects NOTARGAS (ref. POCI-01-0145-FEDER-030661) and “SusPhotoSolutions - Soluções Fotovoltaicas Sustentáveis”, PO Centro 2020 (ref. CENTRO-01-0145-FEDER-000005). Thanks are due to the Portuguese Foundation for Science and Technology (FCT) / Ministry of Science, Technology and Higher Education (MCTES) for the financial support to CESAM (UIDP/50017/2020+UIDB/50017/2020+LA/P/0094/2020), and CICECO (UIDB/50011/2020 & UIDP/50011/2020), through national funds. The authors also acknowledge the Portuguese Foundation for Science and Technology for providing financial support to the PhD scholarship granted to Luís Ruivo (ref. SFRH/BD/129901/2017) and Helena Gomes (ref. 2020.09864.BD). The authors sincerely thank Mr. Bill Fuerst for his support during the development of the work.

References

[1] Huber GW, Iborra S, Corma A. Synthesis of transportation fuels from biomass: Chemistry, catalysts, and engineering. Chem Rev 2006;106:4044–98. https://doi.org/10.1021/cr068360d.

[2] Fremaux S, Beheshti SM, Ghassemi H, Shahsavan-Markadeh R. An experimental study on hydrogen-rich gas production via steam gasification of biomass in a research-scale fluidized bed. Energy Convers Manag 2015;91:427–32. https://doi.org/10.1016/j.enconman.2014.12.048.

[3] Sikarwar VS, Zhao M, Clough P, Yao J, Zhong X, Memon MZ, et al. An overview of advances in biomass gasification. Energy Environ Sci 2016;9:2939–77. https://doi.org/10.1039/c6ee00935b.

[4] Xu C, Donald J, Byambajav E, Ohtsuka Y. Recent advances in catalysts for hot-gas removal of tar and NH3 from biomass gasification. Fuel 2010. https://doi.org/10.1016/j.fuel.2010.02.014.

[5] Abu El-Rub Z, Bramer EA, Brem G. Review of catalysts for tar elimination in biomass gasification processes. Ind Eng Chem Res 2004;43:6911–9. https://doi.org/10.1021/ie0498403.

[6] Sikarwar VS, Zhao M, Fennell PS, Shah N, Anthony EJ. Progress in biofuel production from gasification. Prog Energy Combust Sci 2017. https://doi.org/10.1016/j.pecs.2017.04.001.

[7] Balakos MW, Chuang SSC. CO disproportionation on Ni-based catalysts. React Kinet Catal Lett 1993;49:7–12. https://doi.org/10.1007/BF02084022.

[8] Kamata H, Tian ZQ, Izumi Y, Choong CKS, Chang J, Schreyer M, et al. Dispersed and high loading Ni catalyst stabilized in porous SiO2 matrix for substituted natural gas production. Catal Today 2018;299:193–200. https://doi.org/10.1016/j.cattod.2017.03.003.

[9] Sues A, Juraščík M, Ptasinski K. Exergetic evaluation of 5 biowastes-to-biofuels routes via gasification. Energy 2010;35:996–1007. https://doi.org/10.1016/j.energy.2009.06.027.

[10] Molino A, Braccio G. Synthetic natural gas SNG production from biomass gasification - Thermodynamics and processing aspects. Fuel 2015;139:425–9. https://doi.org/10.1016/j.fuel.2014.09.005.

[11] De La Osa AR, De Lucas A, Valverde JL, Romero A, Monteagudo I, Sánchez P. Performance of a sulfur-resistant commercial WGS catalyst employing industrial coal-derived syngas feed. Int J Hydrogen Energy 2011;36:44–51. https://doi.org/10.1016/j.ijhydene.2010.08.127.

[12] Lee DW, Lee MS, Lee JY, Kim S, Eom HJ, Moon DJ, et al. The review of Cr-free Fe-based catalysts for high-temperature water-gas shift reactions. Catal Today 2013;210:2–9. https://doi.org/10.1016/j.cattod.2012.12.012.

[13] Levalley TL, Richard AR, Fan M. The progress in water gas shift and steam reforming hydrogen production technologies - A review. Int J Hydrogen Energy 2014;39:16983–7000. https://doi.org/10.1016/j.ijhydene.2014.08.041.

[14] Lang C, Sécordel X, Kiennemann A, Courson C. Water gas shift catalysts for hydrogen production from biomass steam gasification. Fuel Process Technol 2017;156:246–52. https://doi.org/10.1016/j.fuproc.2016.09.004.

[15] Roberge TM, Blavo SO, Holt C, Matter PH, Kuhn JN. Effect of molybdenum on the sulfur-tolerance of cerium-cobalt mixed oxide water-gas shift catalysts. Top Catal 2013;56:1892–8. https://doi.org/10.1007/s11244-013-0125-z.

[16] Wang H, Lian Y, Zhang Q, Li Q, Fang W, Yang Y. MgO-Al2O3 mixed oxides-supported co-mo-based catalysts for high-temperature water-gas shift reaction. Catal Letters 2008;126:100–5. https://doi.org/10.1007/s10562-008-9587-1.

[17] Reddy GK, Boolchand P, Smirniotis PG. Unexpected behavior of copper in modified ferrites during high temperature WGS reaction-aspects of Fe 3+ ↔ Fe 2+ redox chemistry from

Mössbauer and XPS studies. J Phys Chem C 2012;116:11019–31. https://doi.org/10.1021/jp301090d.

[18] Zou J, Oladipo J, Fu S, Al-Rahbi A, Yang H, Wu C, et al. Hydrogen production from cellulose catalytic gasification on CeO2/Fe2O3 catalyst. Energy Convers Manag 2018;171:241–8. https://doi.org/10.1016/j.enconman.2018.05.104.

[19] Kung HH. Deactivation of methanol synthesis catalysts - a review. Catal Today 1992;11:443–53. https://doi.org/10.1016/0920-5861(92)80037-N.

[20] Devi L, Ptasinski KJ, Janssen FJJG. A review of the primary measures for tar elimination in biomass gasification processes. Biomass and Bioenergy 2003;24:125–40. https://doi.org/10.1016/S0961-9534(02)00102-2.

[21] Heidenreich S, Foscolo PU. New concepts in biomass gasification. Prog Energy Combust Sci 2015;46:72–95. https://doi.org/10.1016/j.pecs.2014.06.002.

[22] Nam H, Wang S, Sanjeev KC, Seo MW, Adhikari S, Shakya R, et al. Enriched hydrogen production over air and air-steam fluidized bed gasification in a bubbling fluidized bed reactor with CaO: Effects of biomass and bed material catalys. Energy Convers Manag 2020;225:113408. https://doi.org/10.1016/j.enconman.2020.113408.

[23] Detchusananard T, Im-orb K, Ponpesh P, Arpornwichanop A. Biomass gasification integrated with CO2 capture processes for high-purity hydrogen production: Process performance and energy analysis. Energy Convers Manag 2018;171:1560–72. https://doi.org/10.1016/j.enconman.2018.06.072.

[24] Udomsirichakorn J, Salam PA. Review of hydrogen-enriched gas production from steam gasification of biomass: The prospect of CaO-based chemical looping gasification. Renew Sustain Energy Rev 2014;30:565–79. https://doi.org/10.1016/j.rser.2013.10.013.

[25] Tuomi S, Kaisalo N, Simell P, Kurkela E. Effect of pressure on tar decomposition activity of different bed materials in biomass gasification conditions. Fuel 2015;158:293–305. https://doi.org/10.1016/j.fuel.2015.05.051.

[26] Huang BS, Chen HY, Chuang KH, Yang RX, Wey MY. Hydrogen production by biomass gasification in a fluidized-bed reactor promoted by an Fe/CaO catalyst. Int J Hydrogen Energy 2012;37:6511–8. https://doi.org/10.1016/j.ijhydene.2012.01.071.

[27] Ismail M, Liu W, Dunstan MT, Scott SA. Development and performance of iron based oxygen carriers containing calcium ferrites for chemical looping combustion and production of hydrogen. Int J Hydrogen Energy 2016;41:4073–84. https://doi.org/10.1016/j.ijhydene.2015.11.066.

[28] Zamboni I, Zimmermann Y, Kiennemann A, Courson C. Improvement of steam reforming of toluene by CO2 capture using Fe/CaO-Ca12Al14O33 bi-functional materials. Int J Hydrogen Energy 2015;40:5297–304. https://doi.org/10.1016/j.ijhydene.2015.01.065.

[29] Hill JM. Sustainable and/or waste sources for catalysts: Porous carbon development and gasification. Catal Today 2017;285:204–10. https://doi.org/10.1016/j.cattod.2016.12.033.

[30] Balakrishnan M, Batra VS, Hargreaves JSJ, Pulford ID. Waste materials – catalytic opportunities: An overview of the application of large scale waste materials as resources for catalytic applications. Green Chem 2011;13:16–24. https://doi.org/10.1039/c0gc00685h.

[31] Shan R, Zhao C, Lv P, Yuan H, Yao J. Catalytic applications of calcium rich waste materials for biodiesel: Current state and perspectives. Energy Convers Manag 2016;127:273–83. https://doi.org/10.1016/j.enconman.2016.09.018.

[32] Hasanbeigi A, Price L, Lin E. Emerging energy-efficiency and CO 2 emission-reduction technologies for cement and concrete production: A technical review. Renew Sustain Energy Rev 2012;16:6220–38. https://doi.org/10.1016/j.rser.2012.07.019.

[33] Tam VWY, Gao XF, Tam CM, Ng KM. Physio-chemical reactions in recycle aggregate concrete. J Hazard Mater 2009;163:823–8. https://doi.org/10.1016/j.jhazmat.2008.07.031.

[34] Popa T, Fan M, Argyle MD, Dyar MD, Gao Y, Tang J, et al. H2 and COx generation from coal

gasification catalyzed by a cost-effective iron catalyst. Appl Catal A Gen 2013;464–465:207–17. https://doi.org/10.1016/j.apcata.2013.05.038.

[35] Kang K, Azargohar R, Dalai AK, Wang H. Hydrogen production from lignin, cellulose and waste biomass via supercritical water gasification: Catalyst activity and process optimization study. Energy Convers Manag 2016;117:528–37. https://doi.org/10.1016/j.enconman.2016.03.008.

[36] Hughes SW. Archimedes revisited: A faster, better, cheaper method of accurately measuring the volume of small objects. Phys Educ 2005;40:468–74. https://doi.org/10.1088/0031-9120/40/5/008.

[37] Ryu HJ, Saito F. Single particle crushing of nonmetallic inorganic brittle materials. Solid State Ionics 1991;47:35–50. https://doi.org/10.1016/0167-2738(91)90177-D.

[38] Taguchi G, Chowdhury S, Wu Y. Quality Engineering: The Taguchi Method. Taguchi's Qual. Eng. Handb., John Wiley & Sons, Inc.; 2004, p. 56–123. https://doi.org/10.1002/9780470258354.

[39] Pio DT, Gomes HGMF, Ruivo LCM, Matos MAA, Monteiro JF, Frade JR, et al. Concrete as low-cost catalyst to improve gas quality during biomass gasification in a pilot-scale gasifier. Energy 2021;233:120931. https://doi.org/10.1016/j.energy.2021.120931.

[40] Channiwala SA, Parikh PP. A unified correlation for estimating HHV of solid, liquid and gaseous fuels. Fuel 2002;81:1051–63.

[41] Acharya B, Dutta A, Basu P. Circulating-fluidized-bed-based calcium-looping gasifier: Experimental studies on the calcination-carbonation cycle. Ind Eng Chem Res 2012;51:8652–60. https://doi.org/10.1021/ie300629a.

[42] Ruivo LCM, Pio DT, Yaremchenko AA, Tarelho LAC, Frade JR, Kantarelis E, et al. Iron-based catalyst (Fe2-xNixTiO5) for tar decomposition in biomass gasification. Fuel 2021;300:120859. https://doi.org/10.1016/j.fuel.2021.120859.

[43] Morandeau A, Thiéry M, Dangla P. Investigation of the carbonation mechanism of CH and C-S-H in terms of kinetics, microstructure changes and moisture properties. Cem Concr Res 2014;56:153–70. https://doi.org/10.1016/j.cemconres.2013.11.015.

[44] Baraj E, Ciahotný K, Hlinčík T. The water gas shift reaction: Catalysts and reaction mechanism. Fuel 2021;288:119817. https://doi.org/10.1016/j.fuel.2020.119817.

[45] Courtault B. Synthèse de la spurrite. Bull La Société Française Minéralogie Cristallogr 1964;87:527–31. https://doi.org/10.3406/bulmi.1964.5773.

[46] Bolio-Arceo H, Glasser FP. Formation of spurrite, Ca5(SiO4)2CO3. Cem Concr Res 1990;20:301–7. https://doi.org/10.1016/0008-8846(90)90084-B.

[47] Karunadasa KSP, Manoratne CH, Pitawala HMTGA, Rajapakse RMG. Thermal decomposition of calcium carbonate (calcite polymorph) as examined by in-situ high-temperature X-ray powder diffraction. J Phys Chem Solids 2019;134:21–8. https://doi.org/10.1016/j.jpcs.2019.05.023.

[48] Suzuki K, Ito S, Nishikawa T, Shinno I. Effect of Na, K and Fe on the formation of α- and β-Ca2SiO4. Cem Concr Res 1986;16:885–92. https://doi.org/10.1016/0008-8846(86)90012-8.

[49] Popa T, Xu G, Barton TF, Argyle MD. High temperature water gas shift catalysts with alumina. Appl Catal A Gen 2010;379:15–23. https://doi.org/10.1016/j.apcata.2010.02.021.

[50] Zhu M, Wachs IE. Iron-Based Catalysts for the High-Temperature Water-Gas Shift (HT-WGS) Reaction: A Review. ACS Catal 2016. https://doi.org/10.1021/acscatal.5b02594.

[51] Lin CH, Chen CL, Wang JH. Mechanistic studies of water-gas-shift reaction on transition metals. J Phys Chem C 2011;115:18582–8. https://doi.org/10.1021/jp2034467.

[52] Florin NH, Harris AT. Enhanced hydrogen production from biomass with in situ carbon dioxide capture using calcium oxide sorbents. Chem Eng Sci 2008;63:287–316. https://doi.org/10.1016/j.ces.2007.09.011.

[53] Li B, Wei L, Yang H, Wang X, Chen H. The enhancing mechanism of calcium oxide on water

gas shift reaction for hydrogen production. Energy 2014;68:248–54. https://doi.org/10.1016/j.energy.2014.02.088.

[54] Basu P. Biomass Gasification, Pyrolysis and Torrefaction: Practical Design and Theory. 2013. https://doi.org/10.1016/C2011-0-07564-6.

[55] Rhodes C, Hutchings GJ, Ward AM. Water-gas shift reaction: finding the mechanistic boundary. Catal Today 1995;23:43–58. https://doi.org/10.1016/0920-5861(94)00135-O.

[56] Reddy GK, Boolchand P, Smirniotis PG. Sulfur tolerant metal doped Fe/Ce catalysts for high temperature WGS reaction at low steam to CO ratios - XPS and Mossbauer spectroscopic study. J Catal 2011;282:258–69. https://doi.org/10.1016/j.jcat.2011.06.016.

[57] Cortazar M, Lopez G, Alvarez J, Amutio M, Bilbao J, Olazar M. Behaviour of primary catalysts in the biomass steam gasification in a fountain confined spouted bed. Fuel 2019;253:1446–56. https://doi.org/10.1016/j.fuel.2019.05.094.

[58] Cortazar M, Santamaria L, Lopez G, Alvarez J, Amutio M, Bilbao J, et al. Fe/olivine as primary catalyst in the biomass steam gasification in a fountain confined spouted bed reactor. J Ind Eng Chem 2021;99:364–79. https://doi.org/10.1016/j.jiec.2021.04.046.

[59] Xie Y, Xiao J, Shen L, Wang J, Zhu J, Hao J. Effects of Ca-based catalysts on biomass gasification with steam in a circulating spout-fluid bed reactor. Energy and Fuels 2010;24:3256–61. https://doi.org/10.1021/ef100081w.

[60] Zeng X, Fang M, Lv T, Tian J, Xia Z, Cen J, et al. Enhanced hydrogen production by the catalytic alkaline thermal gasification of cellulose with Ni/Fe dual-functional CaO based catalysts. Int J Hydrogen Energy 2021;46:32783–99. https://doi.org/10.1016/j.ijhydene.2021.07.142.

[61] Ashraf W, Olek J. Carbonation behavior of hydraulic and non-hydraulic calcium silicates: potential of utilizing low-lime calcium silicates in cement-based materials. J Mater Sci 2016;51:6173–91. https://doi.org/10.1007/s10853-016-9909-4.

[62] Chang CF, Chen JW. The experimental investigation of concrete carbonation depth. Cem Concr Res 2006;36:1760–7. https://doi.org/10.1016/j.cemconres.2004.07.025.

[63] Zhang Z, Xie Y, Xu X, Pan H, Tang R. Transformation of amorphous calcium carbonate into aragonite. J Cryst Growth 2012;343:62–6. https://doi.org/10.1016/j.jcrysgro.2012.01.025.

[64] Tang C, Zhu J, Li Z, Zhu R, Zhou Q, Wei J, et al. Surface chemistry and reactivity of SiO 2 polymorphs: A comparative study on α-quartz and α-cristobalite. Appl Surf Sci 2015;355:1161–7. https://doi.org/10.1016/j.apsusc.2015.07.214.

[65] Coenen K, Gallucci F, Mezari B, Hensen E, van Sint Annaland M. An in-situ IR study on the adsorption of CO2 and H2O on hydrotalcites. J CO2 Util 2018;24:228–39. https://doi.org/10.1016/j.jcou.2018.01.008.

[66] Udomsirichakorn J, Basu P, Abdul Salam P, Acharya B. CaO-based chemical looping gasification of biomass for hydrogen-enriched gas production with in situ CO2 capture and tar reduction. Fuel Process Technol 2014;127:7–12. https://doi.org/10.1016/j.fuproc.2014.06.007.

[67] Chan MSC, Liu W, Ismail M, Yang Y, Scott SA, Dennis JS. Improving hydrogen yields, and hydrogen: Steam ratio in the chemical looping production of hydrogen using Ca2Fe2O5. Chem Eng J 2016;296:406–11. https://doi.org/10.1016/j.cej.2016.03.132.

[68] Zamboni I, Courson C, Kiennemann A. Fe-Ca interactions in Fe-based/CaO catalyst/sorbent for CO2 sorption and hydrogen production from toluene steam reforming. Appl Catal B Environ 2017;203:154–65. https://doi.org/10.1016/j.apcatb.2016.10.024.

[69] Han L, Liu Q, Lin K, Wang Q, Rong N, Liang X, et al. Enhanced hydrogen production via catalytic toluene reforming with in situ carbon dioxide capture: Effects of a hybrid iron-calcium composite prepared by impregnation. Energy Convers Manag 2020;214:112834. https://doi.org/10.1016/j.enconman.2020.112834.

[70] Zamboni I, Courson C, Kiennemann A. Synthesis of Fe/CaO active sorbent for CO2

absorption and tars removal in biomass gasification. Catal Today 2011;176:197–201. https://doi.org/10.1016/j.cattod.2011.01.014.

[71] Rhodes C, Williams BP, King F, Hutchings GJ. Promotion of Fe3O4/Cr2O3 high temperature water gas shift catalyst. Catal Commun 2002;3:381–4. https://doi.org/10.1016/S1566-7367(02)00156-5.

[72] Okano K, Ohtake H, Kunisada M, Takano H, Toda M. Phosphate recovery using amorphous calcium silicate hydrates. In: Ohtake H. TS, editor. Phosphorus Recover. Recycl., 2018, p. 435–47. https://doi.org/10.1007/978-981-10-8031-9_30.

[73] Young A, Henderson S, Buchanan L, Hall D, Bishop C. Failure of commercial extruded catalysts in simple compression and bulk thermal cycling. Int J Appl Ceram Technol 2018;15:74–88. https://doi.org/10.1111/ijac.12788.

[74] Nordgreen T, Nemanova V, Engvall K, Sjöström K. Iron-based materials as tar depletion catalysts in biomass gasification: Dependency on oxygen potential. Fuel 2012;95:71–8. https://doi.org/10.1016/j.fuel.2011.06.002.

[75] Smith G V., Tjandra S, Musoiu M, Wiltowski T, Notheisz F, Bartók M, et al. Modified activities and selectivities of silated-oxidized-reduced Pd and Pt catalysts. J Catal 1996;161:441–50. https://doi.org/10.1006/jcat.1996.0202.

Supplementary Material

Table S1 – Molar flow rates obtained at the reactor inlet and outlet during catalytic WGS experiments.

Experiment	Trial	*Experimental Conditions*			*Inlet Molar Flow Rates (mol·min^{-1})*			*Outlet Molar Flow Rates (mol·min^{-1})*					*Carbon Balance*
		T (ºC)	% Concrete	S/CO	N_2	CO	H_2O	N_2	CO	H_2	CO_2	H_2O	ΔC
Blank	1	500	Al_2O_3	1	2.743E-02	3.047E-03	3.042E-03	2.743E-02	2.865E-03	2.867E-07	2.166E-06	9.016E-03	94.4 %
	2			3	2.743E-02	3.047E-03	9.016E-03	2.743E-02	2.879E-03	2.233E-06	5.108E-06	9.014E-03	
L1	1	500	0	1	2.743E-02	3.047E-03	3.042E-03	2.743E-02	2.632E-03	2.198E-04	2.422E-04	2.800E-03	95.4 %
	2				2.743E-02	3.047E-03	3.042E-03	2.743E-02	2.676E-03	2.465E-04	2.620E-04	2.780E-03	
L2	1	500	0.25	2	2.743E-02	3.047E-03	6.029E-03	2.743E-02	2.448E-03	4.333E-04	4.298E-04	5.596E-03	95.8 %
	2				2.743E-02	3.047E-03	6.029E-03	2.743E-02	2.483E-03	4.997E-04	4.779E-04	5.530E-03	
L3	1	500	0.50	3	2.743E-02	3.047E-03	9.016E-03	2.743E-02	1.594E-03	1.288E-03	1.282E-03	7.728E-03	94.0 %
	2				2.743E-02	3.047E-03	9.016E-03	2.743E-02	1.544E-03	1.353E-03	1.309E-03	7.663E-03	
L4	1	600	0	2	2.743E-02	3.047E-03	6.029E-03	2.743E-02	2.171E-03	7.911E-04	7.905E-04	5.238E-03	97.3 %
	2				2.743E-02	3.047E-03	6.029E-03	2.743E-02	2.164E-03	7.960E-04	8.031E-04	5.233E-03	
L5	1	600	0.25	3	2.743E-02	3.047E-03	9.016E-03	2.743E-02	1.629E-03	1.271E-03	1.273E-03	7.745E-03	94.9 %
	2				2.743E-02	3.047E-03	9.016E-03	2.743E-02	1.625E-03	1.241E-03	1.258E-03	7.775E-03	
L6	1	600	0.50	1	2.743E-02	3.047E-03	3.042E-03	2.743E-02	1.970E-03	9.826E-04	9.661E-04	2.060E-03	92.5 %
	2				2.743E-02	3.047E-03	3.042E-03	2.743E-02	1.693E-03	1.026E-03	1.009E-03	2.016E-03	
L7	1	700	0	3	2.743E-02	3.047E-03	9.016E-03	2.743E-02	1.710E-03	1.162E-03	1.161E-03	7.854E-03	94.3 %
	2				2.743E-02	3.047E-03	9.016E-03	2.743E-02	1.619E-03	1.289E-03	1.254E-03	7.727E-03	
L8	1	700	0.25	1	2.743E-02	3.047E-03	3.042E-03	2.743E-02	1.919E-03	9.702E-04	8.936E-04	2.072E-03	91.5 %
	2				2.743E-02	3.047E-03	3.042E-03	2.743E-02	1.823E-03	1.019E-03	9.382E-04	2.024E-03	
L9	1	700	0.50	2	2.743E-02	3.047E-03	6.029E-03	2.743E-02	1.149E-03	1.612E-03	1.491E-03	4.418E-03	90.4 %
	2				2.743E-02	3.047E-03	6.029E-03	2.743E-02	1.238E-03	1.780E-03	1.630E-03	4.250E-03	

Table S2 – Elemental analysis (wt.%) of the spent 50%C-Fe catalyst after regeneration cycles.

Element	Fresh 50%C-Fe	Spent 50%C-Fe
Fe	30.12	41.71
O	40.30	37.28
Si	19.76	12.96
Ca	7.63	4.71
Al	1.68	2.72
Mg	0.33	0.36
Ti	0.08	0.10
Mn	0.09	0.12
Cl	-	0.04
S	-	0.01

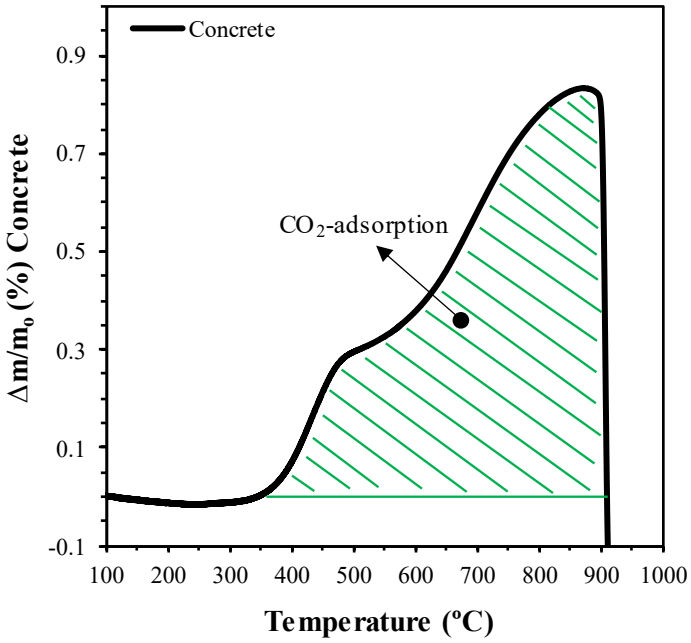

Figure S1 – Relative weight change of heating concrete sample aged for 1 month in CO_2 at 1°C/min.

4. CONCLUSIONS AND FUTURE WORK

The challenge of moving toward a carbon-neutral and more sustainable economy will inevitably require drastic transformation of the energy sector, and fuel-derived commodities. Thermal conversion of lignocellulosic biomass through gasification processes can be important in this context, given H_2+CO-based gas mixtures which can be used as commodities for other industrial applications. However, implementation of large-scale technologies still face important challenges, mostly related to the presence of unwanted tar compounds which cause operational constrains. This requires improved gasification technologies with higher efficiency and the catalytic upgrading of the biomass-derived gas by tar conversion to meet the requirements of producer gas for different end-use applications. For this purpose, catalysts should be designed taking into account sustainability and low cost criteria in the selection of materials, with potential applicability in technologies with limited economic feasibility.

Consequently, this thesis sought to increase scientific knowledge in the field of catalytic gasification of lignocellulosic biomass by exploiting the potential of low-cost materials as a feasible alternative to other expensive synthetic catalysts. This was based on the design of iron-based catalytic systems with different structure types and adjusted compositions, seeking enhanced performance by optimizing their redox behaviour and CO_2 storage ability by reversible carbonation/decarbonation of alkaline earth components. Selected catalysts were tested under realistic conditions to get insights into their contribution to both tar conversion and H_2 promotion, and relevant catalytic mechanisms. The results indicated that the developed materials are potential candidates for catalytic hot gas upgrading applications, exhibiting comparable performance to other catalysts found in literature. Nevertheless, further experimental and theoretical developments are still needed before those materials might be applicable in future biomass gasification concepts.

Downstream application of an ilmenite-based catalyst with low Ni content was explored for tar steam reforming. The material was prepared by combining mechanical activation and microwave firing, showing strong metal-support interactions between Ni and Fe_2TiO_5 structure. Though a uniform distribution of active species was observed, microstructural studies suggest potential aggregation of Ni particles after thermal treatment of the catalyst. In addition, typical mineral-based catalysts are characterized as dense materials with lower surface area and porosity. This create a window of opportunity to enhance the performance of such materials, since structural properties exhibit a positive correlation with catalytic activity and stability. Therefore, future research with the developed

catalytic system could focus on investigating alternative synthesis routes to improve their structural properties. A potential processing route could be based on emulsification techniques, aiming to obtain porous supports with cellular microstructures (monoliths and granules). In addition, these porous structures may be further functionalized with adjusted metal loads and controlled heat treatment at lower temperature to induce nanostructured metallic precipitates with uniform size distribution.

The $Fe_{2-x}Ni_xTiO_5$ catalyst showed a high tar conversion ability when exposed to biomass-derived gas from a bubbling fluidized bed gasifier. However, a significant drop in catalyst activity was observed at longer times on stream, due to oxidation of iron active sites imposed by redox conditions of biomass gasification, which need to be considered as a critical parameter in enhancing catalyst performance. Thermodynamic calculations also suggest the deactivation of Ni active sites as a result of sulfur poisoning, which may also explain the decline in tar decomposition. Considering the poor tolerance of Ni to sulphur, future work could focus on purification strategies for prior H_2S removal at high temperature. This might be based on cellular adsorbents, processed from low-cost alkaline-earth metals based-materials such as calcium silicates, with recognized hydrothermal resistance.

Incorporation of a highly gas permeable $Fe_{2-x}Mn_xO_3$ catalyst into the freeboard zone of a biomass gasifier was investigated as alternative for downstream removal of biomass-derived tar. The main focus here was to increase lattice oxygen mobility by Mn addition, seeking to promote tar conversion by oxidation reactions without compromising the efficiency of the process. The catalyst showed high activity in converting tar compounds, facilitated by the variable oxygen stoichiometry of mixed Fe/Mn oxides, which promoted oxidation reactions. Other process parameters, such as carbon conversion efficiency and cold gas efficiency, were also improved which confirms its successful application. Post-mortem analysis of the spent catalyst showed presence of sulfur, although this does not prevent enhanced catalytic activity, probably due to wide redox stability of divalent manganese oxide and its greater sulphur tolerance in gasification conditions.

Though $Fe_{2-x}Mn_xO_3$ catalysts seems a highly promising strategy for tar abatement, longer exposure tests are necessary to evaluate the prospective application of such materials in industrial biomass gasification processes. The presence of impurities such as sulfur and alkali compounds imposes demanding challenges to sustain the catalytic activity of active sites and to ensure long term stability, by minimizing the effects of impurities. Ash and char particles interactions can also have a deleterious impact on the in-situ operation of iron-containing materials Limitations of the available experimental infrastructure did not allow proper long-term assessment of these effects. This highlights the need for further

development of laboratory procedures and equipment in order to reach better understanding of all these aspects related to the applicability of metal-containing materials in biomass gasification. Thus, it would be interesting to design experiments with controlled contents of biomass-derived impurities (e.g. HCl and H_2S) for a detailed understanding of gas-solid interactions at longer times, to validate theoretical models and to determine corresponding kinetic parameters of catalyst poisoning mechanisms. The outcomes of these studies are considered of major relevance since they will make it possible to define potential regeneration processes.

Following the same in-situ operation approach, one assessed the applicability of a granulated siderite/concrete composite catalyst to promote the WGS reaction for H_2-enriched gas production from biomass steam gasification. Taguchi experimental design was implemented to seek optimal operating conditions for H_2 production. The catalyst exhibited a significant impact on H_2 production during consecutive operation cycles, which is attributed to the redox behaviour of iron oxides with mixed valence, derived from the siderite precursor, with corresponding oxygen storage ability, and extended conditions for carbonation/decarbonation of the concrete precursor, which may provide catalytic active sites for intermediate species, and may promote reaction steps assisted by CO_2 storage.

The continuous operation of the granular $FeCO_3$/Concrete catalyst resulted in the formation of microcracks and loss of active species on the surface of material due to thermal-induced stresses. Mechanical failure of catalyst may also affect the pressure drop and local temperature, which causes maldistribution of gas flow across the catalytic reactor with negative impact on the overall performance of the gasification process. However, a high strength may also result in lower porosity, causing decrease in the catalyst performance due to internal diffusion limitations. Based on the above considerations, future research should focus on the mechanical reliability of the catalyst. To address this issue, bulk mechanical studies should be performed, including the application of a theoretical approach to simulate numerically the mechanical behavior of packed bed particles (granules and pellets). Furthermore, the elastic behavior and crushing strength measurements must be correlated with degradation of catalytic activity under realistic operating conditions, in order to determine suitable structural and microstructural developments required for industrial applications.

Regarding tar conversion mechanisms, the enthalpy associated with these reactions may represent an important fraction of the sensible heat of producer gas, possibly affecting catalytic performance by local cooling of active sites. In the case of industrial-scale catalytic applications, gas-solid reactions are usually carried out in fixed bed reactors, and truly isothermal conditions are seldom reached in the packed bed. As a result, high energy inputs are involved in reforming and cracking processes to balance heat transfer limitations, which points out the necessity to explore alternative energy efficient methods.

In this perspective, microwave-assisted operation can significantly improve the performance of tar conversion catalysts. Compared with conventional heating, where heat is shifted from the surface to the core of material through conduction driven by temperature gradients, microwaves induces local heating by direct conversion of the electromagnetic field into heat; this promotes direct heating of catalyst particles, preventing their undercooling by endothermic reactions such as tar conversion. The effectiveness of the process will depend on the microwave-absorbing ability of catalysts, which is mainly dictated by their dielectric and magnetic properties. Therefore, future research should focus on improving the performance of such catalytic systems to optimize their properties for prospective microwave-assisted operation.

It should be noted that the catalytic concepts explored in this work are flexible for compositional, structural and redox changes, with expected impact on the catalytic activity and other relevant properties for prospective materials with additional functionalities such as self-heating ability. Depending on the redox conditions of the gas atmosphere, those materials allow different compounds to be obtained, in which magnetic ($FeTiO_3$, Fe_3O_4) or dielectric (Fe_2TiO_4, $MnFe_2O_4$) properties may confer new functionalities for magnetic separation and/or microwave self-heating. This implies the development of experimental infrastructure to perform extensive experimental studies, starting from reactions with synthetic gas mixtures and then scale-up to realistic gasification conditions. Dielectric measurements (e.g. dielectric constant and loss factor) should be used as guidelines to select catalysts with adequate properties for microwave-assisted operation. Post-mortem analysis of the spent catalysts should also be performed in order to evaluate potential degradation mechanisms during time on stream.

APPENDIX – OTHER RELATED PAPERS

Energy Conversion and Management 229 (2021) 113749

Contents lists available at ScienceDirect

Energy Conversion and Management

journal homepage: www.elsevier.com/locate/enconman

Tar formation during eucalyptus gasification in a bubbling fluidized bed reactor: Effect of feedstock and reactor bed composition

D.T. Pio [a,*], L.C.M. Ruivo [a], L.A.C. Tarelho [a], J.R. Frade [b], E. Kantarelis [c], K. Engvall [c]

[a] Department of Environment and Planning & Centre for Environmental and Marine Studies (CESAM), University of Aveiro, Campus Universitário de Santiago, Aveiro, Portugal
[b] Department of Materials Engineering and Ceramics & Aveiro Institute of Materials (CICECO), University of Aveiro, Campus Universitário de Santiago, Aveiro, Portugal
[c] Department of Chemical Engineering, KTH Royal Institute of Technology, SE-100 44 Stockholm, Sweden

ARTICLE INFO

Keywords:
Gasification
Biomass
Tars
Ash
Bubbling fluidized bed
Eucalyptus

ABSTRACT

Tar compounds are inevitably present in the raw producer gas from biomass gasification and currently represent the main barrier for the commercial breakthrough of gasification technologies. In the present work, tar concentration in the producer gas from direct gasification of distinct types of residual forest biomass from eucalyptus in a 5 kW_{th} bubbling fluidized bed reactor was investigated. The influence of the feedstock chemical composition and gasifier operation time was evaluated. Average tar concentration values in the raw producer gas were between 1.5 and 13.3 g/Nm^3, representing a tar production between 8.4 and 67.0 g tar/kg biomass db, which surpasses suggested tar concentration limits for various potential applications for the producer gas. Major average tar compounds present in the tar sampled from the raw producer gas were benzene (47.1 %wt), toluene (21.6 %wt), naphthalene (10 %wt) and indene (6.4 %wt). A significant decay of the tar concentration in the producer gas was observed with increasing gasifier operation time, namely up to 50% within 45 min of operation, indicating its dependency on inorganics (e.g., $CaCO_3$, KCl, maximum 5.5 %wt) and solid carbon (maximum 22.7 %wt) accumulation in the reactor bed.

1. Introduction

The commercialization of large-scale biomass gasification plants still face technical and economic challenges associated with the presence of tars in the producer gas [1–4]. Tars are a mixture of highly aromatic organic condensable compounds formed during thermal or partial-oxidation (gasification) regimes of any organic material [5]. The composition of tars is highly dependent on the thermal conversion process temperature and can be divided in primary (e.g., phenol), secondary (e.g., benzene, toluene, xylene) and tertiary (e.g., pyrene, indene, naphthalene) products, roughly formed at 200 to 500 °C, 500 to 1000 °C and over 700 °C, respectively [3,5]; primary and tertiary tars are mutually exclusive, being that primary products are destroyed before tertiary products appear [5]. In bubbling fluidized bed (BFB) gasifiers, as the operation takes place between 700 and 850 °C [6], a mixture of second and tertiary tar products can be expected in the producer gas [5]. These undesired compounds represent a not negligible part of the chemical energy in the producer gas, which may be lost upon condensation [7]. Tars are also a major obstacle, causing several operating problems during the gasification process and downstream use of the producer gas, such as surface corrosion, blocking and fouling of engines, filter and pipe plugging and catalyst deactivation, leading to general malfunctions of equipment, breakdowns in operation and low efficiency [2,8,9].

The tar concentration in a producer gas from BFB gasifiers typically revolves around 1 to 30 g/Nm^3 [5,10], which is higher than the suggested tar concentration limit for most potential producer gas applications [4]. The employment of gas cleaning equipment for tar removal often turns the process economically unattractive. Accordingly, the effect of gasification operating parameters on tar compounds formation and concentration has been widely investigated in the literature, with particular emphasis on temperature [11–15], equivalence ratio (ER) [11,16], pressure [17], residence time [18] and reactor bottom bed material [9,10,19]. In general, tar concentration in the producer gas decreases with temperature, ER and pressure increase [20]. Using active bed materials (e.g., dolomite, limestone and olivine) has also been demonstrated as a strategy to reduce tar concentration in the producer gas [10,19,20].

The effect of the chemical properties of the biomass feedstock has

* Corresponding author.
E-mail address: danieltp@ua.pt (D.T. Pio).

https://doi.org/10.1016/j.enconman.2020.113749
Received 29 September 2020; Received in revised form 24 November 2020; Accepted 6 December 2020
Available online 24 December 2020

Nomenclature

AAEM	Alkali and Alkaline Earth Metals (Ca, K, Mg, Na and Ba)
BFB	Bubbling fluidized bed
C	Carbon (monoatomic)
CCE	Carbon conversion efficiency [%]
CGE	Cold gas efficiency [%]
daf	Dry ash free
db	Dry basis
EDS	Energy Dispersive X-ray Spectroscopy
ER	Equivalence ratio
ETS	Gasification experiments with a tar sampling start between 17 and 32 min
FID	Flame Ionization Detector
GHG	Greenhouse Gas
H	Atomic hydrogen
i	Gaseous compound CO_2, CO, CH_4 and C_2H_4
ICP-SFMS	Induced Coupled Plasma Mass Sector Field Mass Spectrometry
LHV	Lower heating value [MJ/Nm^3]
LHV_F	Lower heating value of the biomass [MJ/kg db]
LHV_G	Lower heating value of the dry gas produced [MJ/Nm^3]
LTS	Gasification experiments with a tar sampling start between 119 and 129 min
M_C	Molar mass of Carbon [kg/mol]
mF	Biomass (dry basis) mass flow rate [kg db/s]
N	Atomic nitrogen
NL	Refers to liter at normal pressure (1.013×10^5 Pa) and temperature (0 °C)
Nm^3	Refers to m^3 at normal pressure (1.013×10^5 Pa) and temperature (0 °C)
O	Atomic oxygen
P_G	Absolute pressure of the dry gas [Pa]
R	Ideal gas constant [$J.mol^{-1}.K^{-1}$]
RFB	Residual forest biomass
S	Atomic sulfur
SEM	Scanning Electron Microscopy
SPA	Solid Phase Adsorption
SPE	Solid Phase Extraction
TCD	Thermal Conductivity Detector
T_G	Absolute temperature of the dry gas [T]
V_G	Dry gas volumetric flow rate [Nm^3/s]
W_{CF}	Weight fraction of Carbon in the biomass [kg C/kg biomass db]
Y_{gas}	Dry gas specific production [Nm^3 dry gas/kg dry biomass]
y_i	Molar fraction of CO_2, CO, CH_4, C_2H_4, in the dry gas produced
%v	Volume percentage [%]
%wt	Weight percentage [%]

Greek symbols

$\varepsilon_{C,I}$	Molar fraction of Carbon in i [mol C/mol i]

also been researched [21–26]. Yu et al., [23] compared the major biomass components (i.e. cellulose, hemicellulose and lignin) in relation to their differing tar formation characteristics during gasification and concluded that lignin leads to a higher tar yield with a higher thermal stability. Additionally, Hosoya et al., [24] observed that the primary tar fraction derived from lignin has a significantly lower reactivity than the one derived from cellulose, with the latter easily gasified into permanent gases. In accordance, Zhou et al., [25] showed that the main fraction of tar in the producer gas from biomass gasification was lignin-derived phenolics. In another study, Wang et al., [26] observed that adding potassium and calcium to the thermal decomposition of cellulose leads to a lower tar yield and an enhanced permanent gases production.

The gasification process is particularly interesting for converting eucalyptus byproducts from the pulp and paper industry due to the possibility of replacing natural gas by producer gas in kiln ovens and boilers, and the suitability of this industry to involve gasification-based biorefinery processes in the future [27]. Pio et al., [6] demonstrated the potential of air gasification of eucalyptus (*Eucalyptus Globulus*) in a pilot-scale BFB reactor, including the analysis of the influence of various operating parameters (e.g, bed temperature and ER) on the production of non-condensable gases. The study, however, did not report on experimental data on tar composition and concentration in the producer gas. Cross et al., [28] studied eucalyptus (*Eucalyptus Benthamii*) air gasification in a bench-scale BFB, focusing on the effect of harvesting age and bark content, and found tar yield between 1.3 and 1.7 g tar/kg biomass db, with higher amounts of naphthalene and indene and lower amounts of benzene (resulting in a lower total tar yield) in the producer gas from the gasification of older eucalyptus samples. Pinto et al., [29] performed steam gasification of eucalyptus (*Eucalyptus Globulus*) in a bench-scale BFB reactor, focusing on the influence of the feedstock torrefaction and pelletization, and found tar concentration in the producer gas between 4 and 16 g/m^3 (values retrieved from figures), with these pretreatment measures leading to a decrease of tar concentration in the raw producer gas of up to 72%. Nonetheless, data regarding tar concentration in the producer gas from eucalyptus gasification is limited and investigation on tar formation during gasification of biomass usually neglects the depth of the influence of the feedstock chemical composition. For example, it is often neglected the catalytic effect promoted by alkali and alkaline earth metals (AAEMs) present in the biomass ashes, which are recognized promoters of tar cracking and reforming reactions [26,30,31]; this highlights the need for additional studies.

Thus, this work investigates tar formation during the direct gasification of distinct types of residual forest biomass (RFB) from eucalyptus (*Eucalyptus Globulus)*, including eucalyptus byproducts from the pulp and paper industry, in a bench-scale BFB reactor. The main objective is to evaluate the influence of the eucalyptus chemical composition, and respective ashes, as well as chars', accumulation in the bed of the BFB gasifier with operation time, on the tar composition and concentration in the producer gas. An inert material (non-porous alumina, Al_2O_3) was used as bed material to minimize any potential activity from the fresh bed material towards char gasification and tar formation [32,33]. This provides valuable data for the evaluation of the gasification process of eucalyptus feedstocks, and consequent integration in the pulp and paper industry, as a valid valorization energetic option. It will also serve as a guideline for future research seeking tar reduction in the producer gas from biomass gasification in BFBs, which is the main barrier for the commercial breakthrough of these technologies [2].

2. Materials and methods

2.1. Characterization of the feedstock

The feedstocks used in the gasification experiments consisted of pellets (2–4 mm) produced from distinct fractions of RFB from eucalyptus (*Eucalyptus Globulus)*, namely:

- Pellets 1 – Eucalyptus wood fines (<1 mm) from industrial operations related to woodchip production from eucalyptus logs in the context of the pulp and paper industry, hereafter, called eucalyptus wood fines.
- Pellets 2 – Eucalyptus wood fines (<1 mm) and eucalyptus leaves.
- Pellets 3 – Eucalyptus branches (<30 mm in diameter).

Table 1
Characteristics of the different types of eucalyptus pellets used as feedstock in the gasification experiments performed in the atmospheric BFB.

	Pellets			
	1	2	3	4
Proximate analysis				
Moisture (%wt)	8.9	8.3	7.9	6.7
Volatile matter (%wt, db)	77.1	79	77.1	80.0
Fixed carbon (%wt, db)	15.6	17.7	18.5	16.6
Ash (%wt, db)	7.3	3.3	4.4	3.4
Ultimate analysis (%wt, db)				
Ash	7.3	3.3	4.4	3.4
C	48.2	50.9	51.4	51.2
H	6.2	6.1	6.1	6.1
N	<0.2	0.9	1.4	1.2
S	0.03	bd	bd	bd
O (by difference)	38.3	38.8	36.7	38.1
Ash composition (mg/kg biomass db)				
Ca	19,856	7392	8052	6800
K	2088	2696	5148	2764
Cl	204	102	4893	75
S	518	281	176	177
P	515	307	471	286
Si	13	151	214	186
Al	322	112	74	117
Mg	718	591	1056	646
Na	558	360	792	462
Mn	112	159	96	109
Fe	147	101	122	115
Ti	5	3	2	2
Zn	9	6	7	5
Ba	24	11	36	19
AAEM	23,244	11,050	15,084	10,691
LHV (MJ/kg biomass db)	18.8	19.6	20.0	19.4

bd – below the detection limit of the method, 100 ppm wt.

- Pellets 4 – Eucalyptus wood fines (<1 mm), eucalyptus leaves and eucalyptus branches (<30 mm in diameter).

The biomass feedstocks preparation included chipping and sieving to a particle size below 5 mm, drying at atmospheric conditions to attain a moisture content between 15 and 20 %wt and pelletizing. The pelletization was performed to increase the uniformity of the physical characteristics of the feedstocks and to improve feeding regularity. The pellets were characterized in terms of relevant properties for the thermochemical conversion of biomass (proximate and ultimate analysis, ash composition, and lower heating value), as shown in Table 1.

The surface morphology and surface elemental composition of the biomass ashes were characterized by Scanning Electron Microscopy (SEM, Hitachi SU-70) and Energy Dispersive X-ray Spectroscopy (EDS, Bruker Quantax 400 detector). The chemical composition of the biomass ashes was determined by Induced Coupled Plasma Mass Sector Field Mass Spectrometry (ICP-SFMS) analysis.

2.2. Methodology and operating conditions

The experimental facility used includes a 5 kW_{th} bubbling fluidized bed (BFB) composed of a bottom bed (50 mm inner diameter, 300 mm height) and a freeboard (104 mm inner diameter, 450 mm height). The larger diameter of the freeboard, in comparison to the fluidized bed, allows for a reduction of the gas velocity, thus decreasing the entrainment of particles from the bottom bed. A schematic diagram of the experimental setup is shown in Fig. 1. A more detailed description of the experimental infrastructure is found elsewhere [34,35].

The operating conditions of the experiments performed in this work are shown in Table 2. The ER was maintained between 0.18 and 0.22 and the bed temperature at 800 °C. The bottom bed of the reactor was composed by Al_2O_3 (approximately 3960 kg/m^3 density) with a particle size between 63 and 125 μm; each gasification experiment started with a fresh Al_2O_3 bed. For the fluidization of the bed, 8.6 NL/min of a

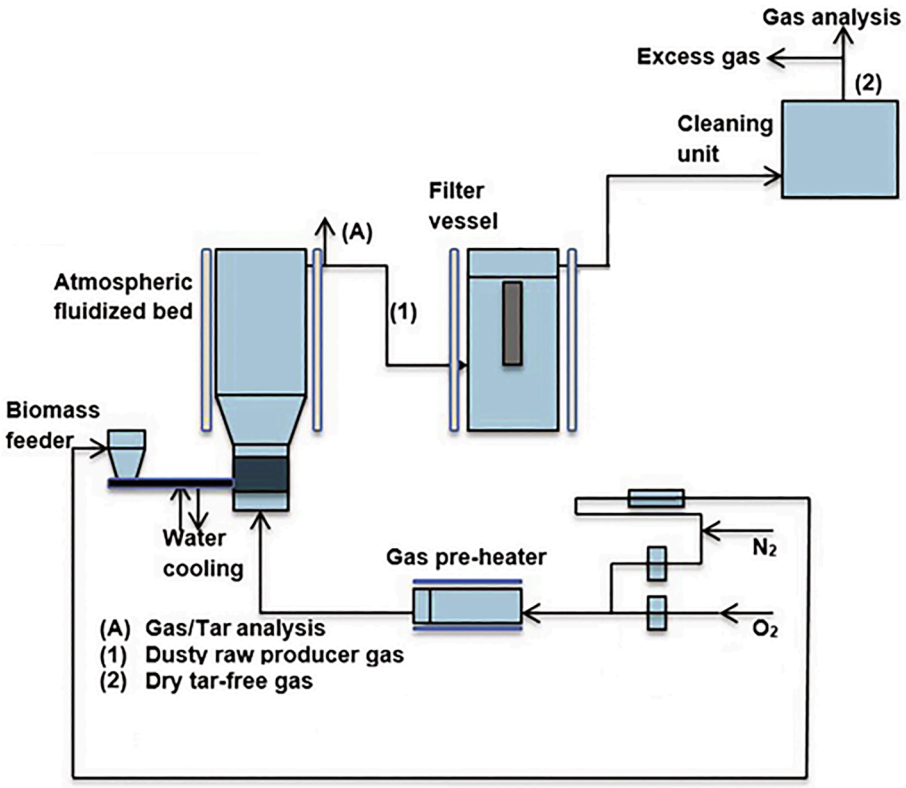

Fig. 1. Schematic view of the experimental infrastructure. Adapted from [34].

Table 2
Operating conditions during the gasification experiments in the BFB reactor.

Experiment reference	Feedstock	Bed material	Gasification agent	Bed temperature [°C]	Biomass feeding rate [g/min]	ER	Tar sampling start** [mins]
LTS	Pellets 1	Al_2O_3	Synthetic mixture O_2/N_2*	800	2.8	0.20	129
	Pellets 2	Al_2O_3	Synthetic mixture O_2/N_2*	800	2.4	0.22	119
ETS	Pellets 3	Al_2O_3	Synthetic mixture O_2/N_2*	800	3.0	0.18	17
	Pellets 4	Al_2O_3	Synthetic mixture O_2/N_2*	800	2.7	0.20	32

*- Synthetic mixture with 5.8 %v O_2 and 94.2 %v N_2.
**- Tar sampling start time after initiating the gasification experiment.

synthetic mixture of O_2 and N_2 (5.8 %v and 94.2 %v, respectively) was used. This synthetic mixture has a significantly lower O_2/N_2 molar ratio (0.06) than atmospheric air (0.27) to promote a higher dilution of the producer gas in N_2 and consequently reduce tar partial pressure and condensation. A flow of 2 NL/min of N_2 was added to the fuel hopper to prevent hot gases from escaping from the reactor through the water-cooled feeding screw, which could cause undesired biomass pyrolysis and consequent clogging and blockage in the feeding system.

The non-condensable gases concentration in the producer gas (after gas drying and cleaning, sampling point 2 in Fig. 1) was determined by a micro gas chromatograph (Thermo Scientific, C2V-200). The tar concentration in the raw producer gas (before gas drying and cleaning, sampling point 1 in Fig. 1) was determined according to the Solid Phase Adsorption (SPA) method [36]. In this regard, a solid phase extraction (SPE) 3 mL tube containing 500 mg of amino radical (NH_2) was coupled with a gastight syringe, which was then used to extract 100 mL gas samples from the exhaust pipe of the reactor in 1-minute procedures. Afterwards, the SPE tube was eluted with tert-butylcyclohexane and dichloromethane to obtain an aromatic fraction, which was then analyzed by GC-FID. In this work, the SPA method was used to determine the concentration of the following tar compounds: benzene, toluene, m/p-xylene, o-xylene, indan, indene, naphthalene, 2-methylnaphthalene, 1-methylnaphthalene, biphenyl, acenaphthylene, acenaphthene, fluorene, phenanthrene, anthracene, fluorantene and pyrene. Depending of various parameters, the relative standard deviation of the method is roughly 10% [37]. More information about the SPA method can be found in [37].

Tar sampling was conducted during two distinct times in each experiment, separated by 45 min. Three tar samples were taken at each time, representing approximately 10 min of operation time. For the experiments, performed with Pellets 1 and Pellets 2 (experiments reference LTS), at least 119 min of gasification were conducted before starting the tar sampling, while for the experiments with Pellets 3 and Pellets 4 (experiments reference ETS), the tar sampling start was performed before 32 min of operation. These operation times were chosen to analyze the effects of char and inorganics accumulation in the reactor bed over time on tar concentration in the raw producer gas.

The gasification process was mainly evaluated based on the combustible gases concentration in the dry and clean producer gas, and consequent lower heating value (LHV), tar concentration in the raw producer gas and three efficiency parameters determined from the experimental data, namely specific dry gas production (Y_{gas}), cold gas efficiency (CGE) and carbon conversion efficiency (CCE). These parameters are typically used in the literature to characterize gasification processes [2,6,38,39].

The LHV of the producer gas was determined based on the concentration of the combustible gases (H_2, CO, CH_4 and C_2H_4) and their respective LHV (at reference conditions, 273 K and 101 kPa) [40]. The efficiency parameters Y_{gas}, CGE and CCE were determined according to the methodology described in [6], through Eqs. (1) to (3):

$$Y_{gas} = \frac{V_G}{m_F} \quad (1)$$

$$CGE[\%] = \frac{V_G \times LHV_G}{m_F \times LHV_F} \times 100 \quad (2)$$

$$CCE[\%] = \frac{V_G \times \frac{P_G}{R \times T_G} \times M_C \times \sum_i \epsilon_{C,i} \times y_i}{m_F \times w_{CF}} \times 100 \quad (3)$$

The reactor bottom bed composition along time during the gasification experiments was estimated by a developed application/approach for a non-stoichiometric thermodynamic equilibrium model, namely NASA Chemical Equilibrium with Applications (https://www.grc.nasa.gov/www/CEAWeb/). The application involved the use of the gasifying agent flow, biomass feeding rate and operation time as model inputs, reflecting an increase with time of the ratio between C, H, N, S, Ca, K, Cl, etc., and the bottom bed material (Al_2O_3). Thus, the approach was implemented considering the molar input (biomass, gasifying agent and fresh reactor bed) and the predicted outputs (most abundant predicted gaseous and solid products). The modelled compounds were assumed to reach equilibrium faster than the tar sampling start time. Quasi equilibrium conditions in the reactor bed were assumed during the tar sampling interval due to the low quantities of ash fed to the reactor along time, in comparison to the bed material. All the reactants were assumed to enter and leave the reactor at process temperature, namely 800 °C. This temperature was assumed as homogenous inside the gasifier. A similar methodology was used by the authors in previous works [41]. Accordingly, the parameters used as input in the model were analogous to the ones attained in the gasification experiments (Table 2), namely:

- Feedstock composition: Pellets 1, 2, 3 and 4 (Table 1)
- Biomass feeding rate: 2.4 to 3.0 g/min
- Gasifying agent flow: 0.5 NL/min O_2 and 8.1 NL/min N_2 (the 2 NL/min N_2 added to the fuel hopper were not considered)
- Bed temperature: 800 °C
- Reactor bed: 350 g Al_2O_3
- Pressure: 1 atm
- Operation time: up to 8 h.

3. Results and discussion

The results presented include information regarding the average concentration of CO_2, CO, CH_4, C_2H_4, H_2 in the dry and clean producer

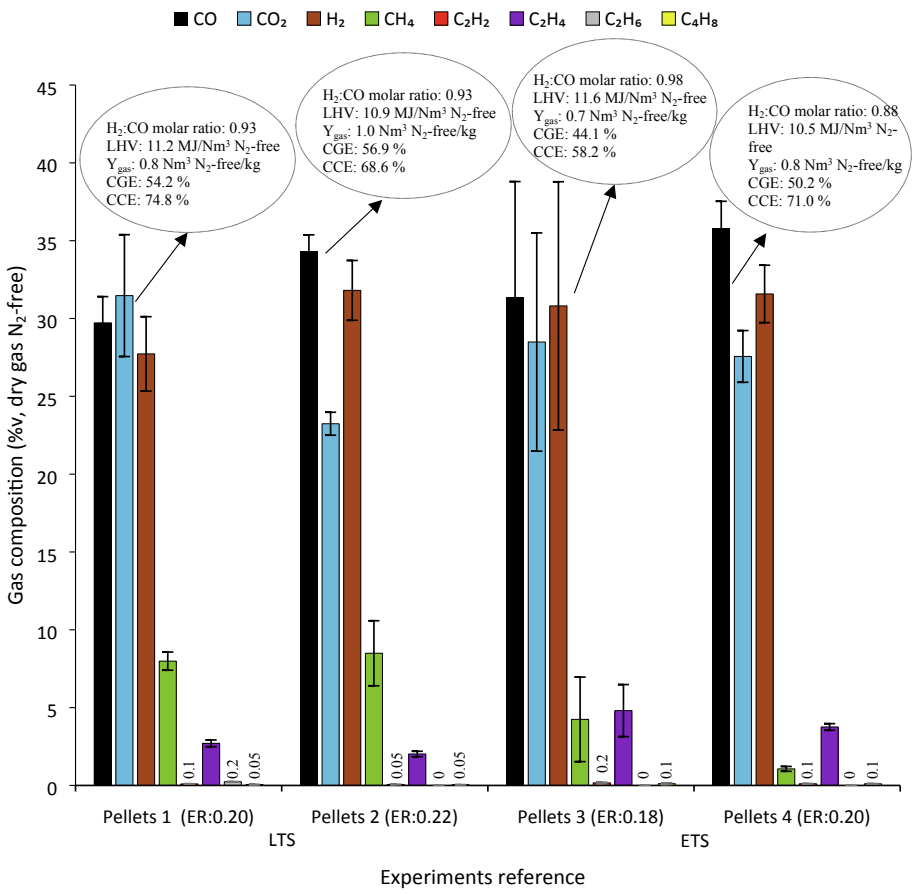

Fig. 2. Average dry gas composition for the gasification experiments performed with different eucalyptus pellets. Legend according to experiments reference in Table 2.

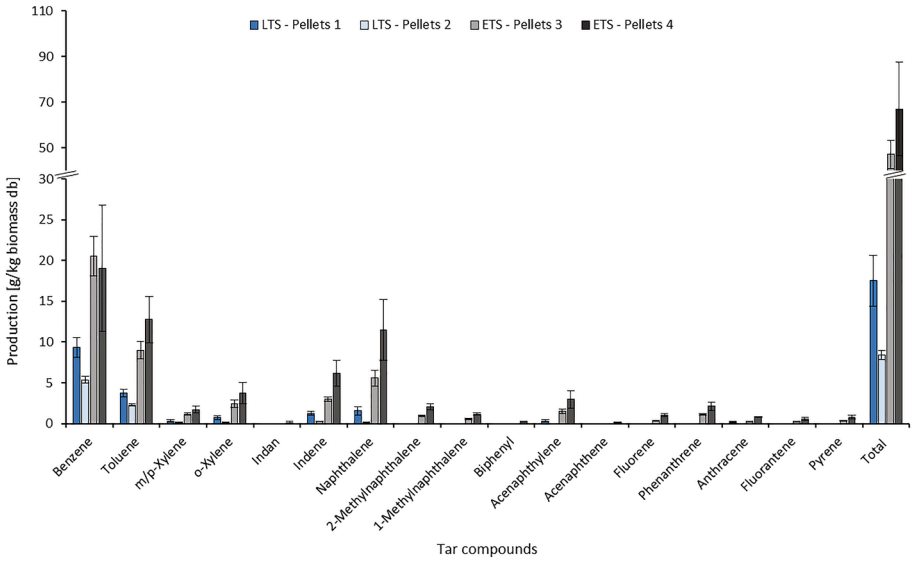

Fig. 3. Tar production values for the different gasification experiments. Legend according to experiments reference in Table 2.

gas and the average tar compounds concentration (e.g., benzene, toluene, xylene, indene, naphthalene) in the raw producer gas, including tar composition profiles over time. The LHV of the dry and clean producer gas and the process efficiency parameters, namely Y_{gas}, CGE and CCE, are also presented and analyzed to characterize the process. The reactor bed composition over time in terms of Al_2O_3, char and inorganic solids, is also estimated from the developed thermodynamic model and correlated to the tar concentration in the producer gas.

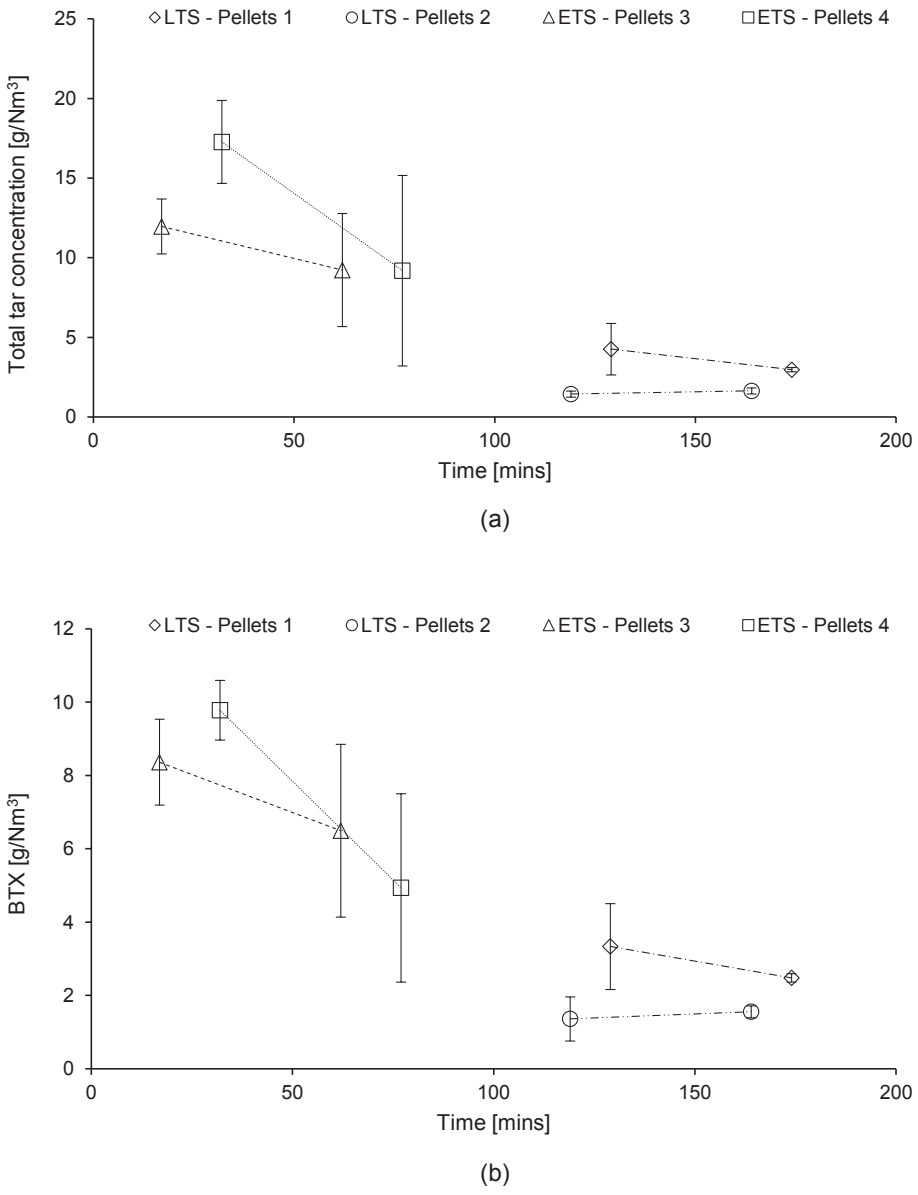

Fig. 4. Decay of the total tar (a), BTX (b), naphthalene (c) and indene (d) concentration in the raw producer gas with operation time. Experiments information in Table 2.

3.1. Gas composition and gasification efficiency parameters

The composition of the dry and clean producer gas (after tar and particles removal) in terms of permanent gases, and the gasification efficiency parameters for the different experiments performed with distinct biomass types, is shown in Fig. 2. In an inert free dry gas basis, the major compounds present in the producer gas are CO, CO_2, H_2, CH_4 and C_2H_4, by decreasing order of abundance. The gasification experiments of distinct eucalyptus pellets with similar operating conditions (temperature around 800 °C and ER between 0.18 and 0.22), showed producer gases with similar permanent gases concentration and analogous efficiency parameters, although some differences were observed regarding the CGE and CCE. This is not surprising because the ER and bed temperature are commonly acknowledged as the main parameters governing the concentration of permanent gases in the producer gas from BFBs biomass gasification processes [6]; as these parameters were maintained almost constant between experiments, no significant differences in the dry and clean producer gas composition were expected.

The LHV (10.5 to 11.2 MJ/Nm^3) and Y_{gas} (0.7 to 1.0 Nm^3 N_2-free dry gas/kg dry biomass) are in accordance with the values typically found in the literature regarding direct biomass gasification in BFBs with similar

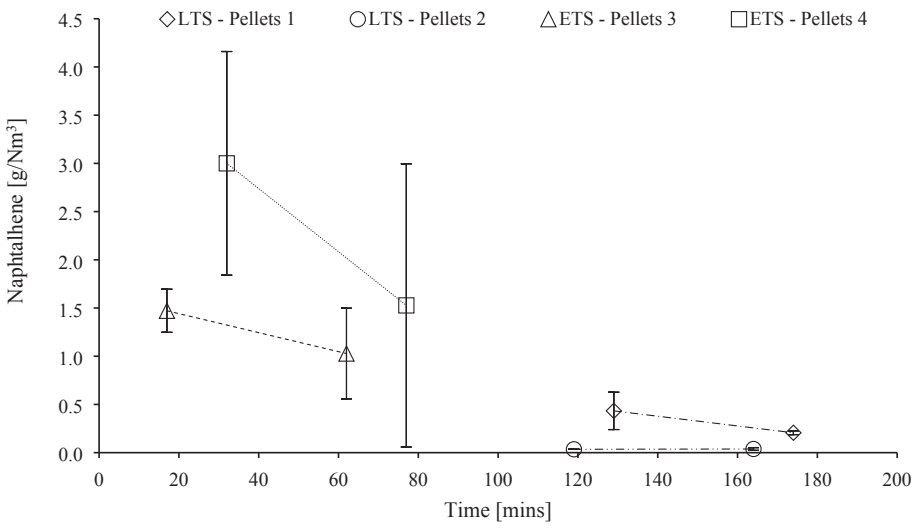

(c)

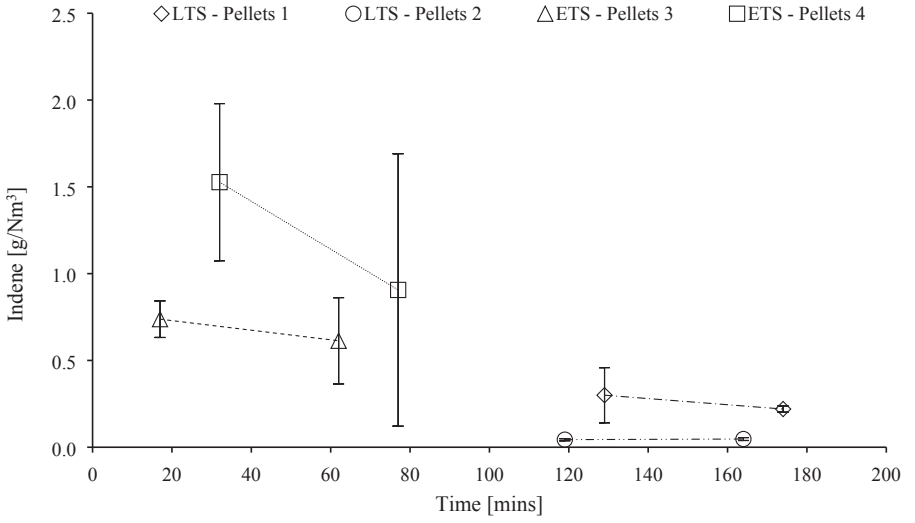

(d)

Fig. 4. (*continued*).

bed temperature and ER [6]. In fact, the LHV is slightly lower and the Y_{gas} slightly higher than commonly reported [6]. Nevertheless, when accounting for N_2 dilution, the LHV of the producer gas is significantly lower (2 to 2.1 MJ/Nm^3 dry gas) and the Y_{gas} significantly higher (4.5 to 5.5 Nm^3 dry gas/kg dry biomass) than the values reported in the literature for direct biomass gasification processes [6]. This is explained by the significantly lower O_2/N_2 ratio (0.06 mol·mol^{-1}) present in the synthetic mixture used as gasifying agent, in comparison with atmospheric air (0.27 mol·mol^{-1}), which causes a higher dilution of the producer gas in N_2.

The CGE (44.1 to 56.9%) and CCE (58.2 to 74.8%) are in the lower to average range of the values typically referred in the literature regarding direct biomass gasification processes in BFBs [6]. The lower values may also be justified by the synthetic mixture of O_2 and N_2 used as gasification agent, and respective low O_2/N_2 ratio (0.06 mol·mol^{-1}). It is argued that the rate of gas char reactions lowers as the O_2/N_2 ratio decreases in the gasifying agent, which can be related to a higher convective cooling effect of the gas phase over the solid phase, instigated by the higher N_2 content and consequent higher gas flow [42,43]. This contributes to lower radiation penetration and lower kinetic rates [43], thus causing lower char reactivity and conversion. In fact, Ismail et al., [44] suggested 0.67 mol·mol^{-1} as the optimal O_2/N_2 ratio for direct biomass gasification processes, which is 10 times higher than the ratio present in the synthetic mixture used in the present work (0.06 mol·mol^{-1}).

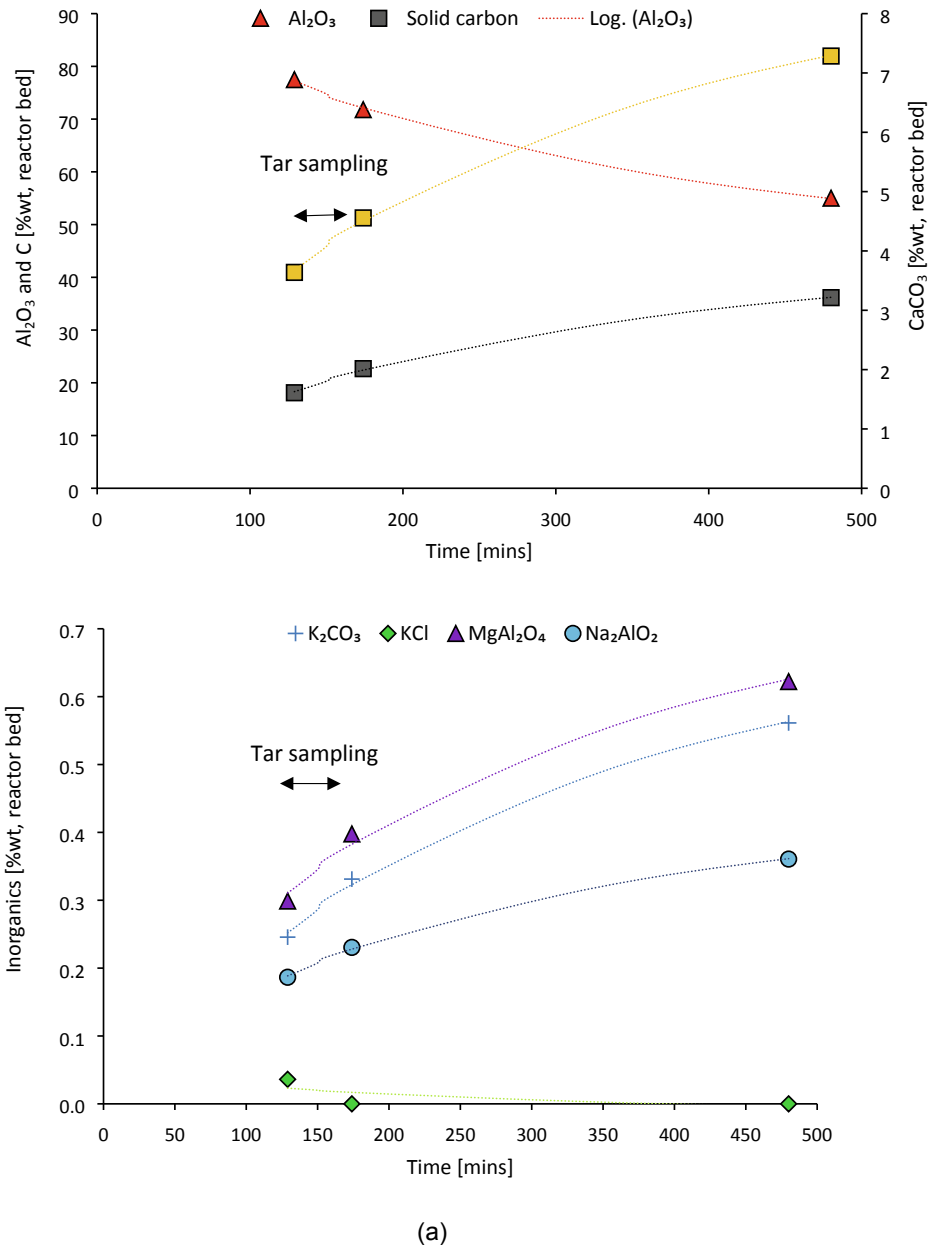

Fig. 5. Equilibrium thermodynamic prediction of the reactor bed composition along time for the experiments LTS – Pellets 1 (a), LTS – Pellets 2 (b), ETS – Pellets 3 (c) and ETS – Pellets 4 (d). Experiments information in Table 2.

3.2. Tar composition and concentration

In Fig. 3, it is shown the tar production per unit of biomass (g tar/kg biomass db) for the distinct gasification experiments performed with different eucalyptus RFB pellets and similar operating parameters (e.g., bed temperature, ER, fluidization velocity). In average, the highest relative abundant compounds are benzene (47.1 %wt), toluene (21.6 %wt), naphthalene (10.0 %wt) and indene (6.4 %wt). Other compounds found include acenaphthylene, xylene, phenanthrene, pyrene, indane, among others. Similar tar composition during other biomass gasification processes has also been shown in the literature [45,46]. However, depending on the operating conditions (e.g., bed temperature), some authors also refer phenol, xylene or naphthalene as the main tar compounds found in the raw producer gas [5,47–49].

Significant distinct total tar production values, namely between 8.4 and 67.0 g tar/kg biomass db, which represent 1.5 and 13.3 g/Nm^3 concentration in the producer gas, are observed in this work; the gasification of Pellets 2 and 4 display the lowest and highest tar production, respectively. Considering that similar operating parameters (e.g., bed temperature, ER, fluidization velocity) were maintained between gasification experiments, these results suggest that the tar production, and consequent concentration in the producer gas, is highly dependent on

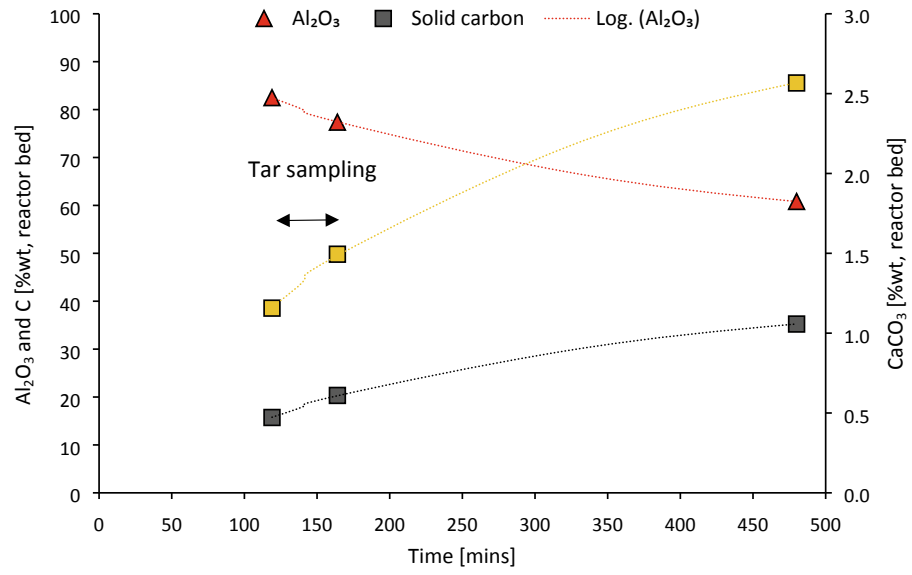

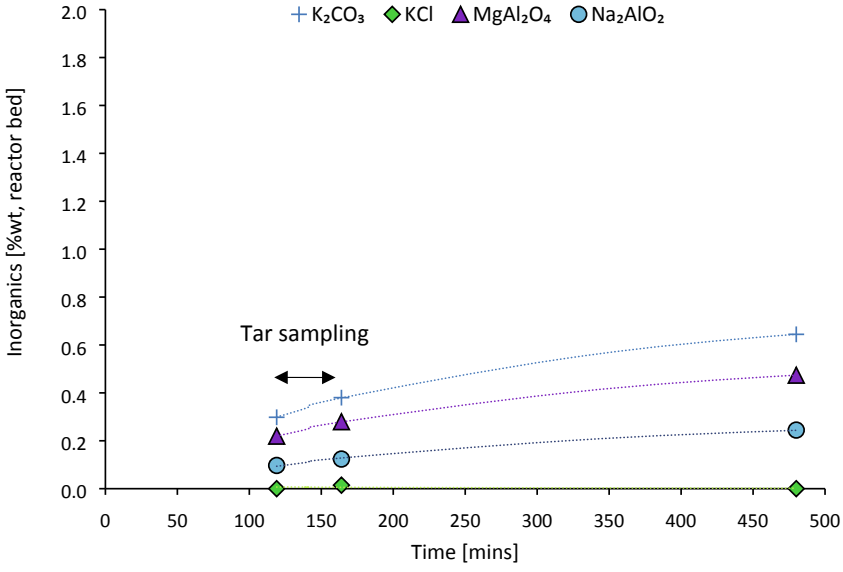

(b)

Fig. 5. (*continued*).

the feedstock characteristics and gasification operation time. In fact, for experiments with an early tar sampling start (17 to 32 min after starting the gasification experiments, reference ETS in Table 2), the tar production is significantly higher than in the experiments with a late tar sampling start (119 to 129 min after starting the gasification experiments, reference LTS in Table 2), namely 47.2 to 67.0 g tar/kg biomass db and 8.4 to 17.5 g tar/kg biomass db, respectively. This is further discussed in Section 3.2.1.

The tar concentration values obtained are in agreement with the literature for biomass direct gasification in fluidized beds (1 to 30 g/Nm^3) [5,10], and are significantly higher than the acceptable tar concentration limits for using the producer gas in fuel cells (1 mg/Nm^3), compressors (50 to 500 mg/Nm^3), internal combustion engines (50 mg/Nm^3) and gas turbines (5 mg/Nm^3) [4,9,50–53]. Even if benzene is excluded from the critical tar components, as suggested in the definition proposed by the International Energy Agency [9,54], the tar concentration of the remaining compounds is still higher (0.6 to 9.5 g/Nm^3) than the suggested tar concentration limits referred for the distinct potential applications for the producer gas. It is important to note that a higher nitrogen content was used in the synthetic gasifying agent, in comparison with air, and, consequently, this tar concentration is diluted in nitrogen, indicating that tar concentration in the raw producer gas most likely would be higher if air was used as gasifying agent. Thus, it is essential to remove the major quantity of tar from the producer gas from

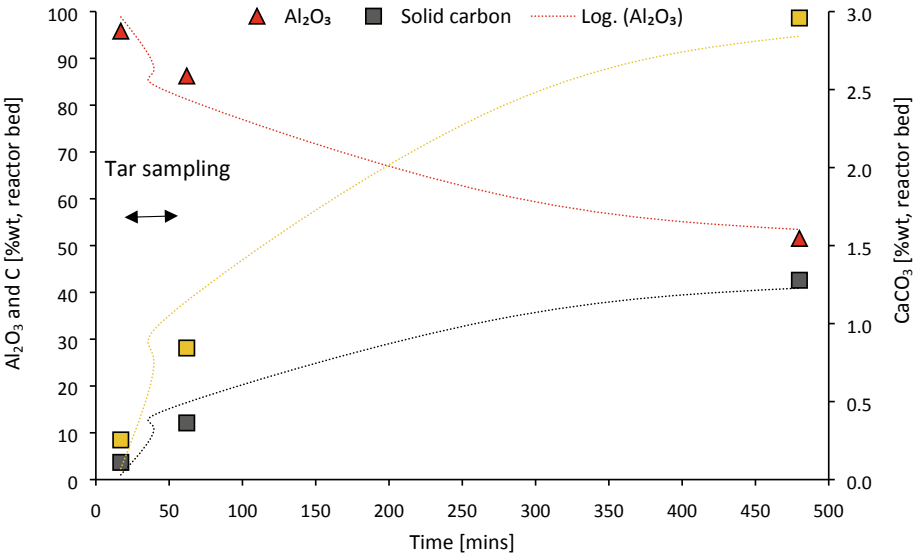

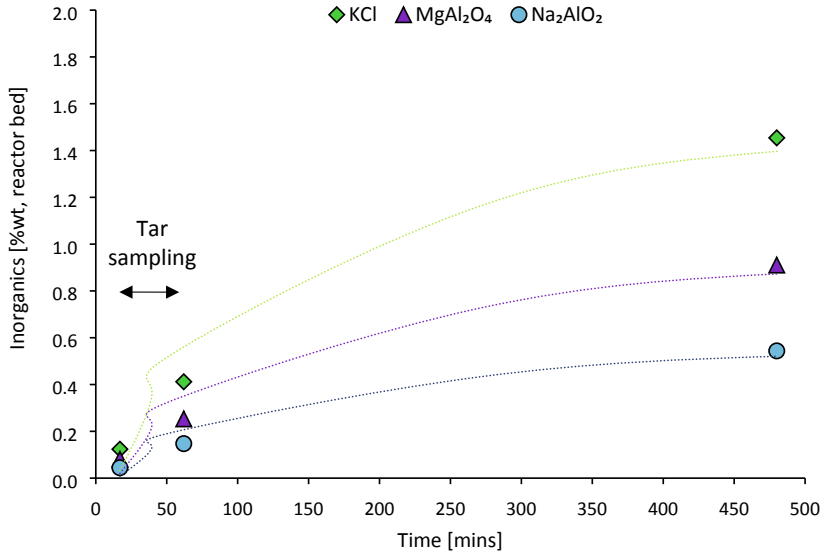

(c)

Fig. 5. (*continued*).

eucalyptus direct gasification to attain a gas quality, according to technical specifications, applicable to combustion engines, gas turbines or fuel cells.

3.2.1. *Influence of gasification operation time*

Fig. 4 shows the decay of the total tar, BTX (benzene, toluene and xylene), naphthalene and indene concentration values with operation time for each gasification experiment. These tar compounds follow a similar behavior, i.e., a decay of concentration with time, which is especially relevant for experiments with a tar sampling start between 17 and 32 min (ETS, Table 2). For these experiments, an average decrease of up to 50% in tar concentration can be observed within 45 min of operation. Note that the BTX concentration remains higher than the concentration of the original fractions of polyaromatic tars (indene and naphthalene), even after long operation times, which can be associated to the cracking of larger tar molecules to BTX compounds. For experiments with a tar sampling start between 119 and 129 min (LTS, Table 2), the decay of tar concentration with time was significantly smaller or

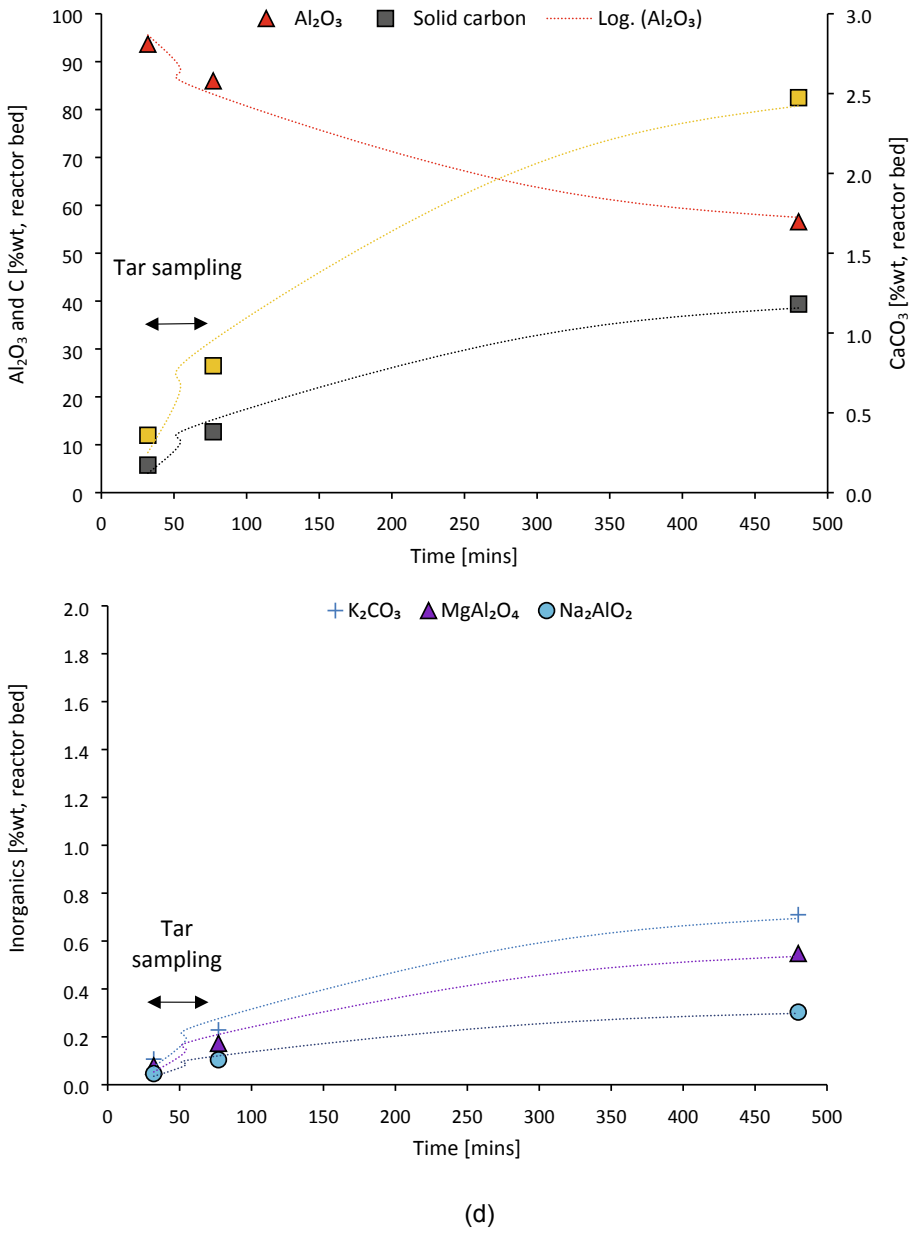

(d)

Fig. 5. (*continued*).

inexistent. Furthermore, the variability of tar concentration values for three successive samplings is significantly lower for experiments LTS, as exemplified by the error bars in Fig. 4. This indicates that the gasification process attained steady-state conditions in terms of tar concentration in the producer gas.

Considering all the gasification experiments made, a decrease of the total tar concentration of up to 5 times is observed with increasing operation time (Fig. 4, (a)). In fact, for experiments LTS, the average total tar concentration was found between 1.5 and 3.6 g/Nm^3 (8.4 and 17.5 g tar/kg biomass db), which are lower values than commonly referred for fluidized beds [5]. Even when discounting the dilution caused by the low O_2/N_2 ratio present in the synthetic mixture used as gasifying agent (by mathematically removing the N_2 volumetric concentration present in the producer gas), the lowest average total tar concentration for experiments LTS was 8.8 g/Nm^3 N_2-free, which is still a lower value than commonly reported for direct (air) biomass gasification in atmospheric fluidized beds at 0.20 ER and 800 °C [55].

This decay of tar concentration in the raw producer gas along time indicates a dependency of tar formation on the accumulation of char and ash in the reactor bottom bed. It is important to note that each experiment started with a fresh Al_2O_3 bed, and then there was an increase of inorganics and char concentration in the reactor bottom bed as the gasification process progressed, as shown by the results from the developed equilibrium thermodynamic model (Fig. 5). In fact, the equilibrium thermodynamic predictions indicate that these compounds concentration increased with time during all gasification experiments performed, and that equilibrium in terms of bed composition was still far from being attained, suggesting that long times of operation can be beneficial to reduce tar concentration in the producer gas. Accordingly, the reactor bed showed higher contents of char and inorganics (e.g., $CaCO_3$, K_2CO_3, KCl, $Mg_2Al_2O_4$, Na_2AlO_2) in experiments LTS than in experiments ETS (Fig. 5). However, some exceptions can also be observed, such as the higher content of KCl predicted for experiment ETS – Pellets 3, which can be justified by the high content of K and Cl present

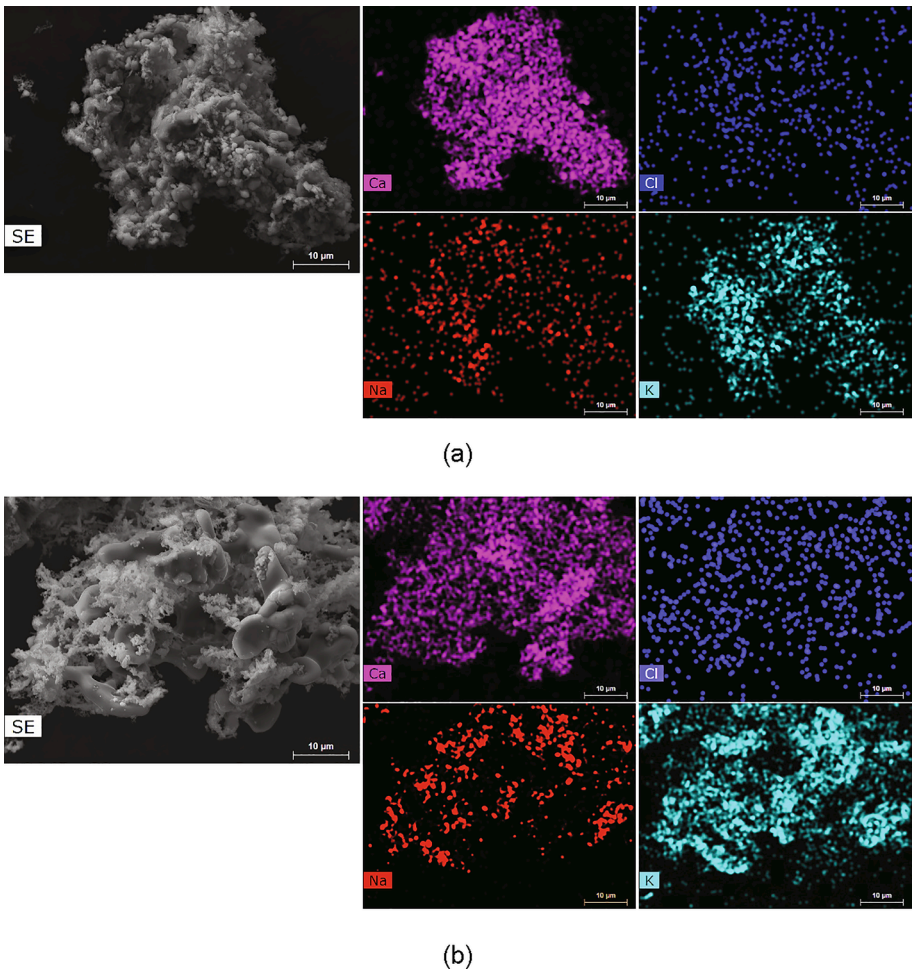

Fig. 6. SEM micrographs of a representative ash particle from Pellets 1 (a) and Pellets 3 (b), and respective Ca, Cl, Na and K elemental intensity maps.

in these pellets (Table 1, Fig. 6), implying that these elements may be associated in the original biomass; this may also be important regarding deposit formation and corrosion issues in heat exchangers, due to the formation of low meting point eutectic layers from emitted KCl [56,57].

Thus, an evident trend between tar concentration decrease in the producer gas and the increase of char and inorganics concentration in the reactor bottom bed (predicted by the equilibrium thermodynamic calculations) can be observed (Fig. 7). This observed effect could be explained by the catalytic activity promoted by the chars and inorganics present in the reactor bed, which are recognized promoters of tar cracking and corresponding conversion to lighter gaseous species during gasification processes [39,58–61]. In this respect, $CaCO_3$ was predicted to be the most abundant inorganic solid present in the reactor bed (0.4 and 4.6 %wt), which can be formed through the capture of CO_2 by CaO via a carbonation reaction [62]. CaO is a recognized catalyst for gasification processes [62–66], acknowledged to be able to catalytically reform tar compounds from higher ring species into polycyclic aromatic hydrocarbons with fewer ring species [62]. Accordingly, $CaCO_3$/CaO undoubtedly had a significant effect on tar reduction in the producer gas by promoting tar reforming/cracking reactions into gaseous products.

The results also show that at operation times longer than 2 to 3 h, the tar concentration decay stops (Fig. 4); this indicates that a limit for the catalytic effect promoted by the inorganics and char on the tar cracking was attained. Therefore, it can be inferred that further operation time and consequent additional ash and char accumulation in the bottom bed would not lead to lower tar concentration in the producer gas.

Fig. 8 shows the dependence of the LHV of the dry and clean producer gas with operation time and tar concentration in the raw producer gas, revealing a trend for the increase of LHV with operation time increase and tar concentration decrease. This can be related to the occurrence of tar cracking, and respective conversion to lighter combustible gases (e.g., H_2 and CO), and to an increase in carbon conversion. Based on the information obtained in this work, it is not possible to effectively quantify the contribution of each phenomenon to the producer gas LHV increase; it is suggested that this is performed in future studies. Nevertheless, this corroborates the previously discussed occurrence of the accumulation of inorganics with time in the reactor bottom bed, and consequent catalytic activity, resulting in tar concentration reduction in the producer gas. This may be relevant for the conceptualization of prediction models to support large-scale biomass gasification facilities that lack capacity to properly monitor tar concentration in the producer gas, as previously seen in other works [2]. In

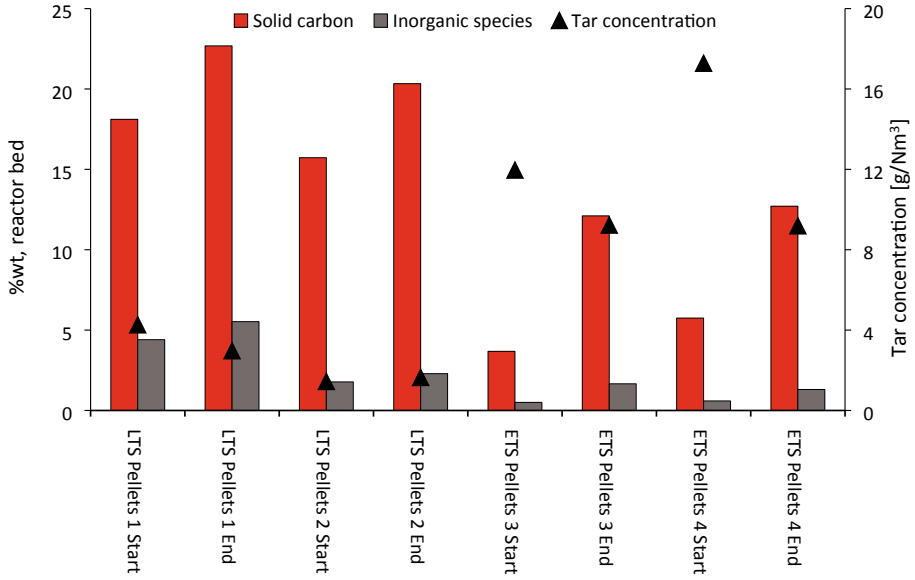

Fig. 7. Relation between the solid carbon and inorganic species content in the reactor bed (predicted by thermodynamic equilibrium) and the tar concentration in the producer gas for the different gasification experiments performed. Experiments information in Table 2.

those cases, by developing a suitable prediction model, it may be possible to associate light combustible gases with tar compounds.

3.2.2. *Influence of feedstock chemical composition*

Despite the above discussed effect of operation time, and consequent char and ash accumulation in the reactor bed, on tar concentration in the raw producer gas, some differences for experiments with similar operation time and analogous operating parameters (e.g., bed temperature, ER, fluidization velocity) can also be observed. This suggests an influence of the characteristics of the distinct eucalyptus RFB feedstocks on tar formation mechanisms.

Fig. 9 shows the variation of BTX, naphthalene and total tar concentration values in relation to several chemical properties of the eucalyptus RFB pellets, namely ash, volatile matter, fixed carbon and oxygen and carbon content. In experiments ETS, a significant decrease of total tar concentration with the increase of ash content in the biomass was observed, which can be explained by a faster ash inventory increase in the bottom bed reactor as the gasification progresses, with consequent catalytic effects promoted by the inorganics [39], as previously discussed. It is important to note that the higher ash content present in Pellets 3 also has a significantly higher content of K and Cl (Table 1) than the ash present in Pellets 4, consequently causing the accumulation of KCl in the reactor bottom bed (Fig. 5 (c)). This indicates that the ash present in Pellets 3 has a higher catalytic activity for tar cracking and reforming than the ash present in Pellets 4, due to its high content of K, which is a recognized catalyst in gasification processes [67–69], and that this may be relevant in terms of tar production.

In experiments LTS, the increase of ash content did not lead to a lower tar concentration, suggesting that the reactive system converged to a nearly steady state regime in terms of potential ash catalytic effects, meaning that further ash accumulation in the bed would not result in a higher tar cracking and consequent lower concentration in the producer gas, as previously inferred in Section 3.2.1.

Conclusively, these results indicate that the ash content and ash composition were the feedstock characteristics with highest influence on tar production. However, as the gasification process progresses, and the reactor bed gets richer in inorganic and char solids, these parameters influence on tar formation appear to decrease. Regarding other analyzed parameters (e.g., volatile matter, carbon and oxygen content), no obvious trends were observed, which may be explained by the similar composition of the eucalyptus RFB pellets (Table 1) and the operation time exerting a prevailing effect, as previously discussed. Important to note that the physical characteristics of the eucalyptus feedstocks were not evaluated in the present work. In fact, the distinct parts of the eucalyptus (e.g., branches, leaves) were processed to pellets to increase the uniformity of the physical characteristics of the feedstocks.

4. Conclusions

This work characterizes and evaluates the gasification of distinct types of RFB derived from eucalyptus with a synthetic mixture of O_2/N_2 (0.06 mol·mol^{-1}) in a 5 kW_{th} bench-scale BFB, focusing on tar composition and concentration in the producer gas.

The major components found in the clean and dry producer gas were CO, CO_2, H_2, CH_4 and C_2H_4 by decreasing order of abundance. The LHV of the clean and dry producer gas (2.0 to 2.1 MJ/Nm^3) was significantly lower than commonly reported in the literature for direct gasification processes, however, the Y_{gas} (4.5 to 5.5 Nm^3 dry gas/kg dry biomass) was significantly higher; the CGE (44.1 to 56.8%) and CCE (58.2 to 74.8%) were in the lower to average range. This is related to the synthetic mixture used as gasifying agent, which has a significantly lower O_2/N_2 ratio (0.06 mol·mol^{-1}) compared to atmospheric air (0.27 mol·mol^{-1}), and therefore promotes lower char conversion rates and causes a higher dilution of the producer gas in N_2.

The average tar concentration values in the raw producer gas were between 1.5 and 13.3 g/Nm^3, representing a tar production between 8.4

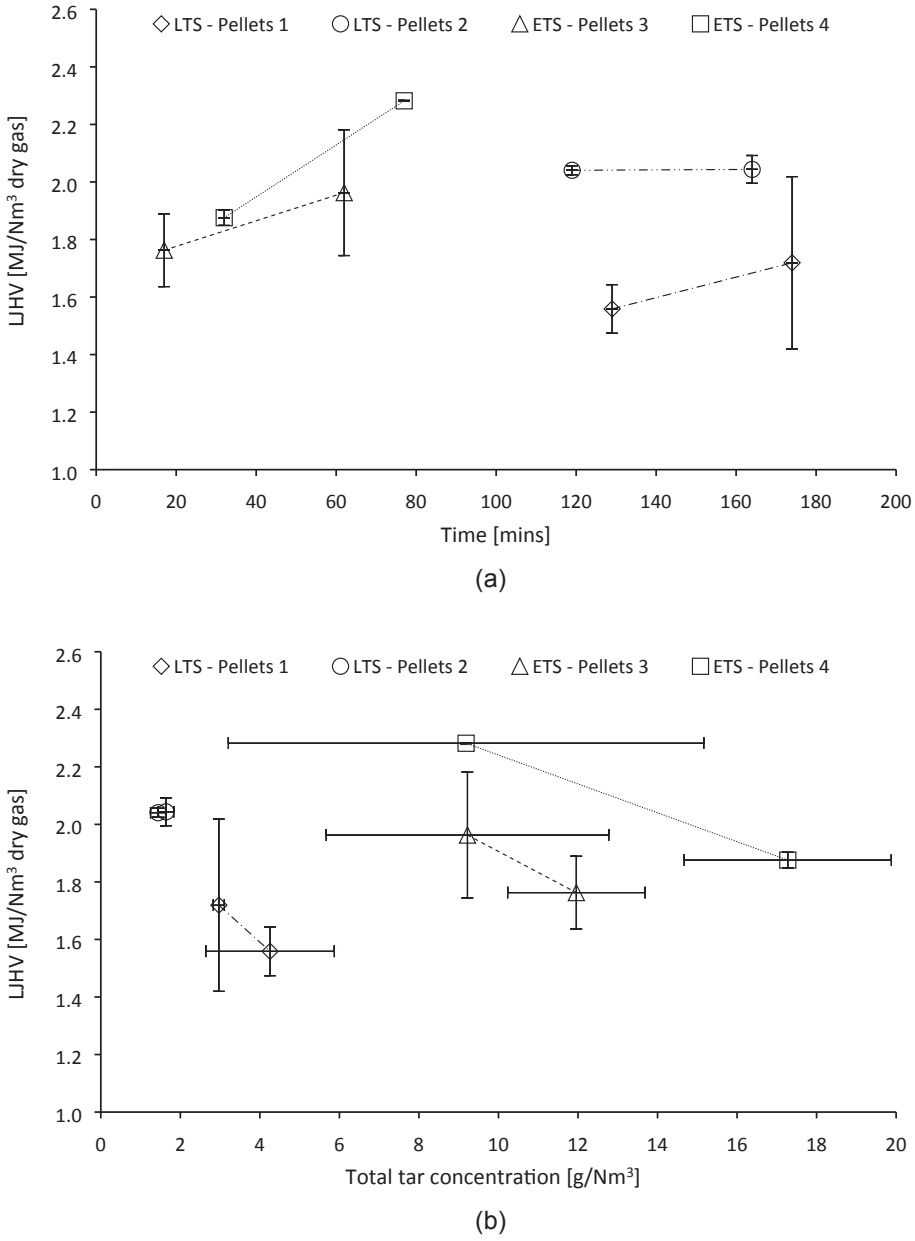

Fig. 8. Variation of the LHV of the dry and clean producer gas with (a) operation time and (b) total tar concentration in the raw producer gas. Experiments information in Table 2.

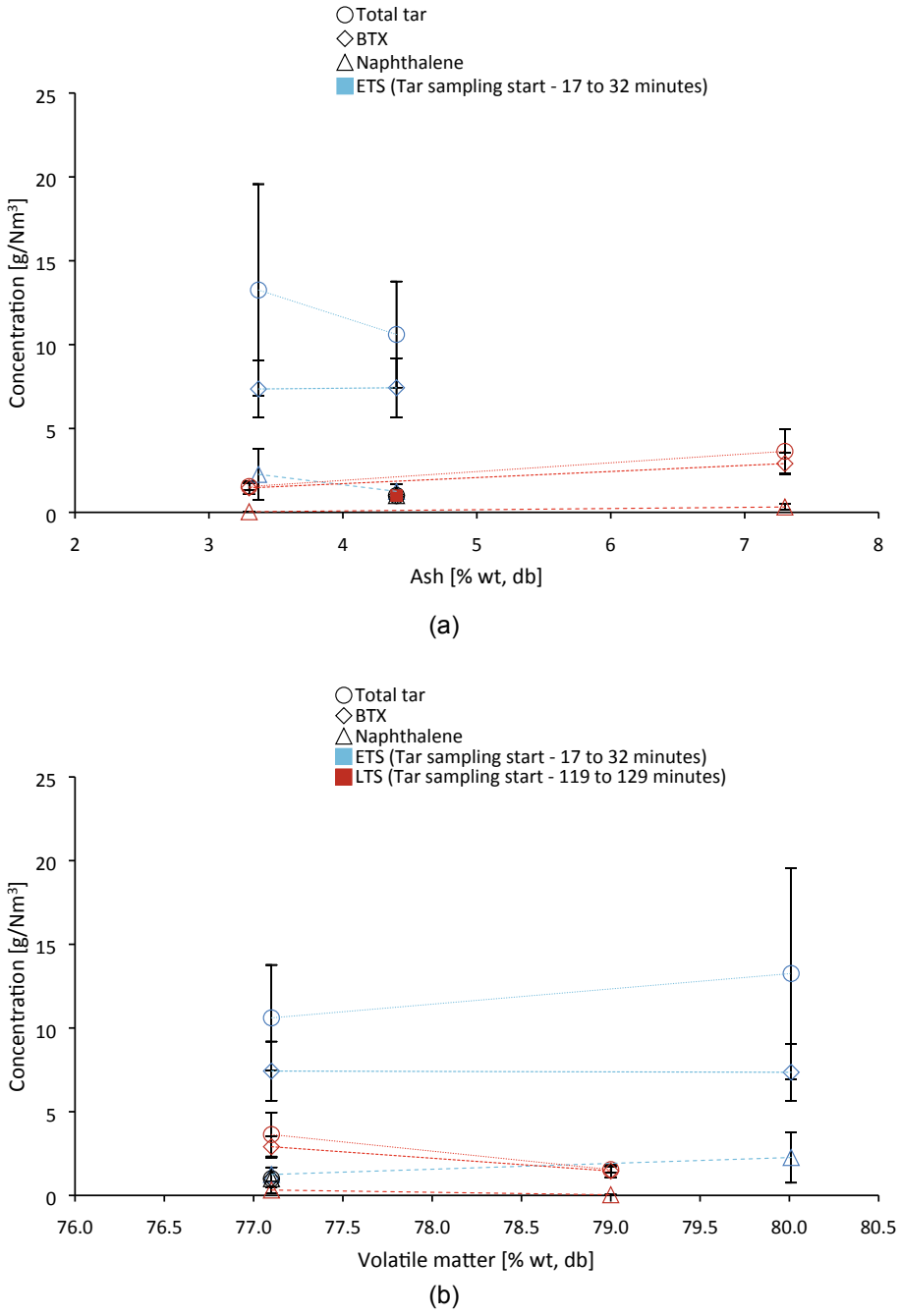

Fig. 9. Variation of total tar, BTX and naphthalene concentration in the raw producer gas with the chemical properties of the eucalyptus RFB pellets used in the gasification experiments: ash (a), volatile matter (b), fixed carbon (c), carbon concentration (d) and oxygen concentration (e). Feedstock characteristics in Table 1 and experiments reference in Table 2.

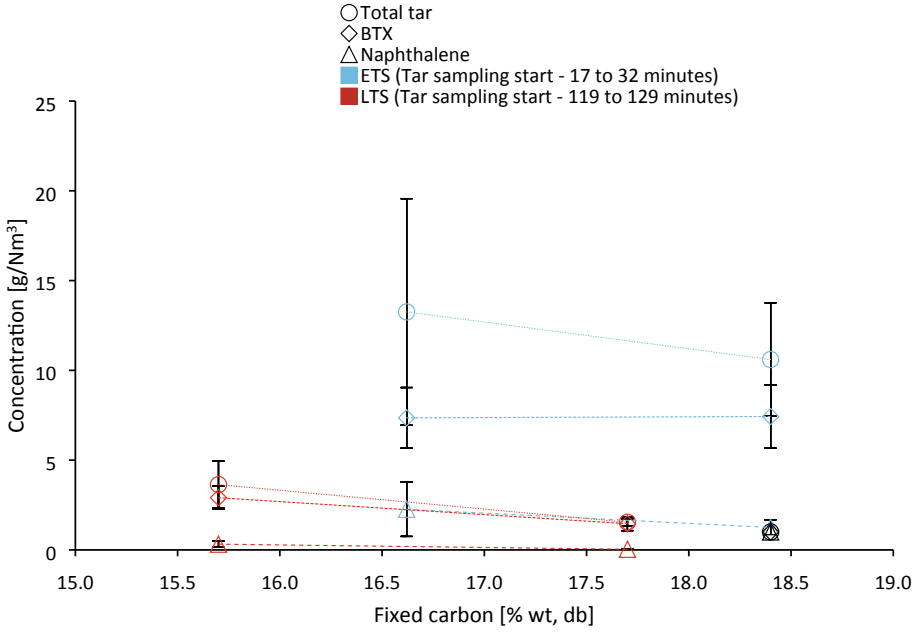

(c)

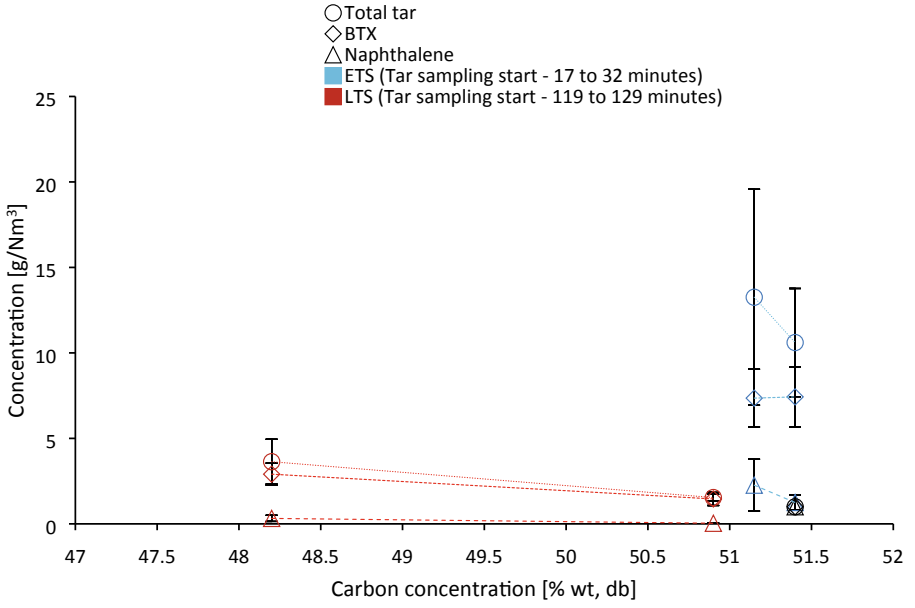

(d)

Fig. 9. (*continued*).

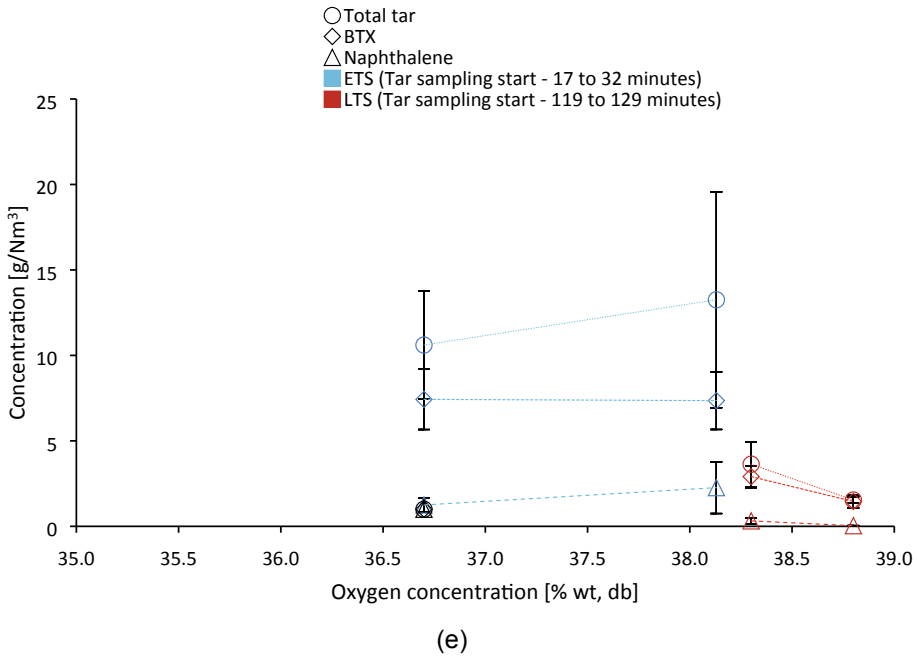

Fig. 9. (*continued*).

and 67.0 g tar/kg biomass db, which are significantly higher values than the tar concentration limits for various potential applications of the producer gas (can fall between 0.1 and 500 mg/Nm^3). The major tar compounds detected in the tar samples from the raw producer gas were benzene (47.1 %wt), toluene (21.6 %wt), naphthalene (10 %wt) and indene (6.4 %wt).

The tar concentration in the raw producer gas decayed significantly with the operation time of the gasification experiments. For experiments with a tar sampling start between 17 and 32 min after initiating the gasification process (with a fresh Al_2O_3 bed), a tar concentration approximately 5 times higher, compared to experiments with tar sampling start between 119 and 129 min, was observed. For the prior case, the tar concentration decreased up to 50% within 45 min of operation. For the latter case, the average total tar concentration was between 1.5 and 3.6 g/Nm^3 (8.4 to 17.5 g tar/kg biomass db), which are lower values than commonly reported for fluidized beds. These results indicate the influence of ash and char accumulation in the bed and the catalytic activity of these gasification byproducts for tar reforming/cracking.

The tar concentration showed a negative correlation with solid carbon and inorganics concentration in the reactor bed. It can be estimated that solid carbon (char) and $CaCO_3$/CaO had a significant effect on tar reduction by promoting tar reforming/cracking reactions into non-condensable gaseous products, due to their proven catalytic effect and predicted high accumulation and concentration in the reactor bed. However, 2 to 3 h after the start of the gasification process, the tar concentration decay stopped, indicating a limit for the catalytic effect of ash and char on tar destruction.

The obtained results show the relevance of ash chemistry and ash/char bottom bed inventory during gasification processes in BFB reactors, and give a relevant contribution to support future works seeking tar reduction in the raw producer gas from biomass gasification.

CRediT authorship contribution statement

D.T. Pio: Conceptualization, Methodology, Investigation, Formal analysis, Visualization, Validation, Writing - original draft, Writing - Review & Editing. **L.C.M. Ruivo:** Conceptualization, Investigation, Validation. **L.A.C. Tarelho:** Conceptualization, Formal analysis, Writing - Review & Editing, Supervision, Project administration. **J.R. Frade:** Supervision, Project administration. **E. Kantarelis:** Conceptualization, Formal analysis, Writing - Review & Editing, Supervision, Project administration. **K. Engvall:** Conceptualization, Formal analysis, Writing - Review & Editing, Supervision, Project administration.

Declaration of Competing Interest

The authors declare that they have no known competing financial interests or personal relationships that could have appeared to influence the work reported in this paper.

Acknowledgements

The authors acknowledge the financial support provided through the project NOTARGAS - Novel catalyst concepts for tar-free oxy-steam gasification of biomass (ref. POCI-01-0145-FEDER-030661) and project SusPhotoSolutions - Soluções Fotovoltaicas Sustentáveis, PO Centro 2020 (ref. CENTRO-01-0145-FEDER-000005). Thanks are due to Portuguese Foundation for Science and Technology (FCT)/Ministry of Science, Technology and Higher Education (MCTES) for the financial support to CESAM (UIDP/50017/2020 + UIDB/50017/2020) and CICECO (UIDB/50011/2020 & UIDP/50011/2020), through national funds and Compete 2020, and to BRISK 2 funded by EU Horizon 2020. The authors also acknowledge the FCT and The Navigator Company for providing financial support to the PhD scholarship granted to Daniel Pio (ref. PD/BDE/128620/2017). Thanks are extended to FCT for providing the financial support to the PhD scholarship granted to Luís Ruivo (ref. SFRH/BD/129901/2017). Part of this work was carried out within the Swedish Gasification Centre (SFC) consortium. Funding from the Swedish Energy Agency (34721-2), academic and industrial partners is gratefully acknowledged.

References

[1] Asadullah M. Barriers of commercial power generation using biomass gasification gas: a review. Renew Sustain Energy Rev 2014;29:201–15. https://doi.org/10.1016/j.rser.2013.08.074.

[2] Pio DT, Tarelho LAC, Pinto RG, Matos MAA, Frade JR, Yaremchenko A, Mishra GS, Pinto PCR. Low-cost catalysts for in-situ improvement of producer gas quality during direct gasification of biomass. Energy 2018;165:442–54. https://doi.org/10.1016/j.energy.2018.09.119.

[3] Ren J, Liu Y-L, Zhao X-Y, Cao J-P. Biomass thermochemical conversion: a review on tar elimination from biomass catalytic gasification. J Energy Inst 2020;93(3):1083–98. https://doi.org/10.1016/j.joei.2019.10.003.

[4] Sikarwar VS, Zhao M, Fennell PS, Shah N, Anthony EJ. Progress in biofuel production from gasification. Prog Energy Combust Sci 2017;61:189–248. https://doi.org/10.1016/j.pecs.2017.04.001.

[5] Milne TA, Evans RJ, Abatzoglou N. In: Biomass Gasifier "Tars": Their Nature Formation, and Conversion; 1998. https://doi.org/10.2172/3726.

[6] Pio DT, Tarelho LAC, Matos MAA. Characteristics of the gas produced during biomass direct gasification in an autothermal pilot-scale bubbling fluidized bed reactor. Energy 2017;120:915–28. https://doi.org/10.1016/j.energy.2016.11.145.

[7] De Caprariis B, Bassano C, Deiana P, Palma V, Petrullo A, Scarsella M, et al. Carbon dioxide reforming of tar during biomass gasification. Chem Eng Trans 2014;37:97–102. https://doi.org/10.3303/CET1437017.

[8] Sikarwar Vineet Singh, Zhao Ming, Clough Peter, Yao Joseph, Zhong Xia, Memon Mohammad Zaki, Shah Nilay, Anthony Edward J, Fennell Paul S. An overview of advances in biomass gasification. Energy Environ. Sci. 2016;9(10):2939–77. https://doi.org/10.1039/C6EE00935B.

[9] Valderrama Rios Martha Lucia, González Aldemar Martínez, Lora Electo Eduardo Silva, Almazán del Olmo Oscar Agustin. Reduction of tar generated during biomass gasification: a review. Biomass Bioenergy 2018;108:345–70. https://doi.org/10.1016/j.biombioe.2017.12.002.

[10] Heidenreich S, Müller M, Foscolo PU. Advanced Biomass Gasification. Elsevier 2016. https://doi.org/10.1016/C2015-0-01777-4.

[11] Ponzio Anna, Kalisz Sylwester, Blasiak Wlodzimierz. Effect of operating conditions on tar and gas composition in high temperature air/steam gasification (HTAG) of plastic containing waste. Fuel Process Technol 2006;87(3):223–33. https://doi.org/10.1016/j.fuproc.2005.08.002.

[12] Fagbemi L, Khezami L, Capart R. Pyrolysis products from different biomasses. Appl Energy 2001;69(4):293–306. https://doi.org/10.1016/S0306-2619(01)00013-7.

[13] Morf Philipp, Hasler Philipp, Nussbaumer Thomas. Mechanisms and kinetics of homogeneous secondary reactions of tar from continuous pyrolysis of wood chips. Fuel 2002;81(7):843–53. https://doi.org/10.1016/S0016-2361(01)00216-2.

[14] Brage Claes, Yu Qizhuang, Sjöström Krister. Characteristics of evolution of tar from wood pyrolysis in a fixed-bed reactor. Fuel 1996;75(2):213–9. https://doi.org/10.1016/0016-2361(95)00260-X.

[15] Berrueco C, Montané D, Matas Güell B, del Alamo G. Effect of temperature and dolomite on tar formation during gasification of torrefied biomass in a pressurized fluidized bed. Energy 2014;66:849–59. https://doi.org/10.1016/j.energy.2013.12.035.

[16] Gil Javier, Corella José, Aznar María P, Caballero Miguel A. Biomass gasification in atmospheric and bubbling fluidized bed: Effect of the type of gasifying agent on the product distribution. Biomass Bioenergy 1999;17(5):389–403. https://doi.org/10.1016/S0961-9534(99)00055-0.

[17] Knight Richard A. Experience with raw gas analysis from pressurized gasification of biomass. Biomass Bioenergy 2000;18(1):67–77. https://doi.org/10.1016/S0961-9534(99)00070-7.

[18] Kinoshita CM, Wang Y, Zhou J. Tar formation under different biomass gasification conditions. J Anal Appl Pyrol 1994;29(2):169–81. https://doi.org/10.1016/0165-2370(94)00796-9.

[19] Pfeifer Christoph, Koppatz Stefan, Hofbauer Hermann. Steam gasification of various feedstocks at a dual fluidised bed gasifier: impacts of operation conditions and bed materials. Biomass Conv. Bioref. 2011;1(1):39–53. https://doi.org/10.1007/s13399-011-0007-1.

[20] Devi Lopamudra, Ptasinski Krzysztof J, Janssen Frans JJG. A review of the primary measures for tar elimination in biomass gasification processes. Biomass Bioenergy 2003;24(2):125–40. https://doi.org/10.1016/S0961-9534(02)00102-2.

[21] Wang Shurong, Ru Bin, Dai Gongxin, Shi Zhangjie, Zhou Jinsong, Luo Zhongyang, Ni Mingjiang, Cen Kefa. Mechanism study on the pyrolysis of a synthetic β-O-4 dimer as lignin model compound. Proc Combust Inst 2017;36(2):2225–33. https://doi.org/10.1016/j.proci.2016.07.129.

[22] Qin YuHong, Campen Adam, Wiltowski Tomasz, Feng Jie, Li Wenying. The influence of different chemical compositions in biomass on gasification tar formation. Biomass Bioenergy 2015;83:77–84. https://doi.org/10.1016/j.biombioe.2015.09.001.

[23] Yu Haimiao, Zhang Ze, Li Zeshen, Chen Dezhen. Characteristics of tar formation during cellulose, hemicellulose and lignin gasification. Fuel 2014;118:250–6. https://doi.org/10.1016/j.fuel.2013.10.080.

[24] Hosoya Takashi, Kawamoto Haruo, Saka Shiro. Pyrolysis gasification reactivities of primary tar and char fractions from cellulose and lignin as studied with a closed ampoule reactor. J Anal Appl Pyrol 2008;83(1):71–7. https://doi.org/10.1016/j.jaap.2008.06.002.

[25] Zhou Bingliang, Dichiara Anthony, Zhang Yimeng, Zhang Qisheng, Zhou Jianbin. Tar formation and evolution during biomass gasification: an experimental and theoretical study. Fuel 2018;234:944–53. https://doi.org/10.1016/j.fuel.2018.07.105.

[26] Wang Q, Endo T, Aparu P, Kurogawa H. Study on biomass tar reduction by ash and fluidizing medium in a heterogeneous reaction. Int J Sustain Dev Plan 2014;9:669–79. https://doi.org/10.2495/SDP-V9-N5-669-679.

[27] Pio DT, Tarelho LAC, Pinto PCR. Gasification-based biorefinery integration in the pulp and paper industry: a critical review. Renew Sustain Energy Rev 2020;133:110210. https://doi.org/10.1016/j.rser.2020.110210.

[28] Cross Phillip, Kulkarni Avanti, Nam Hyungseok, Adhikari Sushil, Fasina Oladiran. Bubbling fluidized bed gasification of short rotation Eucalyptus: effect of harvesting age and bark. Biomass Bioenergy 2018;110:98–104. https://doi.org/10.1016/j.biombioe.2018.01.014.

[29] Pinto Filomena, Gominho Jorge, André Rui Neto, Gonçalves David, Miranda Miguel, Varela Francisco, Neves Diogo, Santos João, Lourenço Ana, Pereira Helena. Improvement of gasification performance of Eucalyptus globulus stumps with torrefaction and densification pre-treatments. Fuel 2017;206:289–99. https://doi.org/10.1016/j.fuel.2017.06.008.

[30] Jiang Long, Hu Song, Wang Yi, Su Sheng, Sun Lushi, Xu Boyang, He Limo, Xiang Jun. Catalytic effects of inherent alkali and alkaline earth metallic species on steam gasification of biomass. Int J Hydrogen Energy 2015;40(45):15460–9. https://doi.org/10.1016/j.ijhydene.2015.08.111.

[31] Skoulou V, Kantarelis E, Arvelakis S, Yang W, Zabaniotou A. Effect of biomass leaching on H2 production, ash and tar behavior during high temperature steam gasification (HTSG) process. Int J Hydrogen Energy 2009;34(14):5666–73. https://doi.org/10.1016/j.ijhydene.2009.05.117.

[32] Hakouk K, Klotz M, Di Geronimo E, Ranieri V, Pieterse JAZ, Aranda Almansa G, Steele AM, Thorpe S. Implementation of novel ice-templated materials for conversion of tars from gasification product gas. Fuel Process Technol 2018;181:340–51. https://doi.org/10.1016/j.fuproc.2018.10.009.

[33] Motta Ingrid Lopes, Miranda Nahieh Toscano, Maciel Filho Rubens, Wolf Maciel Maria Regina. Biomass gasification in fluidized beds: a review of biomass moisture content and operating pressure effects. Renew Sustain Energy Rev 2018;94:998–1023. https://doi.org/10.1016/j.rser.2018.06.042.

[34] Moud Pouya H, Andersson Klas J, Lanza Roberto, Pettersson Jan BC, Engvall Klas. Effect of gas phase alkali species on tar reforming catalyst performance: initial characterization and method development. Fuel 2015;154:95–106. https://doi.org/10.1016/j.fuel.2015.03.027.

[35] Nordgreen Thomas, Nemanova Vera, Engvall Klas, Sjöström Krister. Iron-based materials as tar depletion catalysts in biomass gasification: dependency on oxygen potential. Fuel 2012;95:71–8. https://doi.org/10.1016/j.fuel.2011.06.002.

[36] Brage Claes, Yu Qizhuang, Chen Guanxing, Sjöström Krister. Use of amino phase adsorbent for biomass tar sampling and separation. Fuel 1997;76(2):137–42. https://doi.org/10.1016/S0016-2361(96)00199-8.

[37] Israelsson Mikael, Seemann Martin, Thunman Henrik. Assessment of the solid-phase adsorption method for sampling biomass-derived tar in industrial environments. Energy Fuels 2013;27(12):7569–78. https://doi.org/10.1021/ef401893j.

[38] Hervy Maxime, Remy Damien, Dufour Anthony, Mauviel Guillain. Air-blown gasification of Solid Recovered Fuels (SRFs) in lab-scale bubbling fluidized-bed: influence of the operating conditions and of the SRF composition. Energy Convers Manage 2019;181:584–92. https://doi.org/10.1016/j.enconman.2018.12.052.

[39] Pio DT, Tarelho LAC, Tavares AMA, Matos MAA, Silva V. Co-gasification of refused derived fuel and biomass in a pilot-scale bubbling fluidized bed reactor. Energy Convers Manage 2020;206:112476. https://doi.org/10.1016/j.enconman.2020.112476.

[40] Waldheim, L. Nilsson T. Heating value of gases from biomass gasification. 2001.

[41] Pio DT, Tarelho LAC. Empirical and chemical equilibrium modelling for prediction of biomass gasification products in bubbling fluidized beds. Energy 2020;202:117654. https://doi.org/10.1016/j.energy.2020.117654.

[42] de Sales Cristina Ap Vilas Bôas, Maya Diego Mauricio Yepes, Lora Electo Eduardo Silva, Jaén René Lesme, Reyes Arnaldo Martín Martínez, González Aldemar Martínez, Andrade Rubenildo Vieira, Martínez Juan Daniel. Experimental study on biomass (eucalyptus spp.) gasification in a two-stage downdraft reactor by using mixtures of air, saturated steam and oxygen as gasifying agents. Energy Convers Manage 2017;145:314–23. https://doi.org/10.1016/j.enconman.2017.04.101.

[43] Lenis Yuhan A, Pérez Juan F, Melgar Andrés. Fixed bed gasification of Jacaranda Copaia wood: Effect of packing factor and oxygen enriched air. Ind Crops Prod 2016;84:166–75. https://doi.org/10.1016/j.indcrop.2016.01.053.

[44] Ismail TM, Ramos A, Monteiro E, El-Salam MA, Rouboa A, Ramos A, et al. Parametric studies in the gasification agent and fluidization velocity during oxygen-enriched gasification of biomass in a pilot-scale fluidized bed: experimental and numerical assessment. Renew Energy 2020;147:2429–39. https://doi.org/10.1016/j.renene.2019.10.029.

[45] Nemanova Vera, Engvall Klas. Tar variability in the producer gas in a bubbling fluidized bed gasification system. Energy Fuels 2014;28(12):7494–500. https://doi.org/10.1021/ef5015617.

[46] Phuphuakrat Thana, Nipattummakul Nimit, Namioka Tomoaki, Kerdsuwan Somrat, Yoshikawa Kunio. Characterization of tar content in the syngas produced in a downdraft type fixed bed gasification system from dried sewage sludge. Fuel 2010;89(9):2278–84. https://doi.org/10.1016/j.fuel.2010.01.015.

[47] Bangala DN, Abatzoglou N, Martin JP, Chornet E. Catalytic gas conditioning: application to biomass and waste gasification. Ind Eng Chem Res 1997;36:4184–92. https://doi.org/10.1021/ie960785a.

[48] Hernández JJ, Ballesteros R, Aranda G. Characterisation of tars from biomass gasification: effect of the operating conditions. Energy 2013;50:333–42. https://doi.org/10.1016/j.energy.2012.12.005.

[49] Neubert Michael, Reil Stefanie, Wolff Martin, Pöcher Daniel, Stork Hildegard, Ultsch Christoph, Meiler Michael, Messer Julian, Kinzler Ludwig, Dillig Marius, Beer Stefan, Karl Juergen. Experimental comparison of solid phase adsorption (SPA), activated carbon test tubes and tar protocol (DIN CEN/TS 15439) for tar analysis of biomass derived syngas. Biomass Bioenergy 2017;105:443–52. https://doi.org/10.1016/j.biombioe.2017.08.006.

[50] Wang Zhiqi, He Tao, Li Jianqing, Wu Jingli, Qin Jianguang, Liu Guangbo, Han Dezhi, Zi Zhongyue, Li Zhuo, Wu Jinhu. Design and operation of a pilot plant

for biomass to liquid fuels by integrating gasification, DME synthesis and DME to gasoline. Fuel 2016;186:587–96. https://doi.org/10.1016/j.fuel.2016.08.108.
[51] Boerrigter H, Calis HP, Slor DJ, Bodenstaff H. Gas Cleaning for Integrated Biomass Gasification (Bg) and Fischer-Tropsch (Ft) Systems ; Experimental Demonstration of Two Bg-Ft Systems. 2nd World Conf Technol Exhib Biomass Energy, Ind Clim Prot 2004:10–4. doi:ECN-RX–04-041.
[52] Singh RN, Singh SP, Balwanshi JB, Vishwavidhlya DA. Tar removal from Producer Gas: A Review. Res J Eng Sci 2014;3:16–22.
[53] Basu P. Biomass Gasification, Pyrolysis and Torrefaction. Elsevier 2013. https://doi.org/10.1016/C2011-0-07564-6.
[54] Maniatis K, Beenackers AACM. Tar Protocols. IEA Bioenergy Gasification Task. Biomass Bioenergy 2000;18(1):1–4. https://doi.org/10.1016/S0961-9534(99)00072-0.
[55] Narváez Ian, Orío Alberto, Aznar Maria P, Corella José. Biomass gasification with air in an atmospheric bubbling fluidized bed. Effect of six operational variables on the quality of the produced raw gas. Ind. Eng. Chem. Res. 1996;35(7):2110–20. https://doi.org/10.1021/ie9507540.
[56] Yang T, Jia K, Kai X, Sun Y, Li Y, Li R. A study on the migration behavior of K, Na, and Cl during biomass gasification. BioResources 2016;11:7133–44. https://doi.org/10.15376/biores.11.3.7133-7144.
[57] Pio DT, Tarelho LAC, Nunes TFV, Baptista MF, Matos MAA. Co-combustion of residual forest biomass and sludge in a pilot-scale bubbling fluidized bed. J Cleaner Prod 2020;249:119309. https://doi.org/10.1016/j.jclepro.2019.119309.
[58] Yu Ming Ming, Masnadi Mohammad S, Grace John R, Bi Xiaotao T, Lim C Jim, Li Yonghua. Co-gasification of biosolids with biomass: thermogravimetric analysis and pilot scale study in a bubbling fluidized bed reactor. Bioresour Technol 2015;175:51–8. https://doi.org/10.1016/j.biortech.2014.10.045.
[59] Habibi Rozita, Kopyscinski Jan, Masnadi Mohammad S, Lam Jill, Grace John R, Mims Charles A, Hill Josephine M. Co-gasification of biomass and non-biomass feedstocks: synergistic and inhibition effects of switchgrass mixed with sub-bituminous coal and fluid coke during CO 2 gasification. Energy Fuels 2013;27(1):494–500. https://doi.org/10.1021/ef301567h.
[60] Masnadi Mohammad S, Grace John R, Bi Xiaotao T, Lim C Jim, Ellis Naoko, Li Yong Hua, Watkinson A Paul. Single-fuel steam gasification of switchgrass and coal in a bubbling fluidized bed: a comprehensive parametric reference for co-gasification study. Energy 2015;80:133–47. https://doi.org/10.1016/j.energy.2014.11.054.
[61] Buentello-Montoya DA, Zhang X, Li J. The use of gasification solid products as catalysts for tar reforming. Renew Sustain Energy Rev 2019;107:399–412. https://doi.org/10.1016/j.rser.2019.03.021.
[62] Udomsirichakorn Jakkapong, Salam P Abdul. Review of hydrogen-enriched gas production from steam gasification of biomass: the prospect of CaO-based chemical looping gasification. Renew Sustain Energy Rev 2014;30:565–79. https://doi.org/10.1016/j.rser.2013.10.013.
[63] Chiang Kung-Yuh, Chen Ya-Sing, Tsai Wei-Sin, Lu Cheng-Han, Chien Kuang-Li. Effect of calcium based catalyst on production of synthesis gas in gasification of waste bamboo chopsticks. Int J Hydrogen Energy 2012;37(18):13737–45. https://doi.org/10.1016/j.ijhydene.2012.03.042.
[64] Zhou Chunguang, Stuermer Thomas, Gunarathne Rathnayaka, Yang Weihong, Blasiak Wlodzimierz. Effect of calcium oxide on high-temperature steam gasification of municipal solid waste. Fuel 2014;122:36–46. https://doi.org/10.1016/j.fuel.2014.01.029.
[65] Hamad Mohamed A, Radwan Aly M, Heggo Dalia A, Moustafa Tarek. Hydrogen rich gas production from catalytic gasification of biomass. Renewable Energy 2016;85:1290–300. https://doi.org/10.1016/j.renene.2015.07.082.
[66] Nam Hyungseok, Wang Shuang, Sanjeev KC, Seo Myung Won, Adhikari Sushil, Shakya Rajdeep, Lee Doyeon, Shanmugam Saravanan R. Enriched hydrogen production over air and air-steam fluidized bed gasification in a bubbling fluidized bed reactor with CaO: effects of biomass and bed material catalyst. Energy Convers Manage 2020;225:113408. https://doi.org/10.1016/j.enconman.2020.113408.
[67] Dahou T, Defoort F, Khiari B, Labaki M, Dupont C, Jeguirim M. Role of inorganics on the biomass char gasification reactivity: a review involving reaction mechanisms and kinetics models. Renew Sustain Energy Rev 2021;135:110136. https://doi.org/10.1016/j.rser.2020.110136.
[68] Dahou Tilia, Defoort Françoise, Jeguirim Mejdi, Dupont Capucine. Towards understanding the role of K during biomass steam gasification. Fuel 2020;282:118806. https://doi.org/10.1016/j.fuel.2020.118806.
[69] Guo Feiqiang, Li Xiaolei, Liu Yuan, Peng Kuangye, Guo Chenglong, Rao Zhonghao. Catalytic cracking of biomass pyrolysis tar over char-supported catalysts. Energy Convers Manage 2018;167:81–90. https://doi.org/10.1016/j.enconman.2018.04.094.

Available online at www.sciencedirect.com
ScienceDirect
Energy Reports 6 (2020) 325–330
www.elsevier.com/locate/egyr

6th International Conference on Energy and Environment Research, ICEER 2019, 22–25 July, University of Aveiro, Portugal

Ilmenite as low-cost catalyst for producer gas quality improvement from a biomass pilot-scale gasifier

D.T. Pio[a,*], H.G.M.F. Gomes[a], L.A.C. Tarelho[a], L.C.M. Ruivo[a,b], M.A.A. Matos[a], R.G. Pinto[a], J.R. Frade[b], F.M.S. Lemos[c]

[a] *Department of Environment and Planning & Centre for Environmental and Marine Studies (CESAM), University of Aveiro, Campus Universitario de, Santiago 3810-193, Aveiro, Portugal*

[b] *Department of Materials Engineering and Ceramics & Aveiro Institute of Materials (CICECO), University of Aveiro, Campus Universitario de, Santiago 3810-193, Aveiro, Portugal*

[c] *Department of Chemical Engineering, Instituto Superior Técnico, Av. Rovisco, Pais 1049-001, Lisboa, Portugal*

Received 29 July 2019; accepted 25 August 2019

Abstract

In this work, in-situ application of natural occurring ilmenite ($FeTiO_3$) for upgrading the producer gas from a pilot-scale bubbling fluidized bed gasifier was performed and its influence on the gas characteristics and gasifier performance was analyzed.

Without using ilmenite, the producer gas average composition (volumetric basis, dry gas) was 15.2% CO, 7.6% H_2, 3.8% CH_4 and 15.6% CO_2, with 0.50 H_2:CO molar ratio and 5.0 MJ/Nm^3 lower heating value. For this condition, 1.6 Nm^3 gas/kg biomass (dry basis) specific dry gas production, 44.5% cold gas efficiency and 68.4% carbon conversion efficiency were attained.

Using ilmenite as catalyst, the producer gas average composition (volumetric basis, dry gas) was 13.9% CO, 11.7% H_2, 4.0% CH_4 and 17.9% CO_2, with 0.84 H_2:CO molar ratio and 5.1 MJ/Nm^3 lower heating value. For this condition, 1.7 Nm^3 gas/kg biomass (dry basis) specific dry gas production, 49.8% cold gas efficiency and 75.5% carbon conversion efficiency were attained. Thus, in-situ application of ilmenite generally improved the gasifier performance and induced an increase of H_2 concentration and H_2:CO molar ratio in the producer gas of 35.1% and 40.7%, respectively, improving its suitability for advanced gas applications that require high H_2:CO ratios, such as liquid fuels and chemicals synthesis.

Peer-review under responsibility of the scientific committee of the 6th International Conference on Energy and Environment Research, ICEER 2019.

Keywords: Biomass; Bubbling fluidized bed; Catalyst; Gasification; Ilmenite

* Corresponding author.
E-mail addresses: danieltp@ua.pt (D.T. Pio), jfrade@ua.pt (J.R. Frade), francisco.lemos@tecnico.ulisboa.pt (F.M.S. Lemos).

https://doi.org/10.1016/j.egyr.2019.08.063

Peer-review under responsibility of the scientific committee of the 6th International Conference on Energy and Environment Research, ICEER 2019.

Nomenclature

V_G	Dry gas volumetric flow rate (N m^3/s, where N m^3 refers to m^3 at normal pressure (1.013 $\times$ 10^5 Pa) and temperature (273 K))
m_F	Biomass (dry basis) mass flow rate (kg dry basis/s)
LHV_G	Lower heating value of the dry gas produced (MJ/N m^3)
m_F	Biomass (dry basis) mass flow rate (kg dry basis/s)
LHV_F	Lower heating value of the biomass (MJ/kg dry basis)
P_G	Absolute pressure (Pa) of the dry gas
T_G	Absolute temperature (K) of the dry gas
R	Ideal gas constant (8.314 J mol^{-1} K^{-1})
M_C	Molar mass of Carbon (12 $\times$ 10^{-3} kg/mol)
Index I	Gaseous compound CO_2, CO, CH_4, C_2H_4
$\varepsilon_{C,I}$	Molar fraction of Carbon in gaseous compounds containing Carbon ($\varepsilon_{C,CO2} = 1$, $\varepsilon_{C,CO} = 1$, $\varepsilon_{C,CH4} = 1$, $\varepsilon_{C,C2H4} = 2$)
yi	Molar fraction of CO_2, CO, CH_4, C_2H_4, in the dry gas produced
w_{CF}	Mass fraction of Carbon in the biomass (kg C/kg biomass dry basis).

1. Introduction

Energy plays a vital role in the modern society, being essential for economic development and life quality. However, the current worldwide energy supply mainly relies on fossil fuels, resulting in its excessive extraction and consumption. Furthermore, continuous industrialization, population growth and general increase of life quality, increased the worldwide energy supply necessities in the last decades. These behaviors led to negative economic and environmental consequences, being responsible for the depletion of underground carbon resources and emission of large amounts of greenhouse gases (e.g. CO_2) [1]. Thus, the search for alternative fuels that allow sustainable development has been growing, reflected by a significant increase in renewable energies production in the last years [2].

Bearing this, bioenergy is considered as one of the most important routes to mitigate greenhouse gas emissions and replace fossil fuels [3]. Biomass is considered an adjustable and sustainable renewable feedstock to produce energy and chemicals, with the capacity to increase the worldwide energy supply security.

Gasification, which is recognized as a key process for biomass conversion, provides high flexibility by using different kinds of feedstock materials to generate a gaseous product that can be used in distinct applications [3,4]. The process is defined as the thermochemical conversion of organic material (solid or liquid) into a combustible gas mixture, under reducing conditions.

The gaseous product from biomass gasification, after the required refinement and upgrading, can provide different kinds of chemicals and energy carriers [5]. For example, the gas can be applied in direct combustion systems, gas engines and turbines, fuel cells and combined heat and power processes. Methanol [6], dimethyl ether [7], methyl tertiary butyl ether, formaldehyde and acetic acid are commonly referred as obtainable products from this gas [8]. The Fischer–Tropsch process can also be employed to produce synthetic fuels from this gaseous product, such as gasoline and diesel [9].

Nonetheless, even though this conversion process potential is recognized for several applications, some barriers must still be overcome for the general commercialization of biomass gasification technologies, such as the subpar quality of the producer gas (obtained by direct gasification with air), which is diluted in nitrogen and may contain high amounts of tars and low H_2:CO molar ratios [10].

In this regard, catalysts can be applied as primary measures (inside the gasification reactor) or secondary measures (in a post-gasification reactor), to improve the producer gas quality by reforming tar on the catalyst surface, leading to higher contents of hydrogen in the gas.

In this work, natural occurring iron-titanium mineral ($FeTiO_3$, ilmenite) is applied as primary measure to upgrade the raw gas quality in a novel reactor configuration developed here and previously described [10] and its impacts

on the producer gas quality and gasification process efficiency analyzed. Ilmenite is recognized as interesting for this application due to its mechanical and thermochemical properties at high temperature, catalytic activity for tar reforming and high water-gas shift reaction (Eq. (1)) activity [11,12].

$$CO + H_2O \leftrightarrow H_2 + CO_2 \tag{1}$$

2. Experimental work

The experimental infrastructure used in this work was previously described [10,13] and includes a pilot-scale bubbling fluidized bed (BFB) reactor with 80 kW_{th}. For testing the ilmenite mineral, a fixed bed reactor was installed in the freeboard of the BFB reactor, just above the bottom bed and biomass feeding location [10]. The operating conditions of the performed experiments are detailed in Table 1. The fuel used was wood pellets, which was characterized in previous works [13].

The effect of the ilmenite mineral in the producer gas properties and gasification efficiency parameters was evaluated based on a comparison between the composition of the gas sampled after passing the fixed bed reactor filled with ilmenite particles and sampled without passing the fixed bed. The experiments were performed during steady-state conditions of operation, in terms of temperature at different locations of the reactor and exhaust gas composition, as previously described in other experimental work performed in this facility [10,13]. An indication of the raw gas quality improvement is obtained by assuming that any increase in the concentration of combustible light gases, such as H_2, may result from tar destruction reactions promoted by the catalyst [10,14].

Table 1. Pilot-scale gasification experiments and respective operating conditions.

Experiment reference	Fuel	Equivalence ratio	Average bed Temperature [°C]	Biomass feed rate [kg/h]	Air feed rate [L NPT/ min]
Without catalyst	Wood pellets	0.26	809	11	200
With catalyst	Wood pellets	0.26	801	11	200

The lower heating value (LHV) of the dry gas produced during the gasification experiments was determined based on the relative abundance of combustible gases components (H_2, CO, CH_4 and C_2H_4) and their respective LHV (at reference conditions, 273 K and 101 kPa).

The gasification efficiency parameters, namely specific dry gas production (Y_{gas}), cold gas efficiency (CGE) and carbon conversion efficiency (CCE), were determined according to the methodology described in [13], through the following equations [15–17]:

$$Y_{gas} = \frac{V_G}{m_F} \tag{2}$$

$$CGE\,[\%] = \frac{V_G \times LHV_G}{m_F \times LHV_F} \times 100 \tag{3}$$

$$CCE\,[\%] = \frac{V_G \times \frac{P_G}{R \times T_G} \times M_C \times \sum_i \epsilon_{C,i} \times y_i}{m_F \times w_{CF}} \times 100 \tag{4}$$

The crystalline phases of fresh Ilmenite were assessed by powder X-ray diffraction (XRD) (BrukerD8 Advance DaVinci). Diffraction patterns were analyzed using ICDD (International Centre of Diffraction Data, PDF 4). Brunauer–Emmett–Teller (BET) and Barrett–Joyner–Halenda (BJH) measurements were performed to determine the specific surface area and average pore diameter of the particles.

The XRD patterns indicate ilmenite as the main phase ($FeTiO_3$) and alumina (α-Al_2O_3), rutile (TiO_2) and mayenite ($Ca_{12}Al_{14}O_{33}$) as residual phases (Fig. 1). Other relevant characteristics of the fresh ilmenite and the conditions of the catalytic test are shown in Table 2.

3. Results and discussion

The results presented in this section include the composition of the producer gas in terms of CO_2, CO, CH_4, C_2H_4, C_2H_6, C_3H_8, N_2 and H_2, and determined gasification efficiency parameters, namely LHV, Y_{gas}, CGE and CCE, during direct (air) biomass gasification experiments without and with ilmenite applied as in-situ catalyst (inside the gasifier).

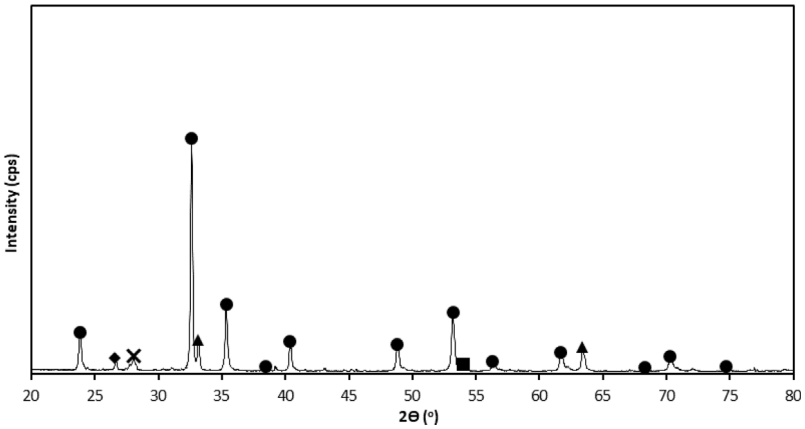

Fig. 1. XRD patterns for ilmenite (α-Al_2O_3 — ▲; SiO_2 — ♦; TiO_2 — **X**; $FeTiO_3$ — ●; $Ca_{12}Al_{14}O_{33}$ — ■).

Table 2. Ilmenite characteristics and test conditions for the fixed bed reactor.

Experiment reference	Catalyst	Particle size [μm]	Apparent density [kg m^{-3}]	Surface specific area [m^2 g^{-1}]	Pore diameter [nm]	Bed mass [g]	Average contact time [s]
With catalyst	Ilmenite	<355	2570	0.52	3–4	200	4.7

The produced gas sampled before passing the fixed bed of ilmenite presented the following average composition (volumetric basis, dry gas): 15.2% CO, 7.6% H_2, 3.8% CH_4, 15.6% CO_2, 1.6% C_2H_4, 0.1% C_2H_6 and 0.1% C_3H_8, and a molar ratio H_2:CO equal to 0.50 (Fig. 2). Based on this gas composition, the following process efficiency parameters were determined:

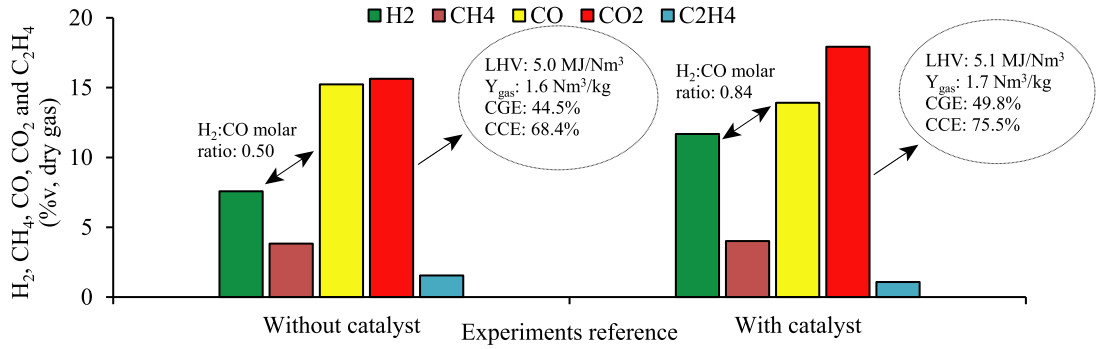

Fig. 2. Composition of the dry gas (H_2, CH_4, CO, CO_2, C_2H_4) for the gasification experiments performed without catalyst and with catalyst.

- LHV = 5.0 MJ/N m^3;
- Y_{gas} = 1.6 N m^3 dry gas/kg dry biomass;
- CGE = 44.5%;
- CCE = 68.4%.

The produced gas sampled after passing the fixed bed of ilmenite presented the following average composition (volumetric basis, dry gas): 13.9% CO, 11.7% H_2, 4.0% CH_4,17.9% CO_2, 1.1% C_2H_4 and 0.2% C_2H_6, and a molar ratio H_2:CO equal to 0.84 (Fig. 2). During this experiment, C_3H_8 was below the detection limit (0.1% volume). Based on this gas composition, the following efficiency parameters were determined:

- LHV = 5.1 MJ/N m^3;
- Y_{gas} = 1.7 N m^3 dry gas/kg dry biomass;
- CGE = 49.8%;

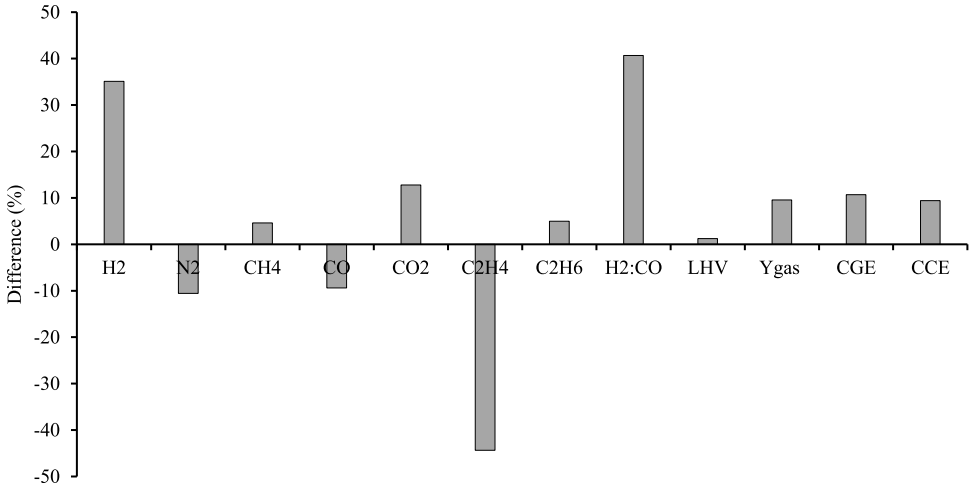

Fig. 3. Influence of the ilmenite mineral on the composition (H_2, N_2, CH_4, CO, CO_2, C_2H_4 and C_2H_6) of the dry gas sampled above the surface of the bed, H_2:CO molar ratio, LHV, Y_{gas}, CGE and CCE.

- CCE = 75.5%.

Thus, it can be observed that the ilmenite in-situ application caused a H_2, CH_4 and CO_2 concentration and H_2:CO molar ratio increase of 35.1%, 4.6%, 12.8% and 40.7%, respectively, while decreasing CO concentration by 9.4% (Fig. 3). Therefore, the producer gas was refined, presenting higher suitability for advanced gas applications, such as synthetic liquid fuels production through Fischer–Tropsch synthesis, which requires a H_2:CO molar ratio of at least 0.6 [9]. The observed increase of CO_2 is not desirable; however, it is a minor inconvenient in the face of the higher H_2:CO ratios attained [9]. In fact, other advanced applications require even higher H_2:CO molar ratios, for example methanol production (molar ratio equal to 2) and dimethyl ether (DME) production (molar ratio equal to 1) [9,18]. This increase in H_2:CO molar ratio, as well as the CO_2 increase, can be related to an increase in water-gas shift activity (Eq. (1)) induced by the ilmenite particles. This phenomenon was previously observed in other gasification processes involving ilmenite [12] and is typically associated to iron-based catalysts [11]. Accordingly, significant H_2:CO molar ratio increases were not observed during in-situ application tests of low-cost catalysts with low iron contents, such as eucalyptus ashes and wood pellets chars, performed in other works here [10].

The ilmenite mineral in-situ application also caused a general increase of approximately 10% for all determined efficiency parameters, except for LHV, which was similar for both experiments (Fig. 3). This similarity is related to the decrease of CO concentration observed in the experiments using ilmenite as catalyst, which accounts for a significant part of the energy content of the producer gas.

4. Conclusions

In this work, the application of ilmenite as low-cost catalyst for the improvement of the producer gas quality was evaluated. The research was focused on the impact of this mineral on the composition of the producer gas, and, consequently, on the efficiency of the gasification process.

The evaluation of the proposed catalytic material was performed by sampling the gas before and after passing a fixed bed of ilmenite inserted 0.2 m above the surface of the bottom bed of the pilot-scale BFB.

The results show that the in-situ application of ilmenite caused a significant H_2 production increase (35.1%) and a slight CO decrease (−9.4%), thus increasing the H_2:CO molar ratio from 0.50 to 0.84. It is also observed a general increase (∼10%) in the determined efficiency parameters, such as Y_{gas}, CGE and CCE. The LHV remained almost unchanged, and this can be explained as a result of CO concentration decrease in the producer gas. Thus, it can be concluded that the in-situ appliance of this mineral for the improvement of the producer gas quality was successful. The increase in H_2:CO molar ratio is a promising result, which was not observed during the application of other low-cost catalysts in other works performed here [10], and can be associated to increased water-gas shift activity induced by the ilmenite. This is interesting because several advanced applications, such as liquid fuels and chemicals synthesis, require H_2:CO molar ratios higher than 0.6 [9].

Acknowledgments

The authors acknowledge the Portuguese Foundation for Science and Technology for the financial support provided through the following projects: PTDC/AAC-AMB/116568/2010 (FCOMP-01-0124-FEDER-019346) – BiomAshTech – Ash impacts during thermochemical conversion of biomass, PTDC/CTM-ENE/2942/2014 - LEANCOMB - Cellular oxide catalysts for emission lean combustion in porous media, project PO Centro 2020 (ref. CENTRO-01-0145- FEDER-000005) – SusPhotoSolutions – Soluções Fotovoltaicas Sustentáveis, project POCI-01-0247-FEDER-021874 – INPACTUS – Innovative Products and Technologies from Eucalyptus and CMU - Policy and Technology Analysis of Waste/Biomass Residue Gasification for Energy Production in Portugal (ref. TMP/0032/2017). Thanks are due for the financial support to CESAM, Portugal (UID/AMB/50017/2019), to FCT/MCTES through national funds, and the co-funding by the FEDER, within the PT2020 Partnership Agreement and Compete 2020, and Compete 2020. The authors also acknowledge the Portuguese Foundation for Science and Technology and The Navigator Company, Portugal for providing financial support to the PhD scholarship granted to Daniel Pio (ref. PD/BDE/128620/2017).

References

[1] Agarwal AK. Biofuels (alcohols and biodiesel) applications as fuels for internal combustion engines. Prog Energy Combust Sci 2007;33:233–71. http://dx.doi.org/10.1016/j.pecs.2006.08.003.

[2] International Renewable Energy Agency. Renewable Energy Statistics 2018. 2018.

[3] Heidenreich S, Foscolo PU. New concepts in biomass gasification. Prog Energy Combust Sci. 2015. http://dx.doi.org/10.1016/j.pecs.2014.06.002.

[4] Clausen LR. Maximizing biofuel production in a thermochemical biorefinery by adding electrolytic hydrogen and by integrating torrefaction with entrained flow gasification. Energy 2015;85:94–104. http://dx.doi.org/10.1016/j.energy.2015.03.089.

[5] Spath PL, Dayton DC. Preliminary screening - technical and economic assessment of synthesis gas to fuels and chemicals with emphasis on the potential for biomass-derived syngas. 2003, http://dx.doi.org/10.2172/15006100.

[6] Puig-Gamero M, Argudo-Santamaria J, Valverde JL, Sánchez P, Sanchez-Silva L. Three integrated process simulation using aspen plus: Pine gasification, syngas cleaning and methanol synthesis. Energy Convers Manag 2018;177:416–27. http://dx.doi.org/10.1016/j.enconman.2018.09.088.

[7] Parvez AM, Wu T, Li S, Miles N, Mujtaba IM. Bio-DME production based on conventional and co_2-enhanced gasification of biomass: A comparative study on exergy and environmental impacts. Biomass Bioenergy 2018;110:105–13. http://dx.doi.org/10.1016/j.biombioe.2018.01.016.

[8] Sikarwar VS, Zhao M, Fennell PS, Shah N, Anthony EJ. Progress in biofuel production from gasification. Prog Energy Combust Sci 2017;61:189–248. http://dx.doi.org/10.1016/j.pecs.2017.04.001.

[9] Ciferno JP, Marano JJ. Benchmarking biomass gasification technologies for fuels, chemicals and hydrogen production. US Department of Energy. National Energy Technology Laboratory; 2002.

[10] Pio DT, Tarelho LAC, Pinto RG, Matos MAA, Frade JR, Yaremchenko A, Mishra GS, Pinto PCR. Low-cost catalysts for in-situ improvement of producer gas quality during direct gasification of biomass. Energy 2018;165:442–54. http://dx.doi.org/10.1016/j.energy.2018.09.119.

[11] Azhar Uddin M, Tsuda H, Wu S, Sasaoka E. Catalytic decomposition of biomass tars with iron oxide catalysts. Fuel 2008;87:451–9. http://dx.doi.org/10.1016/j.fuel.2007.06.021.

[12] Lind F, Seemann M, Thunman H. Continuous catalytic tar reforming of biomass derived raw gas with simultaneous catalyst regeneration. Ind Eng Chem Res 2011;50:11553–62. http://dx.doi.org/10.1021/ie200645s.

[13] Pio DT, Tarelho LAC, Matos MAA. Characteristics of the gas produced during biomass direct gasification in an autothermal pilot-scale bubbling fluidized bed reactor. Energy 2017;120:915–28. http://dx.doi.org/10.1016/j.energy.2016.11.145.

[14] Berrueco C, Montané D, Matas Güell B, del Alamo G. Effect of temperature and dolomite on tar formation during gasification of torrefied biomass in a pressurized fluidized bed. Energy 2014;66:849–59. http://dx.doi.org/10.1016/j.energy.2013.12.035.

[15] Basu P. Combustion and gasification in fluidized beds. first ed.. CRC Press; 2006.

[16] Chen WH, Chen CJ, Hung CI, Shen CH, Hsu HW. A comparison of gasification phenomena among raw biomass, torrefied biomass and coal in an entrained-flow reactor. Appl Energy 2013;112:421–30. http://dx.doi.org/10.1016/j.apenergy.2013.01.034.

[17] Narvaez I, Orıo A, Aznar MP, Corella J. Biomass gasification with air in an atmospheric bubbling fluidized bed, effect of six operational variables on the quality of the produced raw gas. Ind Eng Chem Res 1996;35:2110–20. http://dx.doi.org/10.1021/ie9507540.

[18] Clausen LR, Elmegaard B, Houbak N. Design of novel DME/methanol synthesis plants based on gasification of biomass. 2011.

Energy 233 (2021) 120931

Contents lists available at ScienceDirect

Energy

journal homepage: www.elsevier.com/locate/energy

Concrete as low-cost catalyst to improve gas quality during biomass gasification in a pilot-scale gasifier

D.T. Pio [a, *], H.G.M.F. Gomes [a], L.C.M. Ruivo [a, b], M.A.A. Matos [a], J.F. Monteiro [b], J.R. Frade [b], L.A.C. Tarelho [a]

[a] Department of Environment and Planning & Centre for Environmental and Marine Studies (CESAM), University of Aveiro, Campus Universitário de Santiago, Aveiro, Portugal
[b] Department of Materials Engineering and Ceramics & Aveiro Institute of Materials (CICECO), University of Aveiro, Campus Universitario de Santiago 3810-193, Aveiro, Portugal

ARTICLE INFO

Article history:
Received 28 January 2021
Received in revised form
4 May 2021
Accepted 10 May 2021
Available online 27 May 2021

Keywords:
Catalyst
Concrete
Biomass
Gasification
Bubbling fluidized bed

ABSTRACT

Concrete was evaluated as low-cost catalyst for in-situ application in an autothermal 80 kW_{th} pilot-scale bubbling fluidized bed direct (air) biomass gasifier. To improve the understanding of the observed phenomena, the process was also evaluated in smaller-scale reactive system, namely an externally heated 3 kW_{th} bench-scale bubbling fluidized bed.

Concrete application showed promising results regarding the relative increase of H_2 concentration and H_2/CO molar ratio in the producer gas (up to 99.2 and 77.4%, respectively), indicating that this material can promote the water-gas shift reaction. However, this effect was dependent on the gas-solid contact time and catalyst temperature, being that it was only relevant when these parameters were at least 5.2 s and 746 °C, respectively. A maximum lower heating value of 7.5 MJ/Nm^3 of the producer gas was found with concrete application (23.8% relative increase), which is higher than commonly found in the literature. Relative increases of up to 25.1, 55.3 and 47.0% for the specific dry gas production, cold gas efficiency and carbon conversion efficiency, respectively, were also found, consequently suggesting that, in addition to the promotion of the water-gas shift reaction, this material has potential to promote tar reforming/cracking and carbon gasification reactions.

1. Introduction

The growing environmental and economic concerns related to the use of fossil fuels have been promoting the study of new energy solutions [1,2]. Amongst them, biomass appears as a sustainable option for energy conversion, having some advantages over other types of renewable sources and fossil fuels, including high availability and worldwide distribution, possible application in the current energy carbon infrastructure and potential carbon neutrality [3–5]. However, several problems can be identified when using solid biomass feedstocks, such as handling, mass and heat transfer, material heterogeneity and application [6]. In this regard, gasification can be an interesting solution, since it can process different types of biomass feedstocks to a fuel gas, known as producer gas (PG), which presents easier storage and handling characteristics, and can be used for the generation of heat and power, and as a feedstock for the synthesis of biofuels and chemicals [7–10].

Apart from the desirable compounds of the PG (e.g., H_2), other byproducts are generated during the process, such as soot [11–13] and a complex mixture of condensable organic compounds, known as tars [14]. Tar compounds are undesirable because upon condensation (temperature lower than 400 °C) they cause the clogging and blockage of the equipment downstream the gasifier, consequently being one of the major constraints for PG applications [7]. Therefore, PG upgrade and refinement are mandatory for various potential end-use applications. In this regard, tar removal can be performed by two main types of measures: primary, which are applied inside the reactor, and secondary, which are applied downstream of the gasifier.

The interest in primary measures emerge from their capacity to enable efficient industrial applications by preserving and using the thermal energy of the PG, and lowering the necessity downstream

* Corresponding author.
E-mail address: danieltp@ua.pt (D.T. Pio).

https://doi.org/10.1016/j.energy.2021.120931
0360-5442/

Abbreviations and nomenclature

BET	Brunauer–Emmett–Teller
BFB	Bubbling fluidized bed
BJH	Barrett–Joyner–Halenda
CCE	Carbon conversion efficiency [%]
CEN/TS	European Committee for Standardization Technical Specification
CGE	Cold gas efficiency [%]
db	Dry basis
ER	Equivalence ratio
FTIR	Fourier-transform infrared spectroscopy
GC-TCD	Gas chromatography with thermal conductivity detector
H_2/CO	Molar ratio between hydrogen and carbon monoxide (mol H_2.mol CO^{-1})
i	Gaseous compound CO_2, CO, CH_4, C_2H_4, C_2H_6 and C_3H_8
LHV	Lower heating value [MJ/Nm^3]
LHV_F	Lower heating value of the biomass [MJ/kg db]
LHV_G	Lower heating value of the dry gas produced [MJ/Nm^3]
M_C	Molar mass of Carbon [kg/mol]
m_F	Biomass (dry basis) mass flow rate [kg db/s]
NDIR	Nondispersive infrared
NL	Refers to L at normal pressure (1.013×10^5 Pa) and temperature (0 °C)
Nm^3	Refers to m^3 at normal pressure (1.013×10^5 Pa) and temperature (0 °C)
NPT	Normal pressure (1.013×10^5 Pa) and temperature (0 °C)
PG	Absolute pressure of the dry gas [Pa]
Q_{air}	Air flow rate [NL/min]
$Q_{Biomass}$	Biomass flow rate [kg/h]
R	Ideal gas constant [J.mol^{-1}.K^{-1}]
T_{bed}	Temperature of the reactor bed [°C]
$T_{freeboard}$	Temperature of the reactor freeboard [°C]
TG	Absolute temperature of the dry gas [T]
TC	Thermal conductivity
TCD	Thermal conductivity detector
TGA	Thermogravimetric analysis
V_G	Dry gas volumetric flow rate [Nm^3/s]
w_{CF}	Mass fraction of Carbon in the biomass [kg C/kg biomass db]
Y_{gas}	Dry gas specific production [Nm^3 dry gas/kg dry biomass]
y_i	Molar fraction of CO_2, CO, CH_4, C_2H_4, C_2H_6 and C_3H_8 in the dry gas
%v	Volume percentage [%]
wb	Wet basis
%wt	Weight percentage [%]

Greek symbols

$\varepsilon_{C,I}$	Molar fraction of Carbon in i [mol C/mol i]

cleaning [9,15]. In this regard, the PG can be refined by optimizing the reactor design and process parameters, such as the ER, using active bottom bed materials and applying catalytic materials in an integrated section of the gasifier [9,15,16]; these measures are applicable and under study in the most common type of gasifiers, such as fixed and fluidized beds [17]. Natural minerals (e.g., dolomite, limestone, olivine and ilmenite) have showed promising results when applied in gasification processes, including tar and CO_2 reduction, and H_2 increase [18,19], despite some concerns regarding deactivation [20,21] and fragmentation/attrition and consequent entrainment and elutriation with the upward gasifying agent and PG [18,20]. Amongst these, Ca-based materials ($Ca(OH)_2$/CaO) have been gaining particular interest due to their low-cost and promising activity towards tar and hydrocarbons reforming and carbon gasification reactions [18,22,23].

In a gasification system, $Ca(OH)_2$ will dehydrate to CaO at about 500 °C (Reaction 1), releasing H_2O in the process. The resulting CaO will then act as a CO_2 sorbent (Reaction 2) [24] and tar/hydrocarbon reforming catalyst [25], while the H_2O will act as reactant in other reactions (Reactions 3 to 7), including carbon gasification reactions [22,26]. Following the decrease in CO_2 partial pressure in the PG, the water-gas shift (WGS) reaction (Reaction 3) is driven forward, further increasing the H_2 concentration [22,27]. The drawback of this process is the deactivation of CaO after capturing CO_2, which constitutes a challenge for continuous application in gasification systems [26].

$Ca(OH)_2 \leftrightarrow CaO + H_2O$ Reaction 1

$CaO + CO_2 \leftrightarrow CaCO_3$ Reaction 2

$CO + H_2O \leftrightarrow CO_2 + H_2$ Reaction 3

$C(s) + H_2O \rightarrow CO + H_2$ Reaction 4

$C(s) + 2H_2O \rightarrow CO_2 + 2H_2$ Reaction 5

$C(s) + H_2O \rightarrow \frac{1}{2}CH_4 + \frac{1}{2}CO_2$ Reaction 6

$CH_4 + H_2O \leftrightarrow CO + 3H_2$ Reaction 7

Hamad et al. [22], studied the production of H_2 rich PG from gasification of biomass in a bench-scale fixed bed reactor, using O_2 as gasifying agent and distinct catalytic materials as additives in the biomass feedstocks. The authors found that $Ca(OH)_2$ increased the PG yield and reduced both char and tar production during gasification processes. The authors also reported higher H_2 yields with $Ca(OH)_2$ in comparison to CaO, which can be justified by the H_2O released during the $Ca(OH)_2$ dehydration process. Udomsirichakorn et al. [28], analyzed the combined role of CaO on CO_2 sorbent and tar reforming in a bubbling fluidized bed (BFB) biomass steam gasifier, and found that replacing the reactor sand bed by a CaO bed allowed 20% higher concentration and almost double yield of H_2, and a decrease of 67% in tar content. The authors also found that the tar species shifted from higher to lower ring structures with CaO addition, consequently reducing its carcinogenic potential and dew point, which is relevant regarding health risks and operation hazards, respectively. Nam et al. [25], analyzed the application of CaO as bed material during air and air-steam gasification of biomass in a BFB reactor and found that CaO significantly reduced the tar content by catalyzing thermal cracking and oxidation reactions, and also promoted the WGS reaction leading to an increase of the H_2 concentration. In this study, the combination of steam and CaO allowed a H_2 concentration of approximately 50 %v [25]. Similarly,

Jordan and Akay [29] analyzed the effect of CaO as bed material on tar production and dew point during gasification of cane bagasse in a pilot-scale downdraft gasifier, and found that the use of 2, 3 and 6 %wt in-bed CaO decreased tar yield ranging from 16 to 35%, which corresponded to a tar concentration decrease between 44 and 80% in the PG. The authors also found an increase in PG yield between 17 and 37% and a decrease of tar dew point between 37 and 60 °C.

Despite the promising results reported in these works, information regarding the application of $Ca(OH)_2$/CaO is still scarce, particularly regarding its use as in-situ catalysts in direct (air) pilot-scale biomass BFB gasifiers, and there are still various uncertainties regarding the capacity of these materials towards catalyzing reforming (Reactions 8 and 9) [30] and cracking (Reactions 10 and 11) [31] reactions to effectively reduce tar formation and increase the non-condensable gases yields (e.g., H_2 and CO).

$$C_NH_m + nH_2O \rightarrow \left(\frac{m}{2}+n\right)H_2 + nCO \text{ Reaction 8}$$

$$C_NH_m + nCO_2 \rightarrow \left(\frac{m}{2}\right)H_2 + 2nCO \text{ Reaction 9}$$

$$C_NH_m \rightarrow nC + \left(\frac{m}{2}\right)H_2 \text{ Reaction 10}$$

$$C_NH_m + \left(\frac{4n-m}{2}\right)H_2 \leftrightarrow nCH_4 \text{ Reaction 11}$$

In this context, concrete is one of the most important construction materials, producing more than 900 million tons of waste each year worldwide [32,33]. The composition of concrete usually includes considerable amounts of Ca-based inorganics [34], comprising sand as aggregate material and calcium silicates, mainly dicalcium silicate (Ca_2SiO_4) with residual metastable tricalcium silicate (Ca_3SiO_4), which undergoes immediate hydration in the presence of H_2O, yielding $Ca(OH)_2$ and hydrate calcium silicates. Furthermore, the management of construction wastes is recognized as a relevant issue arising from construction, renovation and demolition activities [35]. Thus, concrete can be an interesting substitute for $Ca(OH)_2$ as a catalyst for biomass gasification processes, and the research for its use in advanced applications is of major interest in the context of circular economy.

Accordingly, in this work, synthetic concrete was tested as in-situ low-cost catalyst for PG upgrading in an autothermal 80 kW_{th} BFB direct (air) biomass gasifier. The catalyst was placed in a fixed bed reactor integrated in the freeboard of the gasifier to avoid catalyst fragmentation and to analyze the solid material impact in the gas-phase reactions, and consequent PG composition changes. The process was also evaluated in an externally heated 3 kW_{th} bench-scale BFB because this smaller-scale reactive system allows a better control of the operating parameters, thus being helpful to study certain specific aspects of the process (e.g., specific controlled temperatures). Considering the potential of Ca-based catalysts, the main objective was the evaluation of the performance of widely available and nominally zero cost concrete wastes [36] as primary measure to upgrade PG quality from direct (air) biomass gasification processes in BFBs with distinct operating parameters (e.g., catalyst temperature and gas-solid contact time). In this context, it was characterized the influence of concrete on the PG composition (CO, CO_2, CH_4, C_2H_4, H_2 and N_2) and lower heating value (LHV), and gasification process efficiency parameters, namely specific dry gas production (Y_{gas}), cold gas efficiency (CGE) and carbon conversion efficiency (CCE). The influence of the catalytic load on the tar concentration in the raw PG was qualitatively inferred and discussed, by assuming that the increase of the concentration of combustion light gases may result from tar destruction reactions promoted by the catalyst, as suggested in other works [15,16,37].

2. Materials and methods

2.1. Feedstock characterization

The feedstock chosen for the gasification experiments was commercial pine (*Pinus Pinaster)* pellets due to three main reasons:

1. Pine (*Pinus Pinaster*) is one of the most abundant tree species in the Portuguese Forests [38].
2. Pelletization allows an increase of the uniformity of the physical characteristics of biomass feedstocks, which leads to improved feeding regularity.
3. This biomass feedstock has an adequate chemical composition (e.g., low ash content) and has previously shown good performance during other gasification studies performed by the authors [39].

For the experiments carried out in the autothermal pilot-scale infrastructure, the pine pellets had 4–6 mm diameter, while for the externally heated bench-scale infrastructure, the pellets were previously grounded and sieved to a size between 2 and 4 mm diameter, due to the lower dimensions of the reactor and respective biomass feeding system. The feedstock was characterized in terms of properties with interest for biomass thermochemical conversion, namely proximate and ultimate analysis, heating value and bulk density (Table 1). The proximate analysis (moisture, volatile matter, ash) was made based on CEN/TS norms [40–42] and the ultimate analysis was performed by an external laboratory, namely using a method that involves the complete and instantaneous oxidation of the sample by flash combustion, and afterwards GC-TCD analysis of the gaseous products. The LHV of the pine pellets was determined based on the correlation developed by Parikh et al. [43], and the bulk density of the biomass particles was determined based on the relation between the volume of the material measured in a graduated cylinder and its respective mass.

2.2. Preparation and characterization of simulated concrete loads

Synthetic concrete samples were prepared by combining Portland cement CIMPOR and quartzite sand, with approximately 1:2 wt ratio, respectively. For this purpose, cement was mixed with sand and stirred evenly at 100 rpm, with a water weight ratio of 0.5 (in relation to the cement/sand mixture). The samples were dried at 25 °C for 24 h on a drying oven with controlled humidity. Afterwards, controlled hydration was performed in an autoclave at 180 °C for 12 h.

Brunauer–Emmett–Teller (BET) and Barrett–Joyner–Halenda (BJH) measurements were performed to determine the specific surface area and average pore diameter of the particles of the fresh solid catalytic samples (Table 2). Prior to these measurements, the samples were degassed under vacuum at 140 °C for 12 h. Thermochemical changes by heating in CO_2 atmosphere for the typical temperature ranges of gasification processes were investigated by

Table 1
Proximate and elemental analysis of the pine pellets used as feedstock in the gasification experiments.

Proximate analysis	
Moisture (%wt, wb)	4.6
Volatile matter (%wt, db)	82.3
Fixed carbon (%wt, db)	17.4
Ash (%wt, db)	0.3
Ultimate analysis (%wt, db)	
Ash	0.3
C	47.5
H	6.2
N	0.1
S	nd
O (by difference)	45.9
LHV (MJ/kg db)	18.0
Bulk density (kg/m^3 wb)	614

db-dry basis; nd-not determined, below the detection limit of the method, 100 ppm wt; wb-wet basis.

thermogravimetric analysis (TGA) (SetSys 16/18 analyzer). The phase composition of the fresh and tested material (post-mortem analysis) was assessed by X-ray diffraction (Panalytical X'Pert Pro^3, in 10−70° 2Θ range with 0.02° step and 100 s of exposition). Post-mortem analysis of the concrete samples after the gasification experiments was also performed by fourier-transform infrared spectroscopy (FTIR) (Mattson, GALAXY SERIES FT-IR 7000).

Thermodynamic predictions of conditions for hydration or carbonation were taken as guidelines for interactions of cement or concrete wastes with components of PG. Since the real system is too complex, it was assumed simplified SiO_2−CaO−H_2O and SiO_2−CaO−CO_2 model systems, based on the main components of concrete, and derived stability diagrams by planar representations of the activity ratio a_{CaO}:a_{SiO2} vs temperature, extending methods proposed for a variety of systems [44–46].

Table 2
Physical-chemical characteristics of the low-cost solid materials used as catalysts in the gasification experiments performed.

		Concrete
Physical characteristics	Particle size [μm]	<3000
	Apparent density [kg·m^{-3}]	1750
	Surface specific area [m^2·g^{-1}]	1.2
	Pore diameter [nm]	9 to 10
Chemical composition [%wt]	Ti	0.058
	Fe	0.731
	Mg	0.372
	Si	32.676
	Al	0.779
	Ca	17.492
	Mn	0.016
	V	–
	S	0.708
	Na	0.057
	Cr	–
	Ni	–
	K	0.400
	P	0.013
	Zn	–
	Co	–
	Zr	–
	Cu	–
	Nb	–
	Cl	0.012
	Sr	–
	Pb	–
	O	46.686

2.3. Experimental infrastructures

2.3.1. Autothermal pilot-scale infrastructure

The BFB pilot-scale experimental infrastructure (Fig. 1) used in this work was described in detail in other works regarding direct (air) gasification of biomass [16,47]. The infrastructure includes a BFB reactor (80 kW_{th}) with 0.25 m internal diameter and a reaction chamber height of 2.3 m. The fluidized bed was operated with a superficial gas velocity of approximately 30 cm/s (at 800 °C), which is approximately two times higher than the determined minimum fluidization velocity (14 cm/s for bottom bed particles with an average granulometry of 700 μm), and in autothermal regime, i.e., no external thermal energy supply was used during the gasification process.

The in-situ testing of catalysts was performed by using a fixed bed reactor (M3, Fig. 1) with 0.125 m height and 0.054 m internal diameter, installed in the freeboard of the BFB gasifier, just above the bottom bed and biomass feeding location; 200 g of concrete were inserted in the fixed bed and a gas sampling flow of approximately 1.3 L/min was used during the gasification experiments. The effect of the low-cost catalysts in the PG and gasification efficiency parameters was evaluated based upon a comparison between the composition of the PG sampled after passing the fixed bed (M3, Fig. 1) and PG sampled without passing the fixed bed (M2, Fig. 1). The PG sampling, conditioning and characterization procedure was described in a previous work performed by the authors [39].

2.3.2. Externally heated bench-scale infrastructure

The bench-scale BFB experimental infrastructure used in this work (Fig. 2) is composed by a 3 kW_{th} BFB reactor with approximately 50 mm internal diameter and a reaction chamber height of 340 mm. The reactor was continuously heated by an electric furnace (4.2. kW_e), and with a superficial gas velocity of around 9 cm/s (at 800 °C), which is significantly higher than the determined minimum fluidization velocity (1 cm/s for bottom bed particles with an average granulometry of 215 μm). The in-situ testing of the concrete was performed by using a fixed-bed reactor (K, Fig. 2) placed in the freeboard of the bench-scale BFB reactor. The fixed-bed reactor consists in a sampling probe with 8 mm internal diameter (K, Fig. 2) with a ceramic wool bed involved in a wire mesh placed at the bottom of the probe. The amount of concrete used in the fixed bed reactor was between 1 and 10 g, depending on the gasification experiment (see Section 2.4), and the PG sampling flow was approximately 0.1 L/min. The PG sampling, conditioning and characterization procedure is analogous to the autothermal pilot-scale gasifier and was described in previous works performed by the authors [39]. The effect of the low-cost catalysts on the PG and gasification efficiency parameters was evaluated based upon a comparison between the composition of the PG sampled in two distinct ways:

i) PG sampled after passing through the sampling probe containing a fixed-bed of concrete wastes (K, Fig. 2).
ii) PG sampled after passing through the sampling probe with an equal amount of inert material (the same sand from the original bottom bed of the BFB reactor), and without any trace of concrete wastes.

2.4. Gasification process parameters and operating conditions

The performance of the gasification process was evaluated based on the composition of the PG (CO, CO_2, CH_4, C_2H_4, C_2H_6, C_3H_8, H_2 and N_2) and respective lower heating value (LHV), and three efficiency parameters determined from the experimental data,

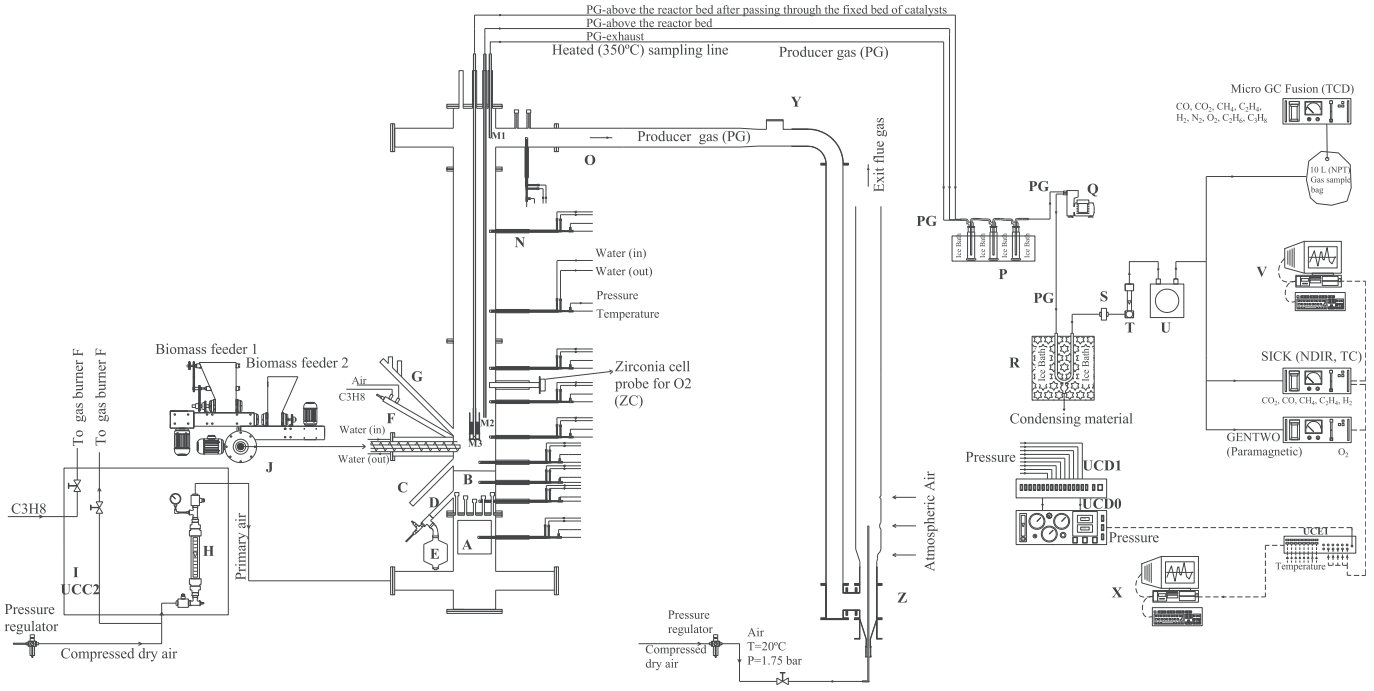

Fig. 1. Schematic layout of the 80 kW_{th} autothermal BFB pilot-scale gasification facility. Dashed line - Electric circuit, Continuous line - Pneumatic circuit, A - Primary air heating system, B - Sand bed, C - Bed solids level control, D - Bed solids discharge, E – Bed solids discharge silo, F - Propane burner for preheating, G - Port for visual inspection of bed surface, H - Air flow meter (primary air), I - Control and command unit (UCC2), J - Biomass feeder, M1 - Probe for sampling the raw exhaust gas, M2 - Probe for sampling the raw gas present above the reactor bed, M3 - Fixed bed reactor with catalyst particles, coupled to a gas sampling probe, N - Water-cooled probe for pressure and temperature monitoring, O - Gas exhaust, P - Gas condensation unit with impingers for condensable gases (water, tars) removal, Q - Gas sampling pump, R - Gas condensation unit for moisture and other condensable gases removal, S - Filter for particle matter/aerosol removal, T - Gas flow meter, U - Dry gas meter, V - Computer for data acquisition from the SICK analyzer, X - Computer for data acquisition, Y - Security exhaust pipe, Z - Raw gas burner, GENTWO – Paramagnetic online gas analyzer for O_2, UCD0, UCD1 - Electro-pneumatic command and gas distribution units, UCE1 - Electronic command unit, Micro GC Fusion - Gas chromatograph with TCD, SICK – NDIR and TC online gas analyzer for CO_2, CO, CH_4, C_2H_4 and H_2.

namely specific dry gas production (Y_{gas}), cold gas efficiency (CGE) and carbon conversion efficiency (CCE). CGE is the ratio between chemical energy present in the PG in relation to the chemical energy present in the feedstock fed [1]. The CCE is the ratio between the carbon present in the PG in terms of gaseous compounds (e.g., CO, CO_2, CH_4, C_2H_4, C_2H_6, C_3H_8) and the carbon present in the feedstock fed [1]. The effect of the concrete was evaluated considering its influence on the value of these parameters. This is a common procedure in the literature for characterizing gasification processes [48] and was used by the authors in previous works [1].

The equivalence ratio (ER) was determined as the ratio between the O_2 added to the gasifier and the stoichiometric O_2 required for the complete oxidation of each biomass feedstock. The stoichiometric O_2 was determined based on the elemental analysis of the feedstocks used (Table 1). The LHV of the dry PG for the distinct gasification experiments was determined based on the concentration of the combustible gases (H_2, CO, CH_4, C_2H_4, C_2H_6 and C_3H_8) and their respective LHV (at reference conditions, 273 K and 101.3 kPa) [49]. The efficiency parameters Y_{gas}, CGE and CCE, were determined following the methodology described in Ref. [39], through Equations 1 to 3.

$$Y_{gas} = \frac{V_G}{m_F} \quad (1)$$

$$CGE\ [\%] = \frac{V_G \times LHV_G}{m_F \times LHV_F} \times 100 \quad (2)$$

$$CCE\ [\%] = \frac{V_G \times \frac{P_G}{R \times T_G} \times M_C \times \sum_i \varepsilon_{C,i} \times y_i}{m_F \times w_{CF}} \times 100 \quad (3)$$

The operating conditions of the gasification experiments performed in the autothermal pilot-scale and externally heated bench-scale BFB reactors are detailed in Table 3. For the pilot-scale reactor, the average ER was maintained at 0.22 and the average bed temperature between 781 and 798 °C. For the bench-scale reactor, the ER was kept at 0.25 and the bed temperature at 800 °C (imposed by an electric furnace and associated temperature controller). These values were chosen following guidelines resulting from previous works performed by the authors, which suggest that an optimal balance between producer gas quality and process efficiency and stability, can be attained for ER ≈ 0.25 and bed temperature ≈800 °C [39]. The average contact time between the sampled PG and the fixed-bed of catalysts was maintained between 0.3 and 3.5 s for the bench-scale reactor, and at 5.2 s for the pilot-scale reactor. The average catalyst temperature was maintained between 585 and 620 °C for the bench-scale reactor and at 746 °C for the pilot-scale reactor (measured by a thermocouple close to the fixed-bed reactor).

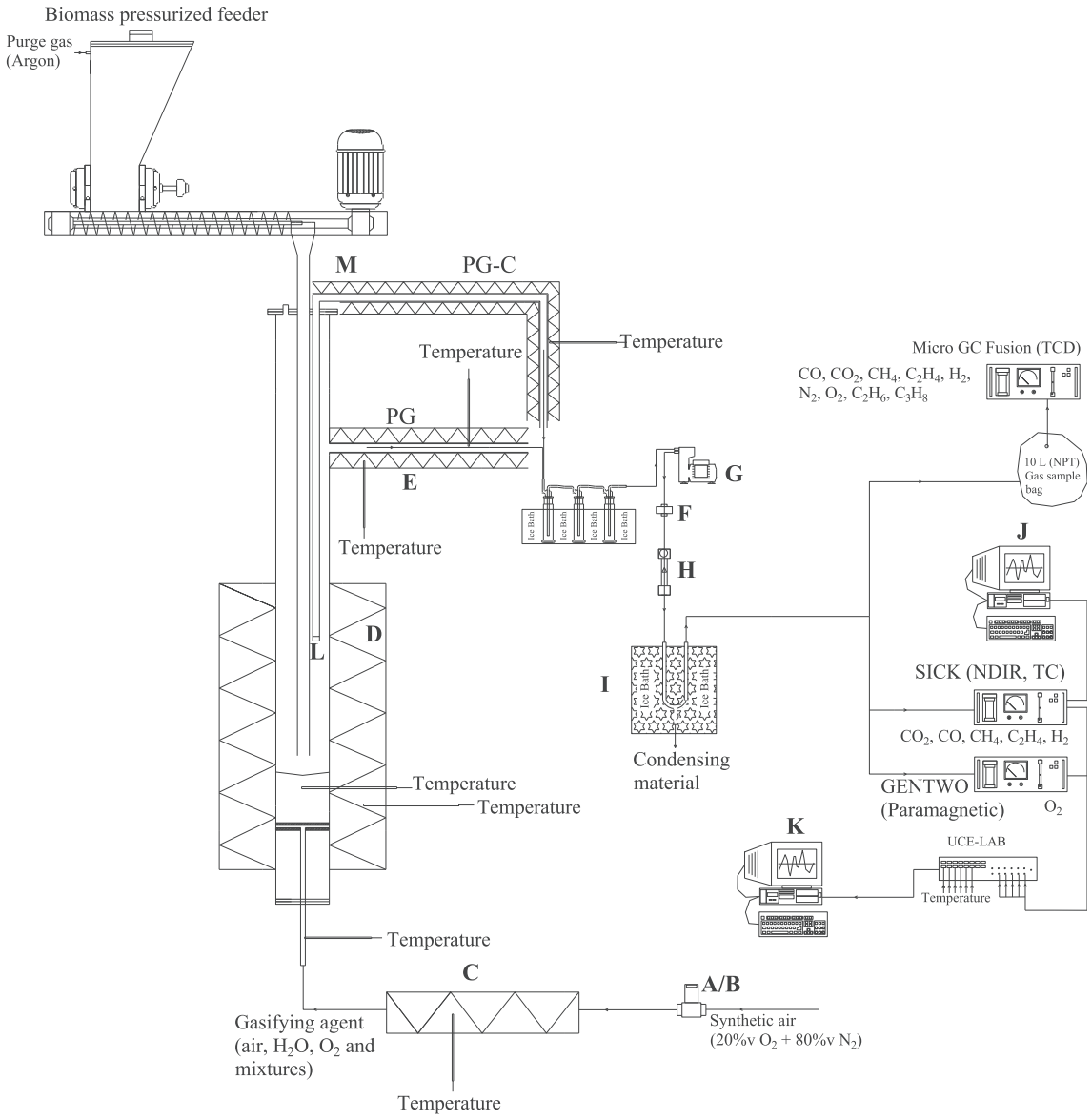

Fig. 2. Schematic layout of the 3 kW_{th} externally heated BFB bench-scale gasification facility. Dashed line - Electric circuit, Continuous line - Pneumatic circuit, A/B – Mass-flow controller, C – Electric furnace to produce steam from liquid water and preheat air, D – Electric furnace to supply heat to the BFB reactor, E – Raw PG exhaust involved by an electric furnace to maintain the PG above 400 °C and avoid tar condensation, F – Filter for particle matter/aerosol removal, G – Gas sampling pump, H – Gas flow meter, I - Gas condensation unit for moisture and other condensable gases removal, J - Computer for data acquisition from SICK analyzer, K - Computer for data acquisition, L – Fixed bed of catalysts, M – Probe involved by an electrical furnace to maintain the PG above 400 °C and avoid tar condensation, PG – Raw producer gas, PG-C - Producer gas that passed through the fixed bed of catalysts, GENTWO – Paramagnetic online gas analyzer for O_2, UCE-LAB - Electronic command unit, Micro GC Fusion - Gas chromatograph with TCD, SICK – NDIR and TC online gas analyzer for CO_2, CO, CH_4, C_2H_4 and H_2.

Table 3
Gasification experiments reference and respective operating conditions.

Experiment reference	Pine pellets granulometry [mm]	BFB scale	ER	T_{bed} [°C]	$Q_{biomass}$ [kg/h]	Q_{air} [NL/min]	Catalyst	$T_{catalyst}$ [°C]	Gas-solid contact time [s]
BP Blank	2 to 4	Bench	0.25	800 ± 5	0.154	2.7	–	–	–
BP Concrete 0.3	2 to 4	Bench	0.25	800 ± 5	0.154	2.7	Concrete	620	≈0.3
BP Concrete 3.5	2 to 4	Bench	0.25	800 ± 5	0.154	2.7	Concrete	585 ±30	≈3.5
PP Blank C	6	Pilot	0.22	781 ±19	13.2	200	–	–	–
PP Concrete 5.2	6	Pilot	0.22	798 ±6	13.2	200	Concrete	746 ±7	≈5.2

*NL – Refers to L at normal pressure (1.013×10^5 Pa) and temperature (0 °C).

3. Results and discussion

3.1. Structural changes of simulated concrete at gasification temperatures

Fig. 3 shows the X-ray diffractogram of the synthetic concrete samples after hydrothermal treatment and after the gasification experiments. Quartz is the main crystalline phase in both cases, combined with di-calcium silicate and traces of other minor phases. Hydrothermal treatment in autoclave also induced formation of an hydrated calcium silicate phase (tobermorite), in close agreement with literature [50], and possibly $Ca(OH)_2$. Onset of $CaCO_3$ (calcite) seems somewhat surprising after autoclave treatment, and should be ascribed to earlier onset of carbonation, probably by uptake of atmospheric CO_2 and reaction with metastable tricalcium silicate, during cement storage.

Thermogravimetry by heating at 5 °C/min in CO_2 atmosphere (Fig. 4) was used to screen expected changes on heating the simulated concrete; this showed several relevant stages. Slight early losses for up to about 300 °C (stage I) can be attributed to the ready decomposition of a minor fraction of hydrated calcium silicate ($Ca_5Si_6O_{17}\cdot nH_2O$), due to its limited thermochemical stability, whereas decomposition of $Ca(OH)_2$ may be superimposed with a first stage of carbonation (stage II), revealed by weight gain (~0.3 % wt). Actually, the mechanisms of decomposition of $Ca(OH)_2$ and onset of carbonation may be interlinked [51]. At about 500 °C, it can be observed the transition towards a third stage with ~0.5 %wt weight gain, probably by a different mechanism of carbonation, and reaching maximum weight gain at temperatures as high as approximately 850 °C; this is followed by a sharp weight loss (stage IV), attributed to the decomposition of a large fraction of $CaCO_3$ formed in the earlier stages. Still, this weight loss (~1.1 wt%) is significantly higher than the previous uptake during stages II and III, possibly because the weight gain in stage II is reduced due to the difference between effective carbonation and additional losses by decomposition of hydrated phases. In addition, the concrete sample may also contain a fraction of $CaCO_3$ before the thermogravimetry experiments in CO_2 atmosphere, as indicated by X-ray diffraction (Fig. 3). Slight losses at even higher temperatures (stage V) suggest that a small fraction of carbonated phases may be retained at relatively high gasification temperatures. However, these steps of carbonation/decarbonation are very likely to depend on kinetics, which displaces these reactions to higher temperatures on heating

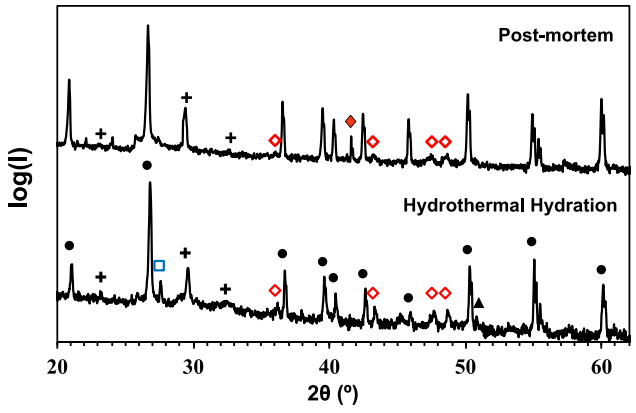

Fig. 3. X-Ray diffractogram of synthetic concrete sample after hydrothermal hydration in autoclave (Hydrothermal Hydration) and after exposure to PG in the gasification experiments (Post-mortem) (● - SiO_2; □ - $Ca_5Si_6O_{17}\cdot nH_2O$; ◊ - $CaCO_3$; + - Ca_2SiO_4, ▲ - $Ca(OH)_2$). Closed diamond peak (◆) at about 41.6° (post-mortem) indicates an aragonite polymorph phase.

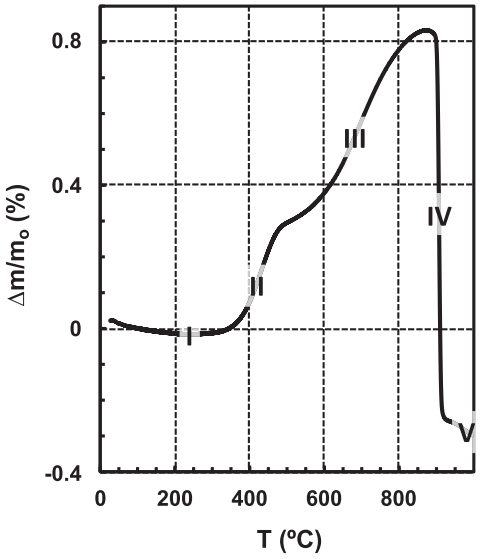

Fig. 4. TGA in CO_2 atmosphere of simulated concrete after hydration in autoclave.

at relatively high rate, and may involve complex structural and microstructural changes of co-existing carbonate and oxide phases [52].

3.2. Thermodynamic assessment of hydration and carbonation of concrete

The phase stability diagram in contact with wet atmospheres (Fig. 5 (a)) show that the stability range of the hydrated calcium silicate ($Ca_5Si_6O_{17}\cdot nH_2O$, T in Fig. 5 (a)) is very limited and should decompose readily on heating. On the contrary, decomposition of $Ca(OH)_2$ may be shifted to temperatures close to 500 °C. Thus, this is consistent with the hypothesis that dehydration extends from stage I to stage II during the TGA experiments (Fig. 4), with co-existence of dehydration and onset of carbonation, which is in close agreement with evidence in relevant literature [51].

Guidelines for carbonation on heating and de-carbonation at sufficiently high temperatures are also provided by the thermodynamic predictions in Fig. 5 (b). The predicted stability range of the carbonated species is up to 600 °C at $pCO_2 = 0.1$ atm or close to 700 °C in an atmosphere of pure CO_2. This is significantly lower than obtained by TGA (Fig. 4), which shows that carbonation may extend for up to about 850 °C, probably because kinetics imposes delays during relatively fast heating. Complex structural changes may also occur during carbonation/de-carbonation processes, extending the effective temperature range [52], even for the simplest system $CaO/CaCO_3$. Thermodynamic predictions also include prospects of onset carbonated calcium silicate phases, depending on the effective activity ratio and temperature range (Fig. 5 (b)). Thus, the relevant temperature range for carbonation/de-carbonation of concrete is within prospective conditions for biomass gasification processes.

3.3. Influence of concrete on the gasification process

The results presented in this Section include the average PG composition (H_2, CO, CO_2, CH_4, C_2H_4), LHV and H_2/CO molar ratio, and gasification efficiency parameters (Y_{gas}, CGE and CCE), for the experiments performed in the autothermal 80 kW_{th} pilot-scale BFB reactor and in the externally heated 3 kW_{th} bench-scale BFB

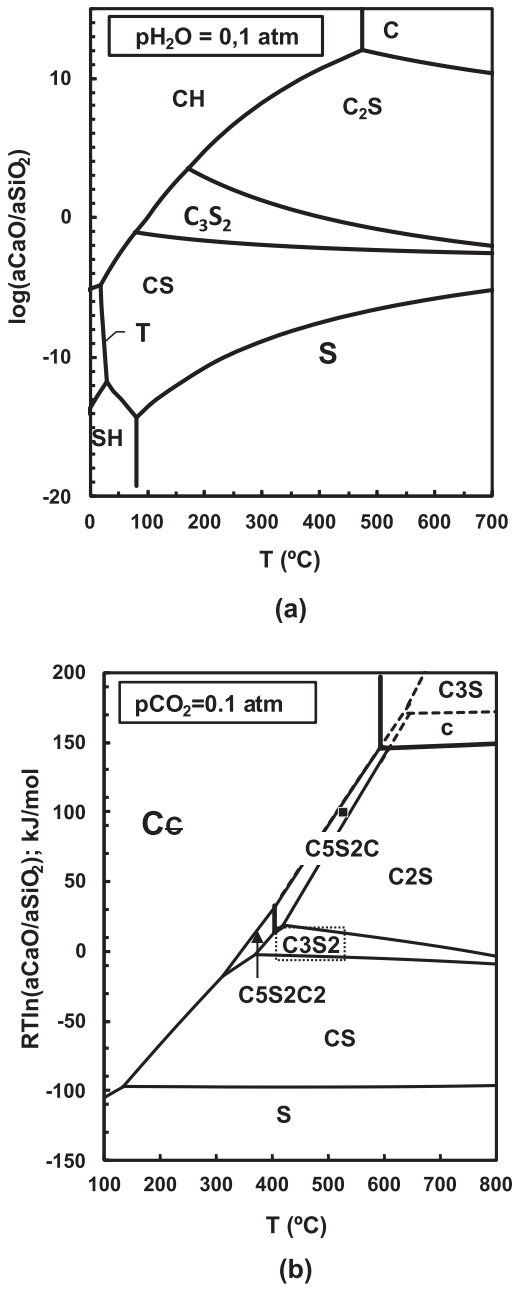

Fig. 5. Phase stability prediction for the CaO–SiO_2 system in contact with wet atmosphere (pH_2O = 0.1 atm) (a) and CO_2 atmosphere (pCO_2 = 0.1 atm) (b), using the classical notation in cement technologies, i.e., C≡CaO; S≡SiO_2; H≡H_2O and Ć≡CO_2.

reactor, with and without the in-situ application of the concrete as in-situ catalyst material for PG upgrading.

3.3.1. Influence on the composition of the PG

For the autothermal pilot-scale BFB, the highest concentration of H_2, CO and CH_4 was found for the experiment PP - Concrete 5.2 (Fig. 6 (a)), namely 16.9, 19.1 and 6.0 %v, respectively, corresponding to an average LHV of 7.5 MJ/Nm^3; these are higher values than commonly reported in the literature for direct (air) gasification of biomass in BFB reactors [39]. These values are also higher than those attained by the application of other low-costs catalyst (e.g., ashes, chars) under similar operating conditions in previous works performed by the authors [16]. Therefore, concrete promoted a relative increase of 99.2, 12.1, 19.0 and 23.8% in the concentration of H_2, CO and CH_4 and LHV (Fig. 6 (b)) respectively, in comparison with the gasification experiment performed under similar conditions but without concrete (PP – Blank C). This increase in H_2 concentration suggests that CaO significantly promoted the WGS reaction (Reaction 3) by performing CO_2 absorption, consequently pushing the reaction forward. Accordingly, the CO_2 concentration did not decrease and was maintained almost constant (relative increase of 1.2%). However, its yield improved from 12.5 to 19.8 g/kg biomass db. Thus, despite the absorption of CO_2 performed by the CaO, the CO_2 concentration and yield in the PG did not decrease possibly due to the consequent WGS reaction promotion and a potential increase in the Y_{gas} (discussed afterwards) that can be associated to both tar reforming and carbon (C-char) gasification reactions.

Since the concrete load was not located at the bottom bed of BFB reactor, but instead was placed in a fixed bed above it (Fig. 1, M3), it should not be expected significant impacts on carbon (C-char) gasification. However, the increased yield of non-condensable gases (64 g/Nm^3 increase for CO_2, CO, H_2, CH_4, C_2H_4, C_2H_6 and C_3H_8) seems too high (Fig. 7, only CO_2, CO and H_2 shown here) to be justified only by tar reforming/cracking. As the tar concentration in PG from biomass gasification in BFB reactors typically revolves around 1–30 g/Nm^3 [53,54], this would mean that even if all tar was converted to non-condensable gases, it could not be sufficient to justify the observed increase in PG yield. Therefore, additional carbon (C-char) conversion may have occurred in the fixed bed reactor containing the synthetic concrete samples, such as carbon particles entrained with the upward gas flow of the reactor or soot/coke deposited on the concrete (further discussed in Section 3.2. in terms of Y_{gas}). This needs to be studied in future works.

The highest H_2/CO molar ratio (0.88 mol·mol^{-1}) was also found for experiment PP – Concrete 5.2; this maximum value can be a direct consequence from the promotion of the WGS reaction with the application of concrete as in-situ catalytic material. This value is suitable for Fischer-Tropsch synthesis processes (minimum ratio recommended 0.6 mol·mol^{-1}), but still needs to be higher for other applications, such as dimethyl ether or methanol production, which require H_2/CO molar ratios of 1 and 2, respectively [55,56].

For the externally heated bench-scale BFB, the highest concentration of CO, H_2 and CH_4 was found for the experiments with in-situ application of concrete with 3.5 s gas-solid contact time (BP – Concrete 3.5), namely 18.2, 6.7 and 4.1 %v, respectively (Fig. 6 (a)); this represented a respective relative increase of 30.7, 45.4 and 30.2%, relative to the reference condition without concrete (BP – Blank). However, the CO_2 concentration also increased in a similar relative amount to these gaseous species, namely 15.6%. Following the same behavior, in experiment BP – Concrete 0.3, relative increases of CO, H_2, CH_4 and CO_2 of 22.0, 13.0, 26.7 and 22.5%, respectively, were found. These similar relative increases, as well as the increase of CO and CO_2, indicate that the catalyst did not have a prominent influence on CO_2 absorption or the WGS reaction (Reaction 3) during the experiments BP – Concrete 3.5 and BP – Concrete 0.3, when compared with the results observed for PP – Concrete 5.2, where CO_2 concentration only showed a slight increase and CO concentration also showed a lower increase (Fig. 6 (b)). Accordingly, the H_2/CO molar ratio in the PG during the experiments in the bench-scale reactor only showed a small increase,

carbon (C-char) gasification reactions.

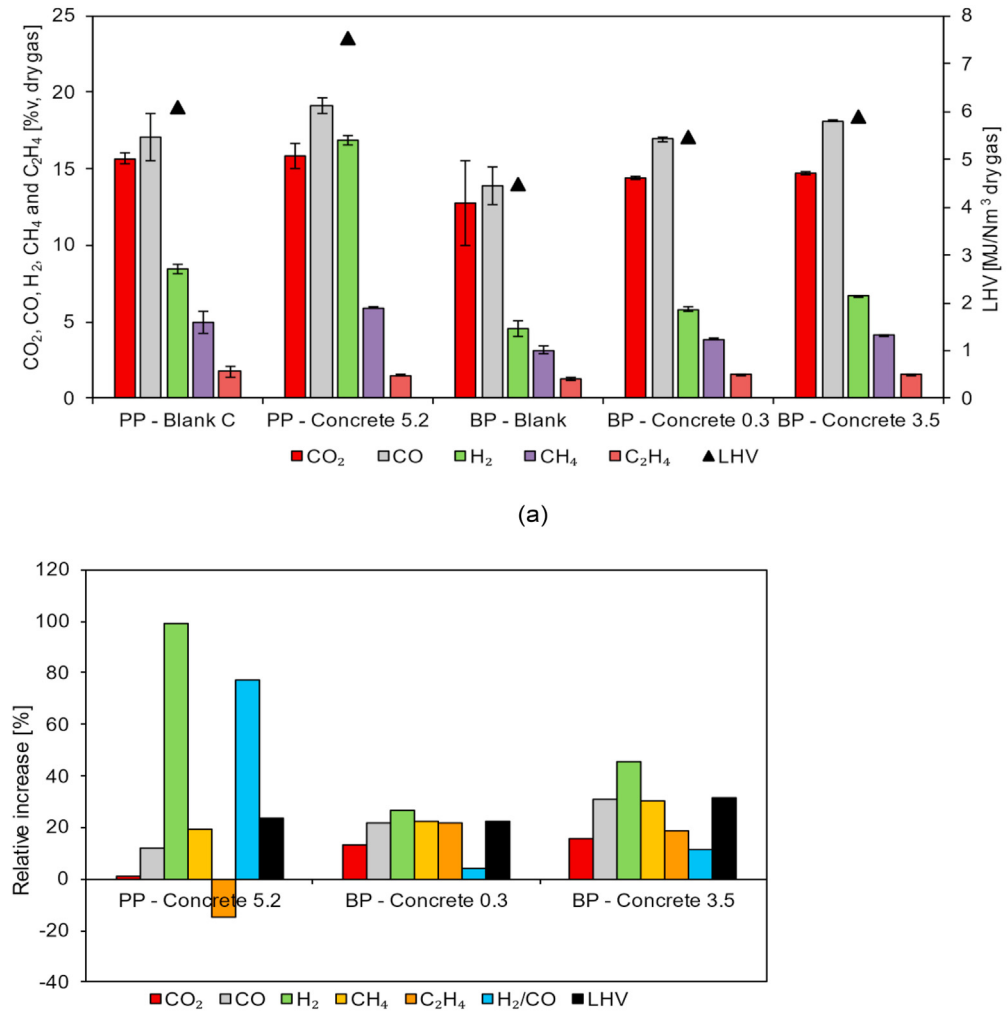

Fig. 6. Dry PG composition and LHV (a), and respective resulting relative variation of these parameters with concrete application (b), for the distinct gasification experiments performed in the pilot-scale and bench-scale fluidized bed reactors. The relative variation is expressed as a percentage increase (or decrease) of these parameters in the experiments with concrete in comparison to the experiments performed under similar operating conditions but without concrete. Experiments reference according to Table 3.

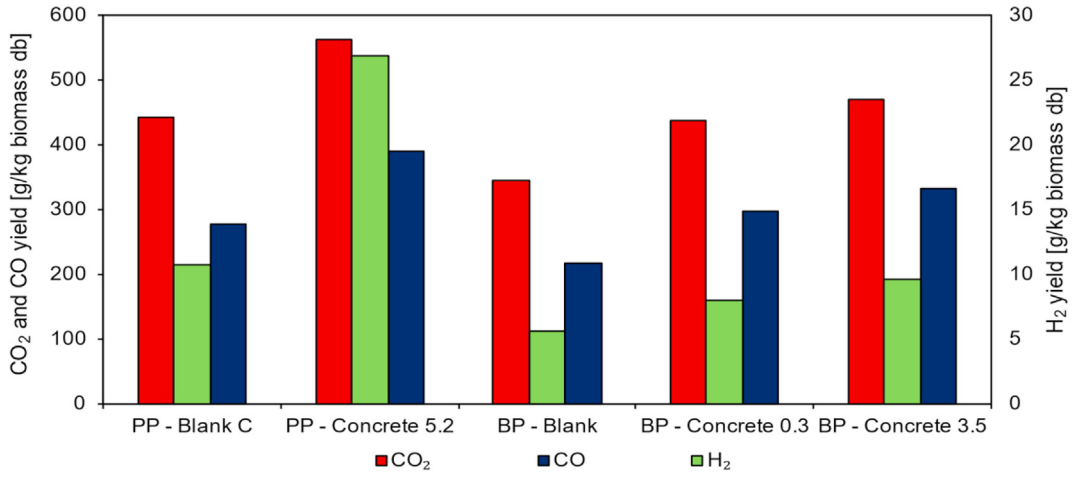

Fig. 7. CO_2, CO and H_2 yield for the distinct gasification experiments performed in the pilot-scale and bench-scale fluidized bed reactors. Experiments reference according to Table 3.

with the maximum relative increase being found for experiment BP – Concrete 3.5, namely 11.2%, when compared to the 77% relative increase of this ratio observed during the experiments made in the pilot-scale reactor.

The justification behind this distinct effect of concrete can be associated to the lower gas-solid contact time and catalyst temperature employed in the bench-scale experiments, in comparison with the experiments performed in the pilot-scale reactor (Table 3). For example, free CaO undergoes irreversible conversion to $CaCO_3$, under the actual conditions of temperature close to 600 °C (bench-scale experiments, BP Concrete 0.3 and BP Concrete 3.5) and in contact with CO_2-rich gases with CO_2:CO molar ratio above 1, as emphasized by the thermodynamic predictions (Fig. 5 (b)). Nonetheless, as the yield of non-condensable gases increased (Fig. 7), it can be inferred that concrete promoted tar reforming during the experiments performed in the bench-scale reactor, despite the lack of significant increased activity of the WGS reaction (reflected by the phenomena discussed above). Accordingly, the concrete also improved the LHV of the PG, with a maximum relative increase of 31.6% found for experiment BP – Concrete 3.5.

In summary, it seems that the influence of the concrete on the PG composition was not as strong in the experiments performed in the bench-scale reactor as in the pilot-scale reactor, particularly regarding the increase in H_2 concentration and the WGS reaction occurrence. This seems to be mainly justified by the lower gas-solid contact time and catalyst temperature employed in this smaller-scale reactor (Table 3). Nevertheless, it must be noted that these reactive systems have inherent distinct operating conditions, thus hindering direct comparisons, which are not the purpose of this work. For example, the bench-scale BFB operates with a lower fluidization velocity (Section 2.3.) and has a higher decay of temperature along the reactor height than the pilot-scale gasifier (Fig. 8), and this is relevant because the forward WGS reaction (consumption of CO and production of H_2) is exothermic and mainly active at temperatures lower than 700 °C [57], among other aspects.

Furthermore, due to the lower dimension and distinct configuration of the bench-scale BFB, an increase in the contact time between the PG and the catalyst led to a decrease of the catalyst average temperature (Table 3), as evidenced by the temperature profile of the reactor (Fig. 8 (a)), thus constituting a trade-off between these parameters. This contrasts with the autothermal pilot-scale BFB, where it is possible to employ high gas-solid contact times at temperatures closer to the reactor bottom bed (Fig. 8 (b)). Therefore, it seems that a high gas-solid contact time (e.g., 5.2 s) and a high catalyst temperature (e.g., 740 °C) is beneficial for the application of concrete as in-situ catalyst, particularly regarding WGS activity and consequent increase of the H_2/CO molar ratio in the PG.

3.3.2. Influence on the gasification efficiency parameters

Fig. 9 (a) shows the efficiency parameters (Y_{gas}, CGE and CCE) determined for the distinct gasification experiments performed. For the pilot-scale BFB reactor, a maximum Y_{gas} of 1.8 Nm^3 dry gas/kg biomass db, CGE of 74.8 and CCE of 90.3% was found for PP – Concrete 5.2. In terms of the literature concerning direct (air) biomass gasification in BFBs, the Y_{gas} is in the medium range and the CGE/CCE in the upper range [39]. These latter are also higher than the values found by the authors in previous works for the

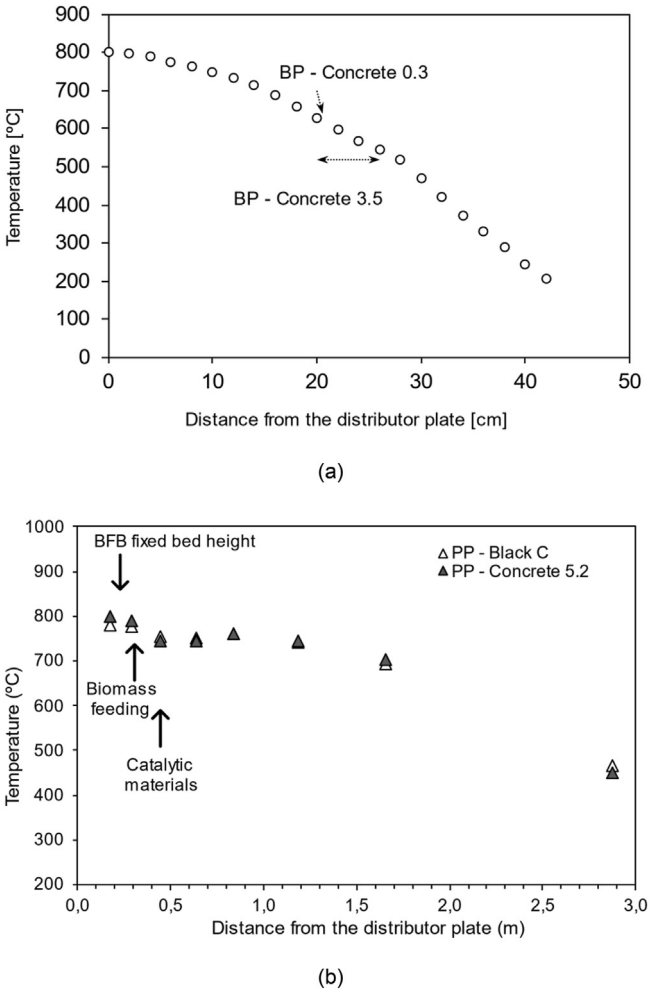

Fig. 8. Average vertical temperature profile in the externally heated bench-scale BFB reactor (a) and autothermal pilot-scale BFB reactor (b). Experiments reference according to Table 3.

application of other low-cost catalysts (e.g., ashes, chars) under similar operating conditions [16]. In terms of comparison with the blank experiment (PP – Blank C), performed under the same operating conditions, relative increases of 25.1, 54.4 and 33.9% were found for the Y_{gas}, CGE and CCE (Fig. 9 (b)), respectively. This indicates the positive influence of concrete on tar reforming/cracking reactions. However, as the increase of Y_{gas} and CCE, namely from 1.4 to 1.8 Nm^3 dry gas/kg biomass db and 67.4–90.3%, respectively, seems to be too high to be caused only by tar destruction, some additional carbon conversion must also have been promoted by this catalytic material, as previously discussed regarding the increase of the non-condensable gases yields (Section 3.4.1, Fig. 7); this needs to be further assessed in future works. For the externally heated bench-scale BFB reactor, the highest relative increases of Y_{gas}, CGE and CCE were found for the experiment BP – Concrete 3.5, namely 18.0, 55.3 and 47.0%, respectively. For BP – Concrete 0.3, the relative increases were lower, which can be associated to the lower gas-solid contact time.

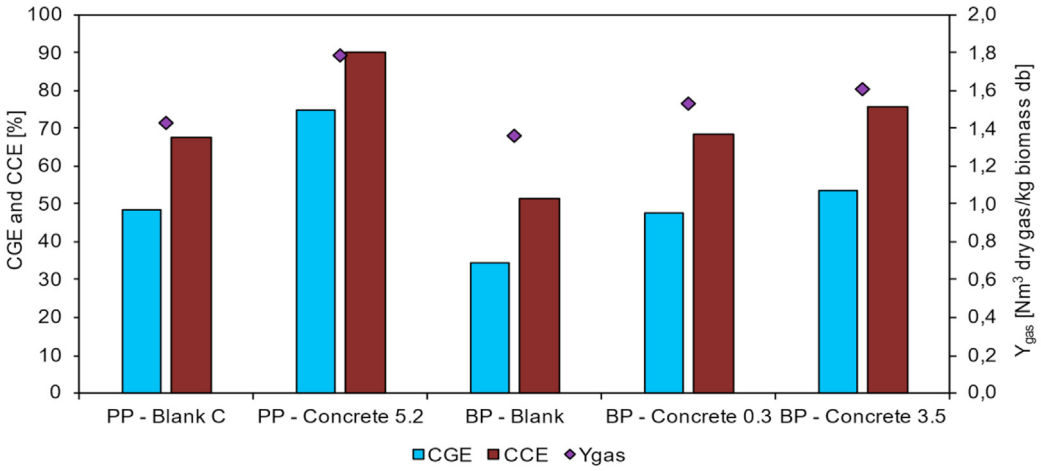

(a)

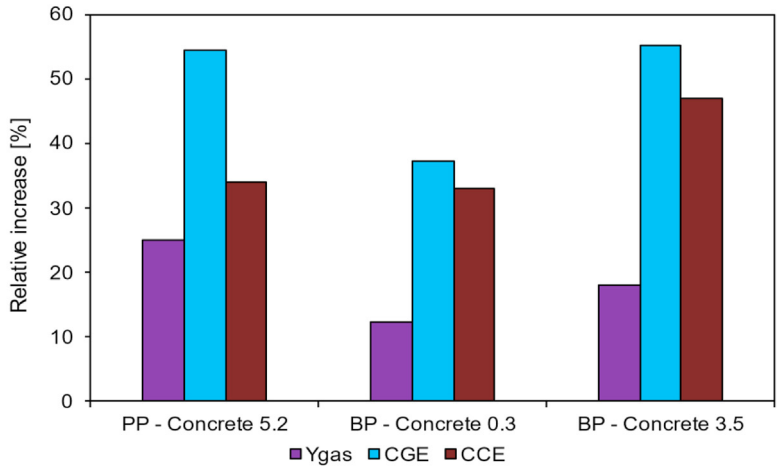

(b)

Fig. 9. Y_{gas}, CGE and CCE (a), and respective resulting relative variation of these parameters with concrete application (b), for the distinct gasification experiments performed in the pilot-scale and bench-scale fluidized bed reactors. The relative variation is expressed as a percentage increase (or decrease) of these parameters in the experiments with concrete in comparison to the experiments performed under similar operating conditions but without concrete. Experiments reference according to Table 3.

3.4. Post-mortem characterization of the catalytic concrete load

The catalytic concrete load was collected after the gasification experiments in the bench-scale reactor for post-mortem analysis by X-Ray diffraction and by FTIR spectroscopy. Differences in X-ray diffractograms before and after gasification emphasize extinction of reflections ascribed to hydrated phases, and changes in the relative intensity of carbonated phases (Fig. 3), possibly combined with structural changes, such as onset of different polymorphs of calcium carbonate (e.g., aragonite polymorph). This is consistent with carbonation/decarbonation changes under the experimental conditions of gasification, from about 585 °C in bench-scale externally heated BFB to 746 °C in the pilot-scale autothermal BFB (Table 3).

The FTIR spectrum (Fig. 10) shows clear evidence of carbonated species, revealed by bands at ~1426 cm^{-1}, ascribed to carbonate group stretching, and ~875 cm^{-1}, ascribed to out of lane C—O bending vibration [58]. The peak at ~669 cm^{-1} is also close to the in-plane bending band (~712 cm^{-1}) or traces of carbonate-sulphate phases such as thaumasite, which may also be present in cement products [59]. In addition, the CO_2 double peak at (~2358 cm^{-1}) indicates CO_2 adsorption ability, by analogy with other materials with reversible CO_2 adsorption for CO_2 capture [60]. On the contrary, it could not be traced any evidence of adsorbed H_2O molecules or bending of OH groups expected for hydrated phases at ~1640 cm^{-1}; this confirms that ready decomposition of previous hydrated phases occurred under the operating conditions of the gasification experiments.

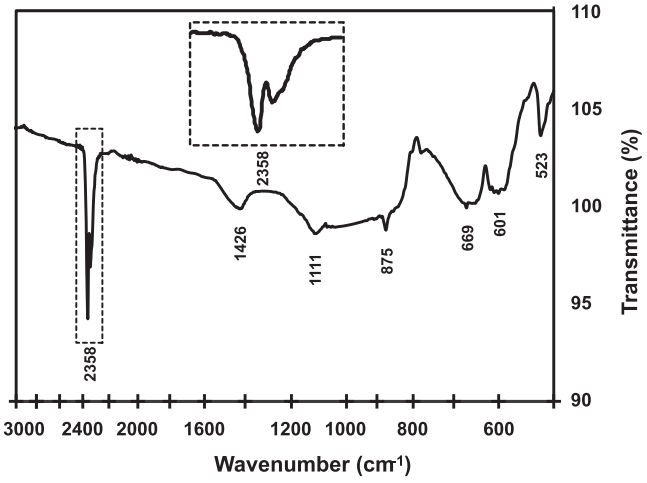

Fig. 10. FTIR spectrum of the concrete load after the gasification experiment performed in the bench-scale reactor.

4. Conclusions

In this work, in-situ application of synthetic concrete for the improvement of the PG quality from biomass gasification was successfully performed in an 80 kW_{th} pilot-scale BFB reactor and 3 kW_{th} bench-scale BFB reactor. The study focused on the improvement of the PG quality in terms of combustible gases yield, particularly H_2 concentration increase, and associated process efficiency parameters.

For the highest gas-solid contact time (5.2 s) and catalyst temperature (746 °C) employed in the gasification experiments (autothermal pilot-scale BFB), the concrete allowed a significant relative increase of H_2 concentration and H_2/CO molar ratio in the PG, namely up to 99.2 and 77.4%, respectively, indicating the capacity of this material to promote the WGS reaction. This can be justified by the ability of free CaO to absorb CO_2, consequently pushing the WGS reaction towards the production of H_2. Simultaneous increase of the LHV of the PG (up to 31.6%, maximum of 7.5 MJ/Nm^3) indicates that the concrete also promoted tar reforming/cracking and carbon gasification reactions, in addition to the WGS reaction. For lower gas-solid contact times (0.3–3.5 s) and relatively low catalyst temperatures (585–620 °C) (externally heated bench-scale BFB), the H_2/CO molar ratio did not show significant increases, indicating that this material did not significantly promoted the WGS reaction under these operating conditions. In part, this can be associated to the free CaO undergoing irreversible conversion to $CaCO_3$ under these circumstances. Nonetheless, the LHV of the PG still increased in similar amounts, consequently indicating that higher gas-solid contact times and catalyst temperature are mainly required for the promotion of the WGS reaction, rather than tar reforming/cracking or carbon gasification reactions.

Regarding the process efficiency parameters, maximum relative increases of 25.1, 55.3 and 47.0% for Y_{gas}, CGE and CCE, respectively, were found. This further indicates the concrete capacity to promote tar reforming/cracking and carbon gasification reactions.

Further work must be performed to fully quantify the effect of the developed synthetic concrete samples, and real concrete wastes from the construction industry, on tar destruction and PG composition, and to determine the influence of long operation times on the decay of the catalytic activity of these solid materials.

Credit author statement

Daniel Torrão Pio (D.T. Pio): Conceptualization, Methodology, Investigation, Formal analysis, Visualization, Validation, Writing – original draft, Writing – review & editing. Helena Gil Martins de Faria Gomes (H.G.M.F. Gomes): Investigation, Visualization, Validation. Luís Carlos Marques Ruivo (L.C.M. Ruivo): Investigation, Validation. Manuel Arlindo Amador de Matos (M.A.A. Matos): Methodology, Supervision. José Filipe Monteiro (J.F. Monteiro): Investigation. Jorge Ribeiro Frade (J.R. Frade): Conceptualization, Writing – review & editing. Luís António da Cruz Tarelho (L.A.C. Tarelho): Conceptualization, Methodology, Formal analysis, Writing – review & editing, Supervision, Project administration.

Declaration of competing interest

The authors declare that they have no known competing financial interests or personal relationships that could have appeared to influence the work reported in this paper.

Acknowledgements

It is acknowledged the financial support from projects NOTARGAS (ref. POCI-01-0145-FEDER-030661), Inpactus – innovative products and technologies from eucalyptus, Project N.° 21874 funded by Portugal 2020 through European Regional Development Fund (ERDF) in the frame of COMPETE 2020 n°246/AXIS II/2017 and SusPhotoSolutions – Soluções Fotovoltaicas Sustentáveis, PO Centro 2020 (ref. CENTRO-01-0145-FEDER-000005). Thanks are also due to the Portuguese Foundation for Science and Technology/Ministry of Science, Technology and Higher Education for the financial support to CESAM (UIDP/50017/2020+UIDB/50017/2020), CICECO (UIDB/50011/2020 & UIDP/50011/2020), through national funds, and PhD grants (PhD grant ref. PD/BDE/128620/2017 (D.T. Pio), PhD grant ref. BIM – INPACTUS/BR07/UA/07-01-2018 (H G M.F. Gomes) and PhD grant ref. SFRH/BD/129901/2017 (L C M. Ruivo)).

References

[1] Pio DT, Tarelho LAC, Tavares AMA, Matos MAA, Silva V. Co-gasification of refused derived fuel and biomass in a pilot-scale bubbling fluidized bed reactor. Energy Convers Manag 2020;206. https://doi.org/10.1016/j.enconman.2020.112476.
[2] Viswanathan K, Ashok B, Pugazhendhi A. Comprehensive study of engine characteristics of novel biodiesel from curry leaf (Murraya koenigii) oil in ceramic layered diesel engine. Fuel 2020;280:118586. https://doi.org/10.1016/j.fuel.2020.118586.
[3] Demirbas A. Biorefineries: for biomass upgrading facilities. Green Energy Technol 2010;26:240. https://doi.org/10.1007/978-1-84882-721-9.
[4] Pio DT, Tarelho LAC, Pinto PCR. Gasification-based biorefinery integration in the pulp and paper industry: a critical review. Renew Sustain Energy Rev 2020;133:110210. https://doi.org/10.1016/j.rser.2020.110210.
[5] Yan J, Sun R, Shen L, Bai H, Jiang S, Xiao Y, et al. Hydrogen-rich syngas production with tar elimination via biomass chemical looping gasification (BCLG) using BaFe2O4/Al2O3 as oxygen carrier. Chem Eng J 2020;387:124107. https://doi.org/10.1016/j.cej.2020.124107.
[6] Pio DT, Tarelho LAC. Empirical and chemical equilibrium modelling for prediction of biomass gasification products in bubbling fluidized beds. Energy 2020;202:117654. https://doi.org/10.1016/j.energy.2020.117654.
[7] Sikarwar VS, Zhao M, Fennell PS, Shah N, Anthony EJ. Progress in biofuel production from gasification. Prog Energy Combust Sci 2017;61:189–248. https://doi.org/10.1016/j.pecs.2017.04.001.
[8] Sikarwar VS, Zhao M, Clough P, Yao J, Zhong X, Memon MZ, et al. An overview of advances in biomass gasification. Energy Environ Sci 2016;9:2939–77. https://doi.org/10.1039/c6ee00935b.
[9] Heidenreich S, Foscolo PU. New concepts in biomass gasification. Prog Energy Combust Sci 2015;46:72–95. https://doi.org/10.1016/j.pecs.2014.06.002.
[10] Pio DT, Tarelho LAC. Industrial gasification systems (>3 MWth) for bioenergy in Europe: current status and future perspectives. Renew Sustain Energy Rev 2021;145:111108. https://doi.org/10.1016/j.rser.2021.111108.
[11] He Q, Guo Q, Umeki K, Ding L, Wang F, Yu G. Soot formation during biomass gasification: a critical review. Renew Sustain Energy Rev 2021;139:110710. https://doi.org/10.1016/j.rser.2021.110710.

[12] D'Anna A, Sirignano M. Detailed kinetic mechanisms of PAH and soot formation. Comput Aided Chem Eng 2019;45:647–72. https://doi.org/10.1016/B978-0-444-64087-1.00012-7.
[13] Wijayanta AT, Saiful Alam M, Nakaso K, Fukai J, Shimizu M. Optimized combustion of biomass volatiles by varying O 2 and CO 2 levels: a numerical simulation using a highly detailed soot formation reaction mechanism. Bioresour Technol 2012;110:645–51. https://doi.org/10.1016/j.biortech.2012.01.068.
[14] Pio DT, Ruivo LCM, Tarelho LAC, Frade JR, Kantarelis E, Engvall K. Tar formation during eucalyptus gasification in a bubbling fluidized bed reactor: effect of feedstock and reactor bed composition. Energy Convers Manag 2021;229:113749. https://doi.org/10.1016/j.enconman.2020.113749.
[15] Devi L, Ptasinski KJ, Janssen FJJG. A review of the primary measures for tar elimination in biomass gasification processes. Biomass Bioenergy 2003;24:125–40. https://doi.org/10.1016/S0961-9534(02)00102-2.
[16] Pio DT, Tarelho LAC, Pinto RG, Matos MAA, Frade JR, Yaremchenko A, et al. Low-cost catalysts for in-situ improvement of producer gas quality during direct gasification of biomass. Energy 2018;165:442–54. https://doi.org/10.1016/j.energy.2018.09.119.
[17] Basu P. Biomass gasification, pyrolysis and torrefaction: practical design and theory. 2013. https://doi.org/10.1016/C2011-0-07564-6.
[18] Islam MW. A review of dolomite catalyst for biomass gasification tar removal. Fuel 2020;267:117095. https://doi.org/10.1016/j.fuel.2020.117095.
[19] Cortazar M, Lopez G, Alvarez J, Amutio M, Bilbao J, Olazar M. Behaviour of primary catalysts in the biomass steam gasification in a fountain confined spouted bed. Fuel 2019;253:1446–56. https://doi.org/10.1016/j.fuel.2019.05.094.
[20] Zhou C, Rosén C, Engvall K. Fragmentation of dolomite bed material at elevated temperature in the presence of H2O & CO2: implications for fluidized bed gasification. Fuel 2020;260:116340. https://doi.org/10.1016/j.fuel.2019.116340.
[21] Fuchs J, Schmid JC, Müller S, Hofbauer H. Dual fluidized bed gasification of biomass with selective carbon dioxide removal and limestone as bed material: a review. Renew Sustain Energy Rev 2019;107:212–31. https://doi.org/10.1016/j.rser.2019.03.013.
[22] Hamad MA, Radwan AM, Heggo DA, Moustafa T. Hydrogen rich gas production from catalytic gasification of biomass. Renew Energy 2016;85:1290–300. https://doi.org/10.1016/j.renene.2015.07.082.
[23] Abu El-Rub Z, Bramer EA, Brem G. Review of catalysts for tar elimination in biomass gasification processes. Ind Eng Chem Res 2004;43:6911–9. https://doi.org/10.1021/ie0498403.
[24] Chai Y, Gao N, Wang M, Wu C. H2 production from co-pyrolysis/gasification of waste plastics and biomass under novel catalyst Ni-CaO-C. Chem Eng J 2020;382:122947. https://doi.org/10.1016/j.cej.2019.122947.
[25] Nam H, Wang S, Sanjeev KC, Seo MW, Adhikari S, Shakya R, et al. Enriched hydrogen production over air and air-steam fluidized bed gasification in a bubbling fluidized bed reactor with CaO: effects of biomass and bed material catalyst. Energy Convers Manag 2020;225:113408. https://doi.org/10.1016/j.enconman.2020.113408.
[26] Udomsirichakorn J, Salam PA. Review of hydrogen-enriched gas production from steam gasification of biomass: the prospect of CaO-based chemical looping gasification. Renew Sustain Energy Rev 2014;30:565–79. https://doi.org/10.1016/j.rser.2013.10.013.
[27] Zhou C, Stuermer T, Gunarathne R, Yang W, Blasiak W. Effect of calcium oxide on high-temperature steam gasification of municipal solid waste. Fuel 2014;122:36–46. https://doi.org/10.1016/j.fuel.2014.01.029.
[28] Udomsirichakorn J, Basu P, Salam PA, Acharya B. Effect of CaO on tar reforming to hydrogen-enriched gas with in-process CO2 capture in a bubbling fluidized bed biomass steam gasifier. Int J Hydrogen Energy 2013;38:14495–504. https://doi.org/10.1016/j.ijhydene.2013.09.055.
[29] Jordan CA, Akay G. Effect of CaO on tar production and dew point depression during gasification of fuel cane bagasse in a novel downdraft gasifier. Fuel Process Technol 2013;106:654–60. https://doi.org/10.1016/j.fuproc.2012.09.061.
[30] Valderrama Rios ML, González AM, Lora EES, Almazán del Olmo OA. Reduction of tar generated during biomass gasification: a review. Biomass Bioenergy 2018;108:345–70. https://doi.org/10.1016/j.biombioe.2017.12.002.
[31] Abdoulmoumine N, Adhikari S, Kulkarni A, Chattanathan S. A review on biomass gasification syngas cleanup. Appl Energy 2015;155:294–307. https://doi.org/10.1016/j.apenergy.2015.05.095.
[32] Poulikakos LD, Papadaskalopoulou C, Hofko B, Gschösser F, Cannone Falchetto A, Bueno M, et al. Harvesting the unexplored potential of European waste materials for road construction. Resour Conserv Recycl 2017;116:32–44. https://doi.org/10.1016/j.resconrec.2016.09.008.
[33] Vieira L de BP, de Figueiredo AD, Moriggi T, John VM. Waste generation from the production of ready-mixed concrete. Waste Manag 2019;94:146–52. https://doi.org/10.1016/j.wasman.2019.05.043.
[34] Lee T, Jang SH, Jung S, Kim S, Park YK, Moon DH, et al. CO2 effects on catalytic pyrolysis of yard trimming over concrete waste. Chem Eng J 2020;396:125331. https://doi.org/10.1016/j.cej.2020.125331.
[35] Qin L, Gao X. Recycling of waste autoclaved aerated concrete powder in Portland cement by accelerated carbonation. Waste Manag 2019;89:254–64. https://doi.org/10.1016/j.wasman.2019.04.018.
[36] Bahij S, Omary S, Feugeas F, Faqiri A. Fresh and hardened properties of concrete containing different forms of plastic waste – a review. Waste Manag 2020;113:157–75. https://doi.org/10.1016/j.wasman.2020.05.048.
[37] Berrueco C, Montané D, Matas Güell B, del Alamo G. Effect of temperature and dolomite on tar formation during gasification of torrefied biomass in a pressurized fluidized bed. Energy 2014;66:849–59. https://doi.org/10.1016/j.energy.2013.12.035.
[38] Instituto da Conservação da Natureza e das Florestas (ICNF). Perfil Florestal - Portugal. 2018. p. 1–4.
[39] Pio DT, Tarelho LAC, Matos MAA. Characteristics of the gas produced during biomass direct gasification in an autothermal pilot-scale bubbling fluidized bed reactor. Energy 2017;120:915–28. https://doi.org/10.1016/j.energy.2016.11.145.
[40] CEN/TS 15148 Solid biofuels. Method for the determination of the content of volatile matter. 2005.
[41] CEN/TS 14775 Solid biofuels. Method for the determination of ash content. 2004.
[42] CEN/TS 14774-1 Solid biofuels. Methods for determination of moisture content - oven dry method - Part 1: total moisture - reference method. 2004.
[43] Parikh J, Channiwala SA, Ghosal GK. A correlation for calculating HHV from proximate analysis of solid fuels. Fuel 2005;84:487–94. https://doi.org/10.1016/j.fuel.2004.10.010.
[44] Yokokawa H, Kawada T, Dokiya M. Construction of chemical potential diagrams for metal-metal-nonmetal systems: applications to the decomposition of double oxides. J Am Ceram Soc 1989;72:2104–10. https://doi.org/10.1111/j.1151-2916.1989.tb06039.x.
[45] Yokokawa H. Generalized chemical potential diagram and its applications to chemical reactions at interfaces between dissimilar materials. J Phase Equil 1999;20:258–87. https://doi.org/10.1361/105497199770335794.
[46] Brandão A, Monteiro JF, Kovalevsky AV, Fagg DP, Kharton VV, Frade JR. Guidelines for improving resistance to CO2 of materials for solid state electrochemical systems. Solid State Ionics 2011;192:16–20. https://doi.org/10.1016/j.ssi.2010.02.006.
[47] Pio DT, Gomes HGMF, Tarelho LAC, Ruivo LCM, Matos MAA, Pinto RG, et al. Ilmenite as low-cost catalyst for producer gas quality improvement from a biomass pilot-scale gasifier. Energy Rep 2020;6:325–30. https://doi.org/10.1016/j.egyr.2019.08.063.
[48] Hervy M, Remy D, Dufour A, Mauviel G. Air-blown gasification of Solid Recovered Fuels (SRFs) in lab-scale bubbling fluidized-bed: influence of the operating conditions and of the SRF composition. Energy Convers Manag 2019;181:584–92. https://doi.org/10.1016/j.enconman.2018.12.052.
[49] Waldheim L, Nilsson T. Heating value of gases from biomass gasification. 2001.
[50] Guo X, Shi H, Dick WA. Compressive strength and microstructural characteristics of class C fly ash geopolymer. Cement Concr Compos 2010;32:142–7. https://doi.org/10.1016/j.cemconcomp.2009.11.003.
[51] Skocek J, Zajac M, Ben Haha M. Carbon Capture and Utilization by mineralization of cement pastes derived from recycled concrete. Sci Rep 2020;10:1–12. https://doi.org/10.1038/s41598-020-62503-z.
[52] Karunadasa KSP, Manoratne CH, Pitawala HMTGA, Rajapakse RMG. Thermal decomposition of calcium carbonate (calcite polymorph) as examined by in-situ high-temperature X-ray powder diffraction. J Phys Chem Solid 2019;134:21–8. https://doi.org/10.1016/j.jpcs.2019.05.023.
[53] Milne T a, Evans RJ, Abatzoglou N. Biomass gasifier "tars": their nature. Formation, and Conversion; 1998. https://doi.org/10.2172/3726.
[54] Heidenreich S, Müller M, Foscolo PU. Advanced biomass gasification. Elsevier; 2016. https://doi.org/10.1016/C2015-0-01777-4.
[55] Ciferno JP, Marano JJ. Benchmarking biomass gasification technologies for fuels, chemicals and hydrogen production. 2002.
[56] Clausen LR, Elmegaard B, Houbak N. Design of novel DME/methanol synthesis plants based on gasification of biomass. 2011.
[57] Wang T, Stiegel G. Integrated gasification combined cycle (IGCC) technologies. Elsevier Inc.; 2016. https://doi.org/10.1016/c2014-0-00849-0.
[58] Gunasekaran S, Anbalagan G. Spectroscopic study of phase transitions in natural calcite mineral. Spectrochim Acta Part A Mol Biomol Spectrosc 2008;69:1246–51. https://doi.org/10.1016/j.saa.2007.06.036.
[59] Collett G, Crammond NJ, Swamy RN, Sharp JH. The role of carbon dioxide in the formation of thaumasite. Cement Concr Res 2004;34:1599–612. https://doi.org/10.1016/j.cemconres.2004.02.024.
[60] Coenen K, Gallucci F, Mezari B, Hensen E, van Sint Annaland M. An in-situ IR study on the adsorption of CO2 and H2O on hydrotalcites. J CO2 Util 2018;24:228–39. https://doi.org/10.1016/j.jcou.2018.01.008.

Ceramics International 48 (2022) 34025–34032

Contents lists available at ScienceDirect

Ceramics International

journal homepage: www.elsevier.com/locate/ceramint

Solid state synthesis of $Ca_2Fe_2O_5$ by reactive firing of calcite and siderite

I. Antunes [a,*], L.C.M. Ruivo [a,b], L.A.C. Tarelho [b], A.A. Yaremchenko [a], J.R. Frade [a]

[a] Department of Materials and Ceramic Engineering, CICECO – Aveiro Institute of Materials, University of Aveiro, 3810-193, Aveiro, Portugal
[b] Department of Environment and Planning, CESAM – Centre for Environmental and Marine Studies, University of Aveiro, 3810-193, Aveiro, Portugal

ARTICLE INFO

Keywords:
Brownmillerite
Siderite
Thermodynamic modelling
Redox buffer

ABSTRACT

The brownmillerite phase $Ca_2Fe_2O_5$ was processed by the reactive firing of calcite and a natural siderite for prospective catalytic applications. Thermogravimetry and X-ray diffraction (XRD) was used to monitor the decomposition of precursors and its dependence on heating rate and atmosphere. Taguchi planning was used to assess the impact of firing temperature, time, and rate of heating on the conversion of precursors reflected by $I_{(121)_{sp}} : I_{(121)_b}$ peak intensity ratio of main XRD reflections of secondary spinel phase $CaFe_2O_4$ and brownmillerite. The onset of additional minor phases ($Ca_2Al_2SiO_7$ and Ca_2SiO_4) was ascribed to the reaction of a fraction of calcia with gangue components of the siderite precursor. Thermodynamic modelling was used as a guideline for synthesis in non-oxidising conditions to hinder the onset of $CaFe_2O_4$. These guidelines allowed one to obtain high conversion to $Ca_2Fe_2O_5$ with enhanced crystallinity at 700 °C, in an inert Ar atmosphere. Faster reactivity at T ≥ 800 °C in this oxygen-lean atmosphere, leads to highly crystalline $Ca_2Fe_2O_5$ coexisting with the onset of wustite and/or metallic Fe, which account for the oxygen balance, and calcium silicates, by reaction of calcia with silica.

1. Introduction

$Ca_2Fe_2O_5$ has been proposed as a cost-effective material for alternative energy technologies such as the production of renewable synthetic fuels [1], oxygen storage materials for chemical looping [2,3], catalysts for lignocellulosic biomass [4] or coal [5] gasification or related redox processes. Its brownmillerite structure $A_2B_2O_5$ may be related to the corresponding oxygen-deficient perovskite $ABO_{3-\delta}$ by ordering the oxygen vacancies and combining cations in tetrahedral and octahedral coordinations. These structural features combined with a wide redox stability range of $Ca_2Fe_2O_5$ and its tolerance to structural changes and phase transformations contribute to the demonstrated catalytic performance.

Processing of single-phase $Ca_2Fe_2O_5$ by solid state reaction of common and low-cost precursors (Fe_2O_3 + $CaCO_3$ mixtures) requires relatively high temperatures, often above 1000 °C [6], and much above the lower temperature limit determined by thermodynamic equilibrium:

$$\Delta G_R + RTln(pCO_2) = 0 \quad (1)$$

where the Gibbs free energy of reaction

$$2\ CaCO_3 + Fe_2O_3 \rightarrow 2\ CO_2 + Ca_2Fe_2O_5 \quad (2)$$

was calculated as $\Delta G_R \approx 77.7 - 0.1034T(\mathrm{K}) + 8.85{\cdot}10^{-6}T(\mathrm{K})^2$ as shown in Fig. 1. Thus, the onset of reactivity should be expected from T > 807 K (= 514 °C), even in contact with a CO_2-rich atmosphere, converging to $pCO_2 \approx 1atm$ and $\Delta G_R \approx 0$. Kinetic limitations may be due to sluggish diffusion control, mainly for relatively coarse reactant powders, and/or insufficient homogeneity of the reactants mixture; this may explain the use of several calcination steps with intermediate regrindings [6] or preliminar activation of reactants by high energy milling [7]. Other authors proposed alternative methods to process $Ca_2Fe_2O_5$ based catalysts, often based on expensive precursors or complex methods, such as the nitrate-glycine method [8] or sol-gel [3,9]. These methods may jeopardise their applicability in technologies with limited economic feasibility, such as biomass gasification.

$Ca_2Fe_2O_5$ may also form readily by solid state reaction between calcia and partially reduced Fe oxides (e.g., wustite), yielding FeO/$Ca_2Fe_2O_5$/CaO multilayers [10]. The dynamics of sinter ore [11] confirms that the divalent oxide (wustite) promotes the formation of $Ca_2Fe_2O_5$ relative to magnetite or hematite. Though one cannot confirm the redox conditions of the sinter ore, these conditions are likely to deviate significantly from the effective stability range of wustite, taking into account that the valence state evolves from divalent (Fe^{2+}) in wustite, to trivalent (Fe^{3+}) in the brownmillerite. In addition, solid state reaction may be promoted by the deviations from equilibrium. Those

* Corresponding author.
E-mail address: isabel.antunes@ua.pt (I. Antunes).

https://doi.org/10.1016/j.ceramint.2022.08.002
Received 26 February 2022; Received in revised form 16 July 2022; Accepted 1 August 2022
Available online 7 August 2022

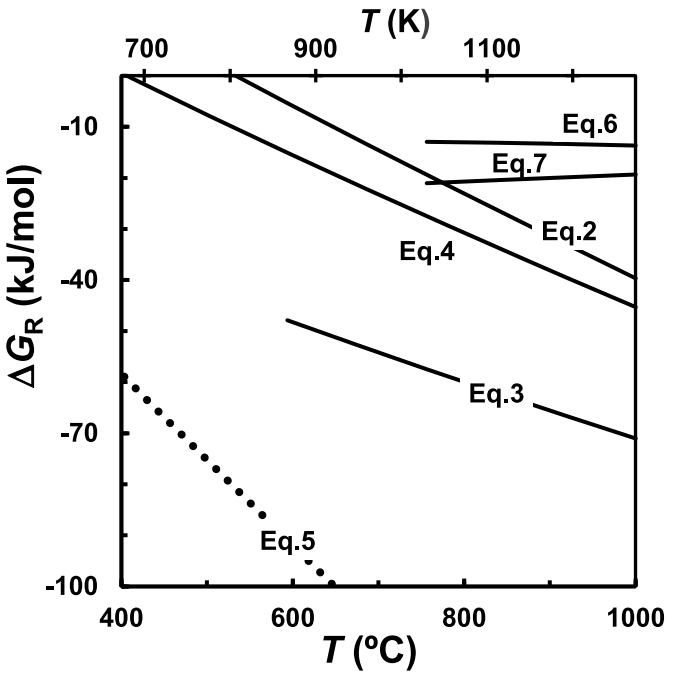

Fig. 1. Gibbs free energy of reactions of synthesis of $Ca_2Fe_2O_5$ from alternative oxide or carbonate precursors (Eqs. (2)–(7)).

authors demonstrated that reaction with hematite is more likely to induce the formation of $CaFe_2O_4$ and/or $CaFe_3O_5$ as intermediate phases. In addition, thermodynamic predictions of the overall reactions indicate more favourable conditions for reactivity between calcite and wustite (Eq. (3)) when compared with corresponding reactions with hematite (Eq. (2)) or with magnetite (Eq. (4)), as also shown in Fig. 1.

$$2\ CaCO_3 + 2\ FeO + 0.5\ O_2 \rightarrow 2\ CO_2 + Ca_2Fe_2O_5 \quad (3)$$

$$2\ CaCO_3 + 2/3\ Fe_3O_4 + 1/6\ O_2 \rightarrow 2\ CO_2 + Ca_2Fe_2O_5 \quad (4)$$

The proposed kinetic mechanism for the reaction of calcite with wustite was related to the diffusion of Ca^{2+} into the wustite precursor and mixed transport (Fe^{3+} and $h^{\bullet}$) in the brownmillerite layer [10], yielding a $\sim 3\ \mu m$ thick $Ca_2Fe_2O_5$ layer after 1 h at 1273 K. The estimated diffusivity of Fe^{3+} was $\sim 6 \times 10^{-8}$ cm^2/s.

Thus, the main purpose of this work was to demonstrate the feasibility of processing from natural minerals such as siderite, with ideal composition $FeCO_3$, and calcite ($CaCO_3$) as follows:

$$2\ CaCO_3 + 2\ FeCO_3 + 0.5\ O_2 \rightarrow 4\ CO_2 + Ca_2Fe_2O_5 \quad (5)$$

Note that $FeCO_3$ is an uncommon mineral with divalent oxidation state (Fe^{2+}), raising prospects for enhanced reactivity, as predicted also by thermodynamic predictions (Fig. 1).

Eq. (5) relies on the assumption that synthesis of the brownmillerite phase occurs before decomposition of carbonate precursors; this is unlikely, at least in what concerns $FeCO_3$, which may yield hematite in oxidising conditions or partially reduced oxides in non-oxidising atmospheres. Thus, the main potential advantages of siderite as an alternative precursor may rely on its oxidation state and ability to control its decomposition to adjust the oxidation, structure and microstructural features of the intermediate iron oxides, with impact on subsequent reactions.

Eqs. (2)-(4) also assume that synthesis of the browmillerite occurs before the previous decomposition of the calcite precursor; this may also be delayed by kinetic limitations, such as diffusion control across the reaction products. Thus, one may also consider preceding decomposition of both carbonate precursors before reactions between calcia and iron oxides:

$$2\ CaO + Fe_2O_3 \rightarrow Ca_2Fe_2O_5 \quad (6)$$

$$2\ CaO + 2/3\ Fe_3O_4 + 1/6\ O_2 \rightarrow Ca_2Fe_2O_5 \quad (7)$$

Thermodynamic predictions (Fig. 1) show that these reactions are less favourable than the corresponding reactions with calcite.

One also intended to assess the impact of typical gangue components of the siderite precursor, taking into account that phase purity and composition of natural siderites usually deviate from the nominal composition $FeCO_3$ depending on their origin in the natural environment [12] and subsequent transformations [13]. Significant fractions of silica, alumina and alkaline-earth components are often found. These additional components must be taken into account to adjust the siderite: calcite ratio for the stoichiometric brownmillerite, and may also raise concerns about incorporation in the brownmillerite structure, as expected for $Ca_2Fe_{2-y}Al_yO_5$ [6], or onset of secondary phases, such as calcium silicates (e.g. Ca_2SiO_4) with impact on the effective Ca:Fe ratio by easy reactivity with calcite.

2. Materials and methods

Calcite ($CaCO_3$, Sigma-Aldrich) and a natural siderite (SIDCO Minerals Inc.) were used as precursors for preparation of $Ca_2Fe_2O_5$ by reactive firing. The X-ray diffraction of natural siderite showed $FeCO_3$ as the main crystalline phase, combined with quartz (SiO_2). Further chemical analysis by XRF spectrometry (Philips PW 1400/00) also revealed the presence of a significant fraction of Al and minor quantities of other elements, such as alkaline earth elements (Ca and Mg). The elemental composition (Table 1) was estimated from XRF data, assuming the presence of Fe, alkali and alkaline earth metals as carbonates phase and the remaining elements in oxide form.

Stoichiometric mixtures of $CaCO_3$ and siderite (based on the elemental fraction of Fe) were ball milled (Retsch PM 100) in ethanol (50 mL), at 300 rpm, for 11 h, using a Teflon vial (~140 cm^3) and zirconia balls ($\varnothing = 1$ cm). The ball to powder weight ratio was ~10:1. The resultant mixture was dried at 60 °C, overnight. An alternative milling procedure was performed in dry conditions, at 500 rpm, for 8 h, keeping the ball to powder weight ratio, and using the same equipment and milling material. Undue heating was avoided by milling for periods of 5 min with a subsequent pause of 2 min and reversal of the direction of rotation. X-ray diffraction analysis of powders before and after milling was performed to monitor phase changes induced by milling.

Thermogravimetric analysis of siderite samples and stoichiometric calcite + siderite mixtures dry milled at 500 rpm for 8 h, was performed using a SETARAM SetSys 16/18 instrument in flowing air on heating/cooling at 2 °C/min or 8 °C/min. Additional experiment with similar temperature profile was performed for siderite in CO_2. Both stoichiometric precursors mixtures, milled in ethanol at 300 rpm for 11 h and dry milled at 500 rpm for 8 h, were compacted in disc shape and fired in air with different firing cycles. These firing cycles were designed by Taguchi planning [14–16] with selected values of heating and cooling rates, β, firing temperature, T_f, and firing time, t_f, to assess the effects of firing conditions on the $Ca_2Fe_2O_5$ formation. The resulting fired samples were analysed by X-ray diffraction using a PANalytical X'Pert PRO[3]

Table 1
Cation elemental composition of siderite estimated from XRF data.

Element	*at.* (%)
Fe	80.85
Si	10.75
Al	6.20
Mg	0.93
Ca	0.86
Mn	0.23
Ti	0.17

diffractometer (CuK_α radiation) equipped with graphite monochromator along with the Panalytical HighScore Plus 4.7 software with PDF-4 database. These difractograms were recorded in the range 2θ = 10–90° with step = 0.02°. Additional firing experiments were performed in air and in argon to re-assess the effects of temperature, and to analyse the effect of firing atmosphere. Also, heat treatments of siderite in N_2 and 10% H_2 – 90% N_2 atmospheres were carried out to study the effect of non-oxidising conditions in its thermal decomposition.

Thermodynamic-based analyses were used as guidelines to understand the redox behaviour in non-oxidising atmospheres of the system Ca–Fe–O. These thermodynamic predictions may be derived on stability diagrams of a_{Fe}: a_{Ca} activity ratio and partial pressure of a reacting gas (O_2, CO_2, etc.), as proposed earlier for other systems [17,18], or on the corresponding chemical potential difference $\Delta\mu_{Fe}$ - $\Delta\mu_{Ca}$ and oxygen chemical potential $\Delta\mu_{O_2}$. The methodology adopted is based on the derivation of representative reactions for 2-phase equilibria, and then obtain relevant values of pO_2, a_{Fe}:a_{Ca}, or a_{Fe}:a_{Ca} *vs* pO_2 from the relevant mass action constants. The thermodynamic properties (standard formation enthapies, standard entropies and heat capacities) required for the themodynamic calculations were retrieved from a thermochemical database (FactSage,GTT Technologies [19]).

3. Results and discussion

3.1. Effect of milling on reacting mixtures

The X-ray diffractogram of the initial powder mixture only shows clear evidence of calcite ($CaCO_3$), combined with the main phase of the siderite precursor ($FeCO_3$) and its main impurity (quartz). Other elements may be incorporated in the carbonate phase (e.g., Mg, Ca, Mn) or in the amorphous fraction (e.g., Al). A strong amorphization of the initial mixture was observed after dry milling of the stoichiometric powder mixture at 500 rpm for 8 h with significant lowering and enlargement of $CaCO_3$ and $FeCO_3$ diffraction peaks (Fig. 2). The (101) reflection of quartz is a suitable standard to emphasize relative intensity changes, as shown in Table 2; this indicates that milling has greater effects on calcite. Still, one does not find any evidence of the onset of transformation to alternative polymorphs or additional phases induced by high-energy milling. Note that the intensity is represented in a square root scale to emphasize the presence of minor additional phases. After lower energy milling, in ethanol (300 rpm, 11 h), one only finds a slight decrease in the $I_{(104)_c} : I_{(101)_q}$ intensity ratio, without significant effect on the siderite phase. In addition, one did not find any evidence of decomposition of carbonate precursors by high-energy milling.

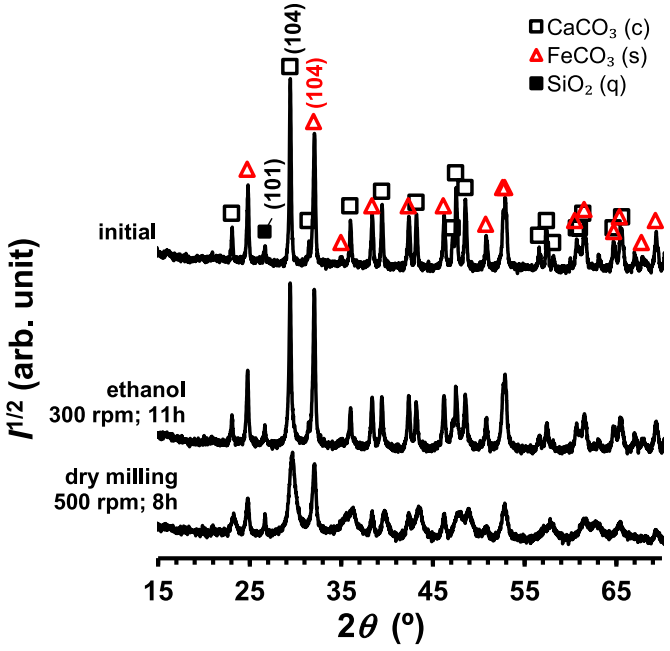

Fig. 2. X-ray patterns of the stoichiometric mixture of calcite and siderite: initial (as-mixed); after milling in ethanol at 300 rpm for 11 h and after dry milling at 500 rpm for 8 h.

Table 2
Main peak intensity ratio of the calcite (*c*) and siderite (*s*) phases, relative to quartz (*q*).

Milling schedule	$I_{(104)_c} : I_{(101)_q}$	$I_{(104)_s} : I_{(101)_q}$
Initial powder mixture	42	23
Milling in ethanol; 300 rpm; 11h	25	23
Dry milling; 500 rpm; 8 h	7	6

3.2. Thermochemical conditions for decomposition of reactants

Thermogravimetry (Fig. 3) was used to analyse conditions for decomposition of reactant mixtures and its dependence on the heating rate. The initial steps include a peak at temperatures in the range 70–120 °C (*A*) ascribed to evaporation of absorbed humidity, and a subsequent shoulder in the range 200–300 °C (*B*), which is consistent with the temperature range for decomposition of hydrated phases, such as goethite (FeOOH) or its solid solutions with boehmite $Al(OH)_3$ [20]. These contributions are close to peak *C*, in the temperature range expected for siderite decomposition. Burning out of contaminants from Teflon milling vials is also likely to contribute to further losses, probably overlapped with peak C. Peak temperature *D* (Table 3) is close to the results reported for decomposition of mechanically activated calcite [21].

The dependence of these peaks on working conditions is shown in Table 3 to emphasize kinetic delays during fast heating, and the impact of the firing atmosphere. Kinetic delays were estimated by assuming a typical dependence of the decomposition peak temperature T_p on heating rate β, as described by the Kissinger equation [22]:

$$ln\left(\beta \Big/ T_p^2\right) = ln(A_o) - (E_a / R)T_p^{-1} \quad (8)$$

This yielded $A_o \approx 0.44\ K^{-1}{\cdot}min^{-1}$ and $E_a \approx 56$ kJ/mol for decomposition of $FeCO_3$, and a prediction $T_p \approx 486$ K (213 °C) for the decomposition on heating very slowly (0.1 °C/min). Similarly, for the decomposition of calcium carbonate $A_o \approx 1.94 \times 10^4\ K^{-1}{\cdot}min^{-1}$; $E_a \approx$ 181 kJ/mol yielding $T_p \approx 576$ °C for decomposition on heating at 0.1 °C/min. Note that thermodynamic assessment predicts reactivity of calcite with previously formed hematite (**Eq. (2)**) at temperatures above 514 °C (Fig. 1). The decomposition temperature of the siderite component of milled reactants is also lower than the corresponding decomposition temperature of as received siderite.

Early contributions of weight losses at relatively low temperature explain why total cumulative weight losses (~ 44%) are higher than expected for CO_2 losses, by decomposition of carbonates (39 *wt* %). However, this does not consider oxygen uptake by changes in oxidation state, as expected if one assumed decomposition of siderite to wustite. In fact, decomposition in air is likely to yield evolution from divalent Fe^{2+}, in the siderite precursor, to trivalent Fe^{3+} in hematite or oxidised reaction products ($Ca_2Fe_2O_5$ or $CaFe_2O_4$). In these cases, one should expect only 36 *wt* %. Apparently, this should also be expected for nominally inert atmospheres (e.g. N_2 or CO_2). However, this may change by the oxygen balance between CO_2 evolution and at least partial oxidation from Fe^{2+} to Fe^{3+} in O_2 lean conditions, which is more consistent with conversion to magnetite, yielding a CO/CO_2 gas phase:

$$3\ FeCO_3 \rightarrow Fe_3O_4 + 2\ CO_2 + CO \quad (9)$$

Thus, the combined effects of decomposition of carbonates and preferential conversion to magnetite should yield 37 *wt* %, taking into

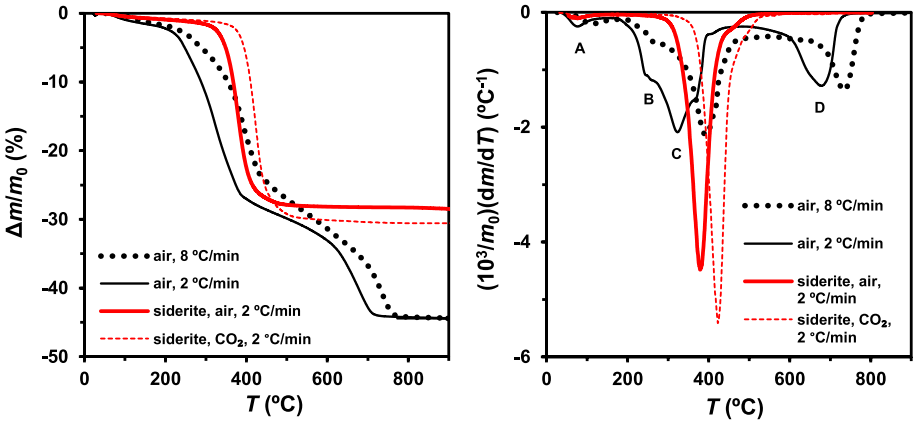

Fig. 3. Thermogravimetry of stoichiometric siderite + calcite powder mixtures dry milled at 500 rpm for 8 h, at 2 °C/min and 8 °C/min in air, and siderite at 2 °C/min in air and CO_2. (*Left*) relative weight loss, and (*right*) derivative thermogravimetric curves.

Table 3
Summary of thermogravimetry results of calcite + siderite mixtures dry milled at 500 rpm for 8 h, in air, and siderite in air and in CO_2.

Reactants	Flow	Heating rate (°C/min)	Peak Temperature (°C)			*wt* loss (%)
			A	C	D	
Calcite + Siderite	Air	2	77	324	679	44.4
Calcite + Siderite	Air	8	112	393	735	44.3
Siderite	Air	2	77	379	–	28.5
Siderite	CO_2	2	83	423	–	30.6

account the co-distribution of valence states in Fe_3O_4 (i.e., 1/3 Fe^{2+} and 2/3 Fe^{3+}). The redox stability range of the magnetite phase is consistent with an ideal stoichiometric ratio CO:CO_2 = 1:2 predicted by **Eq. (9)**.

3.3. Effects of firing schedule

Taguchi planning was used to select different firing schedules to assess the impact of heating rate, upper firing temperature and corresponding dwell time on conversion to the brownmillerite phase $Ca_2Fe_2O_5$ (*b*) relative to secondary spinel phase $CaFe_2O_4$ (*sp*) (Table 4); this was assessed by X-ray diffraction based on the intensity ratio of their most intense reflections $I_{(121)_{sp}} : I_{(141)_b}$. The first study was based on the initial powder mixture with stoichiometric $CaCO_3$:$FeCO_3$ ratio, which was milled at 300 rpm for 11 h in ethanol.

Table 4
Taguchi plan to evaluate the impact of firing conditions on relative conversion to the secondary spinel phase $CaFe_2O_4$ (*sp*) and brownmillerite phase $Ca_2Fe_2O_5$ (*b*) accounted for by their peak intensity ratio, $I_{(121)_{sp}} : I_{(141)_b}$, and other residual phases, for siderite + calcite powder mixtures milled in ethanol at 300 rpm for 11 h.

Experiment	β (°C/min)	T (°C)	t (h)	$I_{(121)_{sp}} : I_{(141)_b}$	Other phases
E1	2	800	1	0	SiO_2, CaO, Fe_2O_3
E2	2	900	2	0.16	$Ca_2Al_2SiO_7$, Fe_2O_3
E3	2	1000	4	0.33	$Ca_2Al_2SiO_7$, Ca_2SiO_4
E4	4	800	2	0	SiO_2, CaO, Fe_2O_3
E5	4	900	4	0.17	$Ca_2Al_2SiO_7$, Fe_2O_3
E6	4	1000	1	0.29	$Ca_2Al_2SiO_7$, Ca_2SiO_4
E7	8	800	4	0	SiO_2, CaO, Fe_2O_3
E8	8	900	1	0.18	$Ca_2Al_2SiO_7$, CaO
E9	8	1000	2	0.33	$Ca_2Al_2SiO_7$, Ca_2SiO_4

X-ray diffraction patterns in Fig. 4 show prevailing conversion of calcite and siderite precursors to $Ca_2Fe_2O_5$ with significant fractions of $CaFe_2O_4$, mainly at the highest temperature. Oxide by-products (Fe_2O_3 and CaO) are also observed at the lowest temperatures suggesting that the main mechanisms may include initial steps of direct decomposition of the carbonate precursors to corresponding oxides before subsequent conversion to browmillerite. In fact, $FeCO_3$ decomposes readily on heating, probably before reaching 400 °C, and $CaCO_3$ is also likely to decompose on heating before reaching 800 °C (Fig. 3). However, traces of hematite are retained even after firing at 900 °C (experiments E2 and E5) as revealed mainly by the (116) reflection at $2\theta \approx 54.09°$. Note that the main peak (104) of hematite at $2\theta \approx 33.15°$ overlaps with the (200) reflection of $Ca_2Fe_2O_5$. In fact, the (104) reflection of hematite (Fe_2O_3) is

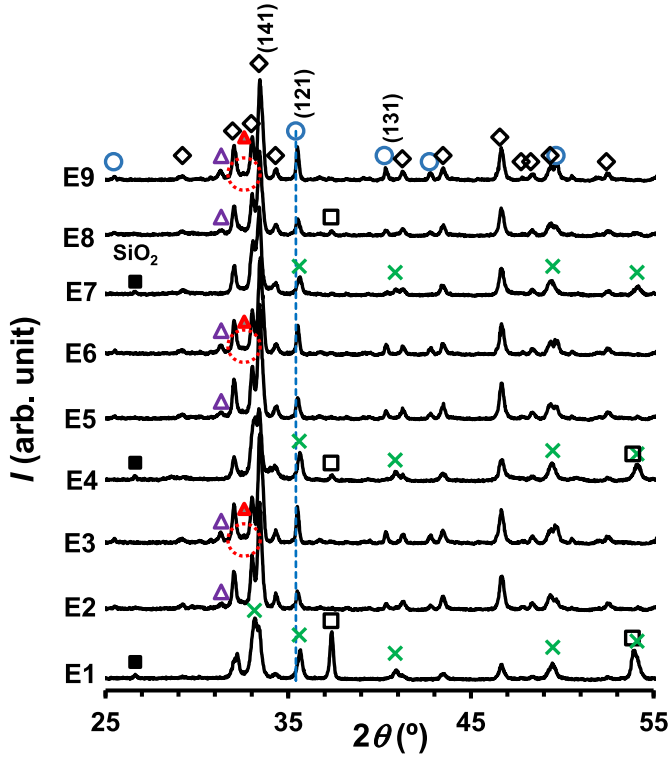

Fig. 4. X-ray diffractograms of samples prepared with powder mixtures milled in ethanol at 300 rpm and for 11 h. Different symbols denote reflections ascribed to $Ca_2Fe_2O_5$ (◊), $CaFe_2O_4$ (o), $Ca_2Al_2SiO_7$ (△), Ca_2SiO_4 (▲), SiO_2 (■), CaO (□) and Fe_2O_3 (X).

observed only for samples fired at 800 °C when conversion to $Ca_2Fe_2O_5$ is lowest, and its crystallinity is the poorest. Similarly, the (116) reflection of Fe_2O_3 ($2\theta \approx 54.09°$) overlaps partially with the (220) reflection of CaO ($2\theta \approx 53.86°$). Still, traces of CaO are observed mainly at 800 °C and for a short time (experiment E1). Longer dwell time promotes a greater conversion of CaO to brownmillerite (experiment E7).

Results for experiments with the lowest plateau temperature (E1, E4 and E7) also show the presence of quartz (SiO_2), which is the main gangue component of the natural siderite precursor. On the contrary, one could not find traces of alumina suggesting that this gangue component is incorporated in the main browmillerite phase or in minor secondary products. In fact, one finds traces of $Ca_2Al_2SiO_7$ which also incorporates a fraction of silica. The overall balance of silica may be accounted for by the onset of di-calcium silicate (Ca_2SiO_4) as marked in Fig. 4. Note that detection of this phase relies only on the (112) reflection at $2\theta \approx 32.61°$ (JCPDS file 01-080-0942) because other reflections are superimposed on reflections of the main phases. Thus, one assumes that conversion of hematite, calcia, silica and alumina may be described by:

$$Fe_2O_3 + x\ \ Al_2O_3 + 2\,CaO + y\ \ SiO_2 \rightarrow$$

$$x\,Ca_2Al_2SiO_7 + (y-x)\ \ Ca_2SiO_4 + 2y\ \ CaFe_2O_4 + (1-2y)\,Ca_2Fe_2O_5 \quad (10)$$

This indicates that onset of the main secondary phase ($CaFe_2O_4$) is triggered and probably determined mainly by incorporation of silica in additional phases ($Ca_2Al_2SiO_7$ and Ca_2SiO_4) and corresponding depression of the available Ca: Fe ratio, as also shown by X-ray diffractograms in Fig. 4. However, this is insufficient for precise quantification, and one considered the intensity ratio of the main reflections of $CaFe_2O_4$ and $Ca_2Fe_2O_5$, $I_{(121)_{sp}} : I_{(141)_b}$, as a guideline for the relative contribution of the main secondary phase.

The correlation matrix (Table 5) identifies the impact of firing parameters on $I_{(121)_{sp}} : I_{(141)_b}$ with very a good correlation with temperature and negligible correlation with the heating rate or firing time; this is confirmed by plotting averaged results for every level of each independent firing parameter (Fig. 5). Dependence on the heating rate and dwell time is nearly flat, with a very poor signal-to-noise ratio and high scattering. Thus, one should not overestimate the effect of dwell time suggested by some individual experiments (e.g. E7). This prevailing dependence on temperature is also consistent with the onset of $Ca_2Al_2SiO_7$ and Ca_2SiO_4 at the highest temperatures, with the corresponding depletion of available Ca and increased contents of secondary phase $CaFe_2O_4$ with low Ca:Fe ratio. Thus, one expects optimization of the contents of brownmillerite by enhancing the reactivity of the Ca and Fe-based precursors at lower temperatures ($T \leq 800$ °C), while the reactivity of quartz is still prevented.

Enhanced reactivity is expected after higher energy milling [7], namely by increasing the kinetic energy of impacting balls. Thus, the Taguchi plan was repeated with a more reactive powder mixture, obtained by dry milling at 500 rpm for 8 h, which yielded more extensive structural changes (Fig. 2). The corresponding X-ray diffractograms (Fig. 6) confirm enhanced reactivity indicated by the absence of reflections ascribed to CaO and decreased peak intensities of Fe_2O_3. Formation of $CaFe_2O_4$ is also suppressed, except for experiments at the highest temperature (E3, E6 and E9), and traces for experiment E5 with firing at 900 °C. This temperature dependence of the corresponding peak intensity ratio $I_{(121)_{sp}} : I_{(141)_b}$, is also shown in Fig. 5, as previously found for samples prepared from powder mixtures milled in milder conditions. One observes a sharper transition from results at 900 °C to 1000 °C for samples which were fired after activation at higher energy.

Table 5
Correlation matrix between the peak intensity ratio $I_{(121)_{sp}} : I_{(141)_b}$ and firing parameters for stoichiometric calcite + siderite mixtures after milling in ethanol at 300 rpm for 11 h and after dry milling at 500 rpm for 8 h.

Firing Parameters	$I_{(121)_{sp}} : I_{(141)_b}$	
	Milling in ethanol 300 rpm, 11 h	Dry milling 500 rpm, 8 h
β (°C/min)	0.03	0.05
T_p (°C)	0.99	0.88
t (h)	0.03	0.07

The onset of the aluminosilicate $Ca_2Al_2SiO_7$ is less obvious for fired samples processed from dry milled powders (Fig. 6) than for samples obtained after milder milling in ethanol (Fig. 4), possibly because alumina may be incorporated in the main phases, taking into account ready substitution of Fe by Al in $Ca_2Fe_{2-y}Al_yO_5$ [6]; this is suggested by a slight shift in brownmillerite reflections (Fig. 6) due to differences in ionic radius of Al^{3+} and Fe^{3+}. One may also consider the possibility of complex quaternary SFCA phases in the SiO_2–Fe_2O_3–CaO–Al_2O_3 system [21]. Quartz is still retained after firing at 800 °C (E1, E4 and E7 in Fig. 6) but is hardly detected after firing at higher temperatures when one observes onset of the (112) reflection of Ca_2SiO_4 at $2\theta \approx 32.61°$.

Figs. 4 and 6 still suggest that high heating rate and long firing time (E7) are most suitable to reach high conversion and best resolution of the main reflections of the intended brownmillerite phase ($Ca_2Fe_2O_5$) at relatively low temperatures. Thus, additional experiments were performed in a wider temperature range (700–1000 °C), with a heating rate of 8 °C/min, and a dwell time of 4 h or 1 h, to confirm the temperature dependence and the effect of time (Fig. 7). One observes conversion to $Ca_2Fe_2O_5$ even after firing at 700 °C in air for 4 h, with enhanced crystallinity at higher temperatures; this suggests that conversion to the brownmillerite phase overlaps, at least partially, with conditions for decomposition of calcite (Fig. 3), as described by **Eq. (2)**. Quartz (SiO_2) and hematite are detected up to 800 °C, and the onset of the secondary phase $CaFe_2O_4$ occurs on firing at $T \geq 900$ °C for 4 h; this represents a significant fraction of the reaction products as indicated by the peak intensity ratio $I_{(121)_{sp}} : I_{(141)_b}$ which reaches values of 0.24 at 900 °C and 0.49 at 1000 °C after 4 h. Still, this phase is only observed for the longest time (4 h) at 900 °C and is hardly detected for 1 h. At 1000 °C the peak intensity ratio drops from 0.49 after 4 h to 0.32 after 1 h; this shows that the effect of time must also be taken into account and that short time is best suited to avoid the secondary phase $CaFe_2O_4$.

3.4. Effects of firing atmosphere

In addition, one may consider firing in non-oxidising atmospheres based on thermodynamic guidelines (Fig. 8). In fact, the phase stability diagram of the Ca–Fe–O system may be very complex [23], including several additional phases such as, $CaFe_3O_5$, $CaFe_4O_7$, $CaFe_5O_7$, $Ca_4Fe_9O_{17}$ and $Ca_4Fe_{17}O_{29}$. Thus, one only considered approximate phase stability diagrams, based on the actual phases detected by X-ray diffraction, to allow a comprehensive interpretation of relevant thermochemical conditions. These stability diagrams show that $Ca_2Fe_2O_5$ or $CaFe_2O_4$ only co-exist in oxidising conditions and for specific values of a_{Fe}:a_{Ca} ratio and pO_2 along the 2-phase line. The thermodynamic driving force for conversion of reactant oxides is higher for $Ca_2Fe_2O_5$ than for $CaFe_2O_4$ as marked by chemical potential differences across these phases. Thus, the onset of significant fractions of $CaFe_2O_4$ may be attributed to effective depletion of Ca rather than a higher driving force. Note also that the redox stability range of $Ca_2Fe_2O_5$ depends on the chemical potential difference $\Delta\mu_{Fe}$ - $\Delta\mu_{Ca}$ with prospects to extend the stability in oxidising conditions. Onset of $CaFe_2O_4$ may be prevented by firing under non-oxidising conditions, when brownmillerite may co-exists with magnetite (Fe_3O_4), wustite (FeO) or metallic Fe. The corresponding CO_2: CO ranges are shown in the secondary X-axis to emphasize conditions expected after decomposition of siderite in a non-oxidising atmosphere (see **Eq. (2)**); this suggests $Ca_2Fe_2O_5$/Fe_3O_4 equilibrium in a wide redox range, whereas the $Ca_2Fe_2O_5$/Fe_2O_3 interface is excluded. Thus, these

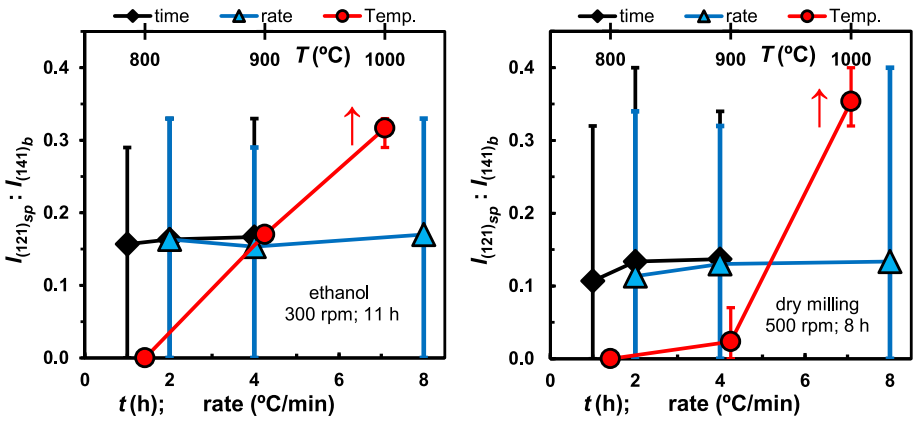

Fig. 5. Averaged dependence of the secondary to brownmillerite peak intensity ratio $I_{(121)_{sp}} : I_{(141)_b}$, on firing parameters for stoichiometric calcite + siderite mixtures milled in ethanol at 300 rpm for 11 h (*left*) or dry milled at 500 rpm for 8 h (*right*).

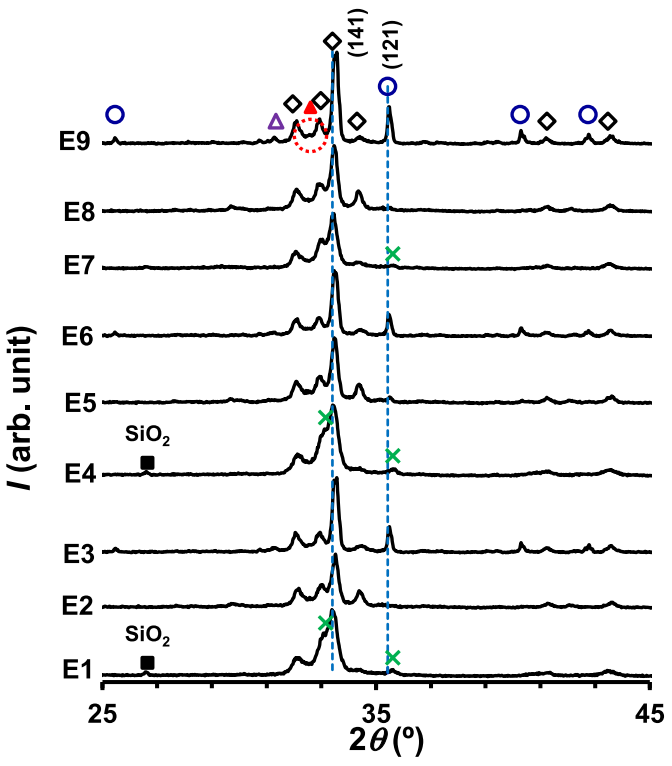

Fig. 6. X-ray diffractograms of samples prepared with powder mixtures dry-milled at 500 rpm for 8 h. Different symbols denote reflections ascribed to $Ca_2Fe_2O_5$ (◊), $CaFe_2O_4$ (o), $Ca_2Al_2SiO_7$ (△), Ca_2SiO_4 (▲), SiO_2 (■) and Fe_2O_3 (X).

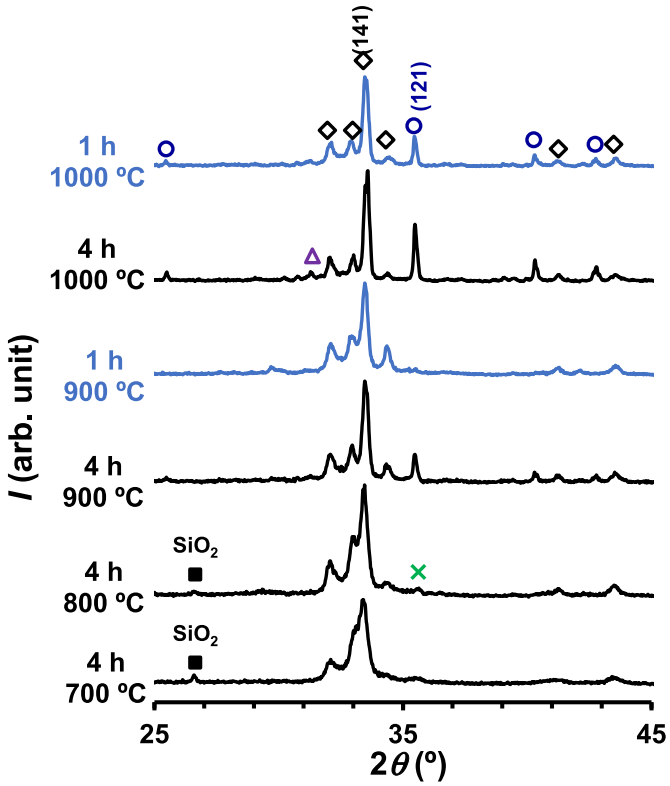

Fig. 7. X-Ray diffractograms of samples prepared with powder mixtures dry-milled at 500 rpm for 8 h and fired at different temperatures for 4 h or 1 h. Different symbols denote reflections ascribed to $Ca_2Fe_2O_5$ (◊) $CaFe_2O_4$ (o), $Ca_2Al_2SiO_7$ (△), SiO_2 (■) and Fe_2O_3 (X).

phases only co-exist in non-equilibrium conditions with incomplete conversion, as found after firing at 800 °C (Figs. 4 and 6).

Heat treatments of siderite in N_2 or reducing 10% H_2 – 90% N_2 atmospheres were performed to characterize the first step of decomposition of the siderite precursor in non-oxidising conditions and to identify suitable conditions to retain magnetite as the intermediate phase, based on the thermodynamic guidelines of Fig. 8. Though hematite should be expected in equilibrium with the inert atmosphere N_2 ($pO_2 \approx 10^{-4}$ atm), decomposition in this atmosphere yields magnetite (Fig. 9) indicating that co-generation of CO_2 and CO sets an effective redox buffer, as described by **Eq. (9)**. In fact, the stoichiometric ratio CO_2:CO = 2:1 is slightly displaced from the reducing stability limit of magnetite (CO_2: CO ≈ 1.6 at 700 °C), as shown in Fig. 8, thus explaining the absence of other iron oxides when decomposition occurs in an inert atmosphere. Still, the CO_2:CO buffer is changed by decomposition of siderite in the reducing 10% H_2 – 90% N_2 atmosphere, which displaces the self-buffer condition to the Fe_3O_4/FeO boundary (Fig. 9).

The previous study of the impact of non-oxidising atmospheres on the decomposition of the siderite precursor showed that oxygen-lean inert atmospheres are best suited to set a appropriate self redox buffer without additional risks and the cost of a reducing atmosphere. Thus, additional firing experiments were performed in a standard Ar atmosphere (Fig. 10); this confirmed high conversion to $Ca_2Fe_2O_5$ and enhanced crystallinity in an inert atmosphere, even at 700 °C, confirming that synthesis of the brownmillerite phase overlaps with conditions for decomposition of calcite (Fig. 3). Firing in an inert

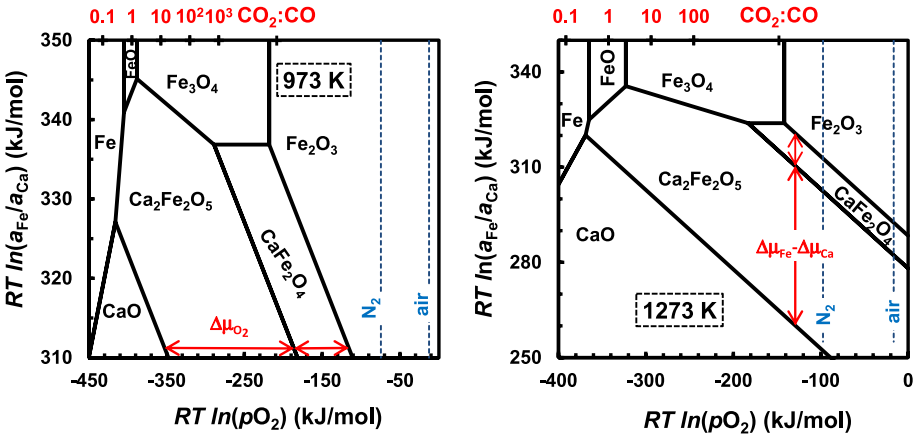

Fig. 8. Thermodynamic stability diagrams for the system Ca–Fe–O at 973 K and 1273 K.

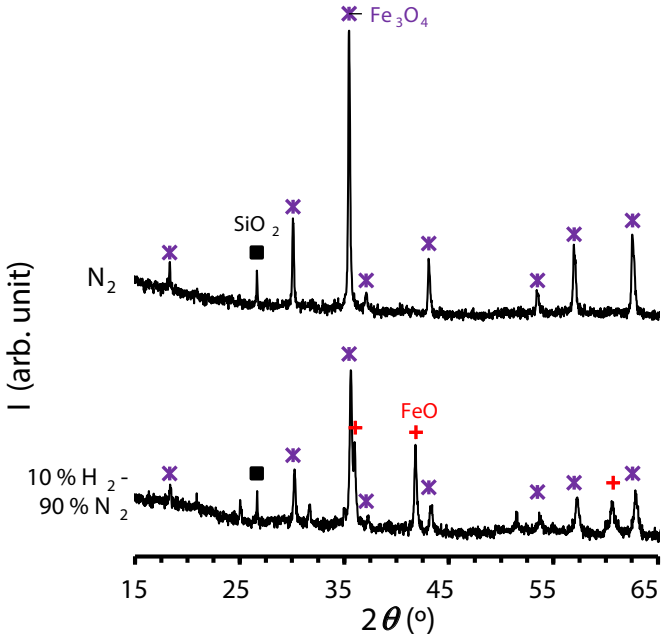

Fig. 9. X-ray diffractograms of siderite samples after calcination at 700 °C for 1 h with heating rate of 5 °C/min in N_2 or 10% H_2 – 90% N_2 atmospheres. Different symbols denote reflections ascribed to Fe_3O_4 (✱), FeO (+) and SiO_2 (■).

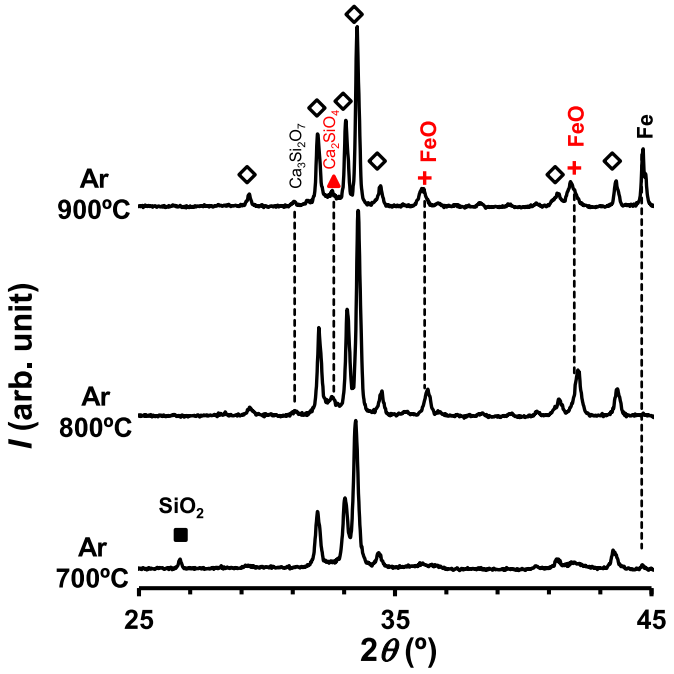

Fig. 10. X-ray diffractograms of samples prepared with powder mixtures dry-milled at 500 rpm for 8 h and fired at different temperatures in Ar with a heating rate of 8 °C/min and firing time of 4 h. Different symbols denote reflections ascribed to $Ca_2Fe_2O_5$ (◊), Ca_2SiO_4 (▲), FeO (+) and SiO_2 (■). Reflections ascribed to metallic Fe and calcium silicate $Ca_3Si_2O_7$ are also marked.

atmosphere also yields much better crystallinity and absence of the secondary $CaFe_2O_4$ phase, even after firing at 900 °C. However, one observes the formation of a wustite phase and/or metallic Fe at T ≥ 800 °C. These results were unexpected but may be understood by taking into account that early decomposition of the siderite precursor in inert atmosphere yields mainly a partially reduced phase Fe_3O_4 (Fig. 9), and that subsequent incorporation in the browmillerite phase implies oxidation to the trivalent state. Thus, conversion to the brownmillerite phase requires oxygen supply, which cannot be supplied by the oxygen lean atmosphere, and must rely on the partial reduction of a fraction of magnetite to wustite (Eq. (11)) or even reduction to metallic Fe (Eq. (12)):

$$Fe_3O_4 + 2\ CaO \rightarrow Ca_2Fe_2O_5 + FeO \quad (11)$$

$$0.75\ Fe_3O_4 + 2\ CaO \rightarrow Ca_2Fe_2O_5 + 0.25\ Fe \quad (12)$$

Faster kinetics at 900 °C in O_2-lean conditions also implies faster oxygen demand and, thus, co-existence of metallic Fe with FeO, whereas a lower conversion rate at 800 °C explains the nearly exclusive onset of FeO. In fact, the first step of the overall process is decomposition of $FeCO_3$, and its kinetics depends on the actual atmosphere. Though wustite may be formed as a transient product in inert atmospheres [24], it is unstable at temperatures below about 500 °C, possibly decomposing to magnetite and metallic Fe in O_2-lean atmospheres, ($4\ FeO \rightarrow Fe_3O_4 + Fe$), depending on the heating rate and firing temperature. Subsequent conversion to the brownmillerite phase at the final dwell temperatures also depends on the limited supply of oxygen in O_2-lean atmospheres, shifting to reducing atmospheres, as described by Eqs. (3) and (4), or inducing partial reduction of magnetite to wustite or even metallic Fe, as given by Eqs. (11) and (12). The XRD patterns in Fig. 10 also confirm greater segregation of Ca-rich secondary phases (silicates) at 800 °C and 900 °C, in close agreement with deviations from the ideal stoichiometric ratio (Ca: Fe ≈ 1:1), which drops to Ca:Fe ≈ 0.67 in Eq. (11), or Ca:Fe ≈

0.89 in Eq. (12).

In addition, the stoichiometry of the wustite phase ($Fe_{1-x}O$) is likely to change with temperature, as indicated by the shift of its XRD reflections. This reveals lattice contraction at 800 °C due to increasing deviation from stoichiometry and corresponding compensation by a fraction of trivalent Fe^{3+} with a smaller ionic radius, as expected for a mechanism of gradual reduction of magnetite → wustite → Fe with the corresponding change in lattice parameter of the wustite phase and/or its phase transformation [25].

4. Conclusions

Reactivity between calcite and natural siderite was found to depend on the preliminary activation by high energy-milling, which induced partial amorphization in addition to homogenization of the precursors. Thermogravimetry shows that the siderite precursor decomposes readily on heating, with a peak at temperatures in the range 320–430 °C depending on heating rate, milling and atmosphere. The peak ascribed to the decomposition of calcite was found at 670–740 °C. Taguchi planning allowed one to assess the relative contributions of firing temperature, time, and rate of heating on the conversion of precursors, reflected by $I_{(121)_{sp}} : I_{(141)_b}$ peak intensity ratio of main XRD reflections of secondary phase $CaFe_2O_4$, and browmillerite; this peak intensity ratio depends mainly on temperature. Additional minor phases are formed by reactions between calcia and gangue components of the natural siderite precursor, usually at T ≥ 900 °C, leading to effective Ca-deficiency and increasing contents of $CaFe_2O_4$. Thermodynamic modelling is suitable to identify redox conditions in less common non-oxidising atmospheres, from inert to reducing, to prevent the onset of $CaFe_2O_4$. The first step of decomposition of the siderite precursor in inert atmosphere yielded a self CO_2/CO redox buffer co-existing with magnetite as a single intermediate iron oxide. This buffer condition allowed one to obtain high conversion by reaction of magnetite with calcite, even at 700 °C, yielding $Ca_2Fe_2O_5$ with enhanced crystallinity. Faster reactivity at T ≥ 800 °C under these oxygen-lean conditions yielded wustite and/or metallic Fe to maintain the oxygen balance, while the corresponding excess of calcia reacts with silica.

Declaration of competing interest

The authors declare that they have no known competing financial interests or personal relationships that could have appeared to influence the work reported in this paper.

Acknowledgments

This work was developed withing the scope of the projects NOTARGAS (ref. POCI-01-0145-FEDER-030661), CICECO – Aveiro Institute of Materials, UIDB/50011/2020, UIDP/50011/2020 & LA/P/0006/2020 and CESAM - Centre for Environmental and Marine Studies, UIDB/50017/2020, UIDP/50017/2020, LA/P/0094/2020, financed by national funds through the FCT/MEC (PIDDAC). L. Ruivo acknowledges to the Portuguese Foundation for Science and Technology for the PhD scholarship grant (ref. SFRH/BD/129901/2017). The authors would also like to thank Aleksandr Bamburov for the experimental assistance, and the SIDCO Minerals Inc. Company for providing the siderite.

References

[1] B.-J. Xue, J. Luo, F. Zhang, Z. Fang, Biodiesel Production from Soybean and Jatropha Oils by Magnetic $CaFe_2O_4$ - $Ca_2Fe_2O_5$ - Based Catalyst, 2014, https://doi.org/10.1016/j.energy.2014.02.082.

[2] M. Ismail, W. Liu, M.S.C. Chan, M.T. Dunstan, S.A. Scott, Synthesis, application, and carbonation behavior of $Ca_2Fe_2O_5$ for chemical looping H_2 production, Energy Fuel. 30 (2016) 6220–6232, https://doi.org/10.1021/acs.energyfuels.6b00631.

[3] Z. Sun, S. Chen, J. Hu, A. Chen, A. Hasan Rony, C.K. Russell, W. Xiang, M. Fan, M. Darby Dyar, E.C. Dklute, $Ca_2Fe_2O_5$: A Promising Oxygen Carrier for CO/CH_4 Conversion and Almost-Pure H_2 Production with Inherent CO_2 Capture over a Two-step Chemical Looping Hydrogen Generation Process, 2018, https://doi.org/10.1016/j.apenergy.2017.11.005.

[4] Z. Sun, S. Chen, C.K. Russell, J. Hu, A.H. Rony, A. Chen, L. Duan, J. Boman, J. Tang, T. Chien, M. Fan, W. Xiang, Improvement of H_2-Rich Gas Production with Tar Abatement from Pine Wood Conversion over Bi-functional $Ca_2Fe_2O_5$ Catalyst: Investigation of Inner-Looping Redox Reaction and Promoting Mechanisms, 2017, https://doi.org/10.1016/j.apenergy.2017.12.087.

[5] Y. Wang, P. Niu, H. Zhao, Chemical looping gasification of coal using calcium ferrites as oxygen carrier, Fuel Process. Technol. 192 (2019) 75–86, https://doi.org/10.1016/j.fuproc.2019.04.009.

[6] T.-L. Phan, N. Tran, D.H. Kim, P.T. Tho, B.T. Huy, T.N. Dang, D.-S. Yang, B. Lee, Electronic structure and magnetic properties of Al-doped $Ca_2Fe_2O_5$ brownmillerite compounds, J. Am. Ceram. Soc. 101 (2018) 2181–2189, https://doi.org/10.1111/jace.15357.

[7] B.F. Amorim, M.A. Morales, F. Bohn, A.S. Carriço, S.N. De Medeiros, A.L. Dantas, Synthesis of stoichiometric $Ca_2Fe_2O_5$ nanoparticles by high-energy ball milling and thermal annealing, Phys. B Condens. Matter 488 (2016) 43–48, https://doi.org/10.1016/j.physb.2016.01.029.

[8] Z. Zhang, W. Wang, Solution combustion synthesis of $CaFe_2O_4$ nanocrystal as a magnetically separable photocatalyst, Mater. Lett. 133 (2014) 212–215, https://doi.org/10.1016/j.matlet.2014.07.050.

[9] K. Gupta, S. Singh, M. Ceretti, M.S.R. Rao, W. Paulus, Scaling of extended defects in nano-sized Brownmillerite $CaFeO_{2.5}$, Phys. Status Solidi Appl. Mater. Sci. 210 (2013) 1771–1777, https://doi.org/10.1002/pssa.201329027.

[10] H. Fukuyama, K. Hossain, K. Nagata, Solid-state reaction kinetics of the system CaO-FeO, Metall. Mater. Trans. B Process Metall. Mater. Process. Sci. 33 (2002) 257–264, https://doi.org/10.1007/s11663-002-0010-9.

[11] J.-W. Jeon, S.-M. Jung, Y. Sasaki, Formation of calcium ferrites under controlled oxygen potentials at 1273 K, ISIJ Int. 50 (2010) 1064–1070, https://doi.org/10.2355/isijinternational.50.1064.

[12] V.N. Kholodov, G.Y. Butuzova, Siderite formation and evolution of sedimentary iron ore deposition in the Earth's history, Geol. Ore Deposits 50 (2008) 299–319, https://doi.org/10.1134/S107570150804003X.

[13] B. Xing, N. Graham, W. Yu, Transformation of siderite to goethite by humic acid in the natural environment, Commun. Chem. 3 (2020), https://doi.org/10.1038/s42004-020-0284-3.

[14] G. Taguchi, S. Chowdhury, Y. Wu, Quality engineering: the Taguchi method, in: Taguchi's Qual. Eng. Handb., John Wiley & Sounds, 2004, pp. 56–123, https://doi.org/10.1002/9780470258354.ch4.

[15] L.N. Harris, Taguchi techniques for quality engineering, in: P.J. Ross (Ed.), Qual. Reliab. Engng. Int., Mcgraw-hill book company, 1988, p. 249, https://doi.org/10.1002/qre.4680050312.

[16] T. Mori, S.-C. Tsai, Taguchi Methods: Benefits, Impacts, Mathematics, Statistics and Applications, ASME Press, 2011, https://doi.org/10.1115/1.859698.

[17] H. Yokokawa, N. Sakai, T. Kawada, M. Dokiya, Thermodynamic stability of perovskites and related compounds in some alkaline earth-transition metal-oxygen systems, J. Solid State Chem. 94 (1991) 106–120, https://doi.org/10.1016/0022-4596(91)90225-7.

[18] A. Brandão, J.F. Monteiro, A.V. Kovalevsky, D.P. Fagg, V.V. Kharton, J.R. Frade, Guidelines for improving resistance to CO_2 of materials for solid state electrochemical systems, in: Solid State Ionics, 2011, pp. 16–20, https://doi.org/10.1016/j.ssi.2010.02.006.

[19] C.W. Bale, P. Chartrand, S.A. Degterov, G. Eriksson, K. Hack, R. Ben Mahfoud, J. Melançon, A.D. Pelton, S. Petersen, FactSage thermochemical software and databases, Calphad 26 (2002) 189–228, https://doi.org/10.1016/S0364-5916(02)00035-4.

[20] S. Song, F. Jia, C. Peng, Study on decomposition of goethite/siderite in thermal modification through XRD, SEM and TGA measurements, Surf. Rev. Lett. 21 (2014), https://doi.org/10.1142/S0218625X1450019X.

[21] K. Wieczorek-Ciurowa, J.G. Shirokov, M. Paryło, Use of thermogravimetry to assess the effect of mechanical activation of selected inorganic salts, J. Therm. Anal. Calorim. 60 (2000) 59–65, https://doi.org/10.1023/A:1010116417154.

[22] H.E. Kissinger, Variation of peak temperature with heating rate in differential thermal analysis, J. Res. Natl. Bur. Stand. 57 (1956) 217–221.

[23] T. Hidayat, D. Shishin, S.A. Decterov, E. Jak, Thermodynamic optimization of the Ca-Fe-O system, Metall. Mater. Trans. B 47 (2016) 256–281, https://doi.org/10.1007/s11663-015-0501-0.

[24] P.K. Gallagher, S. St, J. Warne, Thermomagnetometry and thermal decomposition of siderite, Thermochim. Acta 43 (1981) 253–267, https://doi.org/10.1016/0040-6031(81)85183-0.

[25] M. Stir, K. Ishizaki, S. Vaucher, R. Nicula, Mechanism and kinetics of the reduction of magnetite to iron during heating in a microwave E-field maximum, J. Appl. Phys. 105 (2009), https://doi.org/10.1063/1.3148264.